Helmholtz resonators with integrated vibrating cantilevers for low-frequency noise control in aircraft sidewalls

Vom Promotionsausschuss der
Technischen Universität Hamburg
zur Erlangung des akademischen Grades
Doktor-Ingenieur (Dr.-Ing.)
genehmigte Dissertation (Monografie)

von
Hannah Hoppen
aus Nordhorn

2025

https://doi.org/10.15480/882.16226
https://orcid.org/0000-0001-7971-250X

1. Gutachter: Prof. Dr.-Ing. Otto von Estorff
2. Gutachter: Prof. Dr.-Ing. Wolfgang Gleine

Tag der mündlichen Prüfung: 09. Juli 2025

Für meine Familie.

Danksagung

Die vorliegende Dissertation wurde durch das Bundesministerium für Wirtschaft und Energie im Rahmen des Verbundprojekts Flight-LAB sowie durch ein Stipendium von Pro Exzellenzia Plus finanziell und ideell unterstützt. Ich danke beiden Fördergebern und den mitwirkenden Netzwerkpartnern herzlich.

Herrn Prof. Dr.-Ing. Wolfgang Gleine von der Hochschule für Angewandte Wissenschaften Hamburg danke ich für seine engagierte Betreuung, die inspirierenden Diskussionen und seine Unterstützung während der Promotion. Ebenso danke ich Herrn Prof. Dr.-Ing. Otto von Estorff, der mir die Promotion an der Technischen Universität Hamburg ermöglicht hat und mich stets mit praktischen Tipps und motivierenden Worten begleitet hat. Prof. Dr. Ralf God danke ich für die Übernahme des Vorsitzes der Prüfungskommission.

Für die Unterstützung bei der Vorbereitung und Durchführung der Experimente danke ich den Mitarbeitenden des Leichtbaulabors, des Labors für Kabine und Kabinensysteme, der Akustiklabore, bei Airbus und an der HAW Hamburg, sowie der studentischen Gruppe „Neues Fliegen“. Mein besonderer Dank gilt Bernd Schröder, Thomas Sterr und Marwin Peschmann für ihre kreativen Ideen und ihre Geduld bei den Iterationsschritten während des Probenbaus. Matthias Fehling, Christian Wischmann und Fabian Moser danke ich für ihre Hilfe bei verschiedenen Messkampagnen.

Meinen Mitdoktoranden Dr.-Ing. Florian Albrecht, Dr. Daniel Sadra und Dr.-Ing. Maximilian Schutzeichel danke ich für den wertvollen Austausch und ihr hilfreiches Feedback bei der Vorbereitung von Konferenzvorträgen.

Ich möchte mich ausdrücklich bei Dr.-Ing. Patrick Cordes und Dr.-Ing. Felix Langfeldt für das sorgfältige Korrekturlesen dieser Arbeit bedanken. Felix danke ich darüber hinaus für die gemeinsame Zeit im Büro, die zahlreichen fachlichen Diskussionen und seine stets motivierende Unterstützung in allen Phasen dieser Arbeit.

Von Herzen danke ich meinen Eltern, meinen Schwestern und meinen Freunden, die mich in der „Rush hour des Lebens“ begleitet und mir stets Rückhalt gegeben haben. Besonders danke ich meinem Ehemann Gerrit, der mir den nötigen Raum für meine Arbeit gegeben hat und immer an mich geglaubt hat. Unseren Kindern Ole und Pia danke ich für ihr Lachen, ihre Freude und die vielen kleinen Momente, die mir während der intensiven Arbeitsphasen Kraft, Inspiration und unerwartete Pausen geschenkt haben.

Abstract

For more efficient aircraft engines, the trend is toward larger bypass ratios and gear-driven fans or counter-rotating open-rotor engines. As a result, engine noise emissions will change to include not only broadband noise, but also discrete frequencies with high sound pressure levels in the low-frequency range. The current aircraft sidewall can be considered acoustically as a double wall consisting of the outer fuselage skin and the inner cabin lining with insulation material sandwiched in between these layers. This is a sufficient sound barrier in the high-frequency range i.e. above 1000 Hz, but in the low-frequency range, where a number of tones from the future aircraft engines are expected, the sound insulation is less effective in reducing noise. Due to lightweight aircraft design principles, better sound insulation cannot be achieved by increasing the double wall mass or spacing. Therefore, there is a need for a new concept of an aircraft sidewall with improved low-frequency sound insulation that does not notably increase the weight or space constraints of the conventional wall.

To address this challenge, this work presents a novel Helmholtz resonator type with two resonance frequencies integrated into an aircraft-like double wall to improve the sound transmission loss over a broader frequency spectrum, especially in the low-frequency range. The resonator incorporates a U-shaped slit that forms a cantilever. This cantilever provides a second resonance frequency, effectively broadening the frequency range with significant noise reduction. Constructed of a lightweight closed-cell foam, the resonator maintains its weight and volume compared to conventional Helmholtz resonators, offering a distinct advantage over the Helmholtz resonators with two resonance frequencies presented in the current literature.

In addition, an analytical model for the Helmholtz resonator with integrated cantilever is developed in this thesis. This model allows an accurate determination of resonance frequencies and an evaluation of the absorption and transmission behavior. Furthermore, the model is verified and validated by finite element simulations and experiments, respectively, and extended to analyze multi-layer structures using the transfer matrix method. Parameter studies based on these analytical models are used to identify tuning mechanisms of the resonance frequencies and geometry parameters that influence the noise reduction behavior of the resonator. Optimization calculations were carried out to design

a resonator panel that, when integrated into the aircraft sidewall, expands the frequency range of increased transmission loss in the low-frequency domain. This sound insulation improvement was successfully demonstrated in a laboratory test setup.

Contents

Nomenclature

Functions and scalars

a	Acceleration
$a_{\mathrm{CL}i}$	Modal participation factor of cantilever modes
b_{HR}	Modal participation factor of cantilever modes
$a_{n_y n_z}$	Modal participation factor of pressure amplitudes
c_0	Speed of sound
c	Spring stiffness
d	Layer thickness
f	Frequency
k	Wave number
k_i	Eigenvalues of cantilever mode shapes
i	Imaginary unit ($\mathrm{i} = \sqrt{-1}$)
m	Mass
m''	Surface mass density
l	Length or distance, respectively
l	Length of cantilever
p	Pressure
r	Sound pressure reflection coefficient
r_{s}	Flow resistance
$r_{n_y n_z}$	Trial functions of pressure modes
$s_{n_y n_z}$	Trial functions of particle velocity modes
s	Spacing
t	Sound pressure transmission coefficient
t	Time
t_{s}	Cantilever height
u	Displacement
v	(Particle) velocity
w	Width of cantilever
w_{s}	Width of slit

x, y, z	Cartesian coordinates
A	Cross section
B	Bandwidth
A_i, B_i, C_i, D_i	Elements of cantilever eigenvector
C_{HRCL}	Coupling parameter
D	Diameter
D	Cantilever mode factor
D_{w}	Flexural rigidity
E	Young's modulus
F	Force
F	Helmholtz resonator mode factor
H	Height of the resonator unit cell
H_{d}	Hydraulic diameter
H_{DW}	Double wall spacing
H_{GW}	Height of glass wool layer
H_{p}	Height of the resonator foam panel
H_{n1}	Transfer function with the reference being Mic. 1
I	Intensity
I_0	Modified Bessel function of first kind
I_y	Area moment of inertia
J	Cantilever-Helmholtz resonator-coupling factor
K	Cantilever-Helmholtz resonator-coupling factor
K	Bulk modulus
L	Length of the resonator unit cell
L_{p}	Length of the resonator panel
N	Total number of pressure modes
N_y	Number of pressure modes in y-direction
N_z	Number of pressure modes in z-direction
P	Power
Pr	Prandtl number
R_{HR}	Viscous losses in Helmholtz resonator neck
R_{s}	Specific gas constant
S	Area
S_{11}	Auto spectrum of microphone 1
S_{n1}	Cross spectrum of microphone n and 1
T	Temperature

$T_{i,j}$	(i,j)-element of transfer matrix
V	Volume
W	Width of the resonator unit cell
W_{p}	Width of the resonator panel
Z	Impedance
Z_0	Characteristic impedance
Z_{w}	Wall impedance
Z_{R}	Radiation impedance
α	Sound absorption coefficient
α_∞	Tortuosity
$\beta_{n_y n_z}$	Propagation constants
γ	Coherence
δ	Sound power dissipation coefficient
δ_{v}	Viscous boundary layer thickness
ε	Percentage difference in the relative bandwidth
ζ	Damping ratio
η	Structural loss factor
η_0	Dynamic viscosity of air
θ	Angle of incidence
κ	Adiabatic exponent / ratio of specific heats
λ	Wavelength
λ_i	Natural frequencies of cantilever modes
ν	Poisson's ratio
ρ	Density
ρ	Sound power reflection coefficient
σ	Flow resistivity
σ_{CL}	Area ratio of the cantilever to the unit cell
σ_{HR}	Area ratio of the Helmholtz resonator to the unit cell
σ_{R}	Radiation efficiency
τ	Sound power transmission coefficient
φ	Porosity
$\phi_{\mathrm{CL},i}$	Trial functions of cantilever mode shapes
ϕ_{HR}	Volumetric filling ratio
$\phi_{n_y n_z}$	Trial functions of pressure modes
ω	Angular frequency

Γ	Non-dimensional rotational end-fixity parameter
Γ_m	Rotational stiffness
Δ	Difference
Λ	Viscous characteristic length
Λ'	Thermal characteristic length
Φ	Phase angle
Ω	Dimensionless frequency

Matrices and vectors

Vectors and matrices are denoted as bold variables throughout this work.

$\mathbf{a}$	Amplitudes of the particle velocity
$\mathbf{b}$	Fluid-structure coupling vector
$\mathbf{c}$	Fluid-structure coupling vector
$\mathbf{e}$	Fluid-fluid coupling vector
$\mathbf{g}$	Fluid-fluid coupling vector
$\mathbf{p}$	Vector of design variables
$\mathbf{x}$	Vector of the unknowns
$\mathbf{v}$	Particle velocity
$\mathbf{A}$	Fluid modes
$\mathbf{S}$	System matrix
$\mathbf{T}$	Transfer matrix

Indices

a	Air
c	Coincidence
c	Characteristic
d	Damped, dissipated
d	Standing wave resonance
f	Finite-size
g	Glue
i	Incident

l	Lower
m	Mean
n	Normal
p	Panel
r	Reflected
s	Slit
t	Transmitted
u	Upper
v	Viscous
w	Wall
A	Mic. A
B	Mic. B
F	Fluid
L	Left side
L	Length
R	Right side
V	Volume
W	Width
ad	Standing wave anti-resonance
cav	Cavity
cont	Continuous
cr	Critical
diff	Diffuse
eff	Effective
eq	Equivalent
ext	External
fus	Fuselage
iso	Isothermal
lay	Layer
lim	Limiting
limp	Limp
lin	Lining
max	Maximum
res	Resonator
sp	Specimen

sum	Summed
tot	Total
LPM	Limp porous material
RR	Receiving room
SR	Source room
TR	Tonraum

Operators and other symbols

∇	Nabla operator
Δ	Laplace operator
Re	Real part
Im	Imaginary part

Abbreviations

CL	Cantilever
CROR	Counter-rotating open-rotor engines
DW	Double wall
FFT	Fast Fourier Transform
GFRP	Glass fiber reinforced plastic
GW	Glass wool
HR	Helmholtz resonator
HRCL	Helmholtz resonator with integrated cantilever
MDF	Medium-density fiberboard
Mic.	Microphone
PMMA	Polymethylmethacrylate
PMI	Polymethacrylimide
Ref.	Reference
TL	Transmission loss
UHBR	Ultra-high bypass ratio

1. Introduction

1.1. Background and motivation

As the transportation sector is the second largest contributor to global carbon emissions and climate change [136], manufacturers are challenged to continually reduce fuel consumption. Among various measures, the aircraft industry is focusing on minimizing fuel consumption by reducing the overall weight of the aircraft, optimizing its aerodynamics, and developing more efficient engines. The trend in developing more fuel-efficient engines is toward larger, gear-driven engines with ultra-high bypass ratios (abbreviated as UHBR) and counter-rotating open-rotor engines (abbreviated as CROR). However, both types of engines have the disadvantage of emitting a sound spectrum dominated by low-frequency tones. Tonal components at the blade passing frequencies and their harmonics are generated by the rotor/stator interaction in the UHBR and the propeller blades of the CROR, respectively [99, 131]. These low-frequency tones penetrate the current cabin wall more effectively than higher frequency sound, resulting in a high noise level in the cabin.

Exposure to high noise levels can cause health problems and significantly reduce crew and passenger comfort. A quiet cabin is therefore an important selling point for aircraft manufacturers. This requires the development of new noise control measures that can be integrated into today's aircraft sidewalls. In addition to high acoustic effectiveness, these noise control measures must meet other aircraft-related requirements, such as strict weight and space constraints, fire-resistant materials, low manufacturing effort and cost, and easy installation within the existing cabin design of the aircraft [121]. A recent study [84] indicates an overall reduction of the in-cabin cruise noise level compared to jet engines of the 1990s. However, the study shows a significant presence of low-frequency noise below 1000 Hz. This highlights the ongoing need to improve the low-frequency noise reduction of aircraft sidewalls while maintaining space and weight requirements, which is the focus of this thesis.

1.2. State of the art

The current aircraft sidewall, as shown in Fig. 1.1, can be considered acoustically as a double wall (DW) consisting of the outer fuselage structure (skin and stiffeners) and the inner cabin lining with embedded insulation, typically glass wool [97, 102]. While this configuration provides an effective sound barrier in the high-frequency range, i.e. above 1000 Hz, it is less effective in the low-frequency range, where multiple tones from future aircraft engines are expected. This is partly due to the low absorption behavior of thin acoustic insulation layers at low frequencies, and partly due to the drop in transmission loss at the double wall resonance frequency, both of which are described in detail in Chapter 2. The following subsections provide an overview of possible means to improve the transmission loss of double walls, as well as resonator designs with multiple resonance frequencies.

1.2.1. General measures to improve the transmission loss of double walls

In general, improving the transmission loss (TL) of a double wall in the low-frequency range can be achieved by increasing the wall spacing or by increasing the surface mass density of the walls. However, in various transportation applications such as aerospace, automotive, or rail, neither mass nor spacing can be added due to stringent weight and space requirements.

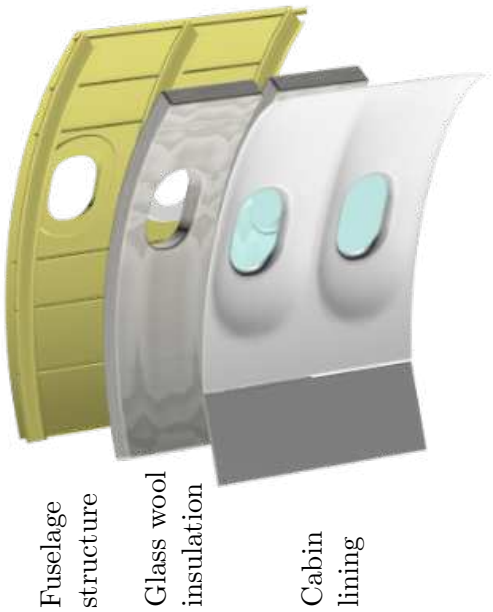

Figure 1.1: Drawing of the typical setup of an aircraft sidewall.

The transmission loss can be improved by replacing the air layer inside the double wall with a gas of different acoustic impedance, thereby increasing the impedance mismatch experienced by the sound wave. Experimental evidence supporting this approach has been demonstrated with helium for a single honeycomb panel [107] and also for double wall setups [7]. In Ref. [7], a broadband low-frequency transmission loss improvement ΔTL of approximately 7 dB between 180 and 250 Hz, as well as an improvement in the higher frequency range above 500 Hz of 10 dB or more, is demonstrated for a double wall setup under diffuse field incidence. Although this method offers a significant increase in transmission loss with minimal weight penalty, it requires substantial modifications to the wall infrastructure to contain helium within the double wall spacing. This limitation explains why the method has not yet been widely adopted for improving the transmission loss of double walls.

Microperforated absorbers can be integrated into double walls to increase the absorption within the air gap at low frequencies [114, 135]. In Ref. [114], microperforated absorbers were designed to enhance the transmission loss of double walls near the double wall resonance frequency. Analytical calculations predicted an increase of 2 to 5 dB in transmission loss for normal incidence sound around the double wall resonance frequency at 200 Hz. Small-scale impedance tube measurements under normal incidence demonstrated an improvement of approximately 2.5 dB in the higher frequency range above 400 Hz. Energy dissipation in microperforated absorbers occurs due to the movement of air within the perforations, resulting in viscous losses. However, the implementation of microperforated absorbers faces two manufacturing challenges: Firstly, to function as a broadband absorber, the holes should have a diameter of less than 0.2 mm combined with a perforation ratio around 0.05 %, resulting in more than 100,000 holes per square meter [119]. Secondly, the microperforated absorber must be relatively stiff to prevent structural resonances within the frequency range of interest and to ensure that the relative velocity of air movement inside the perforations is not affected [15, 119]. Consequently, the design of lightweight microperforated absorbers is difficult.

Easier to manufacture are insulation layers with embedded mass inclusions implemented in the double wall spacing. Refs. [65] and [123] demonstrate the potential of foam layers with embedded masses to reduce the sound radiation of single panels in the low-frequency range. These foam layers can also be integrated into a representative aircraft double wall to reduce the vibration levels of the fuselage wall, potentially reducing sound transmission through the double wall. However, an increased transmission loss has not been demonstrated [59, 60]. A similar approach was explored in Ref. [100], where vibration absorbers with cylindrically shaped masses embedded in a foam layer between a double wall were developed and optimized to reduce the dynamic response of double wall panels. However, a

proof-of-concept experimental setup to verify the resulting transmission loss improvement has not been conducted.

The term *vibration absorber* has also been used to describe small, laser-cut resonant mass-spring structures made of polymethylmethacrylate (PMMA) that have been attached to aircraft floor panels to reduce their vibration [121]. These dynamic vibration absorbers, arranged in a repeating structure, are referred to as vibro-acoustic metamaterials in subsequent research publications [24, 33]. Among other applications, these metamaterials were applied to the lighter wall of a double wall assembly to increase the transmission loss at the double wall resonance frequency [33]. This configuration achieved an insertion loss improvement (compared to a mass equivalent double wall) of approximately 8 dB in a narrow frequency band around the double wall resonance frequency of around 530 Hz measured in a small acoustic cabin. Likewise, additively manufactured resonators have been applied to a fuselage structure panel to increase the transmission loss at the resonance frequency of the cylindrical structure, the so-called ring frequency, which depends on the cylinder radius and longitudinal wave velocity [40].

The term *metamaterial* describes an artificial material with properties not found in nature. Typically, metamaterials consist of a periodic arrangement of unit cells of conventional materials. The design and properties of the periodically arranged unit cells can lead to unusual material properties when subjected to wave propagation phenomena, such as negative density and/or negative bulk modulus. This special behavior offers a wide range of revolutionary applications in vibroacoustics.

In recent decades, acoustic metamaterials have received a lot of research attention [31, 87, 89]. Among them, various types of membrane-type acoustic metamaterials have been implemented to improve the transmission loss of double walls [79, 106]. Ref. [79] showed experimentally a diffuse field sound transmission loss improvement of approximately 6 dB at the anti-resonance frequencies of the metamaterials, while the setup has an increased weight of approximately 34 % compared to the empty double wall. Membrane-type acoustic metamaterials consist of a prestressed thin membrane with periodically attached masses, divided by a grid into small unit cells. To overcome the need for a grid structure, which dominates the weight of membrane-type acoustic metamaterials [79], as well as the need for a prestressed membrane, plate-type acoustic metamaterials have been introduced. These plate-type acoustic metamaterials consist of a thin plate with periodically attached masses [77, 86]. The study in Ref. [86] investigated a setup in which a plate-type acoustic metamaterial was applied as the thinner wall of a double wall system. Measurements conducted in a small-scale impedance tube demonstrated a transmission loss improvement of 8 dB at the double wall resonance frequency at 500 Hz. Both types of metamaterials, membrane- and plate-type acoustic metamaterials, are only effective

in a narrow frequency band around their anti-resonance frequency. This limitation can be overcome by arranging the metamaterials in multiple layers, called stacks [144], or by incorporating multiple masses within a unit cell [78, 83]. Another approach to increase the bandwidth is to use plate-type acoustic metamaterials with Helmholtz resonators (HR) as masses. In addition to the anti-resonance frequency of plate-type acoustic metamaterials, the resonance frequency of the Helmholtz resonators introduces a second region of high noise reduction [82].

Although extensively discussed in the literature, Helmholtz resonators are currently receiving considerable attention in the context of metamaterials. For example, periodically arranged Helmholtz resonators with multiple Helmholtz resonators within a unit cell [46, 142, 143] or Helmholtz resonators embedded in a fibrous material are also considered as metamaterials [48, 73]. While stand-alone Helmholtz resonators are only effective in a narrow frequency band around their resonance frequency, properly tuned Helmholtz resonators embedded within the double wall spacing can lead to a broadband improvement in transmission loss [81] in the low to mid frequency region. However, in the higher frequency range, the transmission loss is lower compared to a double wall without resonators. Kuntz et al. [70] integrated different Helmholtz resonators into one or both walls of an aircraft double wall. One example of theses resonators were specifically tuned to the propeller tones of propeller-driven aircraft, achieving a substantial noise reduction of 13 dB at the resonator resonance frequencies compared to the same configuration with closed resonators. In Ref. [132], Helmholtz resonators embedded in the insulation within the air space of a double wall and tuned to the double wall resonance frequency were found to increase the transmission loss in a small band around the resonance frequency. However, Mason and Fahy [95] observed that Helmholtz resonators tuned to resonance frequencies higher than the double wall resonance frequency could result in a broadband improvement in transmission loss. The explanation given by Langfeldt et al. [81] is as follows: Helmholtz resonators embedded in the double wall spacing result in a reduced stiffness of the air layer. This is because, at frequencies below the resonance frequency of the Helmholtz resonator, the bulk modulus of air with Helmholtz resonators is smaller than the bulk modulus of the air layer without resonators. The reduced stiffness of the air layer with resonators consequently leads to a reduced double wall resonance frequency, thereby increasing the transmission loss with a slope of 18 dB/octave at lower frequencies. The strength of the reduced bulk modulus depends primarily on the filling ratio, defined as the volume of the resonator cavity divided by the volume of the double wall air gap. Both the magnitude and the bandwidth of the transmission loss improvement increases as the filling ratio increases [81]. Therefore, in Ref. [81], a double wall setup with integrated Helmholtz resonators was designed to ensure a high filling ratio of 56 %. Diffuse field

transmission loss measurements showed a peak transmission loss improvement of about 29 dB at the Helmholtz resonator resonance frequency and a broadband transmission loss improvement of 10 dB and more between approximately 250 and 480 Hz, both compared to a mass equivalent double wall.

The above mentioned noise reduction means, that are implemented and measured in double wall setups, are summarized in Table 1.1. The table provides an overview of the actual achieved transmission loss, the frequency regions affected, and the additional weight of the noise reduction means, along with their main advantages and disadvantages. However, these noise control means cannot be directly compared, as the measurement principles vary between normal and diffuse field incident sound. Furthermore, the double wall setups differ in terms of wall masses and wall spacings, which significantly influence the noise reduction potential, as further explained in Section 2.3.3.

Table 1.1 highlights the potential of Helmholtz resonators to improve the transmission loss of double walls in a broadband frequency region. Amongst the listed noise reduction means, the Helmholtz resonators presented in Ref. [81] demonstrate the highest transmission loss improvement, while contributing the least additional weight. This high noise reduction was mainly achieved because of the high filling ratio of the Helmholtz resonators. However, the space available for resonators is often constrained by design principles, limiting the maximum achievable filling ratio. For example, in aircraft sidewalls, the space inside the double wall is also occupied by insulation layers and other systems such as ventilation, further limiting the maximum possible filling ratio. As suggested in [52], Helmholtz resonators with multiple resonance frequencies can be integrated into double walls when the space available for Helmholtz resonators is insufficient. The following subsection gives an overview of Helmholtz resonators with multiple resonance frequencies presented in the literature.

Table 1.1: Summary of noise reduction means incorporated in double walls.

Description of double wall setup	Measurement principle	Eff. noise reduction	Frequency (region)	Surface mass density of noise reduction means	% weight of DW	Double wall spacing	Advantages Disadvantages	Source
		dB	Hz	kg/m^2	%	mm		
Air layer of DW replaced by helium	Diffuse field TL	7 ≥10	180-250 >500	n/a	n/a	n/a	+ Broadband noise reduction + No or little add. weight (not specified in Ref. [7]) − Significant modification of conv. DW necessary	[7]
Microperforated absorber inside DW	TL from imp. tube	(2-5) 2.5	(200) >400	2.7	33	70	+ (Analytically calculated high ΔTL at DW res. freq.) + Broadband ΔTL at high freqs. − Design of lightweight microperforated absorber difficult	[114]
Vibro-acoustic metamaterial outside DW	Small acoustic cabin, IL	8	530	2.4	33	8	+ High noise reduction at resonance frequency − High additional weight and manufacturing effort, each resonator glued separately onto panel	[33]
Membrane-type acous. metam. inside DW	Diffuse field TL	6	145 194	3.5	34	102	+ High noise reduction at anti-resonance frequencies − Narrow frequency region of noise reduction − High additional weight and manufacturing effort	[79]
Plate-type acous. metamaterial as one wall of DW	TL from imp. tube	8	500	1.73	55	25	+ High noise reduction at anti-resonance frequency − Narrow frequency region of noise reduction − High additional weight and manufacturing effort	[86]
Helmholtz res. inside DW	Diffuse field TL	13	234	5.5	30	165	+ High noise attenuation at HR resonance frequency − High additional weight	[70]
Helmholtz res. inside DW	Diffuse field TL	29 ≥10	325 250-480	0.9	12	45	+ High noise attenuation at HR resonance frequency + Broadband noise reduction at low frequencies − High volumetric filling ratio of HR needed	[81]

1.2.2. Helmholtz resonators with multiple resonance frequencies

A general drawback of Helmholtz resonators in absorption applications outside of double walls is their narrow bandwidth. To overcome this limitation, considerable efforts have been made to design Helmholtz resonators with two or more resonance frequencies. One possible design is a double chamber Helmholtz resonator, as proposed similarly by Xu et al. [140] and Tang et al. [133]. This Helmholtz resonator consists of two cavities in series, consequently exhibiting two resonance frequencies and is depicted in Fig. 1.2 a). The addition of the second neck and cavity increases the overall height H and mass of the resonator compared to a single resonator. Griffin et al. [75] present a resonator design with a constant resonator height H but an increased width W. In this design, two Helmholtz resonators are coupled by connecting the cavities with a separating membrane, as shown in Fig. 1.2 b). Another approach is demonstrated by Sanada and Tanaka [120], where a membrane or flexible plate is installed inside the cavity of the Helmholtz resonator to add a second resonance frequency, as visualized in Fig. 1.2 c). Notably, the overall volume of the resonator is not increased compared to a conventional Helmholtz resonator, but the manufacturing effort is heightened by installing a membrane inside the cavity. The manufacturing effort is reduced in the resonator design proposed by Nudehi et al. [110] and Kurdi et al. [71] (as shown in Fig. 1.2 d), where the flexible plate is installed as the

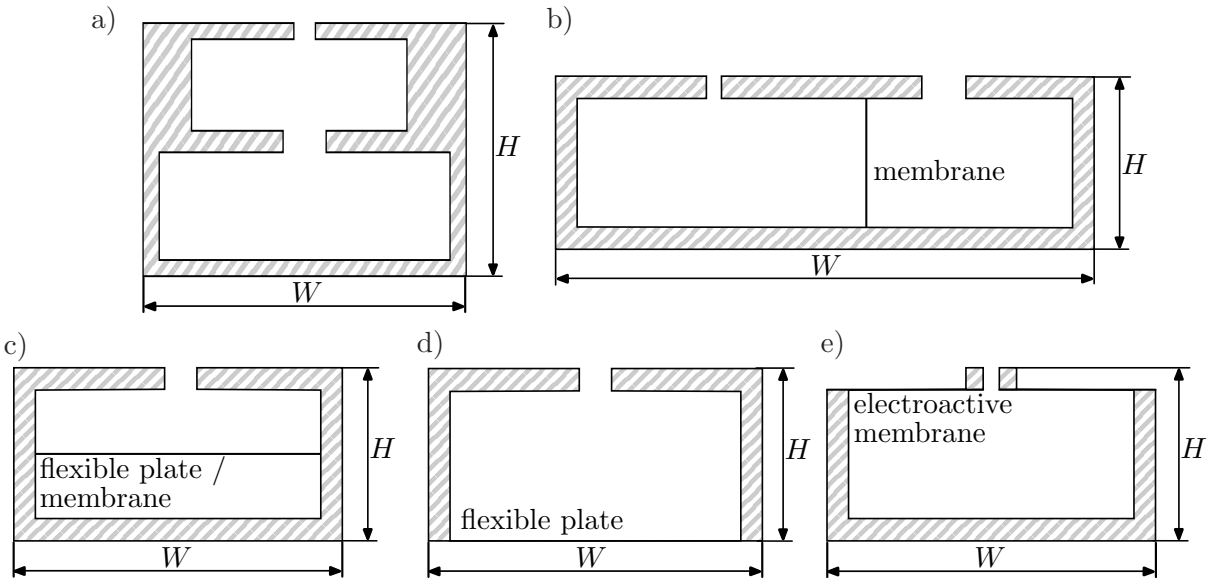

Figure 1.2: Overview of the different designs of Helmholtz resonators with multiple resonance frequencies found in literature. a) Double chamber Helmholtz resonator as in Refs. [133, 140]. b) Two connected Helmholtz resonator cavities separated by a membrane as in Ref. [75]. c) Helmholtz resonator with a membrane inside the cavity as in Ref. [120]. d) Helmholtz resonator with a flexible end plate as in Refs. [71, 110]. e) Helmholtz resonator with an electroactive polymer membrane as in Ref. [120].

resonator end plate. This flexible plate introduces a second resonance peak in addition to the Helmholtz resonator resonance frequency itself. Abbad et al. [1] used an electroactive polymer membrane as the front or end plate to tune the resonance frequency of the membrane, as shown in Fig. 1.2 e). However, it should be noted that the use of a flexible plate or membrane still increases the fabrication effort compared to a conventional Helmholtz resonator due to the use of multiple materials. This literature review emphasizes the need for a new type of resonator with two resonance frequencies that does not increase the size, weight, or manufacturing effort compared to conventional Helmholtz resonators.

The studies cited above on Helmholtz resonators with multiple resonance frequencies have primarily focused on modeling the absorption behavior without accounting volume and weight constraints. Since this work focuses on a resonator that can be embedded in an aircraft double wall, the resonator design must meet high weight and space requirements. These requirements are further specified in Chapter 6 and in Ref. [52]. According to Ref. [98], when noise reduction technologies are implemented, the space requirement reduces to a depth constraint. This is because sound absorbers or metamaterials are typically designed to cover large surface areas, which are considerably larger than the dimensions of a single unit cell in a metamaterial. In particular, the resonator must fit inside the aircraft double wall and therefore must not exceed specific thickness requirements. For the resonators discussed, this corresponds to the maximum height H, as illustrated in Fig. 1.2.

Fig. 1.3 provides an overview of the height and weight of the resonator designs with multiple resonance frequencies found in the literature and cited above. The total weight of the resonators is given in relation to their respective base area, so that the resonators can be compared on the basis of their surface mass densities. The resonance frequencies of the resonators are plotted against the height and surface mass density, respectively.[1]

The yellow shaded areas in Fig. 1.3 represent the space and weight requirements for the noise control treatment to be implemented inside an aircraft double wall, as described in more detail in Chapter 6 and in Ref. [52].

The previously cited Helmholtz resonators with multiple resonance frequencies were not designed for integration into an aircraft side wall. As noted above, these studies focused primarily on modeling the absorption behavior without consideration of volume and weight constraints. As shown in Fig. 1.3, the height and weight of the resonators presented in the literature are outside the tolerated limits: Especially the weight requirement cannot be met by far. An analysis of whether the presented resonators would meet aircraft

[1] Authors were contacted for additional information on their presented resonator designs if not precisely described in the article. If the authors did not respond, the weight of the resonators was estimated from the material and geometry details provided in the literature. The resonator design of Xu et al. [140] is not included in Fig. 1.3 because no material information was provided.

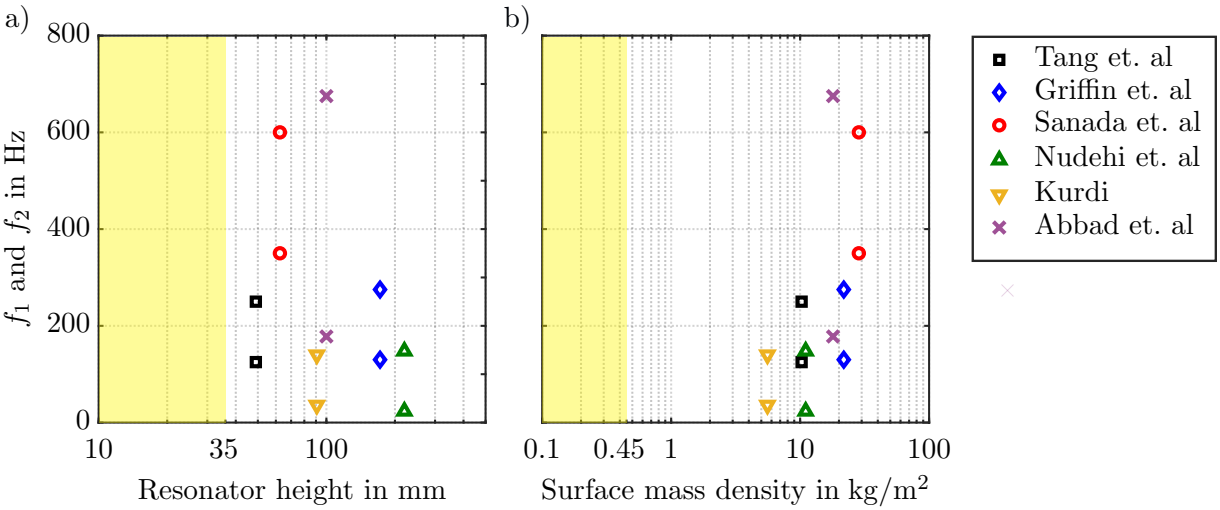

Figure 1.3: Selected properties of Helmholtz resonators found in literature not beeing adapted for aircraft cabin double wall applications. The yellow shaded areas represent the space and weight requirements for the noise control treatment to be implemented inside an aircraft double wall. a) Resonance frequency over resonator height. b) Resonance frequency over resonator surface mass density.

specifications if constructed from alternative materials or with modified dimensions was not conducted.

Instead, a new type of resonator exhibiting two resonance frequencies has been proposed, potentially fulfilling the weight, space, and frequency requirements of the aircraft industry. The design of the new resonator type has been patented [53] and is presented in the following section.

1.3. Novel resonator design

To overcome the aforementioned limitations of Helmholtz resonators with two resonance frequencies, this thesis introduces a Helmholtz resonator design with two resonance frequencies where the overall mass and volume of the resonator remain unchanged compared to a conventional Helmholtz resonator. This is a significant advantage especially for weight and volume-dependent applications such as aerospace or automotive. An additional advantage is that the manufacturing effort for this resonator is no higher than for a similarly constructed conventional Helmholtz resonator.

In this resonator design, a second resonance frequency is introduced by incorporating a cantilever as a mechanical resonator. Photos of the novel Helmholtz resonator are shown in Figs. 1.4 a) and b) for the top and bottom views, respectively. As can be seen, a U-shaped slit forms the neck of the Helmholtz resonator on the top side, with the effect that a cantilever remains between the sides of the “U”. The resonator is designed such that the

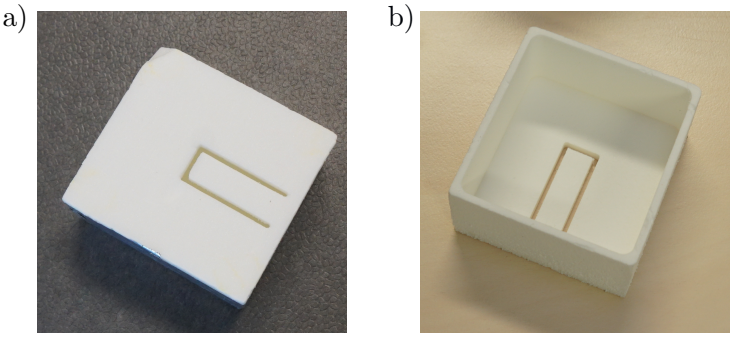

Figure 1.4: Photographs of the novel resonator design. a) Top view. b) Bottom view.

length of the Helmholtz resonator neck is equal to the thickness of the cantilever, and the cantilever is an integral part of the resonator body. The resonator consists of two parts: a resonator body, as shown in Fig. 1.4 b), and a back plate that is bonded to the resonator body. At this stage of development, the resonator is manufactured by milling. The milling process for the resonator with integrated cantilever is no more laborious than that for a conventional Helmholtz resonator. To meet the weight requirements, the resonator is made of a closed-cell foam, which is an unusual material for resonators. The density of this lightweight material is only a small fraction of the density of materials commonly used for acoustic resonators. For example, the density of the foam is about 2.5 % of that of the acrylic glass used for the resonators in Refs. [1, 75, 120, 133] and 1.5 % of that of the aluminum used for the resonators in Refs. [71, 110]. The resonator design presented in this thesis weighs less than 2 g and significantly outperforms the weight of the resonators in the literature.

1.4. Aims and scope of this work

The present study investigates a modified Helmholtz resonator design that combines a classical Helmholtz resonator with a vibrating cantilever. The properties of this coupled resonator design will be investigated with respect to its acoustic performance, the tunability of the resonance frequencies, and its potential for lightweight integration into aircraft sidewalls. The objective is to predict and model the coupled vibroacoustic behavior of the system.

Preliminary considerations indicate that the coupling between the mechanical and acoustic modes must be taken into account due to the lightweight nature of the material, as this can significantly influence the resonant behavior of the resonator.

The expected results will be used to assess the applicability of Helmholtz resonators with integrated cantilevers as a lightweight means to improve the low-frequency sound insulation of double-wall structures in aircraft applications.

To give a brief overview, the research questions answered in this thesis are:

- How can Helmholtz resonators with integrated cantilever be modeled?
- How can the model of the Helmholtz resonator with integrated cantilever be simplified?
- How can the resonance frequencies be tuned?
- How do the geometric dimensions of the resonator influence the noise reduction behavior of the Helmholtz resonator with integrated cantilever?
- Is it possible to further improve the transmission loss of aircraft double walls by inserting Helmholtz resonators with integrated cantilevers compared to embedding conventional Helmholtz resonators?

The thesis is organized as follows: Chapter 2 introduces the necessary theoretical background for the following chapters. In addition to explaining the means of noise control through absorption and transmission loss, the transfer matrix method is introduced. This method is used in analytical models for multi-layer setups. The chapter concludes with an explanation of the measurement techniques used in this research, namely impedance tube and sound transmission loss measurements. Chapter 3 is devoted to the derivation of the analytical model of Helmholtz resonators with integrated cantilevers. The model is used to calculate the resonance frequencies, absorption and transmission behavior of the resonator. Furthermore, this model forms the basis for a transfer matrix of a panel with attached Helmholtz resonators with integrated cantilevers. In Chapter 4, the derived models are verified numerically using the finite element method and validated experimentally. These validated models are then used for parameter studies in Chapter 5. The analysis focuses on the influence of varying geometric and material properties on the resonance frequencies, the absorption coefficient, and the transmission loss of the resonator. The results of Chapter 5 are used in combination with optimization calculations in Chapter 6 to design and construct a resonator panel for an aircraft-like model. The sound transmission loss of different multi-layer setups incorporating this panel is measured to investigate if and how the panel can improve the transmission loss of an aircraft double wall. Finally, Chapter 7 presents a conclusion summarizing the main results of the work. Additionally, it provides an outlook for possible future research activities.

2. Theoretical background

This chapter provides the theoretical background for the derivations and experiments presented in the following chapters. The chapter begins by explaining the basic physical behaviors of sound propagation, sound absorption, and sound transmission. The transfer matrix method is introduced as it is used to analyze multi-layer structures. The chapter concludes with a demonstration of the measurement techniques used and the required equations.

2.1. Sound propagation in compressible non-viscous fluids

In compressible, non-viscous fluids, sound propagates only as longitudinal waves. The sound field is described by the sound pressure p, the sound density ρ and the sound particle velocity $\mathbf{v}$. Sound pressure and density are scalar quantities, while the particle velocity is a vector pointing in the direction of propagation of the sound waves. The fluid parameters (index "tot") consist of a constant static part (index "0") and a time-dependent oscillating part (no index) [85]

$$\begin{aligned} p_{\text{tot}} &= p_0 + p, \\ \mathbf{v}_{\text{tot}} &= \mathbf{v}_0 + \mathbf{v}, \\ \rho_{\text{tot}} &= \rho_0 + \rho. \end{aligned} \tag{2.1}$$

In acoustics, the static part of the pressure p_0, i.e. the ambient pressure, and of the density ρ_0, i.e. the density of the fluid at rest, are typically much larger than their oscillating parts. The following equations are derived under the assumption that the acoustic density perturbations ρ are significantly smaller than the mean density ρ_0 in the fluid and that ρ_0 is independent of location. Applying Newton's second law of motion, to the fluid in all three Cartesian coordinate dimensions yields [85]

$$-\text{grad}(p) = \rho_0 \frac{\partial \mathbf{v}}{\partial t}, \tag{2.2}$$

which is the linearized equation of motion for non-viscous fluids. The linearized conservation of mass equation for the transient, compressible case is

$$\frac{\partial \rho}{\partial t} = -\rho_0 \mathrm{div}(\mathbf{v}). \tag{2.3}$$

In general, acoustic changes of state can be expressed by the adiabatic equation of state, since the heat exchange with the environment can be neglected due to fast density variations. With the adiabatic exponent κ and the speed of sound c_0, the equation for the adiabatic change of state is [101]

$$\frac{\partial p}{\partial \rho} = c_0^2 = \kappa \frac{p_0}{\rho_0}. \tag{2.4}$$

This equation directly relates sound pressure to density variations. The speed of sound

$$c_0 = \sqrt{\kappa R_\mathrm{s} T} = \sqrt{\frac{\kappa p_0}{\rho_0}} \tag{2.5}$$

depends on the temperature T and on the fluid, as the adiabatic exponent κ and the specific gas constant R_s are fluid specific. The linear acoustic wave equation for the pressure is obtained by differentiating Eq. (2.2) with respect to space, differentiating Eq. (2.3) with respect to time t, and using the equation of state (Eq. (2.4))

$$\Delta p = \frac{1}{c_0^2} \frac{\partial^2 p}{\partial t^2}, \tag{2.6}$$

with Δ being the Laplace operator. This equation is called the homogeneous wave equation and it describes the behavior of small sound pressure variations in a fluid in terms of time and space. Assuming time-harmonic oscillations of the sound pressure waves with the time factor $\exp(\mathrm{i}\omega t)$, $\mathrm{i} = \sqrt{-1}$, and the angular frequency $\omega = 2\pi f$, the Helmholtz equation

$$\Delta p + k_0^2 p = 0 \tag{2.7}$$

follows from the wave equation, where the wave number k_0 is defined as

$$k_0 = \frac{\omega}{c_0}. \tag{2.8}$$

For plane waves propagating in x-direction, the solution of the Helmholtz equation for pressure waves can be expressed as

$$p(x) = p_\mathrm{i} \cdot e^{-\mathrm{i}k_0 x} + p_\mathrm{r} \cdot e^{+\mathrm{i}k_0 x}, \tag{2.9}$$

where p_i and p_r are the complex pressure amplitudes traveling in +x and -x-direction, respectively. If the fluid is unbounded, only the pressure wave traveling in +x-direction is considered

$$p(x) = p_\mathrm{i} \cdot e^{-\mathrm{i}k_0 x}. \tag{2.10}$$

The equation of motion (Eq. (2.2)) provides the relationship between pressure and particle velocity. For example, the particle velocity in the x-direction in the time-harmonic case is

$$v_x = -\frac{1}{\mathrm{i}\omega\rho_0}\frac{\partial p}{\partial x}. \tag{2.11}$$

The ratio of the pressure to the normal component of the particle velocity

$$Z = \frac{p}{v_\mathrm{n}} \tag{2.12}$$

is called the acoustic impedance [13]. For plane propagating waves, the acoustic impedance is a real-valued quantity and is characteristic of the medium. It is also known as the characteristic impedance [13]

$$Z_0 = \rho_0 c_0. \tag{2.13}$$

Another fluid-specific quantity is the bulk modulus K_0, which defines the resistance of a fluid to compression and can be expressed as

$$K_0 = \rho_0 c_0^2 = \kappa p_0. \tag{2.14}$$

The acoustic energy flowing through a unit area perpendicular to the specified direction per unit time is described by the sound intensity and can be calculated for plane waves via

$$\mathbf{I} = p \cdot \mathbf{v} = \frac{|p^2|}{2\rho_0 c_0}. \tag{2.15}$$

Integrating the sound intensity over an area perpendicular to the direction of the traveling sound waves gives the sound power

$$P = \int_S \mathbf{I}\mathrm{d}S. \tag{2.16}$$

2.2. Sound absorption

When a sound wave hits a structure, the energy of the incoming wave is partially reflected, partially dissipated, and partially transmitted through the structure, as illustrated in Fig. 2.1. The transmitted part will be discussed in Section 2.3. The reflection of a plane

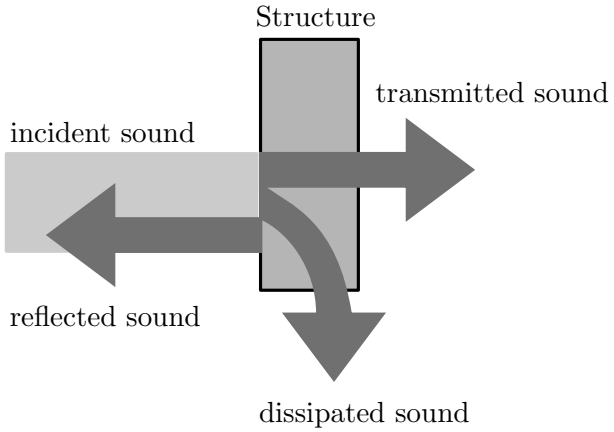

Figure 2.1: Sound reflection, transmission and dissipation of a sound wave at a structure.

wave can be described by the complex sound pressure reflection coefficient r, which is defined as the ratio of the reflected (index "r") and incident (index "i") complex pressure amplitudes (cf. Fig. 2.2)

$$r = \frac{p_\mathrm{r}}{p_\mathrm{i}}, \tag{2.17}$$

or by the sound power reflection coefficient ρ, which is defined as the power ratio of the reflected and incident waves

$$\rho = \frac{P_\mathrm{r}}{P_\mathrm{i}}. \tag{2.18}$$

The pressure and power reflection coefficients are related to each other via

$$\rho = |r|^2. \tag{2.19}$$

The reflection coefficient depends on the wall impedance Z_w of the boundary surface, which characterizes the acoustic properties of the structure. It is defined as the ratio of the sound pressure p to the normal component of the particle velocity v_n at the surface of the structure ($x = 0$ in Fig. 2.2) [101]

$$Z_\mathrm{w} = \frac{p(0)}{v_n(0)}. \tag{2.20}$$

With the wall impedance Z_w and the characteristic impedance of the fluid medium Z_0, the complex pressure reflection coefficient is given by [13]

$$r = \frac{Z_\mathrm{w} - Z_0}{Z_\mathrm{w} + Z_0}. \tag{2.21}$$

Sound absorbing devices are typically characterized by the sound power absorption coefficient. The absorption coefficient quantifies the amount of energy of the incident wave that

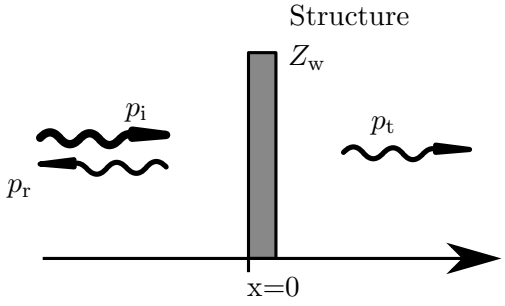

Figure 2.2: Schematic drawing of incident, reflected and transmitted pressure waves.

is not reflected by the structure. The energy is either dissipated (index "d") within the structure, characterized by the dissipation coefficient $\delta = P_d/P_i$, or transmitted (index "t") through the structure, characterized by the transmission coefficient $\tau = P_t/P_i$. The absorption coefficient is the sum of the dissipation and transmission coefficients

$$\alpha = \delta + \tau. \tag{2.22}$$

If the sound absorber is placed in front of a fully reflecting wall, the transmission coefficient is 0 and the absorption coefficient is equal to the dissipation coefficient. It can be calculated for normal incidence sound using [45, 103]

$$\begin{aligned} \alpha &= 1 - |r|^2 \\ &= \frac{4Z_0 \mathrm{Re}(Z_w)}{(\mathrm{Re}(Z_w) + Z_0)^2 + \mathrm{Im}(Z_w)^2}, \end{aligned} \tag{2.23}$$

where $\mathrm{Re}(Z_w)$ and $\mathrm{Im}(Z_w)$ describe the real and imaginary parts of the complex-valued wall impedance, respectively. This equation is called the *matching law*, because it shows that complete absorption ($\alpha = 1$ and $r = 0$) occurs when the wall impedance Z_w is equal to (or matches) the characteristic impedance of the fluid Z_0. Since the characteristic impedance Z_0 is real, complete absorption can only be achieved if the real part of the wall impedance is equal to the characteristic impedance, i.e. $\mathrm{Re}(Z_w) = Z_0$, and the imaginary part of the wall impedance is zero, i.e. $\mathrm{Im}(Z_w) = 0$. Any imaginary part of the wall impedance reduces the absorption behavior.

Various types of sound absorbers are used for general noise control or to influence the acoustic properties of a room. These can be divided into porous sound absorbers and resonant sound absorbers. Porous sound absorbers are also referred to as resistive absorbers, while resonant absorbers are referred to as reactive absorbers. Porous materials are typically made of fibrous, foam, and granular materials and are described in Section 2.2.1. Resonant absorbers can be classified into absorbers based on acoustic and mechanical res-

onators. Acoustic resonant absorbers include perforated plate resonators and Helmholtz resonators, which are used in this thesis and are further discussed in Section 2.2.2. Mechanical resonators include plate absorbers, membrane absorbers, and foil absorbers. The plate, membrane, or foil is placed as a mass in front of a layer of air that acts as a spring, and together they form a mass-spring system. The different types of absorbers can be combined to optimally leverage their specific advantages. Some examples are described by Fuchs [45].

2.2.1. Porous absorbers

Materials that act as porous absorbers are described by two phases: The first phase is called the solid phase and forms the structure, or skeleton, of the material. The second phase is the fluid phase. The solid structure contains internal pores and channels that are saturated with the fluid phase (here: air). When a porous material is set in motion by acoustic excitation, energy is dissipated from the system by the friction of the fluid particles against the skeleton. This means that the kinetic energy of the fluid particle is converted to heat by viscous losses and is inevitably removed from the sound field. Energy dissipation also occurs due to thermal conduction between the fluid and the solid phase, mainly at very low frequencies, as well as due to structural damping of the solid phase, but overall these dissipation mechanisms have a small effect compared to the viscous losses, as discussed in more detail in Ref. [32].

Porous materials absorb sound effectively when the particle velocity amplitude is high. When a plane acoustic wave hits a rigid wall, the maximum particle velocity occurs at a quarter of the acoustic wavelength in front of the wall. Since the acoustic wavelength increases with decreasing frequency, porous absorbers must be very thick to effectively absorb sound at low frequencies. Therefore, porous absorbers are mostly used to absorb high-frequency sound [103]. If an absorber blanket with a thickness smaller than one quarter of the wavelength is to be used, it can be installed with an air gap in front of the rigid wall, such that the combined thickness of the air gap and the absorber blanket corresponds to a quarter wavelength.

Various models for calculating the acoustic behavior of porous materials have been described and presented in literature, e.g. in Refs. [3, 11, 35]. Among them, the equivalent fluid method replaces a layer of a porous material with a layer of an equivalent fluid. Thus, in the equivalent fluid method, the porous material, which has a solid phase and a fluid phase, is modeled by a fluid phase only. The equivalent fluid method is valid only under the long-wavelength condition. This condition is met when the acoustic wavelength is much larger than the microscopic size of the pores and channels in the porous material.

Furthermore, the method is applicable when the elastic properties of the solid phase are negligible or when the solid phase of the porous material is assumed to be motionless [2]. Using this method, the equivalent fluid is described by a complex effective density ρ_{eff} and a complex bulk modulus K_{eff}, both of which are frequency-dependent. In this study, the well-established empirical Johnson-Champoux-Allard model [2] is applied. The model uses five material parameters typical of porous materials:

- **Porosity:** The porosity φ is defined as the ratio of the air volume V_{a} to the total volume V_{tot} of the porous material:

$$\varphi = \frac{V_{\text{a}}}{V_{\text{tot}}} < 1. \tag{2.24}$$

  The porosity is also called open porosity or connected porosity and considers only the volume of air that is not completely surrounded by the frame of the porous material (i.e. closed porosity). The open porosity is close to 1 for most fibrous materials and light foams [2].

- **Tortuosity:** The tortuosity α_∞ characterizes the internal structure of the material and is also known as the structure form factor. When a fluid particle passes through a porous material, it is guided through the structure of the solid phase on a path (with length l_{eff}) that is longer than the thickness d of the sample. The deviation of the different lengths defines the tortuosity, which can be determined experimentally [4]. It is worth noting that different definitions of tortuosity are given in the literature [47]. One expression is the ratio of the mean effective length l_{eff} to the sample thickness d squared

$$\alpha_\infty = \left(\frac{l_{\text{eff}}}{d}\right)^2. \tag{2.25}$$

  The tortuosity is dimensionless and typically has values greater than 1.

- **Flow resistivity:** The flow resistivity σ describes the resistance of a material to air flow. It is defined as the ratio of the pressure difference between both sides of a material $(p_1 - p_2)$ to the mean air velocity v_{m} per unit thickness d of the material and can be expressed by [88]

$$\sigma = \frac{p_2 - p_1}{v_{\text{m}} d}. \tag{2.26}$$

  The flow resistivity, also known as the specific flow resistance, is a material constant that is independent of the thickness of the material. Whereas the flow resistance $r_{\text{s}} = (p_1 - p_2)/V$ increases with increasing material thickness [103]. The flow resistivity of fibrous materials and open-celled foams is generally between 1000 and 100,000 $\text{N}\,\text{s}\,\text{m}^{-4}$.

- **Viscous and thermal characteristic length:** To account for viscous and thermal effects on the effective density and effective bulk modulus of porous layers, Johnson et al. [63] introduced the viscous characteristic length Λ and Champoux and Allard [22] introduced the thermal characteristic length Λ'.

  The viscous and thermal characteristic lengths are average dimensions of the pores and channels of porous materials, that are related to viscous and thermal losses, respectively. As shown in Fig. 2.3, the viscous characteristic length Λ can be seen as the average radius of the smaller pores or channels, and the thermal characteristic length Λ' as the average radius of the larger pores. The viscous and thermal characteristic lengths cannot be measured directly, but can be estimated e.g. using impedance tube measurements [6], while the thermal characteristic length is often about twice the viscous characteristic length $\Lambda' = 2\Lambda$ [2].

To provide specific values, the aircraft-grade glass wool used in this study has a porosity of 0.997, a tortuosity of 1.02, a flow resistivity of 19,300 $\mathrm{N\,s\,m^{-4}}$, a viscous characteristic length of 66 μm, and a thermal characteristic length of 131 μm [62, 90].

The equivalent fluid method distinguishes between rigid and limp porous materials. Metal foams and soft fibrous layers are examples of rigid and limp frame materials, respectively. The limp frame porous material model is applicable without restriction on the frequency range when the elasticity of the frame (i.e. the fiber or foam material) can be neglected, either due to the nature of the material (e.g. lightweight aircraft-grade glass wool) or due to the mounting conditions of a thin foam layer [112]. The equivalent density of the limp porous material is calculated with the equivalent density of a rigid porous material ρ_{eq} and takes into account the inertia added by the limp fiber material [112]

$$\rho_{\mathrm{eq,limp}} = \frac{\rho_{\mathrm{tot}}\rho_{\mathrm{eq}} - \rho_0^2}{\rho_{\mathrm{tot}} + \rho_{\mathrm{eq}} - 2\rho_0}, \tag{2.27}$$

where $\rho_{\mathrm{tot}} = \rho_1 + \varphi\rho_0$ is the total apparent mass of the equivalent fluid limp medium

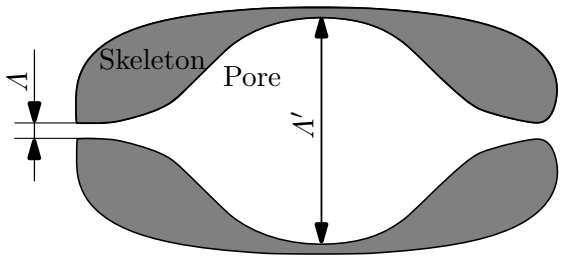

Figure 2.3: Schematic representation of a two-dimensional pore of a porous material, based on [96].

[112], ρ_1 is the bulk density, and φ is the porosity of the porous material. The equivalent density ρ_{eq} can be calculated with empirical models, see for example Refs. [2, 72, 96]. The calculation of the equivalent bulk modulus K_{eq} is identical for limp and rigid porous material and can be calculated with empirical models, which are listed and compared for example in Refs. [2] and [96]. In this work, the well-established, semi-phenomenological Johnson-Champoux-Allard model [6] is used to calculate the equivalent density by

$$\rho_{\mathrm{eq}} = \rho_0 \alpha_\infty \left(1 + \frac{\varphi\sigma}{\mathrm{i}\omega\rho_0\alpha_\infty}\sqrt{1 + \mathrm{i}\frac{4\omega\rho_0\eta_0\alpha_\infty^2}{\sigma^2\varphi^2\Lambda^2}}\right) \tag{2.28}$$

and the equivalent bulk modulus by

$$K_{\mathrm{eq}} = \frac{\kappa p_0}{\kappa - (\kappa-1)\left(1 + \frac{8\eta_0}{\mathrm{i}\omega\rho_0\,\mathrm{Pr}^2\,\Lambda'^2}\sqrt{1 + \mathrm{i}\frac{\omega\rho_0\,\mathrm{Pr}^2\,\Lambda'^2}{16\eta_0}}\right)^{-1}}, \tag{2.29}$$

where η_0 is the dynamic viscosity and Pr is the Prandtl number. Eqs. 2.28 and 2.29 use the five material parameters of the porous material listed above.

Calculating the absorption coefficient of the porous material, requires the wall equivalent impedance $Z_{\mathrm{w,eq}}$ of the porous material [6]

$$Z_{\mathrm{w,eq}} = -i\frac{Z_{\mathrm{c,eq}}}{\varphi}\cot\left(k_{\mathrm{eq}} d_{\mathrm{limp}}\right), \tag{2.30}$$

where $Z_{\mathrm{c,eq}}$, k_{eq} and d_{limp} are the characteristic impedance, the effective wave number and the thickness of the limp porous material, respectively. With the equivalent density and the equivalent bulk modulus, the characteristic impedance

$$Z_{\mathrm{c,eq}} = \sqrt{\rho_{\mathrm{eq,limp}} K_{\mathrm{eq}}} \tag{2.31}$$

and the effective wave number

$$k_{\mathrm{eq}} = \omega\sqrt{\frac{\rho_{\mathrm{eq,limp}}}{K_{\mathrm{eq}}}} \tag{2.32}$$

can be calculated to determine the wall impedance in Eq. (2.30) and finally the absorption coefficient using the matching law (Eq. (2.23)).

2.2.2. Helmholtz resonators

The schematic structure of a Helmholtz resonator is illustrated in Fig. 2.4. Helmholtz resonators consist of an air cavity of arbitrary shape with volume V_{cav} connected to the ambient fluid by an opening called a neck. This neck, with area S_{HR} and length l_{HR}, can

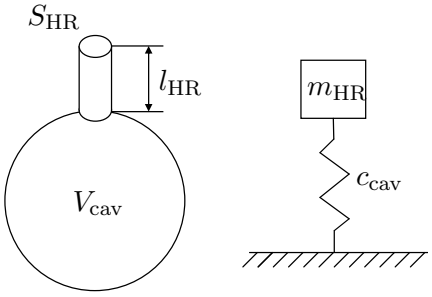

Figure 2.4: Schematic buildup of a Helmholtz resonator and the representative mass-spring system.

also have different shapes, e.g. circular or slit-shaped. Helmholtz resonators with slits are also called slit resonators [127]. The acoustic response of Helmholtz resonators can be modeled using a mass-spring system. The air inside the neck acts as a mass, while the air inside the volume acts as a spring. With the spring stiffness c_{cav} of the air volume

$$c_{\mathrm{cav}} = \frac{\rho_0 c_0^2 S_{\mathrm{HR}}^2}{V_{\mathrm{cav}}}, \tag{2.33}$$

and the air mass inside the resonator neck

$$m_{\mathrm{HR}} = \rho_0 S_{\mathrm{HR}} l_{\mathrm{eff}}, \tag{2.34}$$

the natural angular frequency is given by [146]

$$\omega_{\mathrm{HR}} = \sqrt{\frac{c_{\mathrm{cav}}}{m_{\mathrm{HR}}}} = c_0 \sqrt{\frac{S_{\mathrm{HR}}}{V_{\mathrm{cav}} l_{\mathrm{eff}}}}. \tag{2.35}$$

The term l_{eff} represents the effective length of the neck $l_{\mathrm{eff}} = l_{\mathrm{HR}} + \Delta l_{\mathrm{HR},1} + \Delta l_{\mathrm{HR},2}$, which is the sum of the physical length l_{HR} and the end corrections $\Delta l_{\mathrm{HR},1,2}$ on both sides of the neck. The end correction takes into account the inertial effects that prevent abrupt changes in air velocity at the ends of the neck, which also causes the air near the neck of the resonator to oscillate. In the literature, different calculations of the end corrections are given [68, 122, 146]. The end correction depends on the shape of the orifice (circular, rectangular, slit, etc.) and on the connection of the neck to the volume or to the external fluid (flanged or not, symmetrical or not). For Helmholtz resonators with a circular flanged neck, the end correction $l_{\mathrm{eff}} = l_{\mathrm{HR}} + 2 \cdot 0.82\, r_{\mathrm{HR}}$ is commonly used [122]. Eq. (2.35) points out that low resonance frequencies can be obtained either with large resonator cavities V_{cav}, with long resonator necks l_{HR}, or with small neck opening areas S_{HR}.

Helmholtz resonators are used in room acoustics to absorb low-frequency sound. The absorption behavior of a Helmholtz resonator is narrow-band around the resonance fre-

quency of the resonator. At resonance, most of the kinetic energy is dissipated due to viscous losses of the fluid motion in the neck [85]. The absorption coefficient of a Helmholtz resonator can be calculated using the matching law, cf. Eq. (2.23), where Z_w represents the wall impedance of the Helmholtz resonator [70]

$$Z_{\mathrm{w,HR}} = R_\mathrm{HR} + \mathrm{i}\left(\omega\frac{m_\mathrm{HR}}{S_\mathrm{HR}} + \frac{c_\mathrm{cav}}{\omega S_\mathrm{HR}}\right). \tag{2.36}$$

R_HR accounts for the viscous losses inside the neck and can be calculated with the radius of the neck area r_HR via [70]

$$R_\mathrm{HR} = \frac{l_\mathrm{eff} S_\mathrm{HR}}{\pi r_\mathrm{HR}^3}\sqrt{2\eta_0\rho_0\omega}. \tag{2.37}$$

The absorption coefficient of an example resonator consisting of a spherical cavity with a diameter of 40 mm and an outer cylindrical neck with a length of $l_\mathrm{HR} = 28$ mm and a radius of $r_\mathrm{HR} = 3$ mm is shown in Fig. 2.5. The total thickness of the Helmholtz resonator is the sum of the neck length and the diameter of the cavity and adds up to 68 mm. The absorption coefficient of the Helmholtz resonator is compared to that of aircraft-certified glass wool, as an example of a porous absorber, with the same thickness of 68 mm and the material properties listed in Table 4.6. The absorption coefficients are calculated using the matching law (Eq. (2.23)) with the wall impedances of the Helmholtz resonator (Eq. (2.36)) and of the porous layer (Eq. (2.30)), respectively. The figure clearly shows that a Helmholtz resonator of the same length is able to absorb sound at lower frequencies in a narrow frequency band, while the porous absorber (glass wool) effectively absorbs sound at higher frequencies in a broadband frequency band.

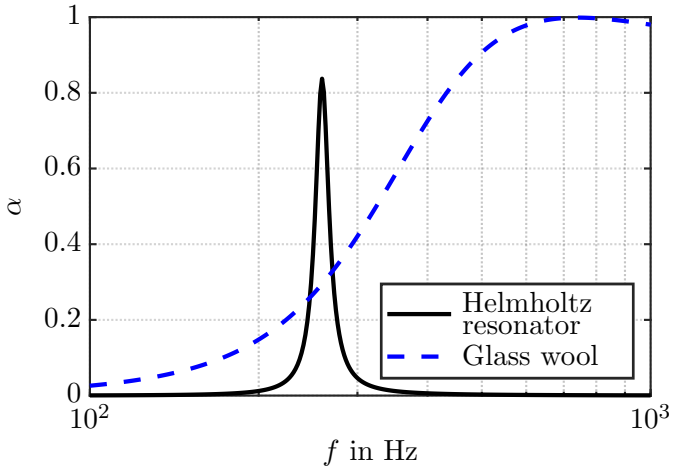

Figure 2.5: Comparison of the absorption coefficient of a Helmholtz resonator (solid black line) and aircraft-certified glass wool (dashed blue line), both with a total thickness of 68 mm.

2.3. Transmission loss

The sound power transmission coefficient τ describes the ability of a partition to reduce the transmission of airborne sound through it. τ generally depends on the frequency and the angle of incidence of the sound wave θ and is defined by the ratio of the transmitted sound power P_t to the incident sound power P_i [103]:

$$\tau = \frac{P_\mathrm{t}}{P_\mathrm{i}}. \tag{2.38}$$

The sound reduction is often described logarithmically in decibels as the transmission loss TL via

$$\mathrm{TL} = -10 \lg \tau. \tag{2.39}$$

The transmission loss can also be calculated using the complex sound pressure transmission factor t via

$$\mathrm{TL} = -20 \lg |t|, \tag{2.40}$$

where t is the ratio of the transmitted and incident complex pressure amplitudes (see Fig. 2.2)

$$t = \frac{p_\mathrm{t}}{p_\mathrm{i}}. \tag{2.41}$$

The sound power and sound pressure transmission coefficients are related by

$$\tau = |t|^2. \tag{2.42}$$

To calculate the transmission loss of a partition in a diffuse incident sound field, the diffuse field transmission coefficient τ_diff is obtained by integrating τ over the incidence angle θ [28]

$$\tau_\mathrm{diff} = \frac{\int_0^{\theta_\mathrm{lim}} \tau\left(\theta\right) \cos\theta \sin\theta \,\mathrm{d}\theta}{\int_0^{\theta_\mathrm{lim}} \cos\theta \sin\theta \,\mathrm{d}\theta}, \tag{2.43}$$

where $\tau\left(\theta\right)$ is the transmission coefficient for a given angle of incidence θ, varying from 0 to θ_lim. Theoretically, the incidence angle ranges between 0° for normal incident sound waves to 90° for grazing incident sound waves. Since the partitions are mounted in frames and niches in laboratory setups, the presence of grazing incidence waves is reduced, resulting in a smaller limiting angle θ_lim. For most laboratory setups, the analytical solution best fits the measured data for limiting angles between 70° and 85° [44, 51, 104]. In numerical simulations, a limiting angle of 78° is commonly chosen [23].

The following is a detailed description of the transmission loss characteristics of resonators, single walls, and double walls, which are common noise control applications.

2.3.1. Helmholtz resonators

The transmission loss of resonators for the case being installed in a duct, surrounded by a layer of air, as inside the impedance tube, is derived below. The schematic structure is shown in Fig. 2.6. The following discussion is valid for low frequencies, where the diameter of the duct as well as the dimensions of the resonator are assumed to be small compared to the acoustic wavelength [103]. Furthermore, the resonator is assumed to be small compared to the duct area.

The incoming wave from the left semi-infinite inlet has a pressure amplitude p_0 and is reflected at the resonator neck opening ($x = 0$), resulting in the one-dimensional pressure field

$$p_1(x) = p_0 \left(e^{-\mathrm{i}kx} + re^{+\mathrm{i}kx}\right), \tag{2.44}$$

and the particle velocity field

$$v_1(x) = \frac{p_0}{\rho_0 c_0} \left(e^{-\mathrm{i}kx} + re^{+\mathrm{i}kx}\right), \tag{2.45}$$

with r being the pressure reflection coefficient. Since the right end of the duct is assumed to be non-reflecting, there is only one transmitted wave with

$$p_2(x) = tp_0 e^{-\mathrm{i}kx}, \tag{2.46}$$

and

$$v_2(x) = t\frac{p_0}{\rho_0 c_0} e^{-\mathrm{i}kx}, \tag{2.47}$$

where t is the pressure transmission coefficient. The unknown reflection coefficient r and transmission coefficient t can be determined by the two boundary conditions at the surface $x = 0$, where the Helmholtz resonator (index "HR") is installed in the duct. Firstly, the three pressures must be equal, i.e.,

$$p_1(0) = p_2(0) = p_{\mathrm{HR}}(0), \tag{2.48}$$

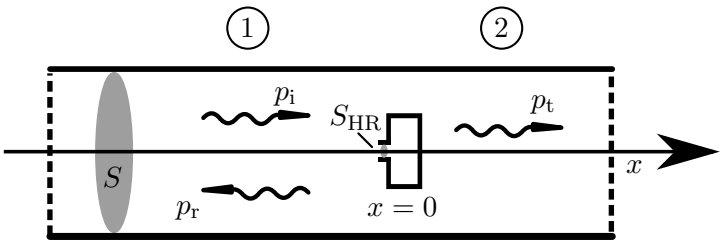

Figure 2.6: Schematic representation of a Helmholtz resonator installed in a duct.

which results in

$$1 - r = t. \tag{2.49}$$

And secondly, by conservation of mass, the volume flow Sv_1 into the node at $x = 0$ is equal to the volume flow out of the node $S_{\mathrm{HR}} v_{\mathrm{HR}}(0) + Sv_2(0)$ [101]

$$Sv_1(0) = S_{\mathrm{HR}} v_{\mathrm{HR}}(0) + Sv_2(0). \tag{2.50}$$

Dividing Eq. (2.50) by $Sp_1(0)$ and considering Eq. (2.48) yields

$$\begin{aligned} \frac{v_1(0)}{p_1(0)} &= \frac{S_{\mathrm{HR}}}{S} \frac{v_{\mathrm{HR}}(0)}{p_1(0)} + \frac{v_2(0)}{p_1(0)} \\ &= \frac{S_{\mathrm{HR}}}{S} \frac{v_{\mathrm{HR}}(0)}{p_{\mathrm{HR}}(0)} + \frac{v_2(0)}{p_2(0)}. \end{aligned} \tag{2.51}$$

Replacing p_1 and v_1 with Eqs. 2.44 and 2.45, and replacing the terms $v_{\mathrm{HR}}(0)/p_{\mathrm{HR}}(0)$ and $v_2(0)/p_2(0)$ by the input impedance of the resonator Z_{HR} and the right part of the tube $\rho_0 c_0$, respectively, simplifies Eq. (2.51) to:

$$\frac{1}{\rho_0 c_0} \frac{1-r}{1+r} = \frac{S_{\mathrm{HR}}}{S} \frac{1}{Z_{\mathrm{HR}}} + \frac{1}{\rho_0 c_0}. \tag{2.52}$$

After inserting Eq. (2.49) and some algebraic steps, the sound pressure transmission factor is calculated as

$$t = \left(1 + \frac{1}{2} \frac{S_{\mathrm{HR}}}{S} \frac{\rho_0 c_0}{Z_{\mathrm{HR}}}\right)^{-1}. \tag{2.53}$$

2.3.2. Single walls

The typical transmission loss of a single homogeneous wall is depicted in Fig. 2.7 and is characterized by four regions, the first two of which only occur for finite-size walls [109]. The transmission loss is stiffness-controlled for frequencies below the first natural frequency of the wall $f_{0,1}$, so that increasing material stiffness leads to an improved transmission loss, as indicated by the dashed line. In this region, the transmission loss curve decreases by 6 dB per octave. In the second region, the transmission loss is controlled by the eigenmodes of the sample, depending on the material and the geometric dimensions of the finite-size wall. Increased damping would smooth the resonant behavior. Due to the low modal density, the resonance plate modes have a large influence on the transmission loss in the low-frequency range. Conversely, at higher frequencies, where the modal density increases, the influence of the plate eigenmodes decreases. The third region, is controlled by the wall mass, and the transmission loss can be calculated using the mass

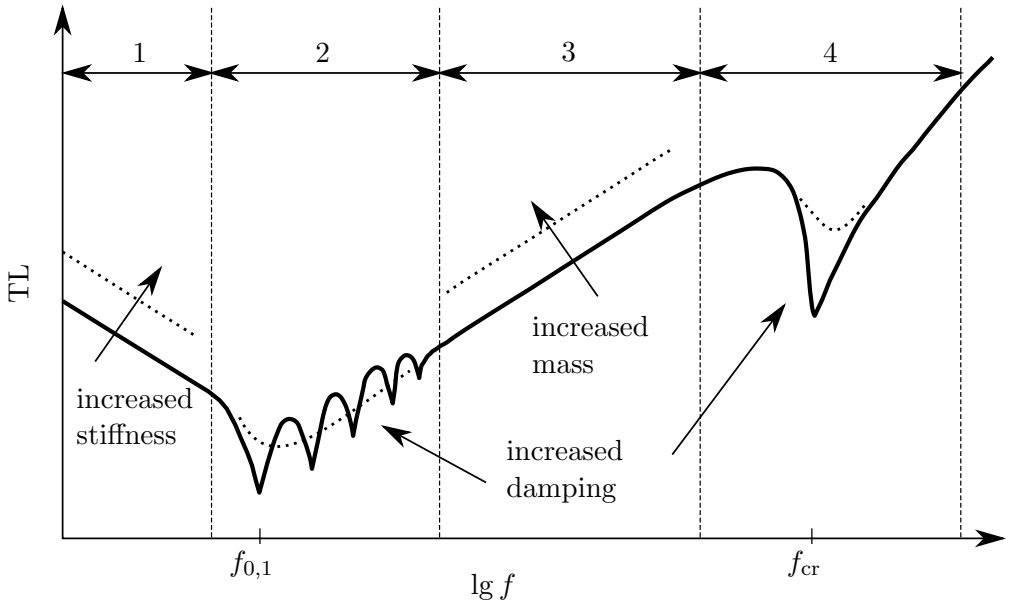

Figure 2.7: Schematic representation of the transmission loss of a homogeneous finite single wall.

law of Berger, which at normal incidence is given by [9]:

$$\mathrm{TL} = 20\,\mathrm{lg}\left|1 + \frac{\mathrm{i}\omega m''}{2\rho_0 c_0}\right|, \tag{2.54}$$

where m'' is the surface mass density of the wall. As indicated by the dashed line, increased mass leads to increased transmission loss. In this region, the transmission loss increases by 6 dB per octave or per doubling of the surface mass density. Under diffuse field incidence, the slope of the transmission loss decreases to about 5 dB per octave [76, 137]. In the fourth region in Fig. 2.7, the transmission loss is controlled by coincidence effects, which occur when the bending wave number of the plate is equal to the trace wave number of the incident sound wave. The lowest coincidence frequency, commonly referred to as the critical frequency f_{cr}, occurs for grazing incidence sound ($\theta = 90°$) and is calculated via:

$$f_{\mathrm{cr}} = \frac{c_0^2}{2\pi}\sqrt{\frac{m''}{D_{\mathrm{w}}}}, \tag{2.55}$$

where

$$D_{\mathrm{w}} = \frac{E d^3}{12\,(1-\nu)} \tag{2.56}$$

is the bending stiffness with the Young's modulus of the wall material E, the wall thickness d, and Poisson's ratio ν. At the coincidence frequency, the free propagating bending waves in the plate and the acoustic field of the incident sound field match perfectly, allowing the incident sound wave to transmit easily through the wall. For angles of incidence θ

less than 90°, the coincidence frequency f_c increases as a function of θ:

$$f_c(\theta) = \frac{f_{cr}}{\sin^2 \theta}. \tag{2.57}$$

To achieve high transmission loss in the frequency range dominated by the mass-law, single walls must be heavy. Since many applications, such as aviation, have not only noise control requirements but also weight requirements for partitions, double wall setups are used to improve transmission loss performance.

2.3.3. Double walls

Double wall structures, as shown schematically in Fig. 2.8 a), consist of two parallel single walls with surface mass densities m_1'' and m_2'' separated by an air gap with thickness H_{DW}. Ideally, there are no solid connections between the walls inside the air gap. In the considered frequency range, the single walls are assumed to be in the mass-controlled frequency range, such that plate resonances and coincidence effects are neglected, as explained in Section 2.3.2. The transmission loss of the double wall is characterized by three regions and is shown in Fig. 2.8 b). The bold solid line represents the transmission loss of the double wall without any insulation, while the dotted line shows the influence of an absorber, such as glass wool, inside the air gap. In the first and second frequency regions, the thickness of the air gap H_{DW} is small compared to the acoustic wavelength ($k_0 H_{DW} << 1$). At low frequencies in the first region, the transmission loss of the double wall corresponds to

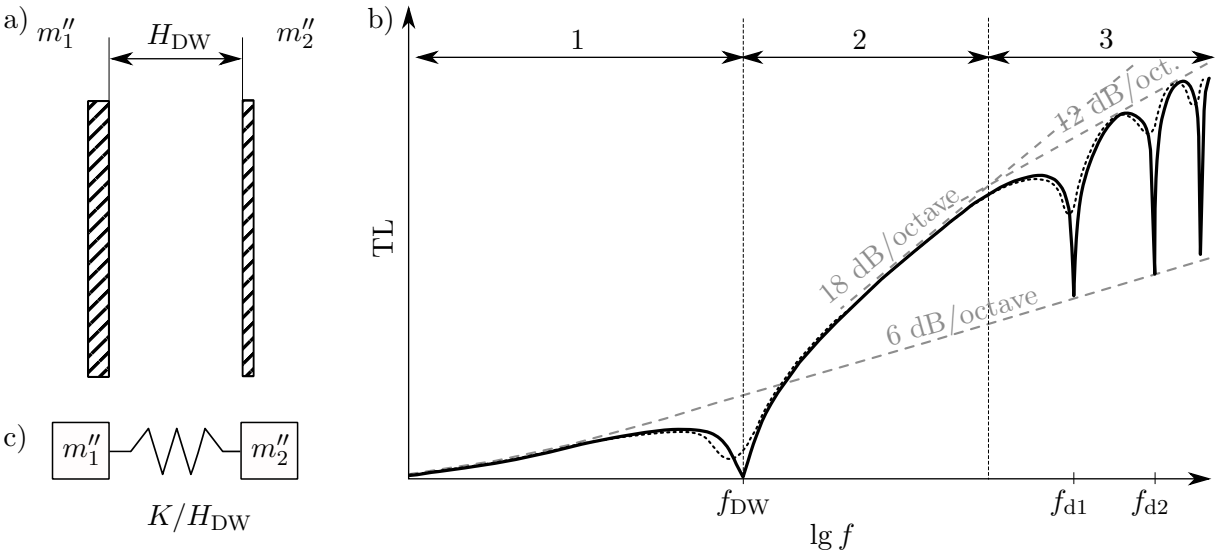

Figure 2.8: Double wall setup. a) Schematic drawing of the double wall setup. b) Schematic representation of the transmission loss for normal incidence sound. c) Mechanical model of the double wall, represented by two masses connected by a spring with the stiffness K/H_{DW}.

the behavior of a single wall in the mass-controlled region with the surface mass density $m'' = m''_1 + m''_2$, so that the transmission loss increases by 6 dB per octave [10]. The dashed line, labeled with 6 dB/octave, in Fig. 2.8 b) denotes the mass law of a mass-equivalent single wall.

In the low-frequency range, where the air gap H_{DW} is small compared to the acoustic wavelength, the double wall can be replaced by the mechanical system of two masses connected by a spring formed by the air volume inside the double wall gap, see Fig. 2.8 c). This mass-spring-mass system has a resonance frequency at which the transmission loss is significantly reduced. The resonance frequency is commonly referred to as the mass-air-mass resonance frequency or double wall resonance frequency f_{DW}, and indicates the transition from the first to the second frequency range in Fig. 2.8 b). With the spring stiffness of the fluid inside the double wall K/H_{DW}, the double wall resonance frequency for an obliquely incident plane wave can be calculated by [44]

$$f_{\mathrm{DW}}(\theta) = \frac{1}{2\pi \cos\theta} \sqrt{\frac{K}{H_{\mathrm{DW}}} \frac{m''_1 + m''_2}{m''_1 m''_2}}. \tag{2.58}$$

If there is no absorber in the air gap, the spring stiffness can be calculated using the bulk modulus of air $K = K_0 = \rho_0 c_0^2$.

For frequencies higher than f_{DW}, indicated by region 2 in Fig. 2.8 b), the transmission loss of the double wall increases by 18 dB per octave, showing an improvement over a single wall with the same surface mass density. The frequency at the transition between region 2 and 3 depends on the double wall spacing H_{DW}. If the double wall spacing is an integer multiple of half the wavelength ($H_{\mathrm{DW}} = n\lambda/2$), standing wave resonances occur at the following frequencies [85]:

$$f_{\mathrm{d}n} = \frac{n c_0}{2 H_{\mathrm{DW}} \cos\theta}. \tag{2.59}$$

At the standing wave resonance frequencies, the displacement of the two walls is nearly identical for normal sound incidence, and the transmission loss is reduced. In the case of no absorber in the air gap, the transmission loss is reduced to the value of the transmission loss of a mass-equivalent single wall, indicated by the lower dashed line. Between the standing wave resonances, anti-resonances occur at

$$f_{\mathrm{ad}n} = \frac{c_0(2n-1)}{4 H_{\mathrm{DW}} \cos\theta}, \tag{2.60}$$

where the transmission loss approximately follows the dashed line with a transmission loss increase of 12 dB per octave. The transition from region 2 to region 3 occurs at the

intersection of the two dashed lines with slopes of 18 dB per octave and 12 dB per octave. This transition is marked by the first anti-resonance frequency for normal incidence sound. To attenuate the drop in transmission loss at the resonance frequencies, an absorber such as glass wool can be embedded within the double wall spacing, as shown in Fig. 2.8 b) by the dotted line [101].

To take the biggest advantage of the double wall behavior, the frequency range of interest should be in the second region in Fig. 2.8 b), i.e. between the double wall resonance frequency f_{DW} and the first anti-resonance frequency f_{ad1}. According to Eq. (2.58), the double wall resonance frequency f_{DW} can be shifted to lower frequencies by reducing the spring stiffness K/H_{DW} or by increasing the wall masses. The effect of lowered double wall resonance frequencies on the transmission loss is represented for three different cases in Figs. 2.9 a)-c) by solid blue lines. The transmission losses are compared to that of an example double wall ($m_1'' = 5.6$ kg/m^2, $m_2'' = 1.6$ kg/m^2 and $H_{\mathrm{DW}} = 0.1$ m), represented by dashed black lines.

In Fig. 2.9 a), the transmission loss of the double wall setup with double wall masses is compared to the reference wall. Doubling the wall masses shifts the double wall resonance frequency f_{DW} to lower frequencies, while the first anti-resonance frequency f_{ad1} is not affected. Thus, the frequency range where the transmission loss increases by 18 dB per octave is broadened, and the transmission loss is essentially improved. However, in many applications, such as aerospace, strict weight requirements must be met, and increasing the wall masses to improve the transmission loss is not acceptable. For a given total surface mass density, the lowest double wall resonance frequency is achieved when both walls have the same surface mass density $m_1'' = m_2''$. This means that region 2 becomes smaller as the surface area densities m_1'' and m_2'' diverge [124].

The spring stiffness can be reduced by reducing the bulk modulus of the fluid K in the air gap or by increasing the thickness of the air gap H_{DW}. Fig. 2.9 b) shows the transmission loss of a double wall with twice the wall distance. If the application allows to increase the air gap H_{DW}, the double wall resonance frequency f_{DW} decreases proportionally to $1/\sqrt{H_{\mathrm{DW}}}$. But the anti-resonance frequency f_{ad}, which limits the second frequency range, decreases proportionally to $1/H_{\mathrm{DW}}$, such that the second frequency range becomes smaller with increasing double wall distance, as can be seen in Fig. 2.9 b).

The bulk modulus can be reduced in three different ways: Firstly, it is possible, but not yet commonly used, to reduce the bulk modulus of the fluid by using low pressure air or a near vacuum in the air gap. Secondly, the use of an absorber reduces the bulk modulus. The effective bulk modulus of air with fibrous absorbers varies between the isothermal bulk modulus $K_{\mathrm{iso}} = \rho_0 c_0^2/\kappa$ for very low frequencies and the adiabatic bulk modulus $K_0 = \rho_0 c_0^2$ for high frequencies, where $\kappa = 1.4$ is the adiabatic exponent (also

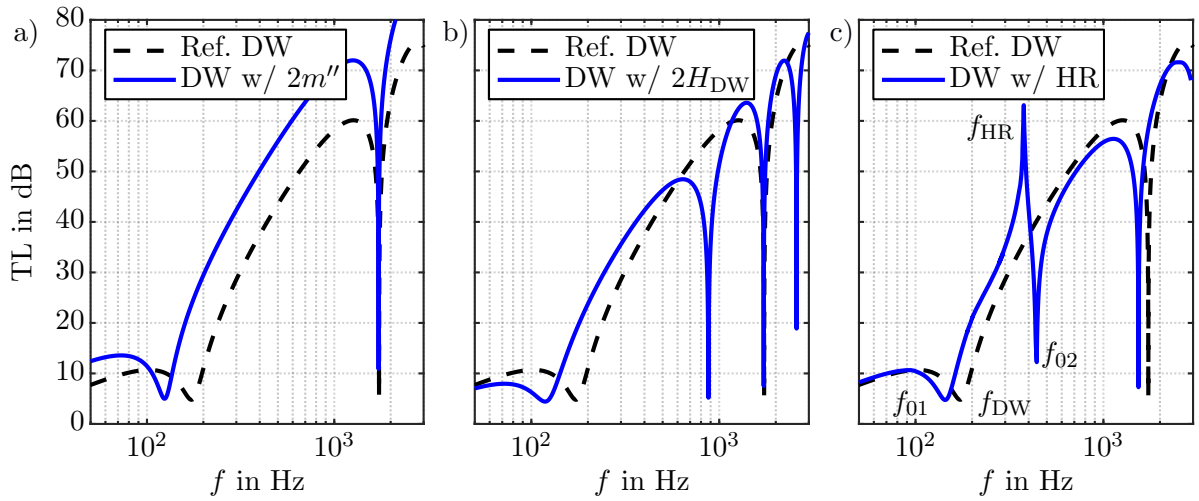

Figure 2.9: Comparison of the transmission loss of a reference double wall setup with a) double surface mass densities but the same wall spacing, b) double wall spacing but the same surface mass densities, and c) embedded Helmholtz resonators but the same surface mass densities and wall spacing.

called the specific heat ratio) of air [43]. The reduction of the bulk modulus depends on the frequency as well as on the air flow resistance [43]. In Ref. [52] it was shown, that the bulk modulus of aircraft-grade glass wool, according to Table 4.6, corresponds to the lower isothermal bulk modulus at frequencies below 430 Hz. Since the double wall resonance frequencies of aircraft sidewalls are typically between 100 and 200 Hz, the double wall resonance frequency can be calculated with the isothermal bulk modulus. This approach results in a double wall resonance frequency that is reduced by a factor of $\sqrt{1/\kappa} \approx 0.845$, as shown qualitatively by the dotted line in Fig. 2.8 b). Thirdly, Helmholtz resonators inserted in the double wall air gap also lead to a reduced bulk modulus of the fluid layer for frequencies lower than the resonance frequency of the Helmholtz resonator f_{HR} [81]. The frequency-dependent bulk modulus K_{eff} of an air layer with embedded Helmholtz resonators can be calculated via [81]

$$K_{\mathrm{eff}} = K \frac{1 - \frac{f_{\mathrm{HR}}}{f_{\mathrm{DW}}}}{1 - (1 - \phi_{\mathrm{HR}}) \frac{f_{\mathrm{HR}}}{f_{\mathrm{DW}}}}, \tag{2.61}$$

where ϕ_{HR} is the volumetric filling ratio, which is defined as the volume of the resonator cavity divided by the finite-size volume of the double wall air gap. As shown in Ref. [81], inserting the frequency-dependent bulk modulus K_{eff} into the equation for calculating the double wall resonance frequency, Eq. (2.58) yields

$$f_0^2 = \frac{1 + \frac{f_{\mathrm{HR}}^2}{f_{\mathrm{DW}}^2} \pm \sqrt{\left(1 - \frac{f_{\mathrm{HR}}^2}{f_{\mathrm{DW}}^2}\right)^2 + 4\phi_{\mathrm{HR}} \frac{f_{\mathrm{HR}}^2}{f_{\mathrm{DW}}^2}}}{2\,(1 - \phi_{\mathrm{HR}})} f_{\mathrm{DW}}^2. \tag{2.62}$$

By inspecting Eq. (2.62) it can be seen that a double wall with integrated Helmholtz resonators has two resonance frequencies f_{01} and f_{02}. The transmission loss of a double wall setup with embedded Helmholtz resonators is depicted in Fig. 2.9 c). Note that the first resonance frequency of the double wall f_{01} is lower than that of the original double wall f_{DW}, without increasing the wall mass or the wall spacing. For frequencies higher than f_{01}, the transmission loss is increased in a broadband frequency range, with the maximum transmission loss increase at the resonance frequency of the Helmholtz resonator f_{HR}. At frequencies higher than the resonance frequency of the Helmholtz resonator, a significant decrease in transmission loss is observed at the second resonance frequency of the double-wall system f_{02}. If both walls of the double wall were rigid, the second resonance frequency would correspond to the tonraum resonance frequency f_{TR} [70]. A tonraum resonator is an oscillator with two cavities connected by an orifice [85]. In this case, one cavity is the cavity of the Helmholtz resonator and the second cavity is the remaining volume of the air space in the double wall that is not occupied by the Helmholtz resonators. The tonraum resonance frequency f_{TR} can be calculated with the resonance frequency of the Helmholtz resonator f_{HR} via [81]

$$f_{\mathrm{TR}} = \frac{f_{\mathrm{HR}}}{\sqrt{1-\phi_{\mathrm{HR}}}}. \tag{2.63}$$

At frequencies higher than f_{02}, the transmission loss of the double wall with Helmholtz resonators (see Fig. 2.9 c)) is reduced compared to the transmission loss of an equivalent double wall without resonators. This can be explained by an increased stiffness of the air layer. The Helmholtz resonators are decoupled from the background fluid and thus the volume of the double wall cavity is effectively reduced by the volume of the Helmholtz resonators. The resulting spring stiffness is increased to $K_{\mathrm{eff}}/(H_{\mathrm{DW}} - H_{\mathrm{HR}})$, where H_{HR} is the height of the resonator.

2.4. Transfer matrix method

The transfer matrix method is a mathematical method for analyzing the propagation of waves through multi-layered structures. In acoustics, it is often used to understand the transmission and reflection of sound waves through barriers such as walls, partitions, and acoustical materials. Acoustic transfer matrices are used for planar structures of infinite dimensions [18]. In this thesis, the transfer matrix method is used to calculate the transmission loss from impedance tube measurements and to analyze the transmission loss of multi-layered structures, such as the sidewall of an aircraft. In general, transfer matrices describe the relationship between the pressure p_{L} and particle velocity v_{L} amplitude on the left hand side (index "L") and the pressure p_{R} and particle velocity v_{R} amplitude on

the right hand side (index "R") of a laterally infinite structure via [36]

$$\begin{pmatrix} p_\mathrm{L} \\ v_\mathrm{L} \end{pmatrix} \underbrace{\begin{bmatrix} T_{11} & T_{12} \\ T_{21} & T_{22} \end{bmatrix}}_{\mathbf{T}} = \begin{pmatrix} p_\mathrm{R} \\ v_\mathrm{R} \end{pmatrix}. \tag{2.64}$$

Once the elements of the transfer matrix $T_{11}, T_{12}, T_{21}, T_{22}$ are determined, a set of acoustic parameters to analyze the acoustic behavior of the structure (e.g. the absorption coefficient, the reflection coefficient, or the transmission coefficient) can be determined. To calculate the transmission loss of a structure with the same fluid on both the incidence and transmission sides, the pressure transmission coefficient for oblique incidence sound with the angle of incidence θ can be calculated via

$$t_\theta = \frac{2}{T_{11} + T_{12}\cos\theta/Z_0 + T_{21}Z_0/\cos\theta + T_{22}}. \tag{2.65}$$

If a component, such as an aircraft sidewall, consists of N_lay layers connected in series, the transfer matrix of the whole structure $\mathbf{T}$ is the product of the transfer matrices $\mathbf{T}_i$ of the individual layers [105]

$$\mathbf{T} = \mathbf{T}_1 \cdot \mathbf{T}_2 \cdot \ldots \cdot \mathbf{T}_{N_\mathrm{lay}} = \prod_{i=1}^{N_\mathrm{lay}} \mathbf{T}_i, \tag{2.66}$$

where the index $i = 1$ describes the first layer on the incident side of the component. In principle, the elements of the transfer matrix $\mathbf{T}$ are complex-valued. The transfer matrices depend on the frequency f and the incidence angle θ of the incoming plane sound wave, as well as on the type of layer. The transfer matrix of the various layers can be determined either numerically through simulations [20, 74] or experimentally using impedance tube measurements [111, 128]. Additionally, analytical models for certain acoustic elements can be found in the literature or can be derived, as demonstrated in Section 3.8 for a Helmholtz resonator panel with integrated cantilevers. The following subsections explain the analytical transfer matrix functions that are established in the literature and used in this thesis. In addition to the resonator layer to be derived in Section 3.8, three other types of layers are also utilized:

- Thin walls that form the cabin lining and fuselage structure,
- Fluid layers in between the walls,
- Insulation layers represented by fiberglass blankets or open-celled foams.

2.4.1. Transfer matrix of a thin wall

With the mechanical wall impedance [2]

$$Z_{\mathrm{w}} = \mathrm{i}\omega m''_{\mathrm{w}} \left(1 - \frac{\omega^2}{\omega_{\mathrm{cr}}^2} \sin^4 \theta\right), \tag{2.67}$$

the surface mass density m''_{w}, and the critical angular frequency $\omega_{\mathrm{cr}} = 2\pi f_{\mathrm{cr}}$ (cf. Eq. (2.55)), the transfer matrix of a thin wall $\mathbf{T}_{\mathrm{w}}$ is calculated as

$$\mathbf{T}_{\mathrm{w}} = \begin{bmatrix} 1 & Z_{\mathrm{w}} \\ 0 & 1 \end{bmatrix}. \tag{2.68}$$

At normal incidence ($\theta = 0°$), the mechanical wall impedance corresponds to that of a limp wall, which can be expressed as $Z_{\mathrm{w}} = \mathrm{i}\omega m''_{\mathrm{w}}$, leading to mass-law behavior for the sound transmission loss of the wall.

2.4.2. Transfer matrix of a fluid layer

The transfer matrix of a fluid layer, denoted as $\mathbf{T}_{\mathrm{F}}$, with the layer thickness d is [36]

$$\mathbf{T}_{\mathrm{F}} = \begin{bmatrix} \cos(k_x d) & \frac{\mathrm{i}\omega\rho_0}{k_x} \sin(k_x d) \\ -\frac{k_x}{\mathrm{i}\omega\rho_0} \sin(k_x d) & \cos(k_x d) \end{bmatrix}, \tag{2.69}$$

where k_x describes the component of the wave number vector of the fluid layer k_{f} in the direction normal to the layer, and ρ_0 is the fluid density in the fluid layer. k_x can be calculated using the dispersion relation $k_x^2 = k_{\mathrm{f}}^2 - k_0^2 \sin^2\theta$, where k_0 is the wave number of the fluid, and θ is the incidence angle [16, 18].

2.4.3. Transfer matrix of a limp porous material layer

The transfer matrix of the limp porous material $\mathbf{T}_{\mathrm{LPM}}$, using the equivalent fluid method, is obtained based on the transfer matrix of a fluid layer $\mathbf{T}_{\mathrm{F}}$, where the density ρ_0 and the component of the wave number vector k_x are replaced by the equivalent density $\rho_{\mathrm{eq,limp}}$ (Eq. (2.27)) and the effective wave number k_{eq} (Eq. (2.32))

$$\mathbf{T}_{\mathrm{LPM}} = \begin{bmatrix} \cos(k_{\mathrm{eq}} d) & \frac{\mathrm{i}\omega\rho_{\mathrm{eq,limp}}}{k_{\mathrm{eq}}} \sin(k_{\mathrm{eq}} d) \\ -\frac{k_{\mathrm{eq}}}{\mathrm{i}\omega\rho_{\mathrm{eq,limp}}} \sin(k_{\mathrm{eq}} d) & \cos(k_{\mathrm{eq}} d) \end{bmatrix}. \tag{2.70}$$

2.4.4. Limitations of the transfer matrix method

The transfer matrix method is a highly efficient approach to quickly determine the acoustic properties of complex structures, even if they consist of many different layers. It should be noted that the effectiveness of this method is due to significant simplifications. For example, the layers are assumed to be flat rather than curved, as in the case of aircraft sidewalls. In addition, the transfer matrix method does not take into account the effects of structure-borne sound bridges or the transmission of near-field sound between adjacent layers. Furthermore, the transfer matrix method considers the layers to be infinite. As a result, the effects of boundary conditions of finite plates or acoustic modes in laterally bounded cavities are not considered. Neglecting these aspects can lead to significant discrepancies when comparing the results with measurements on finite-size samples [19, 138]. To overcome the limitation that the transfer matrix method is only valid for infinite-sized panels, a correction for finite-sized panels is presented in the following subsection.

2.4.5. Finite-size correction of the transmission coefficient

The classical transfer matrix method assumes a structure of infinite lateral size. For transmission loss calculations, the method correlates well with experiments at mid to high frequencies for flat panels. However, there are differences at low frequencies, especially for small-sized panels. Since this study focuses on low-frequency noise control measures and the experimental validation of multi-layer structures performed in a laboratory with panels of finite size, a correction is applied to the sound power transmission coefficient calculated with the transfer matrix. Such corrections have been widely studied in literature, e.g. in Refs. [14, 117, 138]. The different proposed solutions are all based on replacing the radiation efficiency in the receiving room by an equivalent radiation efficiency of a baffled window σ_{R}. The radiation efficiency quantifies the efficiency of a vibrating surface as a sound radiator and is defined as the ratio of the real part of the radiation impedance Z_{R} to the characteristic impedance of the surrounding medium Z_0

$$\sigma_{\mathrm{R}} = \frac{\mathrm{Re}\left(Z_{\mathrm{R}}\right)}{Z_0}. \tag{2.71}$$

In this study, the radiation efficiency is calculated using the reduced-order integral formulation according to Bonfiglio et al. [14]. The authors simplified the calculation of the radiation impedance Z_{R} of Rhazi et al. [117] for square panels such that the radiation

impedance can be calculated numerically via

$$Z_{\mathrm{R}} = \mathrm{i}\rho_0\omega\frac{L}{4\pi}\Bigg(\int_0^{\frac{\pi}{2}}\int_0^{2} e^{\mathrm{i}Ak}\left(4\xi - \frac{k^2\cos^2\xi}{2} + 2k\cos\xi - 2k\sin\xi\right)\cdot\mathrm{Re}\left(I_0\left(\mathrm{i}Ck\right)\right)\,\mathrm{d}k\,\mathrm{d}\xi + \int_{\xi_1}^{\xi_2}\int_2^{2\sqrt{2}} e^{\mathrm{i}Ak}\left(4\xi - \frac{k^2\cos^2\xi}{2} + 2k\cos\xi - 2k\sin\xi\right)\cdot\mathrm{Re}\left(I_0\left(\mathrm{i}Ck\right)\right)\,\mathrm{d}k\,\mathrm{d}\xi\Bigg), \tag{2.72}$$

where L is the length and width of the square panel, $A = -k_0 L/2$, $C = k_0 \sin\theta_0 L/2$, $\xi_1 = \arctan\left(1/2(k^2-4)^{1/2}\right)$, $\xi_2 = \arctan\left(2(k^2-4)^{-1/2}\right)$, and I_0 is the modified Bessel function of the first kind. In Ref. [14] it was shown, that the formula can also be used for rectangular plates with an aspect ratio less than 1:2. The relative error is less than 10 percent for all incidence angles (evaluated between 0 and 78°) and all frequencies above 100 Hz. The relative error decreases with increasing frequency and increasing incidence angle. To use Eq. (2.72) for rectangular plates, the length L is replaced by the geometric mean of the edge lengths L_{p} and W_{p} of the rectangular plate, i.e. $L = (L_{\mathrm{p}}W_{\mathrm{p}})^{1/2}$. To obtain the transmission coefficient of the finite-size panel τ_{f}, the transmission coefficient of the infinite panel τ is multiplied with the radiation efficiency σ_{R} and the cosine of the incidence angle

$$\tau_{\mathrm{f}} = \tau\sigma_{\mathrm{R}}\cos\left(\theta\right). \tag{2.73}$$

The diffuse field transmission coefficient of a finite plate $\tau_{\mathrm{f,diff}}$ can then be obtained by integrating τ_{f} over the incidence angles according to Eq. (2.43).

2.5. Applied measurement techniques

This chapter describes the experimental methods used in this thesis. Impedance tube measurements were performed to determine the absorption coefficient and transmission loss of the newly developed resonator for small samples at normal incidence. Transmission tests were performed to determine the transmission loss of large resonator panels embedded in multi-layered structures under diffuse sound incidence.

2.5.1. Absorption coefficient measurements in an impedance tube

In this thesis, the two-microphone method according to ISO 10534–2 [38] has been used to measure the absorption coefficient of a sample in an impedance tube. Unlike the standing wave method described in ISO 10534–1 [37], the two-microphone method allows the simultaneous evaluation of the absorption coefficient for all excited frequencies. A schematic drawing of the test setup is presented in Fig. 2.10. The figure shows a loudspeaker on the

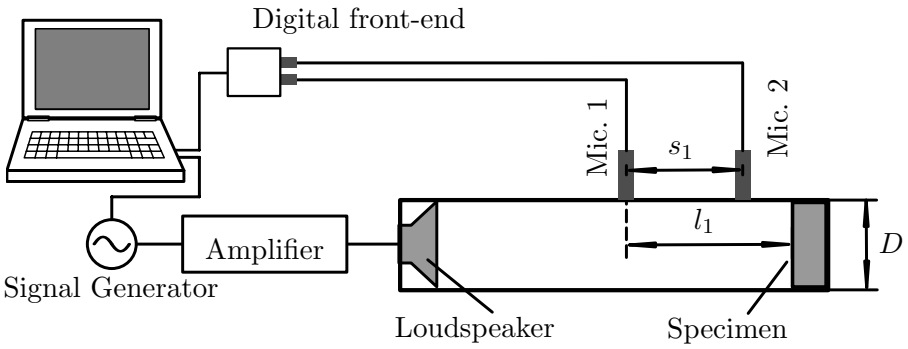

Figure 2.10: Schematic diagram of the impedance tube setup for sound absorption measurements according to ISO 10534–2 [38] using the two-microphone method (Figure based on [80]).

left hand side of the tube emitting a broadband incident sound field. The signal of the sound field is produced by a signal generator and amplified by an amplifier, resulting in a white noise sound field within the tube. Two pressure microphones, Mic. 1 and Mic. 2, measure the pressure of the back-and-forth traveling waves. The microphone signals are then transformed by an A/D converter to calculate the microphone transfer function between the two microphones using a fast Fourier transform (FFT) algorithm. With the auto spectrum $S_{11} = p_1 \cdot p_1^*$ of the reference microphone Mic. 1, where p_1^* is the complex conjugate of the measured pressure p_1, and the cross spectrum $S_{21} = p_2 \cdot p_1^*$, the complex acoustic transfer function H_{21}

$$H_{21} = \frac{S_{21}}{S_{11}}, \tag{2.74}$$

is obtained [38]. The reflection coefficient r

$$r = \frac{H_{21} - e^{-\mathrm{i}ks_1}}{e^{\mathrm{i}ks_1} H_{21}} e^{2\mathrm{i}kl_1} \tag{2.75}$$

is calculated directly from the transfer function, according to ISO 10534–2 [38]. As depicted in Fig. 2.10, s_1 and l_1 are the distances between the two microphones and between Mic. 1 and the resonator front plate, respectively. Using the reflection coefficient, the normal incident absorption coefficient can be calculated with

$$\alpha = 1 - |r^2|. \tag{2.76}$$

The accuracy of the measurements is assessed with the auto spectrum S_{22} of the microphone Mic. 2 by the coherence

$$\gamma = \frac{|{S_{21}}^2|}{S_{11} \cdot S_{22}}. \tag{2.77}$$

which is always smaller than 1 and should ideally be greater than 0.9 [38].

2.5.2. Transmission loss measurements in an impedance tube

In this thesis, the four-microphone method based on the transfer matrix method according to ASTM E2611-09 [5] has been applied to measure the transmission loss of a sample, such as a layer of a porous material, in an impedance tube. The test setup is schematically depicted in Fig. 2.11. Two microphones are installed on each side of the resonator to measure the pressure of the back-and-forth traveling waves. As described in Ref. [5], two measurements with two different tube terminations are required for each sample, if the sample is not symmetrical. The two measurements are referred to as "a" and "b".

To calculate the four unknown elements of the transfer matrix, four transfer functions ($n = 1 \cdots 4$) of the four microphones are calculated with the reference microphone being Mic. 1

$$H_{n,1} = \frac{S_{n1}}{S_{11}}, \tag{2.78}$$

where $S_{n1} = p_n \cdot p_1^*$ are the cross spectra of the four microphones ($n = 1 \cdots 4$). For each tube termination (measurement "a" and "b"), the acoustic wave is decomposed into forward and backward traveling waves on both sides of the sample using the following equations [5]:

$$A = \mathrm{i}\frac{H_{11}e^{-\mathrm{i}kl_1} - H_{21}e^{-\mathrm{i}k(l_1+s_1)}}{2\sin(ks_1)}, \tag{2.79}$$

$$B = \mathrm{i}\frac{H_{21}e^{\mathrm{i}k(l_1+s_1)} - H_{11}e^{\mathrm{i}kl_1}}{2\sin(ks_1)}, \tag{2.80}$$

$$C = \mathrm{i}\frac{H_{31}e^{\mathrm{i}k(l_2+s_2)} - H_{41}e^{\mathrm{i}kl_2}}{2\sin(ks_2)}, \tag{2.81}$$

$$D = \mathrm{i}\frac{H_{41}e^{-\mathrm{i}kl_2} - H_{31}e^{-\mathrm{i}k(l_2+s_2)}}{2\sin(ks_2)}. \tag{2.82}$$

As shown in Fig. 2.11, l_1 and l_2 are the distances between the sample and microphones

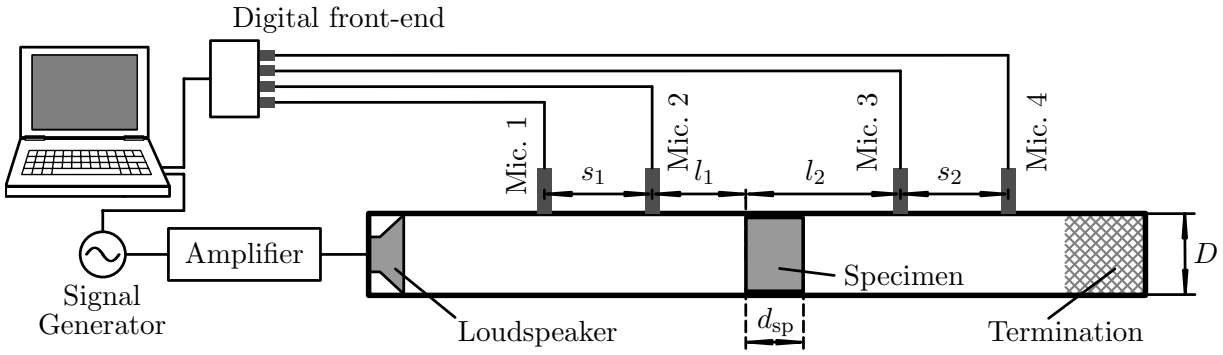

Figure 2.11: Schematic representation of the transmission loss impedance tube measurement using the 4-microphone method according to the ASTM E2611-09 [5] (Figure based on [81]).

Mic. 2 and Mic. 3, respectively. s_1 and s_2 are the microphone spacings between microphones Mic. 1 and Mic. 2 and between microphones Mic. 3 and Mic. 4, respectively.

For each tube termination (measurement "a" and "b"), the sound pressure and particle velocity on both sides of the sample (index "L" and "R" indicate the left and right hand sides of the specimen) are determined using [74]

$$p_{\mathrm{L}} = A + B, \tag{2.83}$$

$$p_{\mathrm{R}} = Ce^{-\mathrm{i}kd_{\mathrm{sp}}} + De^{\mathrm{i}kd_{\mathrm{sp}}}, \tag{2.84}$$

$$v_{\mathrm{L}} = \frac{A - B}{\rho_0 c_0} \tag{2.85}$$

and

$$v_{\mathrm{R}} = \frac{Ce^{-\mathrm{i}kd_{\mathrm{sp}}} - De^{\mathrm{i}kd_{\mathrm{sp}}}}{\rho_0 c_0}, \tag{2.86}$$

where d_{sp} is the thickness of the specimen. The transfer matrix $\mathbf{T}$, which relates the pressure and particle velocity values for both tube terminations (measurement "a" and "b"), is given by

$$\begin{pmatrix} p_{\mathrm{L}} \\ v_{\mathrm{L}} \end{pmatrix}_{a,b} \underbrace{\begin{bmatrix} T_{11} & T_{12} \\ T_{21} & T_{22} \end{bmatrix}}_{\mathbf{T}} = \begin{pmatrix} p_{\mathrm{R}} \\ v_{\mathrm{R}} \end{pmatrix}_{a,b}. \tag{2.87}$$

The components of the transfer matrix $\mathbf{T}$ for the given test sample are calculated with [5]

$$T_{11} = \frac{p_{\mathrm{L,a}} v_{\mathrm{R,b}} - p_{\mathrm{L,b}} v_{\mathrm{R,a}}}{p_{\mathrm{R,a}} v_{\mathrm{R,b}} - p_{\mathrm{R,b}} v_{\mathrm{R,a}}}, \tag{2.88}$$

$$T_{12} = \frac{p_{\mathrm{L,b}} p_{\mathrm{R,a}} - p_{\mathrm{L,a}} p_{\mathrm{R,b}}}{p_{\mathrm{R,a}} v_{\mathrm{R,b}} - p_{\mathrm{R,b}} v_{\mathrm{R,a}}}, \tag{2.89}$$

$$T_{21} = \frac{v_{\mathrm{L,a}} v_{\mathrm{R,b}} - v_{\mathrm{L,b}} v_{\mathrm{R,a}}}{p_{\mathrm{R,a}} v_{\mathrm{R,b}} - p_{\mathrm{R,b}} v_{\mathrm{R,a}}} \tag{2.90}$$

and

$$T_{22} = \frac{p_{\mathrm{R,a}} v_{\mathrm{L,b}} - p_{\mathrm{R,b}} v_{\mathrm{L,a}}}{p_{\mathrm{R,a}} v_{\mathrm{R,b}} - p_{\mathrm{R,b}} v_{\mathrm{R,a}}}. \tag{2.91}$$

The transmission loss TL can then be calculated with the elements of the transfer matrix via

$$\mathrm{TL} = 20 \lg \left(\frac{1}{2} \left| T_{11} + \frac{T_{12}}{Z_0} + Z_0 T_{21} + T_{22} \right| \right). \tag{2.92}$$

2.5.3. Large scale transmission loss measurements

In this thesis, the transmission loss of large resonator panels and of multi-layered setups is measured in a laboratory, where the panel is embedded in a window between a reverberation room and a hemi-anechoic chamber. The measurements are performed according to ISO 15186-1 [39]. The measurement setup is depicted in Fig. 2.12. The specimen is mounted inside a transmission window within a rigid frame. The reverberation room represents the source room, where a diffuse field is excited by a loudspeaker. The sound pressure inside the reverberation room is measured with a pressure microphone mounted on a rotating boom, in order to measure the time and space averaged pressure p_{SR} of the source room. In a diffuse field, sound arrives from each direction with equal magnitude and probability, so that the net intensity is zero. Nevertheless, the unidirectional effective intensity, incident on the panel in the transmission window, can be calculated from the time- and space-averaged pressure p_{SR} using the theoretical relationship [30]

$$I_{\mathrm{i}} = \frac{p_{\mathrm{SR}}^2}{4\rho_0 c_0}. \tag{2.93}$$

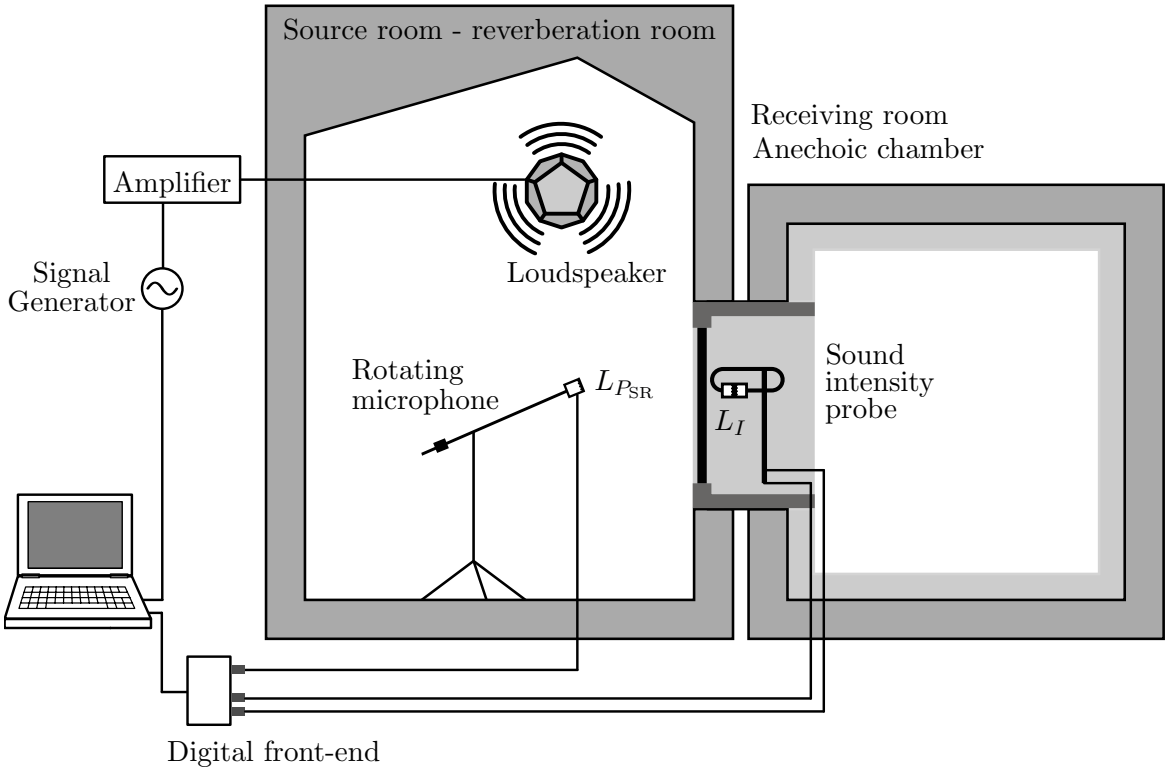

Figure 2.12: Schematic representation of the transmission loss measurement setup between a reverberation room and a hemi-anechoic chamber according to ISO 15186-1 [39].

The transmitted intensity L_t is measured inside the hemi-anechoic chamber using an intensity probe with two pressure microphones (Mic. A and Mic. B) separated by a spacer with the distance $s_\mathrm{A,B}$. The effective intensity is the real part of the product of the pressure amplitude spectrum p_m and the complex conjugate particle velocity amplitude spectrum v_m^* at the same location [126]

$$I_\mathrm{t} = \frac{1}{2}\mathrm{Re}\left(p_\mathrm{m} \cdot v_\mathrm{m}^*\right). \tag{2.94}$$

p_m is the average pressure spectrum

$$p_\mathrm{m} = \frac{1}{2}\left(p_\mathrm{A} + p_\mathrm{B}\right), \tag{2.95}$$

and v_m is the particle velocity spectrum, approximated from the pressure gradient between the two pressure microphones

$$v_\mathrm{m} = -\frac{1}{\mathrm{i}\omega\rho_0 s_\mathrm{A,B}}\left(p_\mathrm{B} - p_\mathrm{A}\right). \tag{2.96}$$

Inserting Eqs. 2.95 and 2.96 into Eq. (2.94) leads to the measured effective intensity spectrum [103]

$$I_\mathrm{t} = \frac{1}{2\omega\rho_0 s_\mathrm{A,B}}\mathrm{Im}\left(p_\mathrm{A} \cdot p_\mathrm{B}^*\right). \tag{2.97}$$

With the incident intensity level of the source room L_i and the transmitted intensity level L_t measured in the receiving room, the transmission loss is given by

$$\mathrm{TL} = L_i - L_t + 10\,\mathrm{lg}\left(\frac{S_\mathrm{SR}}{S_\mathrm{RR}}\right), \tag{2.98}$$

where the area ratio $S_\mathrm{SR}/S_\mathrm{RR}$ takes into account possible differences between the area of the sample facing the source room S_SR and the measurement area S_RR in the receiving room.

3. Analytical model

In this chapter, an analytical model for the Helmholtz resonator with integrated cantilever is derived. Parts of the derivation of this model have also already been published in a conference paper [54] and a peer-reviewed journal paper [57]. The aim of the model is to calculate

- the resonance frequencies of the resonator,
- the absorption coefficient of the resonator,
- the transmission loss of the resonator,
- the transfer matrix of an infinite resonator panel, i.e. for applications where the resonator is installed in a multi-layer setup.

The considered absorber consists of a Helmholtz resonator with an integrated cantilever. A three-dimensional view and photograph of the resonator are shown in Figs. 3.1a) and b), respectively. The cross section and top view of the resonator are depicted schematically in Figs. 3.1c) and d), respectively. The resonator consists of a hollow body with the cavity volume V_{cav}. A U-shaped slit (width w_{s}) is inserted at the top side to form a cantilever (CL) of length l, width w, and area $S_{\mathrm{CL}} = l \cdot w$. The slit also forms the neck of the Helmholtz resonator (HR) with the corresponding area S_{HR}. The thickness of the resonator walls t_{s} defines the length of the neck. This results in the resonator forming a coupled system of an acoustical oscillator (Helmholtz resonator) and a mechanical oscillator (cantilever). Both oscillators are coupled via the fluid in the cavity. The box-shaped resonator body has the height H and the base area $S_{\mathrm{res}} = L \cdot W$, with the length L and width W. A Cartesian coordinate system is defined with the origin at the cantilever root, the top plate parallel to the y-z-plane, the z-coordinate along the cantilever axis, and the x-coordinate inside the Helmholtz resonator cavity.

A harmonic time dependence convention of the form $\exp(\mathrm{i}\omega t)$ is assumed in the following derivations, such that the harmonic physical variables, like pressure and displacements, are represented by their complex-valued frequency-dependent amplitudes.

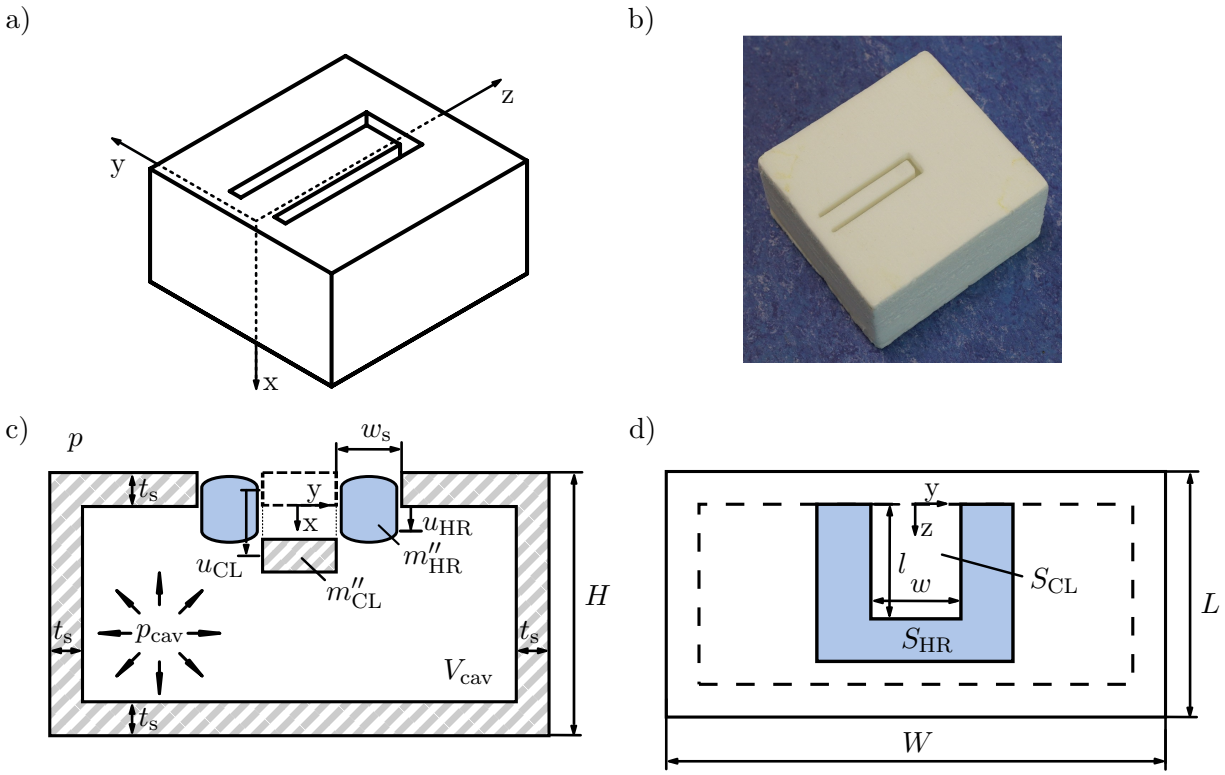

Figure 3.1: Photo and schematic representation of the presented coupled resonant absorber. The blue colored areas represent the fluid volume that is enclosed by the Helmholtz resonator neck. a) Three-dimensional view. b) Photograph. c) Cross section of the resonator. d) Top view of the resonator.

3.1. Equation of motion for the fluid volume in the neck

The equation of motion for the displacement u_{HR} of the fluid volume of the air inside the Helmholtz resonator neck is

$$-\omega^2 u_{\mathrm{HR}} m''_{\mathrm{HR}} + \mathrm{i}\omega R_{\mathrm{HR}} \left(\frac{1}{2} u_{\mathrm{HR}} + \frac{1}{2} \left(u_{\mathrm{HR}} - \bar{u}_{\mathrm{CL}} \right) \right) = p - p_{\mathrm{cav}}, \tag{3.1}$$

with the derivation conducted in A.1. In Eq. (3.1), $p - p_{\mathrm{cav}}$ is the pressure difference between the pressure outside of the resonator p and the pressure inside the resonator cavity p_{cav}. R_{HR} describes the resistance due to viscous losses in the boundary layer in the neck and is related to the neck area S_{HR}. The viscous losses depend on the particle velocity of the air mass in the neck $v_{\mathrm{HR}} = \mathrm{i}\omega u_{\mathrm{HR}}$ and on the relative velocity between the air mass and the cantilever $v_{\mathrm{HR}} - \bar{v}_{\mathrm{CL}}(z) = \mathrm{i}\omega \left(u_{\mathrm{HR}} - \bar{u}_{\mathrm{CL}} \right)$, where $\bar{u}_{\mathrm{CL}}$ is the mean displacement of the cantilever over the cantilever length l

$$\bar{u}_{\mathrm{CL}} = \frac{1}{l} \int_0^l u_{\mathrm{CL}}(z) \, \mathrm{d}z. \tag{3.2}$$

The factor 1/2 means that approximately one half of the slit boundary is attributed to the cantilever and the other half to the top plate of the resonator.

For low frequencies, where the dimensions of the resonator neck are much smaller than the acoustic wavelength, the displacement of the air mass in the neck u_{HR} is assumed to be constant across the neck. The surface mass density of the moving air inside the Helmholtz resonator neck m''_{HR} depends on the air density ρ_0 and the effective neck length, which is defined as the physical length of the neck t_{s} plus the end corrections Δt_{s} on both sides of the neck: $m''_{\mathrm{HR}} = \rho_0(t_{\mathrm{s}}+2\Delta t_{\mathrm{s}})$. In this contribution, the end correction is chosen, according to Smits and Kosten [127], to be

$$2\Delta t_{\mathrm{s}} = -\frac{2w_{\mathrm{s}}}{\pi} \ln\left(\sin\left(\frac{\pi\sigma_{\mathrm{HR}}}{2}\right)\right), \tag{3.3}$$

with the area ratio $\sigma_{\mathrm{HR}} = S_{\mathrm{HR}}/S_{\mathrm{res}}$. A constant pressure profile over the slit area was assumed by Smits and Kosten. The end correction was derived for infinite-length slits with slit widths larger than the viscous boundary layer thickness δ_{v} but smaller than half of the acoustic wavelength and is adopted in this study for finite-length slits. The viscous boundary layer thickness is frequency-dependent and defined as [130]

$$\delta_{\mathrm{v}} = \sqrt{\frac{2\eta_0}{\rho_0\omega}}, \tag{3.4}$$

where η_0 is the dynamic viscosity for air. In the frequency range from 100 Hz to 1000 Hz, which is the focus of this work, the viscous boundary layer thickness is between 0.22 mm and 0.08 mm, which is an order of magnitude smaller, than the slit widths of the resonators. The model of Smits and Kosten for the end correction has been widely used in the literature for slit widths from a few millimeters to a few centimeters, e.g. in Refs. [8, 69, 115]. A model of Ingard [61] was applied to account for viscous losses

$$R_{\mathrm{HR}} = \sqrt{2\eta_0\rho_0\omega}\left(2 + \frac{t_{\mathrm{s}}}{w_{\mathrm{s}}}\right). \tag{3.5}$$

This model has also been used in Refs. [8, 69, 115] to describe the losses in air-filled slits in the low-frequency range, which have slit length to width ratios of the same magnitude as in this contribution.

If the model derived in this contribution is to be applied to microslits, where the viscous boundary layer thickness has the same dimension as the slit width, the mass end correction Δt_{s} and the viscous losses in the neck R_{HR} can be adjusted according to Refs. [2, 92].

3.2. Equation of motion for the cantilever

The equation of motion of the cantilever displacement in the x-direction $u_{\mathrm{CL}}(z)$ with the material density ρ_{CL}, the cross section $A_{\mathrm{CL}} = w \cdot t_{\mathrm{CL}}$, the area moment of inertia $I_y = w \cdot t_{\mathrm{s}}^3/12$, and the Young's modulus E, is [108]

$$-\omega^2 u_{\mathrm{CL}}(z)\rho_{\mathrm{CL}}A_{\mathrm{CL}} - \mathrm{i}\omega R_{\mathrm{HR}}\frac{1}{2}\left(u_{\mathrm{HR}} - u_{\mathrm{CL}}(z)\right)w + \frac{\partial^2}{\partial z^2}\left(EI_y\frac{\partial^2 u_{\mathrm{CL}}(z)}{\partial z^2}\right) = (p - p_{\mathrm{cav}})w, \tag{3.6}$$

where the damping part describes the damping effect from the relative motion between the fluid motion and the cantilever. Mechanical losses due to the structural damping of the cantilever material are introduced by a complex Young's modulus $E = E_{\mathrm{CL}}(1 + \mathrm{i}\eta_{\mathrm{CL}})$, where E_{CL} and η_{CL} are the Young's modulus and the structural loss factor of the cantilever material, respectively. The deflection of the cantilever $u_{\mathrm{CL}}(z)$ is approximated by a modal superposition with the modal participation factors $a_{\mathrm{CL}i}$ and the trial functions $\phi_{\mathrm{CL}i}$ [108]

$$\begin{aligned} u_{\mathrm{CL}}(z) &= \sum_{i=1}^{N} a_{\mathrm{CL}i}\phi_{\mathrm{CL}i}(z) \\ &= \sum_{i=1}^{N} a_{\mathrm{CL}i}\underbrace{\left(A_i\cos(k_i z) + B_i\sin(k_i z) + C_i\cosh(k_i z) + D_i\sinh(k_i z)\right)}_{\phi_{\mathrm{CL}i}}, \end{aligned} \tag{3.7}$$

wherein

$$k_i^2 = \sqrt{\frac{\rho_{\mathrm{CL}}A_{\mathrm{CL}}}{EI_y}}\omega_{\mathrm{CL}i}, \tag{3.8}$$

are the eigenvalues and A_i, B_i, C_i and D_i form the eigenvector, determined by the boundary conditions given in the following paragraph. $\omega_{\mathrm{CL}i}$ is the i-th uncoupled angular resonance frequency of the cantilever. Since the bending stiffness EI_y is constant, the stiffness term of Eq. (3.6) simplifies to the fourth partial derivative of Eq. (3.7)

$$\partial^4 u_{\mathrm{CL}}(z)/\partial z^4 = k_1^4 u_{\mathrm{CL}}(z). \tag{3.9}$$

Using the surface mass density $m''_{\mathrm{CL}} = \rho_{\mathrm{CL}}A_{\mathrm{CL}}/w$, Eq. (3.6) turns to

$$\sum_{i=0}^{N}\left(\omega_{\mathrm{CL}i}^2 + \frac{1}{2}\mathrm{i}\omega\frac{R_{\mathrm{HR}}}{m''_{\mathrm{CL}}} - \omega^2\right)m''_{\mathrm{CL}}u_{\mathrm{CL}i}(z) - \frac{1}{2}\mathrm{i}\omega R_{\mathrm{HR}}u_{\mathrm{HR}} = p - p_{\mathrm{cav}}. \tag{3.10}$$

In the following, the boundary conditions of the cantilever are determined. Since the cantilever is fabricated as an integral part of the resonator body, the cantilever support is not perfectly rigid, but is compliant. The cantilever rotates at the support due to

the moment at the cantilever root. Consequently, the resonance frequency is reduced compared to that of a clamped boundary condition, for which the formula can be found in for example [29]. Therefore, $\omega_{\mathrm{CL}i}$ is calculated according to Mac Bain and Genin [93], who analyzed the influence of the support stiffness on the eigenfrequencies of a cantilever. With the rotational stiffness of the support Γ_{m}, the four boundary conditions (with the notation $u' = \partial u/\partial z$ etc.) for the cantilever are:

1. $u_{\mathrm{CL}}(0) = 0$, no deflection at the support,
2. $\Gamma_{\mathrm{m}} u'_{\mathrm{CL}}(0) = EI_y u''_{\mathrm{CL}}(0)$, slope of the cantilever at the support, due to the rotation,
3. $u''_{\mathrm{CL}}(l) = 0$, no bending moment at the free end of the cantilever,
4. $u'''_{\mathrm{CL}}(l) = 0$, no shear force at the free end of the cantilever.

Mac Bain and Genin introduced the non-dimensional rotational end-fixity parameter Γ

$$\Gamma = \frac{\Gamma_{\mathrm{m}} l}{EI_y}, \tag{3.11}$$

and derived a semi-phenomenological model for calculating Γ. Using this model, the rotational end-fixity parameter Γ can be simplified to

$$\Gamma = 2.267 \frac{l}{t_{\mathrm{s}}}, \tag{3.12}$$

if the given cantilever and the support have the same material properties and geometric dimensions. In this simplified case, Γ is independent of the cantilever width w. Inserting the deflection of the cantilever u_{CL} (Eq. (3.7)) into the boundary conditions results in the following eigenvalue problem:

$$\begin{bmatrix} 1 & 0 & 1 & 0 \\ -k_i^2 l & -\Gamma k_i & k_i^2 l & -\Gamma k_i \\ -k_i^2 \cos(k_i l) & -k_i^2 \sin(k_i l) & k_i^2 \cosh(k_i l) & k_i^2 \sinh(k_i l) \\ k_i^3 \sin(k_i l) & -k_i^3 \cos(k_i l) & k_i^3 \sinh(k_i l) & k_i^3 \cosh(k_i l) \end{bmatrix} \begin{pmatrix} A_i \\ B_i \\ C_i \\ D_i \end{pmatrix} = \begin{pmatrix} 0 \\ 0 \\ 0 \\ 0 \end{pmatrix}. \tag{3.13}$$

Defining λ_i as

$$\lambda_i = k_i l = \omega_{\mathrm{CL}i}^{1/2} \left(\frac{\rho_{\mathrm{CL}} A_{\mathrm{CL}} l^4}{EI_y} \right)^{1/4}, \tag{3.14}$$

and setting the determinant of the coefficient matrix to zero leads to the following transcendental characteristic equation

$$\Gamma = \frac{\lambda_i \left(\sin(\lambda_i) \cosh(\lambda_i) - \cos(\lambda_i) \sinh(\lambda_i) \right)}{\left(1 + \cos(\lambda_i) \cosh(\lambda_i) \right)}. \tag{3.15}$$

This thesis focuses on the two lowest resonance frequencies of the coupled resonator system, which are typically between 200 and 1000 Hz in the present application. Since the cantilever is designed in a way that only the fundamental frequency f_{CL1} falls within the relevant frequency range, only the first eigenmode of the cantilever $u_{\mathrm{CL1}} = a_{\mathrm{CL1}}\phi_{\mathrm{CL1}}$ is considered, to approximate the beam displacement field u_{CL}.

After calculating numerically λ_1 with Eq. (3.12) and Eq. (3.15), the first angular resonance frequency ω_{CL1} and the first eigenvalue k_1 can be determined. The corresponding eigenvector with the coefficients A_1, B_1, C_1 and D_1 can then be calculated by inserting the calculated values k_1 and Γ in Eq. (3.13) and computing the null space of the matrix.

Using the above equations, the second resonance frequency of the cantilever is calculated to be about seven times higher than the first one, which justifies the approach of approximating the beam displacement field by the first eigenform.

3.3. Coupling

3.3.1. Fluid-structure- and fluid-fluid-coupling: pressure field induced by the cantilever deformation and air movement in the Helmholtz resonator neck

Both oscillators are coupled by the cavity, which, at low frequencies, acts as a spring. The governing equation for the air pressure inside the cavity is the Helmholtz equation

$$\left(\Delta + \left(\frac{\omega}{c_0}\right)^2\right) p_{\mathrm{cav}} = 0. \tag{3.16}$$

The air inside the cavity is attributed to the boundary conditions of a rectangular waveguide, with a reflecting end plate and the dimensions $l_y = W - 2t_{\mathrm{s}}$, $l_z = L - 2t_{\mathrm{s}}$ and $l_x = H - 2t_{\mathrm{s}}$ and the cavity volume $V_{\mathrm{cav}} = l_x \cdot l_y \cdot l_z$, see Fig. 3.2. The particle velocity of

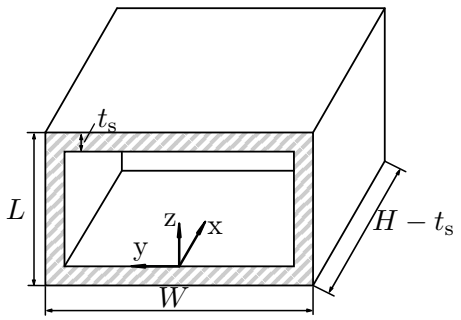

Figure 3.2: Schematic representation of the rectangular acoustic waveguide representing the resonator cavity.

the sound field inside the waveguide is assumed to be zero at the bottom and sidewalls of the waveguide, modeling the walls as rigid. To approximate the sound pressure field inside the rectangular waveguide, the modal expansion method is used with the modal participation factor of the pressure amplitude $a_{n_y n_z}$ and the trial eigenfunctions $\phi_{n_y n_z}(y,z)$ and $r_{n_y n_z}(x)$

$$\begin{aligned} p_{\text{cav}} &\approx \sum_{n=0}^{N} a_{n_y n_z} \phi_{n_y n_z}(y,z) r_{n_y n_z}(x) \\ &= \sum_{n_y=0}^{N_y} \sum_{n_z=0}^{N_z} a_{n_y n_z} \underbrace{\cos\left(\frac{n_z \pi z}{l_z}\right) \cos\left(\frac{n_y \pi (y - l_y/2)}{l_y}\right)}_{\phi_{n_y n_z}} \underbrace{\left(e^{\mathrm{i}\beta_{n_y n_z}(x-l_x)} + e^{-\mathrm{i}\beta_{n_y n_z}(x-l_x)}\right)}_{r_{n_y n_z}}. \end{aligned} \tag{3.17}$$

The trial eigenfunctions in the y- and z-directions $\phi_{n_y n_z}$ respect the pressure maximum at the rigid sidewalls, while the eigenfunctions in the x-direction $r_{n_y n_z}$ incorporate the forward and backward traveling wave, which have the same amplitude due to a fully reflecting sound hard wall at the bottom of the resonator ($x = l_x$). In Eq. (3.17), N_y and N_z are the number of modes in the y- and z-directions, respectively, $N = (N_y+1)(N_z+1)$ is the total number of modes, n_y and n_z are the running index variables, and

$$\beta_{n_y n_z} = \pm\sqrt{\left(\frac{\omega}{c_0}\right)^2 - \left(\frac{n_z \pi}{l_z}\right)^2 - \left(\frac{n_y \pi}{l_y}\right)^2}, \tag{3.18}$$

are the propagation constants. The latter have a positive sign for positive radicants (i.e. real $\beta_{n_y n_z}$) and a negative sign for negative radicants (i.e. imaginary $\beta_{n_y n_z}$). The x-component of the particle velocity inside the cavity $v_{\text{cav},x}$ is

$$\begin{aligned} v_{\text{cav},x} &= -\frac{1}{\mathrm{i}\omega\rho_0} \frac{\partial p_{\text{cav}}}{\partial x} \\ &= \sum_{n=0}^{N} -\frac{a_{n_y n_z}}{\mathrm{i}\omega\rho_0} \underbrace{\cos\left(\frac{n_z \pi z}{l_z}\right) \cos\left(\frac{n_y \pi (y - \frac{l_y}{2})}{l_y}\right)}_{\phi_{n_y n_z}} \underbrace{\mathrm{i}\beta_{n_y n_z} \left(e^{\mathrm{i}\beta_{n_y n_z}(x-l_x)} - e^{-\mathrm{i}\beta_{n_y n_z}(x-l_x)}\right)}_{s_{n_y n_z}}, \end{aligned} \tag{3.19}$$

with p_{cav} given by Eq. (3.17).

The boundary condition for the particle velocity at the top of the cavity (x=0) is defined by the transversal vibration velocity of the top plate, including the vibration velocity of the cantilever, and by the particle velocity of the air in the Helmholtz resonator neck. The

top plate of the resonator is assumed to be rigid except for the cantilever, which vibrates with the velocity $v_{\mathrm{CL}}(z) = \mathrm{i}\omega u_{\mathrm{CL}}(z)$. Thus, for points $P(0,y,z)$ at the top of the cavity, the particle velocity is given by

$$v_{\mathrm{cav},x}(0,y,z) = \begin{cases} \mathrm{i}\omega u_{\mathrm{CL}}(z) & \text{if } P(0,y,z) \text{ on } S_{\mathrm{CL}}, \text{ see Fig. 3.1} \\ \mathrm{i}\omega u_{\mathrm{HR}}(z) & \text{if } P(0,y,z) \text{ on } S_{\mathrm{HR}}, \text{ see Fig. 3.1} \\ 0 & \text{else.} \end{cases} \tag{3.20}$$

To solve Eq. (3.20), $v_{\mathrm{cav},x}$ is replaced by Eq. (3.19) and the displacement u_{CL} can be approximated by Eq. (3.7). Eq. (3.20) is not solved exactly at each point, but approximated by the Galerkin method of weighted residuals, using the trial functions of the fluid as the weighting functions. Therefore, Eq. (3.20) is multiplied by an arbitrary weighting function $\phi_{m_y m_z}(y,z)$ and integrated over the base area of the cavity $S_{\mathrm{cav}} = l_y \cdot l_z$:

$$\begin{aligned} &\sum_{n=0}^{N} -\frac{1}{\mathrm{i}\omega\rho_0} a_{n_y n_z} \underbrace{\mathrm{i}\beta_{n_y n_z}\left(e^{-\mathrm{i}\beta_{n_y n_z} l_x} - e^{+\mathrm{i}\beta_{n_y n_z} l_x}\right)}_{s_{n_y n_z}} \underbrace{\iint_{S_{\mathrm{cav}}} \phi_{m_y m_z}\phi_{n_y n_z}\,\mathrm{d}S}_{w_{m_y m_z n_y n_z} S_{\mathrm{cav}}} \\ &= \mathrm{i}\omega a_{\mathrm{CL1}} \underbrace{\iint_{S_{\mathrm{CL}}} \phi_{m_y m_z}\phi_{\mathrm{CL}}\,\mathrm{d}S}_{b_{m_y m_z}} + \mathrm{i}\omega u_{\mathrm{HR}} \underbrace{\iint_{S_{\mathrm{HR}}} \phi_{m_y m_z}\,\mathrm{d}S}_{e_{m_y m_z}}. \end{aligned} \tag{3.21}$$

Eq. (3.21) describes the continuity condition between the vibration velocity of the plate surface and the particle velocity of the fluid at the top side of the cavity. In Eq. (3.21), $s_{n_y n_z}$ and $w_{m_y m_z n_y n_z}$ are defined as

$$s_{n_y n_z} = 2\beta_{n_y n_z} \sin(\beta_{n_y n_z} l_x) \tag{3.22}$$

and

$$w_{m_y m_z n_y n_z} = \begin{cases} 0 & \text{if } m_y \neq n_y \ \vee \ m_z \neq n_z \\ 1/4 & \text{if } m_y = n_y \neq 0 \ \wedge \ m_z = n_z \neq 0 \\ 1 & \text{if } m_y = n_y = m_z = n_z = 0 \\ 1/2 & \text{else.} \end{cases} \tag{3.23}$$

For clarity, the equations to calculate $b_{m_y m_z}$ and $e_{m_y m_z}$ are listed in the Appendix. Eq. (3.21) can be written in a more compact form using vector-matrix notation as

$$\mathbf{A}\mathbf{a}_{n_y n_z} + \mathbf{b} a_{\mathrm{CL1}} + \mathbf{e} u_{\mathrm{HR}} = \mathbf{0}, \tag{3.24}$$

with the diagonal matrix

$$\mathbf{A} = S_{\text{cav}} \begin{bmatrix} s_{00}w_{0000} & & 0 \\ & \ddots & \\ 0 & & s_{n_y n_z} w_{m_y m_z n_y n_z} \end{bmatrix} \in \mathbb{R}^{N \times N}, \tag{3.25}$$

and the coupling vectors

$$\mathbf{b} = -\rho_0 \omega^2 \begin{bmatrix} b_{00} \\ \vdots \\ b_{m_y m_z} \end{bmatrix} \in \mathbb{R}^{N \times 1} \tag{3.26}$$

and

$$\mathbf{e} = -\rho_0 \omega^2 \begin{bmatrix} e_{00} \\ \vdots \\ e_{m_y m_z} \end{bmatrix} \in \mathbb{R}^{N \times 1}. \tag{3.27}$$

3.3.2. Fluid-structure-coupling: pressure induced cantilever deformation

Eq. (3.10) describes the equation of motion of the cantilever, where the pressure difference $p - p_{\text{cav}}$ depends on the pressure distribution of the fluid at the top of the cavity $p_{\text{cav}}(0,y,z)$, as defined by Eq. (3.17). Inserting Eq. (3.17) into Eq. (3.10) and again using the Galerkin method, multiplying Eq. (3.10) by the trial function ϕ_{CL} as the weighting function and integrating over the cantilever area, yields

$$\begin{aligned} & a_{\text{CL1}}(\omega_{\text{CL1}}^2 + \frac{1}{2}\mathrm{i}\omega \frac{R_{\text{HR}}}{m''_{\text{CL}}} - \omega^2) m''_{\text{CL}} \underbrace{\iint_{S_{\text{CL}}} \phi_{\text{CL}}^2 \, \mathrm{d}S}_{d} - \frac{1}{2}\mathrm{i}\omega R_{\text{HR}} u_{\text{HR}} \underbrace{\iint_{S_{\text{CL}}} \phi_{\text{CL1}} \, \mathrm{d}S}_{h} \\ & = p \underbrace{\iint_{S_{\text{CL}}} \phi_{\text{CL}} \, \mathrm{d}S}_{h} - a_{n_y n_z} \sum_{n=0}^{N} \underbrace{\left(e^{-\mathrm{i}\beta_{n_y n_z} l_x} + e^{\mathrm{i}\beta_{n_y n_z} l_x}\right)}_{r_{n_y n_z}} \underbrace{\iint_{S_{\text{CL}}} \phi_{n_y n_z} \phi_{\text{CL}} \, \mathrm{d}S}_{b_{n_y n_z}}, \end{aligned} \tag{3.28}$$

where the ambient pressure p is assumed to be constant and

$$r_{n_y n_z} = 2 \cos\left(\beta_{n_y n_z} l_x\right). \tag{3.29}$$

The calculations of d and h can be found in the Appendix. Eq. (3.28) can be written in a compact form as

$$\mathbf{c^T a}_{n_y n_z} + D\, a_{\text{CL1}} + K\, u_{\text{HR}} = p\, h, \tag{3.30}$$

with the coupling (row) vector

$$\mathbf{c^T} = \begin{bmatrix} r_{00}b_{00} & \cdots & r_{n_y n_z}b_{n_y n_z} \end{bmatrix} \in \mathbb{R}^{1\times N}, \tag{3.31}$$

and the scalars

$$D = (\omega_{\mathrm{CL1}}^2 + \frac{1}{2}\mathrm{i}\omega\frac{R_{\mathrm{HR}}}{m''_{\mathrm{CL}}} - \omega^2)m''_{\mathrm{CL}}d \tag{3.32}$$

and

$$K = -\frac{1}{2}\mathrm{i}\omega R_{\mathrm{HR}}h. \tag{3.33}$$

3.3.3. Fluid-fluid-coupling: pressure induced movement of the air in the Helmholtz resonator neck

Eq. (3.1) describes the equation of motion of the air mass in the neck of the Helmholtz resonator, assuming a constant pressure profile over the neck. Therefore, the cavity pressure p_{cav} from Eq. (3.17) is averaged over the neck area S_{HR}, using the modal participation factors and the trial functions. Eq. (3.1) can be rewritten as

$$\begin{aligned} &\left(\mathrm{i}\omega R_{\mathrm{HR}} - \omega^2 m''_{\mathrm{HR}}\right) u_{\mathrm{HR}} - \frac{1}{2}\mathrm{i}\omega R_{\mathrm{HR}}\frac{a_{\mathrm{CL1}}}{S_{\mathrm{CL}}}\underbrace{\iint_{S_{\mathrm{CL}}}\phi_{\mathrm{CL1}}\,\mathrm{d}S}_{h} \\ &= p - \frac{a_{n_y n_z}}{S_{\mathrm{HR}}}\sum_{n=0}^{N}\underbrace{\left(e^{-\mathrm{i}\beta_{n_y n_z}l_x} + e^{\mathrm{i}\beta_{n_y n_z}l_x}\right)}_{r_{n_y n_z}}\underbrace{\iint_{S_{\mathrm{HR}}}\phi_{n_y n_z}\,\mathrm{d}S}_{e_{n_y n_z}}, \end{aligned} \tag{3.34}$$

or in a more compact form

$$\mathbf{g^T a}_{n_y n_z} + J a_{\mathrm{CL1}} + F u_{\mathrm{HR}} = p S_{\mathrm{HR}}, \tag{3.35}$$

with the coupling (row) matrix

$$\mathbf{g^T} = \begin{bmatrix} r_{00}e_{00} & \cdots & r_{n_y n_z}e_{n_y n_z} \end{bmatrix} \in \mathbb{R}^{1\times N}, \tag{3.36}$$

and the scalars

$$J = -\frac{1}{2}\mathrm{i}\omega R_{\mathrm{HR}}\frac{S_{\mathrm{HR}}}{S_{\mathrm{CL}}}h \tag{3.37}$$

and

$$F = \left(\mathrm{i}\omega R_{\mathrm{HR}} - \omega^2 m''_{\mathrm{HR}}\right) S_{\mathrm{HR}}. \tag{3.38}$$

The combination of the Eqs. 3.24, 3.30, and 3.35 forms a coupled system of equations for the unknown vector $\mathbf{a_{n_y n_z}}$ and the unknown scalars a_{CL} and u_{HR}, containing the

modal participation factors of the cavity pressure field, the cantilever, and the Helmholtz resonator neck, respectively

$$\underbrace{\begin{bmatrix} \mathbf{A} & \mathbf{b} & \mathbf{e} \\ \mathbf{c^T} & D & K \\ \mathbf{g^T} & J & F \end{bmatrix}}_{\mathbf{S}(\omega)} \underbrace{\begin{pmatrix} \mathbf{a}_{n_y n_z} \\ a_{\mathrm{CL1}} \\ u_{\mathrm{HR}} \end{pmatrix}}_{\mathbf{x}} = p \begin{pmatrix} 0 \\ h \\ S_{\mathrm{HR}} \end{pmatrix}. \tag{3.39}$$

3.4. Simplification for constant cavity pressure

The derived model can be simplified by assuming a constant pressure distribution inside the cavity. This is a reasonable assumption if the dimensions of the cavity are much smaller than the acoustic wavelength. If the pressure is assumed to be constant, n_y and n_z will be zero. After some algebraic steps, the system of equations in Eq. (3.39) can be simplified to

$$\begin{bmatrix} \left(\omega_{\mathrm{CL1}}^2 + \frac{1}{2}\mathrm{i}\omega\frac{R_{\mathrm{HR}}}{m''_{\mathrm{CL}}} - \omega^2\right) m''_{\mathrm{CL}} + \frac{\rho_0 c_0^2}{V_{\mathrm{cav}}} S_{\mathrm{CL}} & -\frac{1}{2}\mathrm{i}\omega R_{\mathrm{HR}} + \frac{\rho_0 c_0^2}{V_{\mathrm{cav}}} S_{\mathrm{HR}} \\ -\frac{1}{2}\mathrm{i}\omega R_{\mathrm{HR}} + \frac{\rho_0 c_0^2}{V_{\mathrm{cav}}} S_{\mathrm{CL}} & \mathrm{i}\omega R_{\mathrm{HR}} - \omega^2 m''_{\mathrm{HR}} + \frac{\rho_0 c_0^2}{V_{\mathrm{cav}}} S_{\mathrm{HR}} \end{bmatrix} \begin{pmatrix} \bar{u}_{\mathrm{CL}} \\ u_{\mathrm{HR}} \end{pmatrix} = p \begin{pmatrix} 1 \\ 1 \end{pmatrix}. \tag{3.40}$$

With the first angular resonance frequency of an uncoupled cantilever ω_{CL1}, the modified angular frequency of the integrated cantilever

$$\omega_{\mathrm{CL,V}}^2 = \omega_{\mathrm{CL1}}^2 + \frac{\rho_0 c_0^2 S_{\mathrm{CL}}}{V_{\mathrm{cav}} m''_{\mathrm{CL}}}, \tag{3.41}$$

can be defined. $\omega_{\mathrm{CL,V}}$ takes into account the additional stiffness $\rho_0 c_0^2 S_{\mathrm{CL}}/V_{\mathrm{cav}}$ due to the air volume of the cavity. With the angular resonance frequency of the uncoupled Helmholtz resonator

$$\omega_{\mathrm{HR}}^2 = \frac{\rho_0 c_0^2 S_{\mathrm{HR}}}{V_{\mathrm{cav}} m''_{\mathrm{HR}}}, \tag{3.42}$$

some further algebraic steps, and neglecting the damping, the coefficient matrix of the system of equations can be represented symmetrically and dimensionless

$$\begin{bmatrix} \left(1 - \frac{\omega^2}{\omega_{\mathrm{CL,V}}^2}\right) \frac{S_{\mathrm{CL}}}{S_{\mathrm{HR}}} & \frac{\rho_0 c_0^2 S_{\mathrm{CL}}}{V_{\mathrm{cav}} m''_{\mathrm{CL}} \omega_{\mathrm{CL,V}}^2} \\ \frac{\rho_0 c_0^2 S_{\mathrm{CL}}}{V_{\mathrm{cav}} m''_{\mathrm{CL}} \omega_{\mathrm{CL,V}}^2} & \left(1 - \frac{\omega^2}{\omega_{\mathrm{HR}}^2}\right) \frac{m''_{\mathrm{HR}} \omega_{\mathrm{HR}}^2}{m''_{\mathrm{CL}} \omega_{\mathrm{CL,V}}^2} \end{bmatrix} \begin{pmatrix} \bar{u}_{\mathrm{CL}} \\ u_{\mathrm{HR}} \end{pmatrix} = p \begin{pmatrix} \frac{S_{\mathrm{CL}}}{S_{\mathrm{HR}} m''_{\mathrm{CL}} \omega_{\mathrm{CL,V}}^2} \\ \frac{1}{m''_{\mathrm{CL}} \omega_{\mathrm{CL,V}}^2} \end{pmatrix}. \tag{3.43}$$

The off-diagonal elements in Eq. (3.43) describe the dimensionless coupling parameter C_{HRCL}, which represents the coupling strength between the two oscillators:

$$C_{\mathrm{HRCL}} = \frac{\rho_0 c_0^2 S_{\mathrm{CL}}}{V_{\mathrm{cav}} m''_{\mathrm{CL}} \omega^2_{\mathrm{CL,V}}} = \frac{\rho_0 c_0^2 wl}{V_{\mathrm{cav}} \rho_{\mathrm{CL}} t_{\mathrm{s}} \omega^2_{\mathrm{CL,V}}} = \frac{\omega^2_{\mathrm{CL,V}} - \omega^2_{\mathrm{CL1}}}{\omega^2_{\mathrm{CL,V}}}. \tag{3.44}$$

C_{HRCL} depends on the bulk modulus of the fluid $\rho_0 c_0^2$, the size of the cavity volume V_{cav}, the size of the cantilever area S_{CL}, the cantilever mass m''_{CL}, and the angular resonance frequency of the cantilever $\omega_{\mathrm{CL,V}}$ stiffened by the air volume of the cavity. The coupling parameter can be further simplified to

$$C_{\mathrm{HRCL}} = \frac{1}{\frac{\omega^2_{\mathrm{CL1}} V_{\mathrm{cav}} m''_{\mathrm{CL}}}{\rho_0 c_0^2 S_{\mathrm{CL}}} + 1} \leq 1, \tag{3.45}$$

such that it can be calculated without $\omega_{\mathrm{CL,V}}$. The meaning behind the coupling parameter can be illustrated as follows: The first row in Eq. (3.43) represents the simplified equation of motion of the cantilever. The cantilever motion also depends on the motion of the air mass in the neck, if the value of C_{HRCL} is different from 0. The second row represents the simplified equation of motion of the Helmholtz resonator, which depends on the motion of the cantilever, if C_{HRCL} is different from 0. Both equations are connected by the off-diagonal elements, which form the non-dimensional coupling parameter. When the coupling parameter is small, the influence of the air motion of the Helmholtz resonator on the displacement of the cantilever (and vice versa) is small, so the value of the coupling parameter defines the coupling strength. The coupling strength between the two oscillators is increased by larger cantilever areas S_{CL} and reduced by larger cavity volumes V_{cav}, larger values of the cantilever mass $m''_{\mathrm{CL}} = \rho_{\mathrm{CL}} t_{\mathrm{s}}$ and larger values of the resonance frequency of the cantilever ω_{CL1}.

3.5. Eigenfrequency calculation

In this section, the eigenfrequencies of the coupled resonator of cantilever and Helmholtz resonator (f_1 and f_2) as well as the integrated cantilever $f_{\mathrm{CL,V}}$ are calculated using the derived analytical model, which takes into account the pressure modes inside the cavity. For comparison, the eigenfrequencies are also calculated with the simplified model assuming a constant pressure profile inside the cavity.

The viscous losses in the boundary layer of the neck R_{HR}, the structural damping of the resonator material and the exterior pressure p are set to zero to form a non-linear eigenvalue problem. The damping behavior of the resonator is ignored because the eigenvalue problem is primarily used to tune the resonance frequencies of the coupled system, especially for preliminary design studies. Neglecting damping simplifies the analysis, since the real-valued undamped angular resonance frequency ω_0 is obtained instead of the complex-

valued damped angular resonance frequency ω_d. For damping ratios ζ less than 0.2, the damped angular resonance frequency can be approximated rather accurately (within 2 %) as [25]

$$\omega_\mathrm{d} \approx \omega_0(1 + \mathrm{i}\zeta). \tag{3.46}$$

The correlation between the damping ratio and the deviation between the damped and undamped angular resonance frequency is demonstrated in Appendix A.3. Eq. (3.46) indicates that, for low damping ratios, the real part of the complex-valued damped angular resonance frequency represents the undamped angular resonance frequency ω_0, while the imaginary part reflects the damping. As calculated in Section 4.4 and Section 6.3, the damping ratios considered in this thesis range from $\zeta = 0.02$ to $\zeta = 0.06$, so that the the damped angular resonance frequency can be approximated with Eq. (3.46).

Using the Newton Trace Method, as described in Ref. [49], to numerically solve the resulting nonlinear eigenvalue problem for the system matrix $\mathbf{S}$ (see Eq. (3.39)), allows to calculate the angular resonance frequencies of the coupled system of cantilever and Helmholtz resonator. Of these, the two lowest angular resonance frequencies ω_1 and ω_2 and the two lowest eigenfrequencies f_1 and f_2, respectively, are considered in this contribution.

The system of equations can also be used to determine the resonance frequency of the integrated cantilever $f_\mathrm{CL,V}$, that is stiffened by the air volume in the cavity. To calculate $f_\mathrm{CL,V}$, the system is considered to consist of a cantilever interacting with the enclosed air volume in the cavity with no resonator neck opening ($S_\mathrm{HR} = 0$). Therefore $f_\mathrm{CL,V}$ can be calculated by solving the eigenvalue problem of the subsystem

$$\begin{bmatrix} \mathbf{A} & \mathbf{b} \\ \mathbf{c^T} & D \end{bmatrix} \begin{pmatrix} \mathbf{a}_{n_y n_z} \\ a_\mathrm{CL1} \end{pmatrix} = \begin{pmatrix} 0 \\ 0 \end{pmatrix}. \tag{3.47}$$

Using the simplified model assuming a constant pressure distribution inside the cavity (Eq. (3.43)), the resonance frequencies f_1 and f_2 of the resonator

$$f_{1,2}^2 = \frac{1}{2}\left(f_\mathrm{HR}^2 + f_\mathrm{CL,V}^2\right) \pm \sqrt{\frac{1}{4}\left(f_\mathrm{HR}^2 + f_\mathrm{CL,V}^2\right)^2 - f_\mathrm{HR}^2 f_\mathrm{CL1}^2}, \tag{3.48}$$

are obtained by solving the characteristic equation of the eigenvalue problem, ignoring the outside pressure p and the viscous losses in the Helmholtz resonator neck R_HR. Eq. (3.48) shows that for the simplified model, the resonance frequencies of the coupled system f_1 and f_2 are calculated with the three resonance frequencies f_HR, f_CL1 and $f_\mathrm{CL,V}$.

3.6. Absorption coefficient

The acoustic absorption coefficient can be calculated using the input impedance Z_{res} of the resonator. As detailed in Section 2.2, the input impedance is defined as

$$Z_{\mathrm{res}} = \frac{p}{v}, \tag{3.49}$$

where p and v are the pressure amplitude and the particle velocity at the top plate of the resonator, respectively, see Fig. 3.1 a). Since the resonator has thin walls, the particle velocity at the top of the resonator ($x = -t_{\mathrm{s}}$) is approximately equal to the velocity at the top of the cavity ($x = 0$) and can be calculated using the derived model. Solving Eq. (3.39) for the modal participation factors in $\mathbf{x}$ for each angular frequency assuming an arbitrary outside pressure amplitude p, allows to calculate the mean displacement of the cantilever $\bar{u}_{\mathrm{CL}}$ and the displacement of the air inside the Helmholtz resonator neck u_{HR}. The average particle velocity for each angular frequency can be calculated using the continuity condition as

$$v = \frac{\mathrm{i}\omega}{S_{\mathrm{res}}} \left(S_{\mathrm{CL}} \bar{u}_{\mathrm{CL}} + S_{\mathrm{HR}} u_{\mathrm{HR}} \right). \tag{3.50}$$

Inserting Eq. (3.50) into Eq. (3.49), gives the input impedance of the resonator, such that the absorption coefficient of the resonator in front of a rigid wall can be calculated via the matching law [103], as derived in Section 2.2

$$\alpha = \frac{4\rho_0 c_0 \frac{S}{S_{\mathrm{res}}} \mathrm{Re}(Z_{\mathrm{res}})}{\left(\frac{S}{S_{\mathrm{res}}} \mathrm{Re}(Z_{\mathrm{res}}) + \rho_0 c_0 \right)^2 + \frac{S^2}{S_{\mathrm{res}}^2} \mathrm{Im}(Z_{\mathrm{res}})^2}. \tag{3.51}$$

In Eq. (3.51), S has been introduced to account for a larger surface area than the resonator base plate S_{res}, see Fig. 3.3. For example, in Subsection 4.2.2, the absorption coefficient is experimentally validated with impedance tube measurements, where the circular cross section S of the impedance tube is larger than the resonator base plate S_{res}.

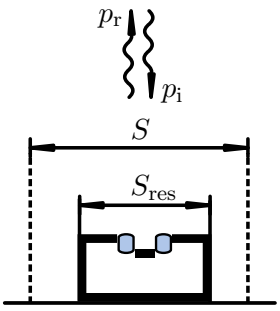

Figure 3.3: Schematic representation of the resonator as a sound absorber, where the surface area S can be larger than the area of the resonator base plate S_{res}.

3.7. Transmission loss

The analytical model can also be used to calculate the transmission loss characteristics of the resonator when the resonator is implemented in a duct surrounded by an air layer, such as an impedance tube for experimental measurements on the resonator. When the dimensions of the resonator are small compared to both the cross section of the duct and to the length of the acoustic wavelength, as is the case at low frequencies, the sound pressure transmission factor t can be calculated as derived in Section 2.3.1 via:

$$t = \left(1 + \frac{1}{2}\frac{S_{\mathrm{res}}}{S}\frac{\rho_0 c_0}{Z_{\mathrm{res}}}\right)^{-1}, \tag{3.52}$$

where Z_{res} is the input impedance as given in Eq. (3.49) and S and S_{res} denote the cross section area of the duct and the base area of the resonator, respectively, as depicted in Fig. 3.4. The transmission loss can be calculated with the sound pressure transmission factor via $\mathrm{TL} = -20\,\lg|t|$.

The resonator in Fig. 3.4 is rotated by 90°, compared to Section 2.3.1, so that the resonator is symmetrical in the direction of the sound waves. This position of the resonator will be later used in the impedance tube measurements, as it was experienced that the coherence of the measured data was higher for symmetrical test samples. While the magnitude of the transmission loss depends on the area covered by the resonator from the cross section of the tube, the location of the resonance frequencies is not affected by this modification.

Finite element simulations were preformed for two example positions of a Helmholtz resonator with integrated cantilever to examine the influence of the resonator position onto the transmission loss. The finite element model is further described in Section 4.3.1. The dimensions of the resonator are listed in Table 4.1 with a cantilever width of 5 mm. The calculated transmission loss values are shown in Fig. 3.5. As stated above, the qualitative trend of the transmission loss of the resonator remains consistent regardless of its orientation, as the resonator is small compared to the acoustic wavelength. However, the magnitude of the transmission loss depends on the percentage of the cross-sectional area of the tube occupied by the resonator. In Section 2.3.1, it was assumed, that the dimensions of the resonator are small compared to the cross section of the tube. Since the

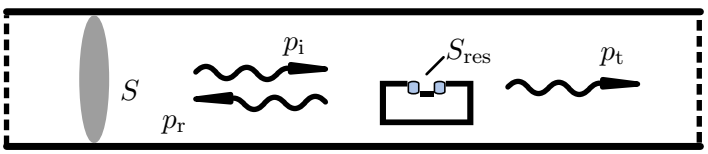

Figure 3.4: Schematic representation of a Helmholtz resonator installed in a duct.

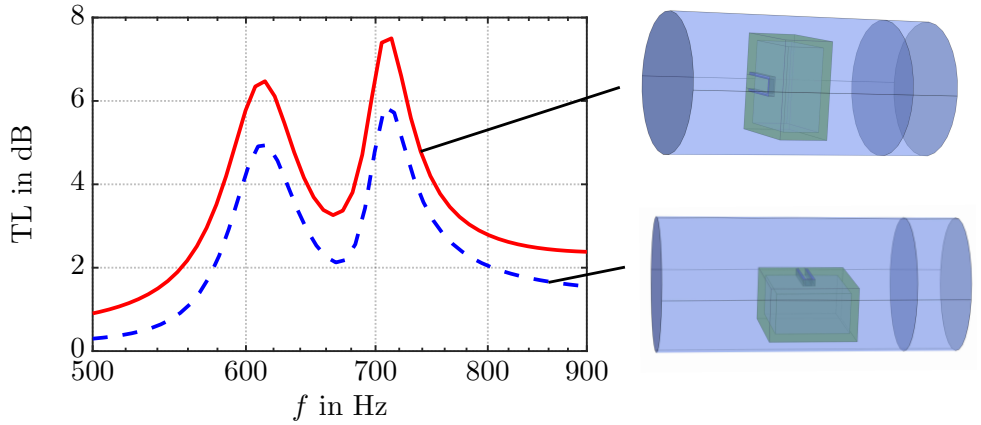

Figure 3.5: Transmission loss characteristics of a Helmholtz resonator with integrated cantilever installed in a duct determined by finite element model simulations. (—) Resonator facing the sound source, (- -) resonator top plate parallel to the direction of sound.

base area of the resonator $S_{\text{res}} = L \cdot W$ is larger than the area of the resonator side $L \cdot H$, the transmission loss is higher when the resonator neck faces the sound source compared to when the resonator neck is parallel to the sound direction.

3.8. Transfer matrix model of the Helmholtz resonator with cantilever

The presented resonator can also be installed in a resonator plate, where several resonators are arranged area-wide to form a resonator array (see Fig. 3.6). In this section, a transfer matrix for an infinite resonator plate will be derived, in order to be able to model the acoustic behavior of the resonator plate installed in a multi-layered setup. Parts of the derivation, such as the equations of motion, have also been published in Ref. [55]. The transfer matrix model published in Ref. [55] could not accurately model the acoustic behavior around the resonance frequencies of the coupled system f_1 and f_2, since the resonance frequencies were calculated to be lower for f_1 and higher for f_2 than seen in the verification. The transfer matrix derived below improves the solution presented in Ref. [55], by using the results of the analytical model proposed in this thesis.

A schematic representation of an infinite resonator panel of Helmholtz resonators with integrated cantilevers is shown in Fig. 3.6. The two oscillators, the Helmholtz resonator and the cantilever, are coupled by the resonator cavity acting as a spring. The displacement u_{HR} of the fluid in the slit as well as the mean displacement $\bar{u}_{\text{CL}}$ of the cantilever beam cause a volume change in the cavity given by

$$\Delta V = \Delta V_{\text{HR}} + \Delta V_{\text{CL}} = -S_{\text{HR}} u_{\text{HR}} - S_{\text{CL}} \bar{u}_{\text{CL}}. \tag{3.53}$$

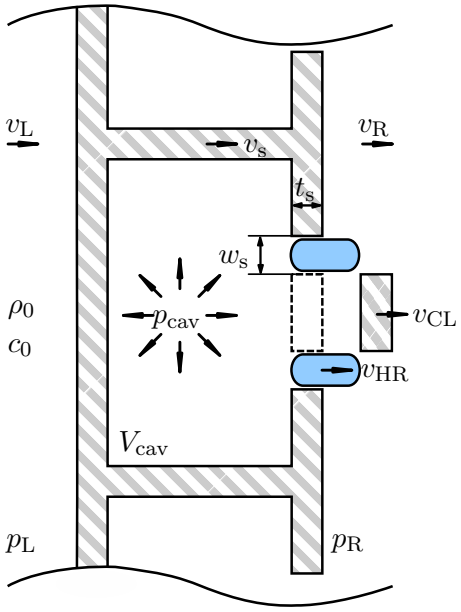

Figure 3.6: Schematic representation of an infinite resonator panel with Helmholtz resonators with integrated cantilevers. The blue filled areas represent the fluid volume in the U-shaped slit of the resonator.

This volume change generates a pressure change p_cav inside the resonator. With the bulk modulus of the fluid $\rho_0 c_0^2$, the pressure inside the resonator is calculated as [67]

$$p_\mathrm{cav} = \rho_0 c_0^2 \frac{\Delta V}{V_\mathrm{cav}}. \tag{3.54}$$

The pressure in the resonator, expressed in terms of the particle velocity of the fluid in the neck $v_\mathrm{HR} = \mathrm{i}\omega u_\mathrm{HR}$, the mean vibration velocity of the cantilever $v_\mathrm{CL} = \mathrm{i}\omega \bar{u}_\mathrm{CL}$, and the vibration velocity of the plate v_s, results in

$$p_\mathrm{cav} = -\frac{\rho_0 c_0^2}{V_\mathrm{cav}} \frac{S_\mathrm{HR}\left(v_\mathrm{HR} - v_\mathrm{s}\right) + S_\mathrm{CL}\left(v_\mathrm{CL} - v_\mathrm{s}\right)}{\mathrm{i}\omega}. \tag{3.55}$$

The equation of motion of the plate is

$$\mathrm{i}\omega m_\mathrm{s}'' v_\mathrm{s} = p_\mathrm{L} - \sigma p_\mathrm{cav} - (1-\sigma)\, p_\mathrm{R}, \tag{3.56}$$

where $\sigma = \sigma_\mathrm{HR} + \sigma_\mathrm{CL}$ denotes the sum of the area ratios of the Helmholtz resonator $\sigma_\mathrm{HR} = S_\mathrm{HR}/S_\mathrm{res}$ and the cantilever $\sigma_\mathrm{CL} = S_\mathrm{CL}/S_\mathrm{res}$ to the area of the unit cell S_res, and p_L and p_R are the pressure amplitudes on the left and right hand sides of the panel. With the pressure difference between the pressure inside the resonator and the pressure on the right side of the resonator $p_\mathrm{cav} - p_\mathrm{R}$, the equation of motion of the particle velocity of the

fluid in the neck is

$$\mathrm{i}\omega m''_{\mathrm{HR}} v_{\mathrm{HR}} = p_{\mathrm{cav}} - p_{\mathrm{R}}, \tag{3.57}$$

and the equation of motion of the mean vibration velocity of the cantilever is

$$\mathrm{i}\omega m''_{\mathrm{CL}} \left(1 - \frac{\omega^2_{\mathrm{CL1}}}{\omega^2}\right) v_{\mathrm{CL}} = p_{\mathrm{cav}} - p_{\mathrm{R}}. \tag{3.58}$$

The continuity constraints for the particle velocity on each side of the panel are given by

$$v_{\mathrm{L}} = v_{\mathrm{s}} \text{ and} \tag{3.59}$$

$$v_{\mathrm{R}} = (1 - \sigma)\, v_{\mathrm{s}} + \sigma_{\mathrm{HR}} v_{\mathrm{HR}} + \sigma_{\mathrm{CL}} v_{\mathrm{CL}}. \tag{3.60}$$

The particle velocity of the air in the resonator neck v_{HR} from Eq. (3.57) and the mean vibration velocity of the cantilever v_{CL} from Eq. (3.58) are inserted into the equation for the cavity pressure p_{cav} (Eq. (3.55)). After some algebraic steps and inserting the relations for the angular frequencies of the uncoupled Helmholtz resonator ω_{HR} (Eq. (3.42)) and of the integrated cantilever $\omega_{\mathrm{CL,V}}$ (Eq. (3.41)), the equation for the cavity pressure p_{cav} (Eq. (3.55)) becomes

$$p_{\mathrm{cav}} = \frac{\left(\frac{\omega^2_{\mathrm{CL,V}} - \omega^2_{\mathrm{CL1}}}{\omega^2_{\mathrm{CL1}} - \omega^2} - \frac{\omega^2_{\mathrm{HR}}}{\omega^2}\right) p_{\mathrm{R}} + \left(\frac{\rho_0 c_0^2}{\mathrm{i}\omega V_{\mathrm{cav}}} \left(S_{\mathrm{HR}} + S_{\mathrm{CL}}\right)\right) v_{\mathrm{L}}}{1 + \frac{\omega^2_{\mathrm{CL,V}} - \omega^2_{\mathrm{CL1}}}{\omega^2_{\mathrm{CL1}} - \omega^2} - \frac{\omega^2_{\mathrm{HR}}}{\omega^2}}. \tag{3.61}$$

To simplify the equations, the dimensionless frequencies of the Helmholtz resonator

$$\Omega^2_{\mathrm{HR}} = \frac{\omega^2_{\mathrm{HR}}}{\omega^2}, \tag{3.62}$$

and of the cantilever

$$\Omega^2_{\mathrm{CL}} = \frac{\omega^2_{\mathrm{CL,V}} - \omega^2_{\mathrm{CL1}}}{\omega^2_{\mathrm{CL1}} - \omega^2}, \tag{3.63}$$

as well as the difference of the dimensionless frequencies

$$\begin{aligned} \Delta\Omega^2 &= \Omega^2_{\mathrm{CL}} - \Omega^2_{\mathrm{HR}} \\ &= \frac{\omega^2_{\mathrm{CL,V}} - \omega^2_{\mathrm{CL1}}}{\omega^2_{\mathrm{CL1}} - \omega^2} - \frac{\omega^2_{\mathrm{HR}}}{\omega^2}, \end{aligned} \tag{3.64}$$

are introduced. Substituting v_{HR} from Eq. (3.57), v_{CL} from Eq. (3.58), and the cavity pressure p_{cav} (Eq. (3.61)) in Eq. (3.60), and after some algebraic steps, the second equation

of the transfer matrix system of equations results in

$$v_{\mathrm{L}} = \frac{\mathrm{i}\omega V_{\mathrm{cav}}}{\rho_0 c_0^2 S_{\mathrm{res}}} \frac{\Delta\Omega^2}{1-\sigma+\Delta\Omega^2} p_{\mathrm{R}} + \frac{1+\Delta\Omega^2}{1-\sigma+\Delta\Omega^2} v_{\mathrm{R}}. \tag{3.65}$$

The first equation of the transfer matrix system can be derived by inserting Eq. (3.61) and Eq. (3.65) in the equation of motion of the plate (Eq. (3.56))

$$\begin{aligned} p_{\mathrm{L}} = &\left(\frac{\Delta\Omega^2}{1-\sigma+\Delta\Omega^2} \left(\frac{\sigma^2}{1+\Delta\Omega^2} - \frac{V_{\mathrm{cav}} m_{\mathrm{s}}'' \omega^2}{\rho_0 c_0^2 S_{\mathrm{res}}} \right) + \frac{1-\sigma+\Delta\Omega^2}{1+\Delta\Omega^2} \right) p_{\mathrm{R}} \\ &+ \left(\mathrm{i}\omega m_{\mathrm{s}}'' \frac{1+\Delta\Omega^2}{1-\sigma+\Delta\Omega^2} + \frac{\rho_0 c_0^2 S_{\mathrm{res}} \sigma^2}{\mathrm{i}\omega V_{\mathrm{cav}} (1-\sigma+\Delta\Omega^2)} \right) v_{\mathrm{R}}. \end{aligned} \tag{3.66}$$

The transfer matrix $\mathbf{T}$ of the Helmholtz resonator plate with integrated cantilevers is then given by

$$\mathbf{T} = \begin{bmatrix} \left(\frac{\Delta\Omega^2}{1-\sigma+\Delta\Omega^2} \left(\frac{\sigma^2}{1+\Delta\Omega^2} - \frac{V_{\mathrm{cav}} m_{\mathrm{s}}'' \omega^2}{\rho_0 c_0^2 S_{\mathrm{res}}} \right) + \frac{1-\sigma+\Delta\Omega^2}{1+\Delta\Omega^2} \right) & \left(\mathrm{i}\omega m_{\mathrm{s}}'' \frac{1+\Delta\Omega^2}{1-\sigma+\Delta\Omega^2} + \frac{\rho_0 c_0^2 S_{\mathrm{res}} \sigma^2}{\mathrm{i}\omega V_{\mathrm{cav}} (1-\sigma+\Delta\Omega^2)} \right) \\ \frac{\mathrm{i}\omega V_{\mathrm{cav}}}{\rho_0 c_0^2 S_{\mathrm{res}}} \frac{\Delta\Omega^2}{1-\sigma+\Delta\Omega^2} & \frac{1+\Delta\Omega^2}{1-\sigma+\Delta\Omega^2} \end{bmatrix}. \tag{3.67}$$

Eq. (3.67) shows, that the transfer matrix depends, besides the geometrical parameters (V_{cav}, S_{res}, and σ) only on the three resonance frequencies f_{HR}, f_{CL1} and $f_{\mathrm{CL,V}}$ (expressed in $\Delta\Omega^2$). The resonance frequency of the integrated cantilever $\omega_{\mathrm{CL,V}}$ is calculated with the eigenvalue problem of Eq. (3.47), i.e. the analytical model taking into account the pressure modes inside the cavity. For multi-layered wall structures, the transfer matrix of the entire wall configuration is obtained by multiplying the transfer matrices of each layer, as explained in Section 2.4. The normal incident sound pressure transmission factor t can be calculated from the elements of $\mathbf{T}$ using

$$t = \frac{2}{T_{11} + T_{12}/(\rho_0 c_0) + T_{21}(\rho_0 c_0) + T_{22}}, \tag{3.68}$$

and leads to the transmission loss of the structure $\mathrm{TL} = -20\,\mathrm{lg}|t|$.

4. Verification and validation of the analytical models

In this chapter, the derived analytical models are verified and validated. The numerical verification was conducted by finite element model simulations using COMSOL Multiphysics [27]. The verification was performed by first comparing the analytically determined eigenfrequencies of the coupled resonator system f_1 and f_2 with those determined by a finite element model. Secondly, the finite element model was also used to verify the sound absorption coefficient of the resonator calculated with the analytical model proposed in this thesis. The absorption coefficient was then validated experimentally. Thirdly, the analytical model to calculate the transmission loss was verified by finite element simulations and validated by impedance tube measurements. Finally, the transfer matrix model to account for multi-layer configurations was verified numerically with finite element simulations and validated experimentally with transmission loss measurements. Parts of this chapter have been published in Refs. [55, 57].

4.1. Verification of the eigenfrequency calculation

The derived analytical model for the calculation of the eigenfrequencies is verified by comparing the analytically determined eigenfrequencies f_1 and f_2 for three different resonator geometries with those determined by a finite element model. This section begins with a description of the finite element model, followed by a comparison of the calculated eigenfrequencies.

The finite element model setup used to determine the resonator eigenfrequencies is shown in Figs. 4.1 a) and b). The geometric and material data of the resonator were modeled according to Table 4.1, with the dimensions according to Fig. 3.1. The material data correspond to a closed-cell foam based on polymethacrylimide (PMI), which will be used for the experimental validations. The data was taken from the manufacturer's data sheet [42]. As in the analytical eigenfrequency calculation, viscous and mechanical losses were not considered in the finite element model used to calculate the eigenfrequencies. Since the resonator geometry is symmetric with respect to the x-z-plane, only one half of

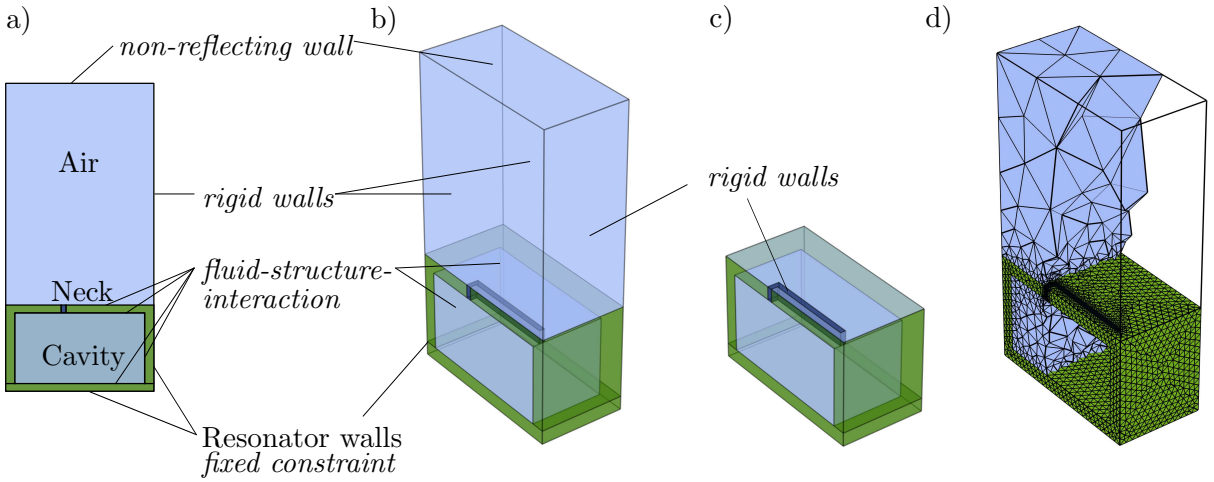

Figure 4.1: Schematic view of the finite element model of the resonator to verify the analytical model for the calculation of the eigenfrequencies. a) and b) Model to determine f_1 and f_2 [a) Two-dimensional view; b) Three-dimensional view.] c) Model to determine $f_{\mathrm{CL,V}}$. d) View of the resonator and the fluid mesh.

the geometry was modeled by finite elements with symmetry boundary conditions along the symmetry plane. The green shaded resonator walls were modeled as a linear elastic material. According to the boundary conditions of the rectangular waveguide in Eq. (3.17), all resonator surfaces except the cantilever were fixed such that they could not vibrate. To account for the rotation at the cantilever support (see Section 3.2), the resonator body was not modeled as rigid. The surface of the cantilever was free to vibrate and fully coupled to the fluid. The light blue shaded domains inside the resonator cavity and on top of the resonator as well as the dark blue shaded resonator neck were modeled as a linear elastic

Table 4.1: Geometric and material data of the modeled resonator used in the numerical simulations.

Description	Symbol	Value	Unit
Resonator width	W	65	mm
Resonator length	L	70	mm
Resonator height	H	40	mm
Cantilever width	w	10	mm
Cantilever length	l	34	mm
Cantilever height and res. wall thickness	t_{s}	5	mm
Slit width	w_{s}	2	mm
Density	ρ_{CL}	32	kg/m^3
Young's modulus	E_{CL}	36	MPa
Structural loss factor	η_{CL}	0.05	-

fluid (air) with the speed of sound $c_0 = 343$ m/s and the density $\rho_0 = 1.2$ kg/m^3. Fluid-structure interaction was considered at the boundaries of the resonator that are in contact with air. Second-order tetrahedral elements were chosen for the entire model. The mesh of the simulation model is depicted in Fig. 4.1 d). The maximum element size of the neck and of the resonator walls were defined to be smaller than half of the slit width w_s and half of the wall thickness t_s, respectively. The maximum element size of the surrounding fluid was defined to be smaller than one tenth of the smallest wavelength of interest, which corresponds to the frequency of 1500 Hz. For the different resonator designs of this study, the lowest resonance frequencies of the Helmholtz resonator f_HR, of the cantilever f_CL and of the coupled system f_1 and f_2 are expected to be less than 1500 Hz. The resonance frequencies f_1 and f_2 are determined by solving the eigenfrequency analysis of the fully coupled finite element model, as depicted in Fig. 4.1 a). The resonance frequency of the uncoupled Helmholtz resonator f_HR and of the cantilever in vacuo f_CL1 are determined by solving the eigenfrequency analysis considering only the fluid and only the structure, respectively. The model for calculating the resonance frequency of the cantilever stiffened by the resonator cavity $f_\mathrm{CL,V}$ is shown in Fig. 4.1 c). It consists of the resonator walls, the cavity volume and the resonator neck. The boundary condition of the outer surface of the resonator neck is modeled as a rigid wall.

Hereinafter, the analytical resonance frequencies were calculated based on the derived system of equations in Eq. (3.39), where the number of modes inside the waveguide was fixed to 20 modes in y- and z-direction ($N_y = N_z = 20$), such that convergence was achieved. Fig. 4.2 demonstrates the convergence of the calculated resonance frequencies f_1 and f_2 of a resonator with the dimensions as given in Table 4.1.

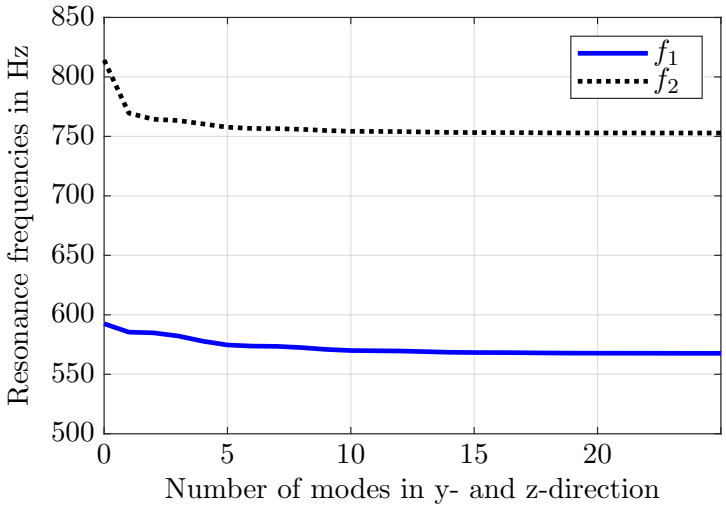

Figure 4.2: Analytically calculated resonance frequencies of the coupled system f_1 and f_2 as a function of the number of modes in the y-and z-direction.

The comparison of the eigenfrequencies was performed exemplarily for varying cantilever lengths and three different resonator heights H. The numerical results are compared with the analytical solutions in Figs. 4.3 a)-f) with the curves representing the analytical results and the symbols representing the numerical results. The general behavior of the different resonator designs is discussed in detail in the parameter study in Chapter 5. In Figs. 4.3 a)-c), the analytically determined resonance frequencies of the coupled system f_1, f_2 and of the uncoupled Helmholtz resonator f_{HR} and cantilever f_{CL1} are compared to numerical results. The comparison is shown for three different resonator heights $H = 20$ mm, 40 mm and 60 mm, keeping the other geometric parameters constant except for the cantilever length l. It can be observed that the resonance frequency of the Helmholtz resonator f_{HR} (in red) increases with increasing cantilever length, since the neck area S_{HR} also increases. In contrast, the resonance frequency of the cantilever in vacuo f_{CL1} (in green) decreases with increasing cantilever length. At the frequency where f_{HR} and f_{CL1} are equal, the resonance frequencies of the coupled system f_1 and f_2 approach each other, but do not become equal. The minimum frequency distance and the coupling between the two resonance frequencies will be discussed further in Section 5.1.

In Figs. 4.3 d)-f), the resonance frequencies of the integrated cantilever $f_{\mathrm{CL,V}}$ are com-

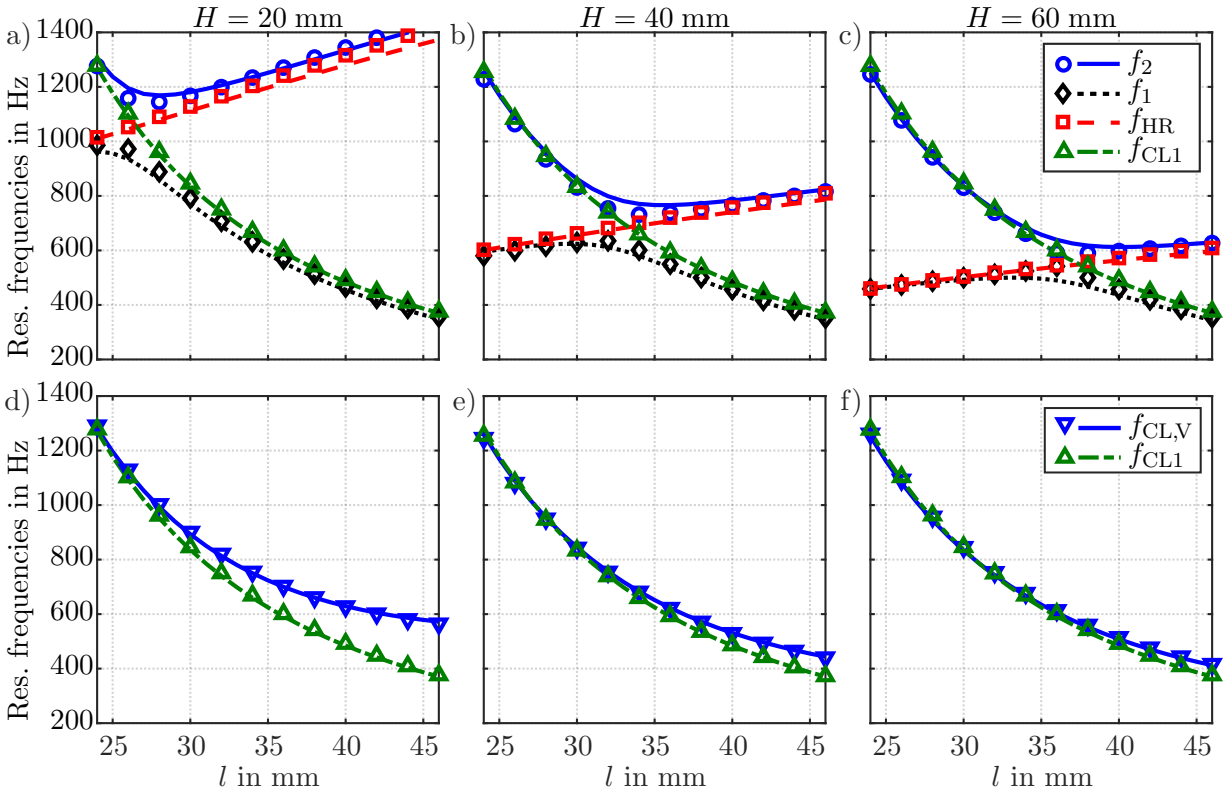

Figure 4.3: Calculated resonance frequencies of the resonator system depending on cantilever length and cavity volume. Symbols: numerical data. Lines: analytical model. a)-c) Comparison of f_1, f_2, f_{HR} and f_{CL1}. d)-f) Comparison of f_{CL1} and $f_{\mathrm{CL,V}}$.

pared with the resonance frequencies of the cantilever in vacuo f_{CL1}. The qualitative trend of f_{CL1} and $f_{\mathrm{CL,V}}$ is similar, while $f_{\mathrm{CL,V}}$ is always larger than f_{CL1}. This behavior can be explained by the fact that the air volume in the cavity stiffens the cantilever and thus leads to a higher resonance frequency. The stiffening behavior is also discussed further in Section 5.1.

The comparison between the numerical results and the analytical results shows a good overall agreement. It is observed that the fundamental resonance frequency of the cantilever in vacuo f_{CL1}, calculated analytically with the model of Mac Bain and Genin [93], agrees well with the numerical calculations. Similarly, the analytical and numerical resonance frequencies of the cantilever stiffened by the cavity volume $f_{\mathrm{CL,V}}$ are in agreement. In Figs. 4.3 a)-c), small deviations are observed for the resonance frequency of the Helmholtz resonator f_{HR}, marked in red. The deviation increases for larger cantilever lengths l and smaller cavity volumes V_{cav}. This difference might be attributed to the end correction for infinite-length slits, which is adopted in the analytical model for finite-length slits. For the considered resonator designs, the maximum relative error is about 3 %, which justifies this approach. Furthermore, the analytically determined resonance frequencies of the coupled system f_1, f_2 are in good agreement with the numerical solutions. The analytical results slightly overestimate the coupling behavior at the cantilever length, where the Helmholtz resonator resonance frequency and the cantilever resonance frequency are equal, resulting in lower values for f_1 and higher values for f_2. The maximum relative error is about 5 %.

4.2. Absorption coefficient

In this section, the analytical model for calculating the absorption coefficient of a Helmholtz resonator with an integrated cantilever, Eq. (3.51), was validated numerically using finite element model simulations and verified experimentally using impedance tube measurements.

4.2.1. Numerical verification

The finite element model to determine the absorption coefficient of the resonator is depicted in Fig. 4.4, with the geometric and material data of the resonator taken from Table 4.1 and Fig. 3.1. The simulation model shown in Figs. 4.4 a) and b) has the same setup and characteristics as the model used to verify the eigenfrequencies (see Fig. 4.1 and Section 4.1). In the following, only the differences necessary for the calculation of the absorption coefficient are described. The model has been adapted to account for mechanical

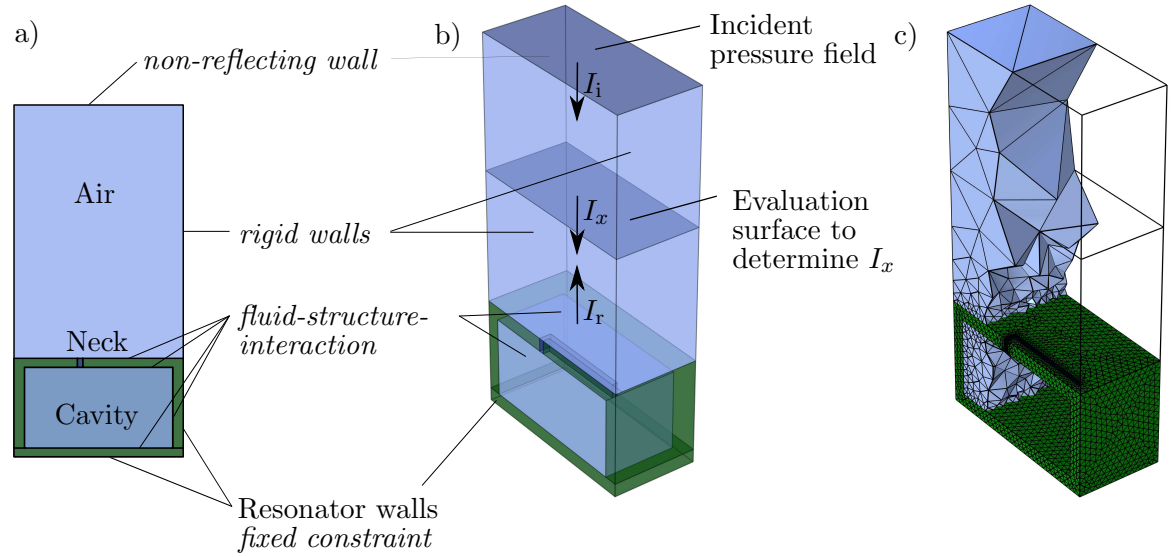

Figure 4.4: Schematic view of the finite element model used to verify the analytical model for calculating the absorption coefficient. a) and b) Different domains and boundary conditions [a) Two-dimensional view; b) Three-dimensional view]. c) View of the resonator and fluid mesh.

and viscous losses. The dark blue shaded domain of the resonator neck was modeled as an equivalent fluid, taking into account viscous boundary layer induced losses. The model uses the equivalent fluid complex wave number k_{eq}, derived in [12],

$$k_{\mathrm{eq}} = \frac{\omega}{c_0} \frac{1}{\sqrt{1 - B\sqrt{\frac{\pi}{\mathrm{i}\omega}}}}, \tag{4.1}$$

where B is

$$B = \frac{4}{H_{\mathrm{d}}} \sqrt{\frac{\eta_0}{\pi \rho_0}} \left(1 + \frac{\kappa - 1}{\sqrt{\mathrm{Pr}}}\right), \tag{4.2}$$

H_{d} is the hydraulic diameter of the slit, $\eta_0 = 18.2 \cdot 10^{-6}$ Pa s is the air dynamic viscosity, $\kappa = 1.4$ is the air specific heat ratio, and $\mathrm{Pr} = 0.71$ is the Prandtl number. The formula is valid for slits, whose effective radius $H_{\mathrm{d}}/2$ is greater than the viscous boundary layer [26]. For comparison, the frequency-dependent viscous boundary layer has a thickness of 0.22 mm at 100 Hz and 0.08 mm at 1000 Hz (cf. Eq. (3.4)), while the effective radius $H_{\mathrm{d}}/2$ is approximately equal to the size of the slit width of the resonator. Thus, for the resonators studied in this thesis, the viscous boundary layer thickness is much smaller than the effective radius and the model of Ref. [12] is applicable. Structural damping of the resonator material has been introduced by a structural loss factor in the linear elastic material. This structural loss factor leads to a complex Young's modulus of the elastic material model [25], which corresponds to how damping was considered in the analytical model. In the simulation model, an incident plane wave with an amplitude of $p_{\mathrm{i}} = 1$ Pa was defined as the excitation and determined the incident sound intensity I_{i}, which can

be calculated for plane waves as

$$I_\mathrm{i} = \frac{|p_\mathrm{i}^2|}{2\rho_0 c_0}. \tag{4.3}$$

The incident sound power P_i is calculated by integrating the sound intensity I_i over the incident area

$$P_\mathrm{i} = \int_S I_\mathrm{i}\,\mathrm{d}S. \tag{4.4}$$

To calculate the reflected sound power P_r, the sound intensity I_x was evaluated on an evaluation surface, parallel to the resonator top plate, as indicated in Fig. 4.1 b). The sound intensity I_x results from the incident and reflected sound field

$$I_x = I_\mathrm{i} - I_\mathrm{r}. \tag{4.5}$$

The absorption coefficient is calculated via

$$\alpha = 1 - \frac{P_\mathrm{r}}{P_\mathrm{i}} = 1 - \frac{\int_S I_\mathrm{r}\,\mathrm{d}S}{P_\mathrm{i}}. \tag{4.6}$$

With Eq. (4.5), the absorption coefficient results to

$$\alpha = 1 - \left(\frac{\int_S I_\mathrm{i}\,\mathrm{d}S}{P_\mathrm{i}} - \frac{\int_S I_x\,\mathrm{d}S}{P_\mathrm{i}} \right). \tag{4.7}$$

In Eq. (4.7), the value of the first fraction is 1, such that the absorption coefficient can be calculated numerically as

$$\alpha = \frac{\int_S I_x\,\mathrm{d}S}{P_\mathrm{i}}, \tag{4.8}$$

which is the ratio of the sound power at the evaluation surface to the incident sound power. The absorption coefficient was evaluated for the resonator geometry specified in Table 4.1, for three different slit widths (1 mm, 2 mm, and 3 mm). In this setup, the surface area S in Eq. (3.51) is equal to the resonator base area S_res. The comparison of the numerically (symbols) and analytically (lines) determined absorption coefficient is shown in Figs. 4.5 a)-c). An overall good agreement between the numerical and analytical data is visible in Figs. 4.5 a)-c), thus the numerical simulations verify the analytical model. Similar to the verification of the resonance frequencies in Figs. 4.3 a)-c), the comparison shows a small deviation in the resonance frequency of the isolated Helmholtz resonator f_HR and of the coupled system f_1 and f_2, while the relative error of the resonance frequencies is within 3 % for the resonator designs shown. Since the peak values of the absorption coefficient agree well between the numerical and analytical results, the modeled damping behavior is verified by the numerical simulations.

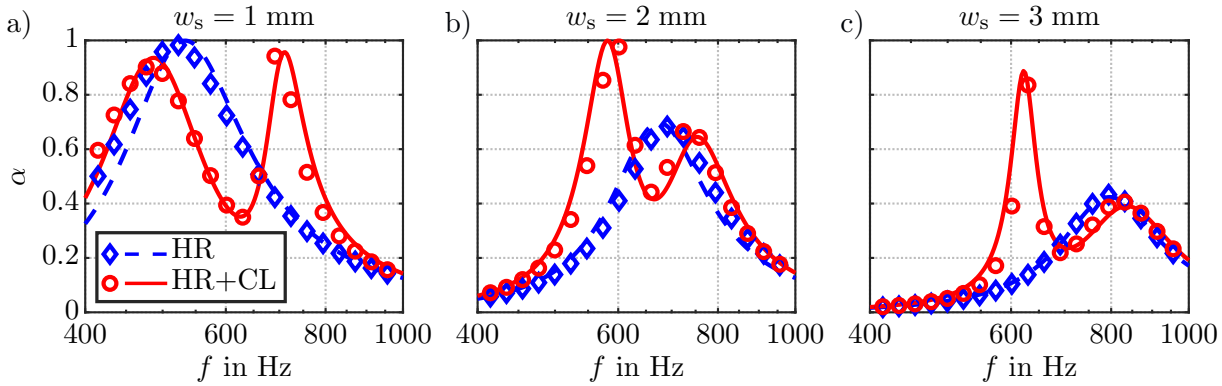

Figure 4.5: Comparison of the analytically (lines) and numerically (symbols) determined absorption coefficient of the uncoupled Helmholtz resonator (HR) and of the Helmholtz resonator with integrated cantilever (HR+CL) for different slit widths. a) 1 mm. b) 2 mm. c) 3 mm.

The value of the absorption maximum of the uncoupled Helmholtz resonator depends on the impedance matching of the input impedance of the slit [103]. The resonator with a slit width of 1 mm in Fig. 4.5 a) exhibits an absorption coefficient of 1, which means that the impedance is perfectly matched, as further discussed in more detail in Section 5.2.1.

The plots clearly show the effect of the integrated cantilever inside the Helmholtz resonator: Because of the second resonance frequency, a second absorption peak is created and the frequency range of high absorption can be broadened. However, there is a minimum between the two absorption peaks. The minimum between the two resonance frequencies arises, since the two modes of the system are coupled. As is well known from the classical two-degree-of-freedom oscillator, see for example Ref. [17, p. 134], the frequency response function has large amplitudes at the resonance frequencies of the coupled system with a distinct minimum in between them. Similarly, the frequency response functions of the mean displacement of the cantilever ($\bar{u}_{\mathrm{CL}}$) and of the displacement of the fluid volume in the neck (u_{HR}) of the resonator with a 2 mm wide slit are visualized for the amplitudes and the phase angles (Φ) in Fig. 4.6 b) and c), respectively.

The resonance frequencies of the coupled systems are characterized by a phase change of both degrees of freedom. At the resonance frequency, the phase angle is $\pi/2$, as visible in Fig. 4.6 c). Analogous to a classical two-degree-of-freedom oscillator, the amplitude of the frequency response function is large at the resonance frequencies and reduced in between the resonance frequencies, as shown in Fig. 4.6 b). The absorption behavior of the resonator is mainly determined by the viscous losses in the Helmholtz resonator neck. The viscous losses in the Helmholtz resonator neck depend on the particle velocity of the air mass in the neck $v_{\mathrm{HR}} = \mathrm{i}\omega u_{\mathrm{HR}}$ and on the relative velocity between the air mass and the cantilever $v_{\mathrm{HR}} - v_{\mathrm{CL}} = \mathrm{i}\omega(u_{\mathrm{HR}} - u_{\mathrm{CL}})$. Both quantities are strongly reduced between the two resonance frequencies, which explains the minimum of the absorption coefficient,

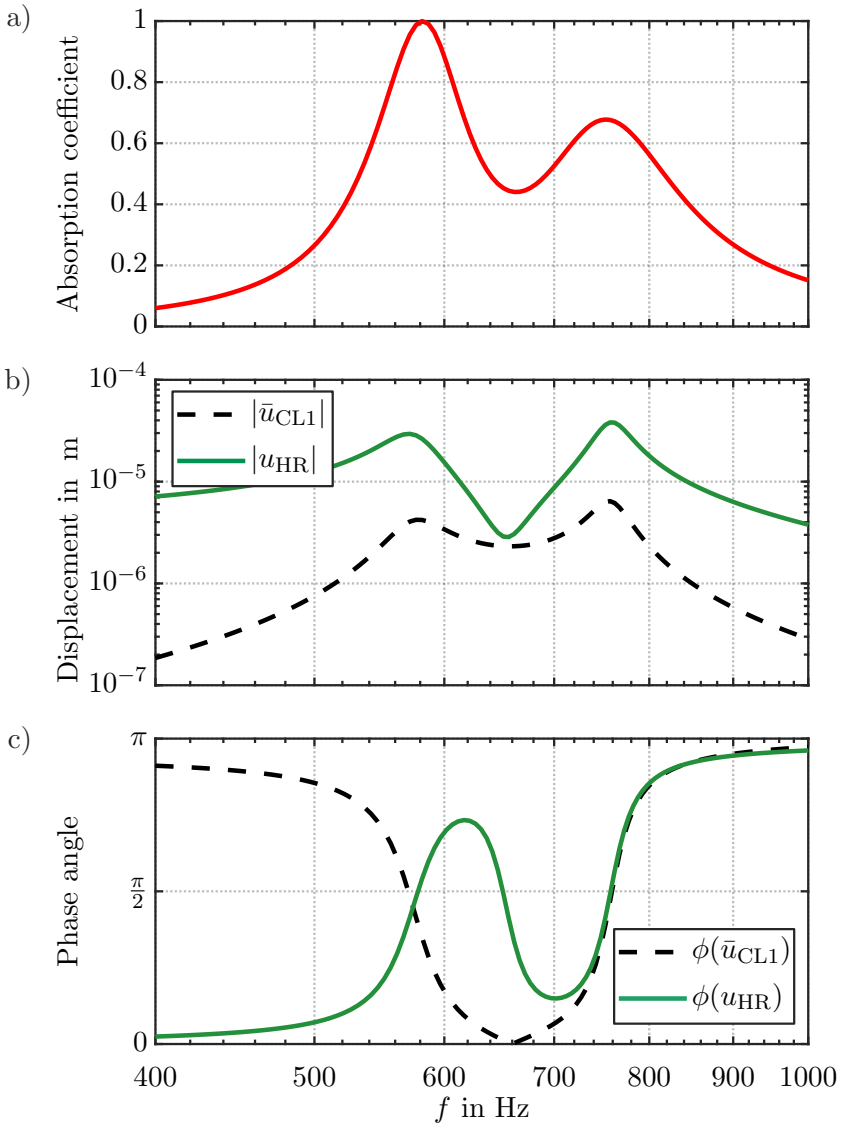

Figure 4.6: Absorption coefficient and frequency response function of the mean displacement of the cantilever ($\bar{u}_{\mathrm{CL}}$) and of the fluid in the neck (u_{HR}) of the Helmholtz resonator with integrated cantilever. a) Absorption coefficient b) Amplitudes. b) Phase angles.

visible in Fig. 4.6 a), between the resonance frequencies. In addition, the fluid mass in the neck experiences a third phase change between the two resonance frequencies at about 650 Hz, as shown by the solid green line in Fig. 4.6 c). At this frequency, the displacement of the fluid volume in the neck is very small, see Fig. 4.6 b). If the coupled system had no damping, the displacement of the fluid volume at this frequency would be zero. In the undamped case, this frequency corresponds to the eigenfrequency of the integrated cantilever $\omega_{\mathrm{CL,V}}$. This means that the integrated cantilever acts as a tuned mass damper to the Helmholtz resonator. Typically, a tuned mass damper is used to isolate unwanted vibrations at a certain frequency, such as the excitation or resonance frequency of the system. While the vibrations at the eigenfrequency of the uncoupled tuned mass damper

are reduced, the addition of the mass adds another degree of freedom to the system and thus another resonance frequency. In the present case of the Helmholtz resonator with integrated cantilever, the second resonance frequency added by the integration of the cantilever is favorable to have a more broadband or second frequency region of high absorption. However, the resonator should be designed so that the absorption minimum between the two resonance frequencies is still acceptably high. The effect of the integrated cantilever on the absorption coefficient of the Helmholtz resonator is examined in more detail in Section 5.2.

4.2.2. Experimental validation

The absorption coefficient of a Helmholtz resonator with integrated cantilever was measured in an impedance tube with the two-microphone setup according to ISO 10534–2, as described in Section 2.5.1. A schematic drawing of the test setup is shown in Fig. 4.7 a). An impedance tube from Brüel&Kjaer, type 4206-T, is used in the present experimental setup. The impedance tube has a diameter of $D = 100\,\text{mm}$ and an incident surface of $S = \pi D^2/4$. The applied microphones (Mic. 1 and Mic. 2) have a diameter of 1/4".

The resonator was made from a closed-cell, PMI-based rigid foam with the trade name Rohacell 31 HF. The geometry of the resonator and the physical parameters of the material, used for the analytical calculations, are given in Table 4.2. The geometric and material properties of the realized resonator differ from those listed in Table 4.1, which were used for numerical verification. The material data were obtained by a fit between an experimental and numerical modal analysis, using the method of model updating of the numerical model, which is further explained in Ref. [118]. The resonator was manufactured by milling and assembled from two parts. The bottom plate of the resonator was fabricated separately and bonded to the resonator body. The bottom side of the res-

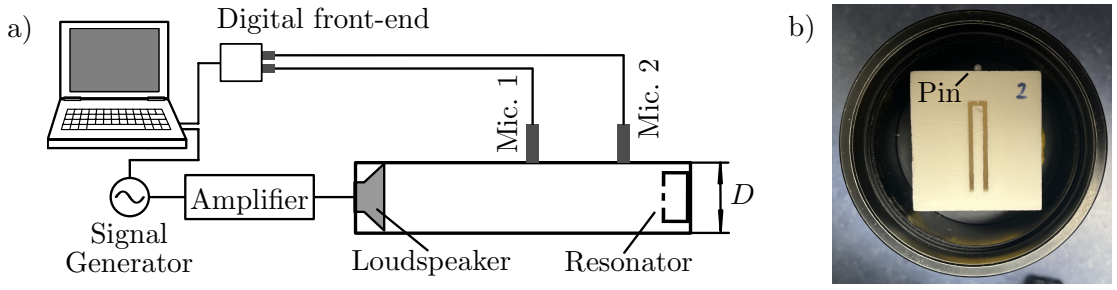

Figure 4.7: Experimental setup for measuring the sound absorption of a Helmholtz resonator with integrated cantilever. a) Schematic drawing of the impedance tube setup. b) Photo of the resonator installed in the impedance tube; visible is the top plate with the U-shaped slit, forming the resonator neck and the cantilever.

Table 4.2: Geometric and material data of the resonator used for the experimental validations.

Description	Symbol	Value	Unit
Resonator width	W	64.3	mm
Resonator length	L	69.1	mm
Resonator height	H	45.6	mm
Cantilever width	w	4	mm
Cantilever length	l	41	mm
Cantilever height and res. wall thickness	t_s	9.8	mm
Slit width	w_s	2.6	mm
Density	ρ_CL	32.2	kg/m^3
Young's modulus	E_CL	34.33	MPa
Structural loss factor	η_CL	0.05	-

onator was attached to the rigid back wall of the impedance tube with putty, so that the Helmholtz resonator neck and cantilever faced the sound source. A photograph of the resonator installed inside the impedance tube is shown in Fig. 4.7 b).

The absorption coefficient of the resonator was compared to that of a conventional Helmholtz resonator. This was achieved by fixing the cantilever with a pin so that only the Helmholtz resonator was active, as shown in Fig. 4.7 b). Fig. 4.8 shows a comparison of the analytical absorption coefficient (lines) from Eq. (3.51) and the absorption coefficient measured in the impedance tube (symbols). Like the verification data in Fig. 4.5, the figure shows the advantage of the Helmholtz resonator with cantilever: a second absorption peak due to the second resonance frequency, which leads to a broader absorption behavior, even if the absorption coefficient of the uncoupled Helmholtz resonator at the resonance frequency is higher. The absorption coefficient of the Helmholtz resonator with cantilever shows a local minimum in between the two absorption peaks.

The measurements show overall good agreement with the analytical solution and thus validate the analytical model. However, the measured resonance frequencies of the coupled system f_1 and f_2 as well as of the Helmholtz resonator f_2 are lower than the analytically calculated resonance frequencies. Additionally, the absorption behavior of the Helmholtz resonator and of the coupled resonator around the second resonance frequency is more broadband in the experiments than predicted analytically.

One explanation for the reduced resonance frequencies is that the model used to account for viscous losses in the resonator neck was derived for smooth surfaces. In contrast, the resonator in the experiment was made of foam by milling, resulting in rough surfaces. Rough surfaces increase the viscous losses in the resonator neck, i.e. increased damping, and lead to lower damped resonance frequencies combined with a more broad-

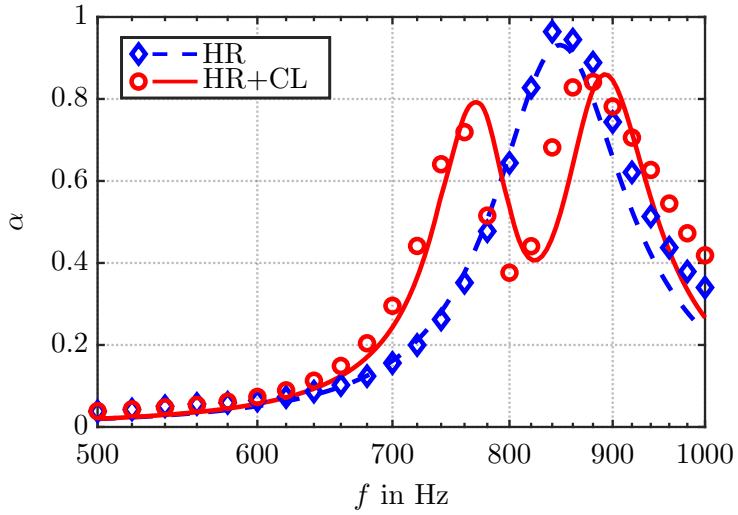

Figure 4.8: Comparison of the analytically calculated (lines) and experimentally measured (symbols) absorption coefficients α of the uncoupled Helmholtz resonator (HR) and the Helmholtz resonator with integrated cantilever (HR+CL).

band absorption behavior. This effect has been demonstrated experimentally for slits with varying surface roughness in Ref. [56]. Analytical approaches to model the input impedance of microperforated plates with periodic (sinusoidal) rough surfaces can be found in Refs. [141, 145] for circular openings and in Ref. [129] for microslits. The implementation of random surface roughness, such as that generated by milling of closed-cell foam, is still the subject of future research and is not covered in this work.

Furthermore, compared to the analytical results, the measured absorption coefficient is slightly higher in the higher frequency range ($f > 900$ Hz) due to bending modes of the resonator walls, which are not considered in the analytical model. The bending modes have been demonstrated by finite element model simulations and laser Doppler vibrometer measurements, of which the latter are further detailed in Ref. [125]. The displacements of the cantilever and of the top surface of the resonator, measured by the laser Doppler vibrometer and calculated by finite element simulations, are shown in Figs. 4.9 a) and b) and Figs. 4.9 c) and d) for two frequencies, respectively. Figs. 4.9 a) and c) show the displacement at around the first resonance frequency of the coupled resonator system f_1. The green and dark blue colors in Figs. 4.9 a) and c) demonstrate, that the displacement of the resonator top plate is nearly zero and can be neglected compared to the displacement of the cantilever. This justifies the approach of modeling the resonator walls as rigid. At higher frequencies, as shown in Fig. 4.9 b) for the laser Doppler vibrometer measurements and in Fig. 4.9 d) for the finite element simulations, the top surface of the resonator exhibits a plate eigenmode. This resonant behavior leads to higher absorption values than analytically calculated, as visible in Fig. 4.8.

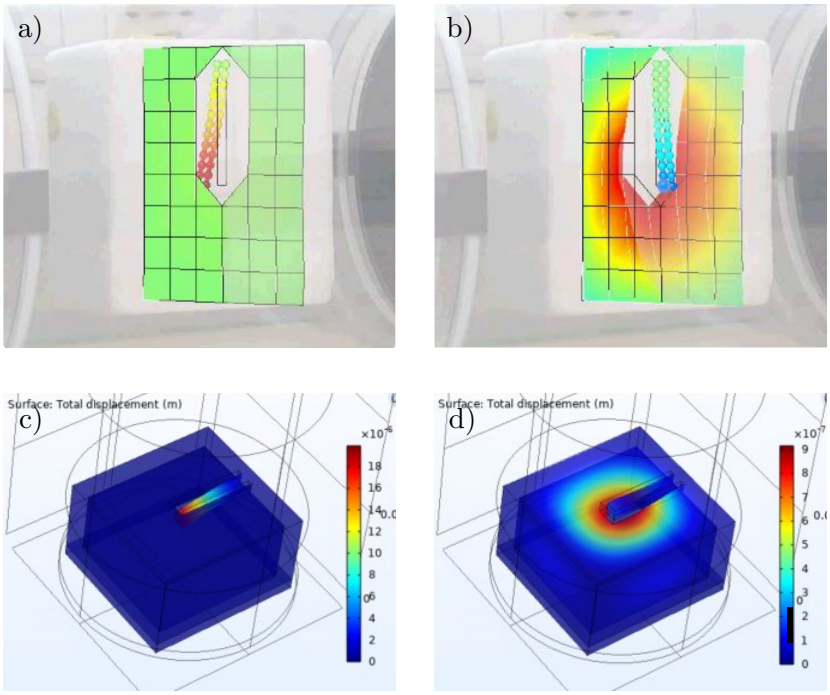

Figure 4.9: Displacement of the cantilever and of the top surface of the resonator. a) Laser Doppler vibrometer measurements at the resonance frequency f_1 [125]. b) Laser Doppler vibrometer measurements at 1500 Hz [125]. c) Finite element simulations at the resonance frequency f_1 d) Finite element simulations at 1800 Hz.

4.3. Transmission loss

This section presents a verification and validation of the analytical model for calculating the transmission loss characteristics of Helmholtz resonators with integrated cantilevers, as referenced in Section 3.7 when the resonator is installed in a duct.

4.3.1. Numerical verification

The model used for the numerical verification is depicted in Fig. 4.10. The resonator with the geometric and material data taken from Table 4.1. is installed in a duct with the same circular cross sectional area S and diameter as the impedance tube used in the experimental validations ($D = 100$ mm, $S = \pi D^2/4$). The simulation model is based on the same principles as the model used to determine the eigenfrequencies and absorption coefficient of the resonator. The setup is complemented by an additional duct on the right side of the resonator to model transmission. The sidewalls of the duct were modeled as rigid walls. The mesh of the simulation model is shown in Fig. 4.10 b). It has the same properties and maximum element size limitations as described in Section 4.1. The left surface of the duct was defined as the excitation plane, with an incident plane wave having an amplitude of 1 Pa. The left and right surfaces of the duct were defined as an

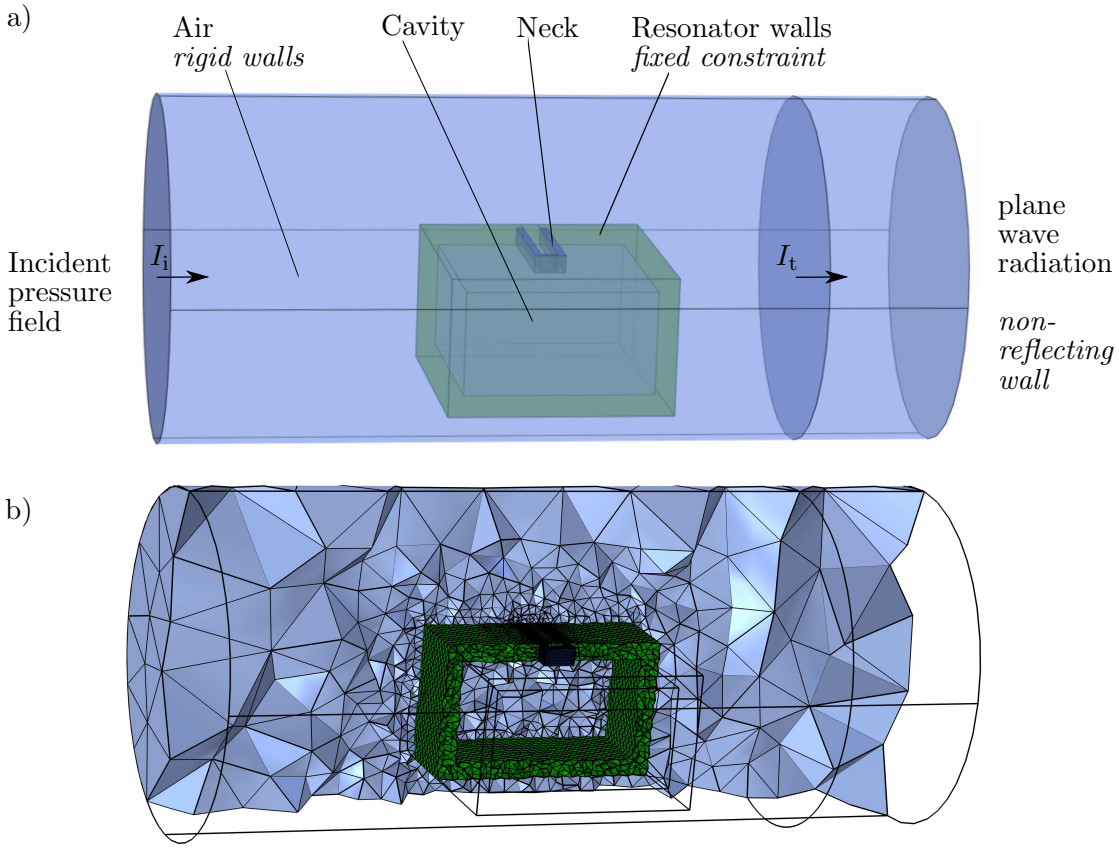

Figure 4.10: Schematic view of the finite element model of the resonator to verify the analytical model for calculating the transmission loss characteristics of the resonator installed in a duct. a) Different domains and boundary conditions. b) View of the resonator and fluid mesh.

infinite half space by terminating the fluid domain with a plane wave radiation boundary condition, representing non-reflecting walls. The incident sound power P_i is determined by integrating the incident sound intensity from Eq. (4.3) in the direction of the duct over the incident surface. The transmitted sound power P_t is obtained by the normal component of the acoustic intensity vector over an evaluation surface parallel to the resonator sidewall and parallel to the duct outlet, as indicated in Fig. 4.10 a). The numerically determined transmission loss for three different slit widths ($w = 1$ mm, $w = 2$ mm and $w = 3$ mm) is compared to the analytically calculated transmission loss in Figs. 4.11 a)-c).

The figures show that the numerical and analytical results for the transmission loss are in very good agreement. Thus, the numerical simulations verify the analytical model. The transmission loss of the Helmholtz resonator with integrated cantilever shows two peaks at the resonance frequencies of the coupled system with a local minimum in between. The minimum in transmission loss is due to the two coupled modes, as explained in Section 4.2.1. The magnitude of the transmission loss is highly dependent on the slit width and will be further analyzed in Section 5.3.

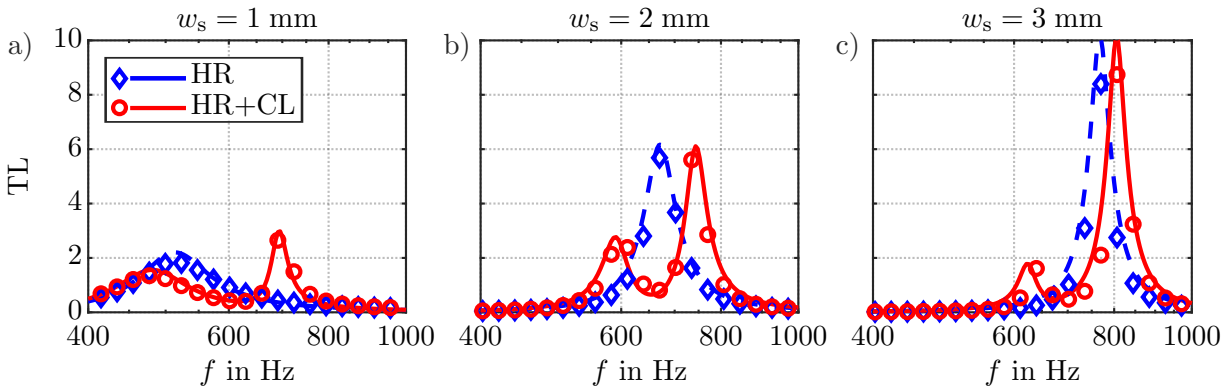

Figure 4.11: Comparison of the analytically calculated (lines) and numerically calculated (symbols) transmission loss characteristics (TL) of the uncoupled Helmholtz resonator (HR) and the Helmholtz resonator with integrated cantilever (HR+CL) installed in a duct for three different slit widths. a) 1 mm. b) 2 mm. c) 3 mm.

4.3.2. Experimental validation

The transmission loss of a Helmholtz resonator with integrated cantilever was measured in an impedance tube (Brüel&Kjaer, type 4206-T) using the four-microphone method according to ASTM E2611-09 [5], as described in Section 2.5.2. A schematic drawing of the test setup is shown in Fig. 4.12 a). The experimental validation of the transmission loss was performed with the same resonator as for the absorption coefficient measurements, with the dimensions and material data given in Table 4.2. Fig. 4.12 b) shows the mounting of the resonator inside the middle part of the impedance tube. The edges of the bottom resonator plate, which were in contact with the impedance tube wall, were fixed to the impedance tube sidewall with putty. The measurement results for the transmission loss of the resonator, calculated using the transfer matrix given in Eq. (2.92), are shown as symbols in Fig. 4.13. They are compared with the analytically calculated transmission loss with Eq. (2.53) (lines) for the resonator with fixed cantilever (HR) and for the Helmholtz resonator with integrated cantilever (HR+CL).

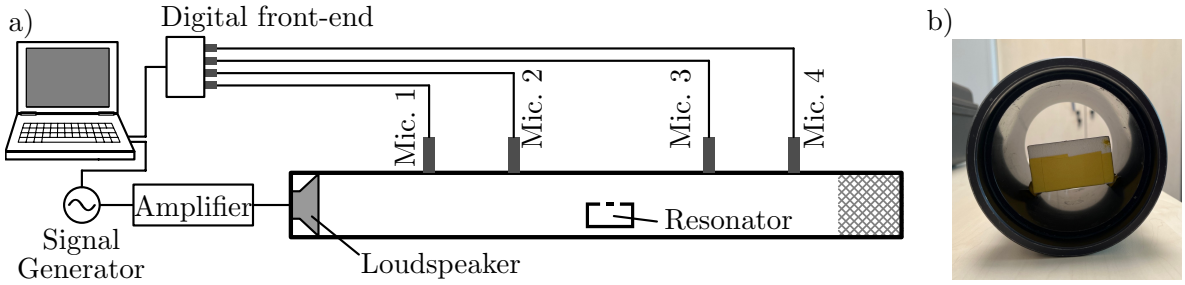

Figure 4.12: Experimental setup for measuring the transmission loss characteristics of a Helmholtz resonator with integrated cantilever surrounded by an air layer. a) Schematic representation of the impedance tube measurement setup. b) Photo of the test sample.

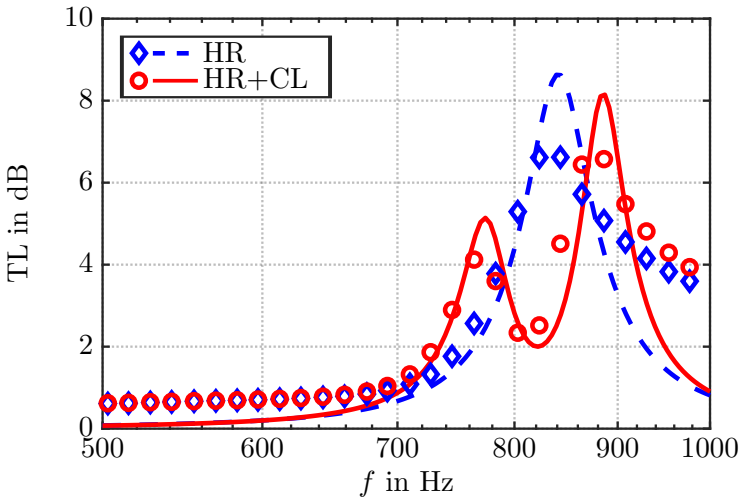

Figure 4.13: Comparison of the analytically calculated (lines) and experimentally measured (symbols) transmission loss characteristics (TL) of the uncoupled Helmholtz resonator (HR) and the Helmholtz resonator with integrated cantilever (HR+CL) installed in a duct.

The comparison in Fig. 4.13 shows that the qualitative trend of the measured transmission loss characteristics is consistent with the analytically calculated transmission loss characteristics and validates the analytical model. However, there are some deviations. Firstly, the measured transmission loss is higher for frequencies above the resonance frequencies, which can again be explained by bending modes of the resonator walls, as already observed in the absorption behavior. Secondly, the experimentally determined resonance frequencies are lower than the analytically predicted values. And thirdly, the measured transmission loss at the resonance frequencies is smaller than predicted analytically. Both the lower resonance frequencies and the reduced transmission loss at the resonance frequencies can be explained by the rough surfaces of the foam resonator. Surface roughness increases the viscous losses in the resonator neck. These elevated viscous losses lead, on the one hand, to lower damped resonance frequencies compared to the undamped resonance frequencies (cf. Appendix A.3). On the other hand, viscous losses result in a better impedance match between the resonator and the incident sound wave, accompanied by increased sound transmission. A larger impedance mismatch with the surrounding fluid leads to stronger reflection of the incident wave and therefore to higher transmission loss. As the viscous losses in the neck increase with increasing surface roughness, this impedance mismatch is reduced, resulting in lower transmission loss values. Ref. [56] experimentally demonstrated that rough surfaces in slit resonators lead to reduced transmission loss and lower resonance frequencies. As noted above, including surface roughness in the analytical model is still under investigation and beyond the scope of this work.

4.4. Multi-layered structures

In this section, the analytical model for calculating the transmission loss of a large panel of Helmholtz resonators with integrated cantilevers determined by the transfer matrix method is validated numerically by finite element model simulations and verified experimentally by transmission loss measurements. The comparison is performed for a single resonator panel and for the resonator panel installed in a double wall. The panel consists of two parts: the resonator back plate and the resonator panel, as depicted in Fig. 4.14 a) for the cross section of the panel. Fig. 4.14 b) shows a unit cell that is periodically arranged to completely cover the resonator back panel. The back panel represents the aircraft lining and will be referred to as the lining (abbreviated as lin.) in the following.

The analytical results of the transmission loss were obtained using the transfer matrix method as described in Section 2.4. The transfer matrix of the Helmholtz resonator panel with integrated cantilever $\mathbf{T}_{\mathrm{HRCL}}$ (Eq. (3.67)) was derived in Section 3.8. In Eq. (3.67), m''_{s} is the surface mass density of the whole panel, which includes the surface mass density of the back plate m''_{lin}, the resonator panel m''_{res}, and the bonding material m''_{g} (only applicable in the experimental validation). Thus the surface mass density of the whole panel is $m''_{\mathrm{s}} = m''_{\mathrm{lin}} + m''_{\mathrm{res}} + m''_{\mathrm{g}}$. The transfer matrix $\mathbf{T}_{\mathrm{HR}}$ of the resonator panel with the uncoupled Helmholtz resonators is calculated using the equation for $\mathbf{T}_{\mathrm{HRCL}}$, with the resonance frequencies of the cantilever f_{CL} and $f_{\mathrm{CL,V}}$ set to zero. The transfer matrix of a mass-equivalent panel without resonators is represented by the transfer matrix of a limp acoustic wall (Eq. (2.68)) with the surface mass density m''_{s}.

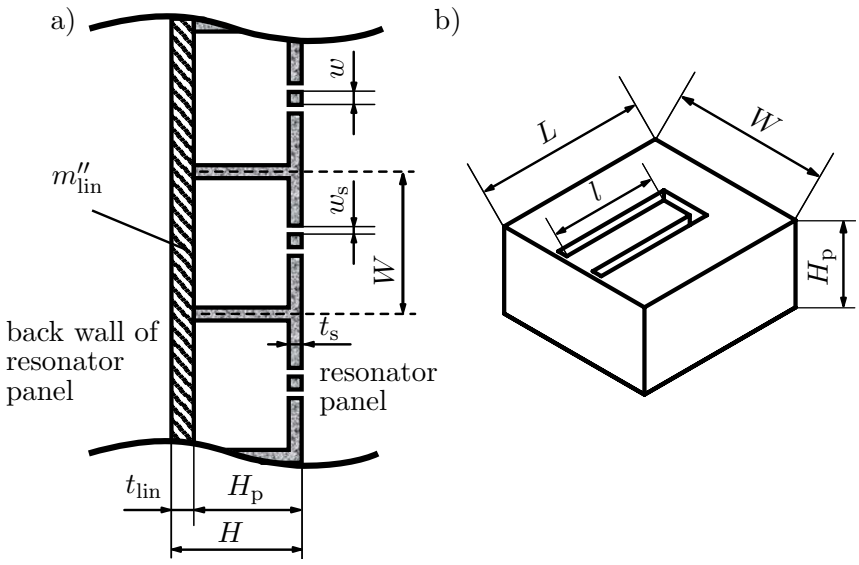

Figure 4.14: Helmholtz resonator panel with integrated cantilevers, consisting of two parts: the resonator back wall and the resonator panel. a) Schematic drawing of the panel cross section. b) Schematic drawing of a unit cell.

4.4.1. Numerical verification

4.4.1.1. Single wall

The model used for the numerical verification of the transmission loss, calculated by the transfer matrix method, is depicted in Figs. 4.15 a)-d) for the single wall. The geometric dimensions of the resonator are given in Table 4.3, with the dimensions according to Fig. 4.14.

The main characteristics of the previously described simulation models are adopted. Similar to the simulation model used to determine the eigenfrequencies, only half of the geometry was modeled with symmetry boundary conditions along the cutting plane and the opposite lateral plane, since the resonator geometry is symmetric with respect to the x-z plane. The transfer matrix method used in the analytical calculations considers an infinite plate. The resonator unit cell is periodically placed on the back plate. The finite element model respects the periodicity of the resonator panel by using periodic boundary conditions on the sidewalls. The symmetric and periodic boundary conditions are shown in

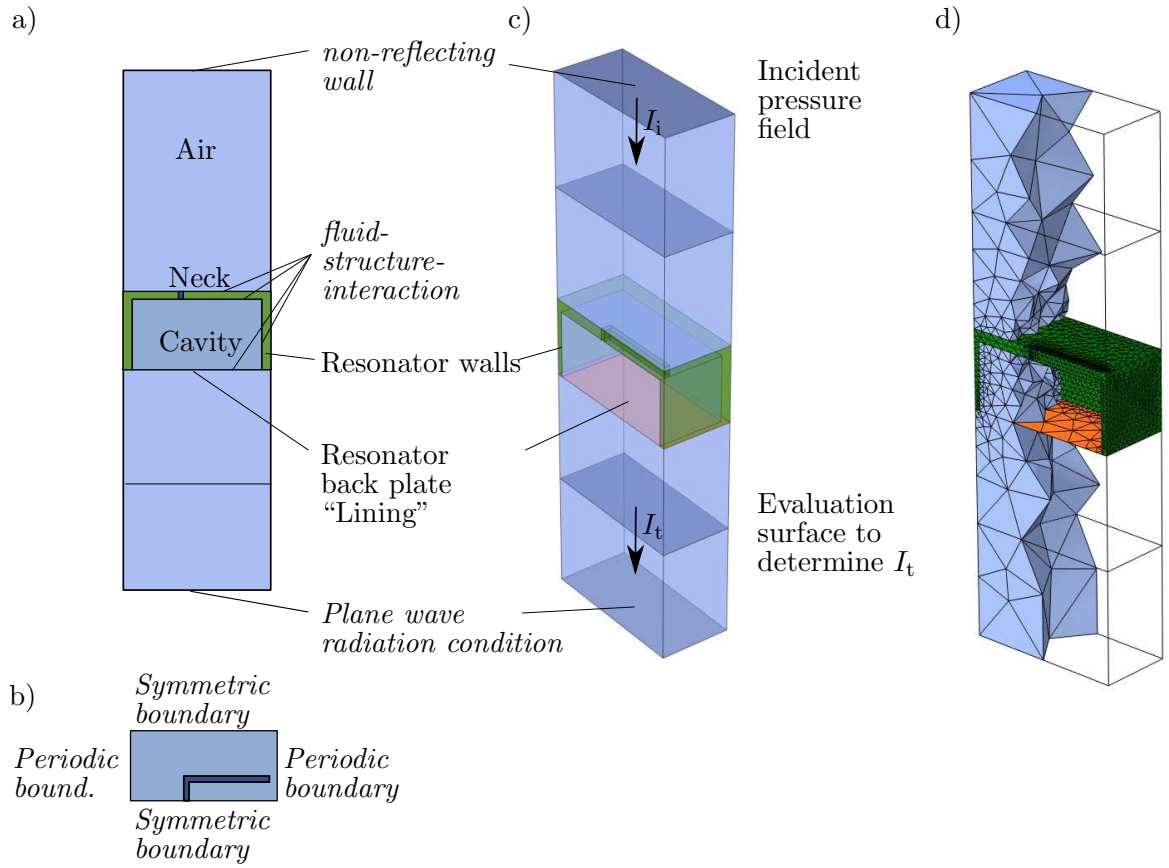

Figure 4.15: Schematic view of the finite element model used to verify the transfer matrix method for calculating the transmission loss of an infinite resonator plate. a)-c) Different domains and boundary conditions [a) Two-dimensional side view; b) Two-dimensional top view; c) Three-dimensional view]. d) View of the resonator and fluid mesh.

Table 4.3: Geometric and material data of the modeled resonator panel used in the numerical simulations.

Description	Symbol	Value	Unit
Unit cell width	W	65	mm
Unit cell length	L	70	mm
Foam panel height	H_p	40	mm
Cantilever width	w	5	mm
Cantilever length	l	36	mm
Cantilever height and res. wall thickness	t_s	5	mm
Slit width	w_s	2	mm
Density	ρ_CL	32	kg/m^3
Young's modulus	E_CL	36	MPa
Structural loss factor	η_CL	0.05	-

Fig. 4.15 b). A normally incident plane wave with an amplitude of 1 Pa was applied as an excitation to the top surface and the incident sound intensity and power were determined according to Eq. (4.3) and Eq. (4.4), respectively. The transmitted sound power

$$P_\mathrm{t} = \int_S I_\mathrm{t} \,\mathrm{d}S \tag{4.9}$$

is determined by integrating the intensity I_t over an evaluation surface parallel to the back plate of the resonator and parallel to the bottom surface of the model, as visualized in Fig. 4.15 c). The sound power transmission coefficient can then be calculated using Eq. (2.38). The bottom surface is modeled as an infinite half space by terminating the fluid domain with a plane wave radiation boundary condition that represents a non-reflecting boundary.

As in the simulation models described earlier, the light blue colored domains are modeled as a compressible fluid (air). The dark blue colored domain inside the Helmholtz resonator neck takes into account the viscous losses and is modeled as an equivalent fluid as described in Section 4.2.1. The green shaded resonator walls are modeled as an elastic solid with the material data given in Table 4.3 (according to Ref. [42]), where the structural damping is accounted for by a structural loss factor. The orange back plate of the resonator is modeled as a 0.8 mm thick shell with the material data given in Table 4.4. The material data correspond to a glass fiber reinforced plastic plate with a surface mass density $m''_\mathrm{lin} = 1.6$ kg/m^2 and was taken from the manufacturer's data sheet [21]. The discretization of the model is based on the eigenfrequency analysis model in Subsection 4.1. The mesh is presented in Fig. 4.15 d). For the shell elements of the resonator back wall, tri-

Table 4.4: Material data of the glass fiber reinforced plastic plate used as the back plate in the numerical simulations and experiments [21].

Description	Symbol	Value	Unit
Density	ρ_{lin}	2000	$\mathrm{kg/m^3}$
Young's modulus	E_{lin}	22	GPa
Poisson's ratio	ν_{lin}	0.18	-

angular elements with a maximum size of one tenth of the smallest wavelength of interest corresponding to 1500 Hz were used.

To calculate the transmission loss analytically with the derived transfer matrix, the resonance frequencies of the Helmholtz resonator f_{HR}, of the cantilever in vacuo f_{CL} and of the cantilever stiffened by the air volume in the cavity $f_{\mathrm{CL,V}}$ are required. The resonance frequencies are calculated using the analytical models from Sections 3.2 to 3.5, taking into account the viscous losses in the neck and the structural damping of the resonator material. Due to the damping, the analytical results are complex-valued, with the real part representing the resonance frequency f_0, and the imaginary part reflecting the damping. For damping ratios ζ smaller than 0.2, the damped resonance frequency f_{d} is approximately $f_{\mathrm{d}} = f_0\,(1 + \mathrm{i}\zeta)$ [25]. The resonance frequencies result in approximately $f_{\mathrm{HR}} = 564\,\mathrm{Hz}$, $f_{\mathrm{CL1}} = 568\,\mathrm{Hz}$, and $f_{\mathrm{CL,V}} = 574\,\mathrm{Hz}$, with damping ratios of about 3 % for the Helmholtz resonator and 2 % for the cantilever. The corresponding resonance frequencies of the coupled system, calculated using Eq. (3.48), are approximately $f_1 = 526$ Hz and $f_2 = 609$ Hz. The surface mass density of the resonator panel is $m''_{\mathrm{res}} = 0.28\,\mathrm{kg/m^2}$, thus the resulting surface mass density of the whole panel including the lining is $m''_{\mathrm{s}} = 1.88\,\mathrm{kg/m^2}$. Fig. 4.16 a) shows the comparison of the analytically calculated transmission loss, represented by lines, and the numerically calculated transmission loss, represented by symbols. Three different panel configurations are compared. Firstly, all resonators are closed (closed. res.), so that only the panel mass contributes to the transmission loss. Secondly, the cantilever was inactive and the Helmholtz resonator acts alone (HR). In the finite element model, this was achieved by applying a fixed boundary condition to the cantilever surface. Thirdly, the transmission loss of the Helmholtz resonator with integrated cantilever (HR+CL) is compared. For the latter two configurations, the insertion loss, which is the difference between the transmission loss with active and closed resonators, is shown in Fig. 4.16 b). The comparison in Figs. 4.16 a) and b) shows an overall good agreement and thus the finite element simulations verify the analytical transfer matrix model. Fig. 4.16 a) shows that the transmission loss of the panel with active resonators is improved at their respective resonance frequencies compared to the panel with closed resonators. The insertion losses of the Helmholtz resonator panel and

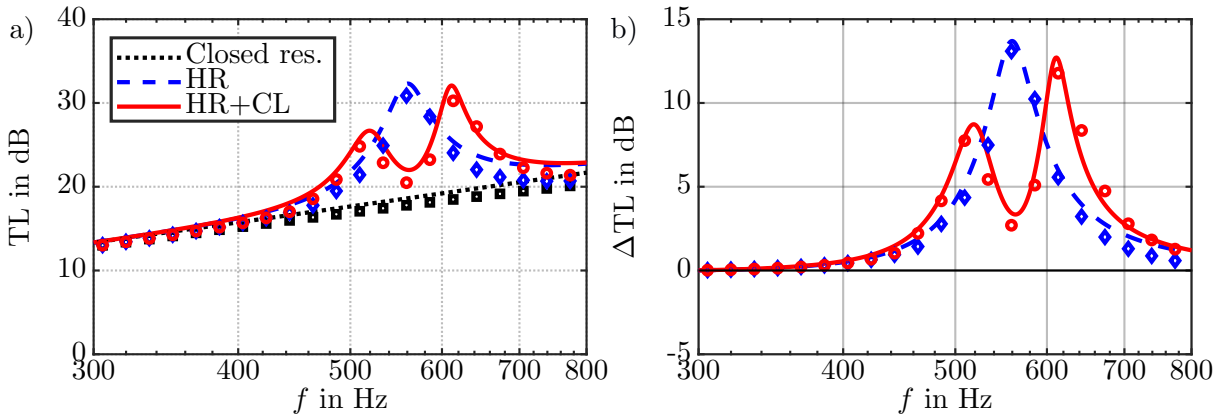

Figure 4.16: Comparison of the analytically calculated (lines) and numerically calculated (symbols) transmission loss TL and insertion loss ΔTL of an infinite panel with closed resonators, with Helmholtz resonators (HR), and Helmholtz resonator with integrated cantilevers (HR+CL). a) Transmission loss. b) Insertion loss.

the Helmholtz resonator panel with integrated cantilever show a peak at about 565 Hz and two peaks at about 520 and 610 Hz, respectively. The insertion loss of the resonator panel with integrated cantilever decreases in between the two peaks. The Helmholtz resonator with integrated cantilever can be designed so that the two peaks of high insertion loss correspond to tones to be attenuated, or so that the frequency range of high insertion loss is increased.

4.4.1.2. Double wall

In this subsection, the transfer matrix method is verified for a multi-layered setup. The general setup is illustrated in Fig. 4.17, where, in addition to the resonator plate, a second wall and an insulation layer have been added. In view of the application of the Helmholtz resonators in aircraft sidewalls, the second wall represents the outer skin of the fuselage with structural elements (such as frames, stringers and clips) and will be referred to as the fuselage (abbreviated as fus.).

The simulation model described in the previous subsection is extended to include a second wall representing the fuselage structure, and by an insulation layer between the resonator panel and the second wall. The extended simulation model for the double wall setup is shown in Figs. 4.18 a)-d). The second wall, representing the fuselage structure, has a distance of $H_{\mathrm{DW}} = 100$ mm from the back plate of the resonator. It is colored in orange and modeled using shell elements. The wall is built from a 8 mm thick medium-density fiberboard with the material data given in Table 4.5 resulting in a surface mass density of $m''_{\mathrm{fus}} = 5.6\ \mathrm{kg/m^2}$. The porous layer has a thickness of $H_{\mathrm{GW}} = 35$ mm and is modeled numerically using the equivalent fluid model of Johnson-Champoux-Allard [2], with the

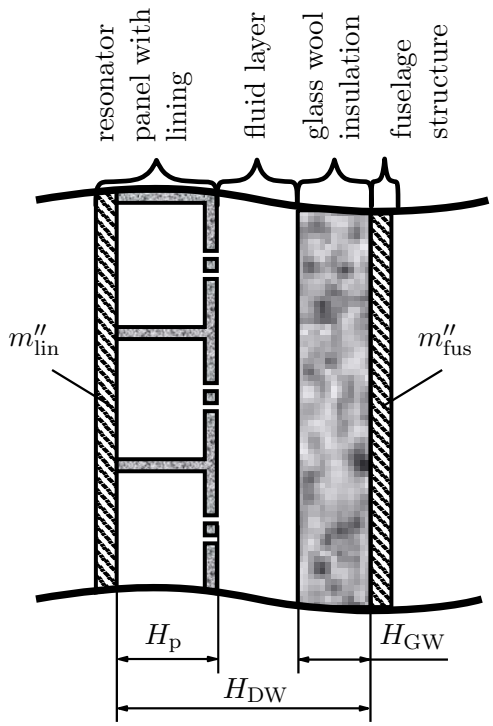

Figure 4.17: Schematic drawing of a double wall setup consisting of a Helmholtz resonator panel with integrated cantilevers, an insulation layer and a second wall.

limp formulation. The material properties of the porous layer are given in Table 4.6, which corresponds to aircraft-certified glass wool, that is usually recognized by its typical pink color. The boundary conditions and discretization settings are taken from the previous simulation models and are depicted in Figs. 4.18 a)-d). The numerical transmission loss is determined by evaluating the incident and transmitted sound intensities I_{i} and I_{t}, as visualized in Fig. 4.18 c) and described in the previous Section.

To analytically calculate the transmission loss of the multi-layered setup, the transfer matrices of the four individual layers are multiplied to obtain the transfer matrix of the entire setup

$$\mathbf{T}_{\mathrm{DW,HRCL}} = \mathbf{T}_{\mathrm{HRCL}} \cdot \mathbf{T}_{\mathrm{F}} \cdot \mathbf{T}_{\mathrm{GW}} \cdot \mathbf{T}_{\mathrm{fus}}, \tag{4.10}$$

where $\mathbf{T}_{\mathrm{F}}$ is the transfer matrix of the fluid layer air with a thickness of 30 mm, calculated

Table 4.5: Material data of the medium-density fiberboard used as the fuselage wall in the numerical simulations and experiments [10].

Description	Symbol	Value	Unit
Density	ρ_{fus}	700	$\mathrm{kg/m^3}$
Young's modulus	E_{fus}	3.7	GPa
Poisson's ratio	ν_{fus}	0.25	-

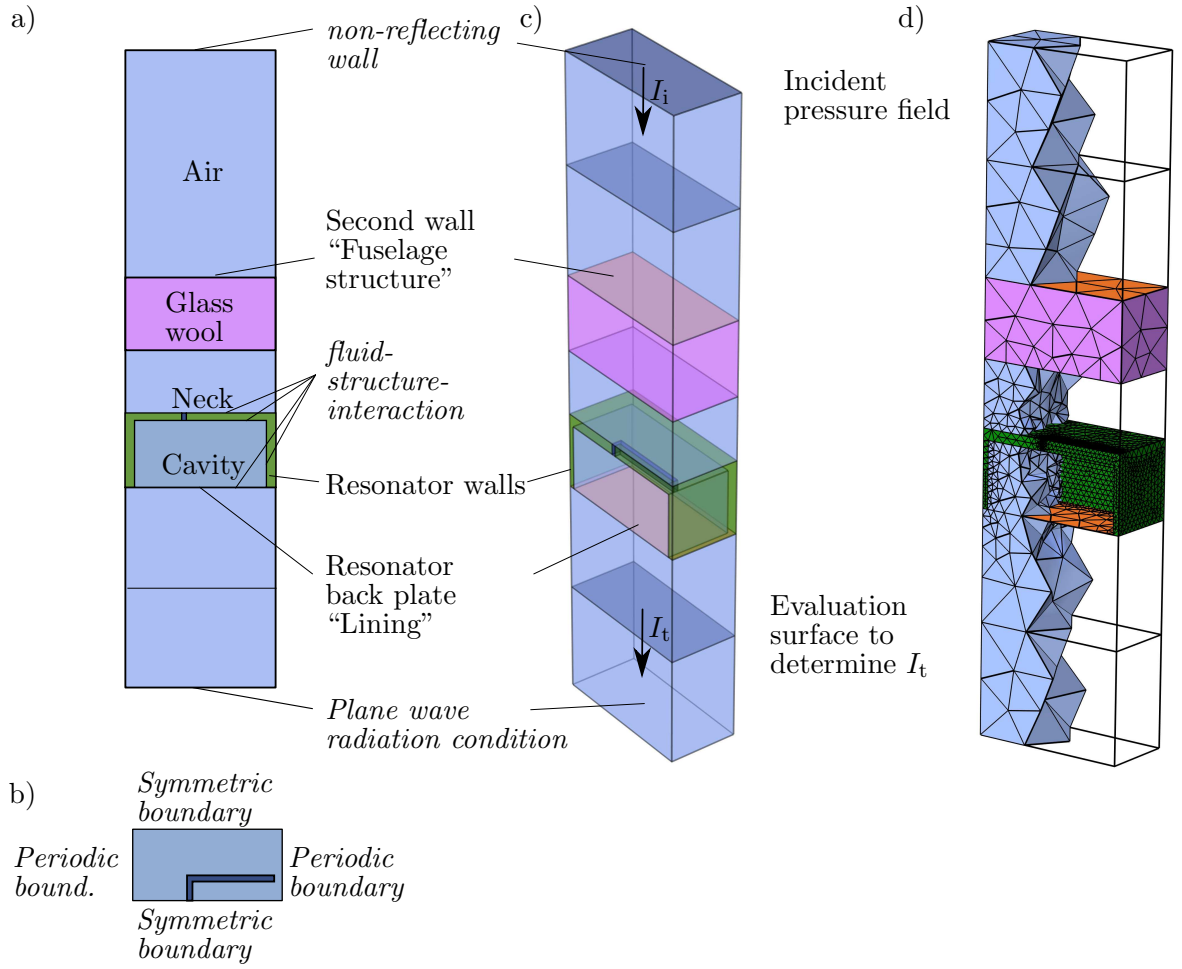

Figure 4.18: Schematic of the finite element model used to verify the transfer matrix method for calculating the transmission loss of a multi-layer setup. a)-c) Different domains and boundary conditions [a) Two-dimensional side view; b) Two-dimensional top view; c) Three-dimensional view]. d) View of the resonator and fluid mesh.

with Eq. (2.69), $\mathbf{T}_{\mathrm{GW}}$ is the transfer matrix of the glass wool insulation with a thickness of 35 mm, calculated as a limp porous material with Eq. (2.70), and $\mathbf{T}_{\mathrm{fus}}$ is the transfer matrix of a limp acoustic wall with the material properties given in Table 4.5 and the surface mass density m''_{fus}. The transmission loss is calculated from the pressure transmission coefficient in Eq. (3.68) with $\mathrm{TL} = -20\,\lg|t|$. To calculate the transmission loss of the double wall setup with the uncoupled Helmholtz resonators, the transfer matrix $\mathbf{T}_{\mathrm{HRCL}}$ is replaced by the transfer matrix of the uncoupled Helmholtz resonator panel $\mathbf{T}_{\mathrm{HR}}$

$$\mathbf{T}_{\mathrm{DW,HR}} = \mathbf{T}_{\mathrm{HR}} \cdot \mathbf{T}_{\mathrm{F}} \cdot \mathbf{T}_{\mathrm{GW}} \cdot \mathbf{T}_{\mathrm{fus}}. \tag{4.11}$$

The transfer matrix of the mass-equivalent double wall is calculated by

$$\mathbf{T}_{\mathrm{DW}} = \mathbf{T}_{\mathrm{res}} \cdot \mathbf{T}_{\mathrm{F}} \cdot \mathbf{T}_{\mathrm{GW}} \cdot \mathbf{T}_{\mathrm{fus}}, \tag{4.12}$$

Table 4.6: Porous material parameters of the aircraft-certified glass wool used in the numerical simulations and in the analytical transfer matrix calculations [62, 90].

Description	Symbol	Value	Unit
Density	ρ_{GW}	5.44	kg/m^3
Porosity	φ	0.997	-
Flow resistivity	σ	19300	Ns/m^4
Tortuosity	α_∞	1.02	-
Viscous char. length	Λ	66	µm
Thermal char. length	Λ'	131	µm

where $\mathbf{T}_{\mathrm{res}}$ is the transfer matrix of a limp acoustic wall with the surface mass density m_{s}'' and the fluid layer has a thickness of 65 mm.

In Fig. 4.19 a) the comparison of the numerically and analytically determined transmission loss is shown for three double wall configurations: a reference mass-equivalent double wall without resonators (Ref. DW), a double wall with a resonator panel with deactivated cantilever (HR) and a double wall with Helmholtz resonators with integrated cantilevers (HR+CL). In Fig. 4.19 b), the comparison for the insertion loss is shown, which in this case is the difference of the transmission loss of the double wall setups with resonators with respect to the transmission loss of the reference double wall. The results show that the numerically and analytically determined transmission losses are in very good agreement. Thus, the numerical simulations verify the analytical model of the transfer matrix method also for a multi-layer structure.

In Fig. 4.19 a) it can be observed that the transmission loss of the multi-layered panels with resonators is improved at the respective resonance frequencies of the Helmholtz

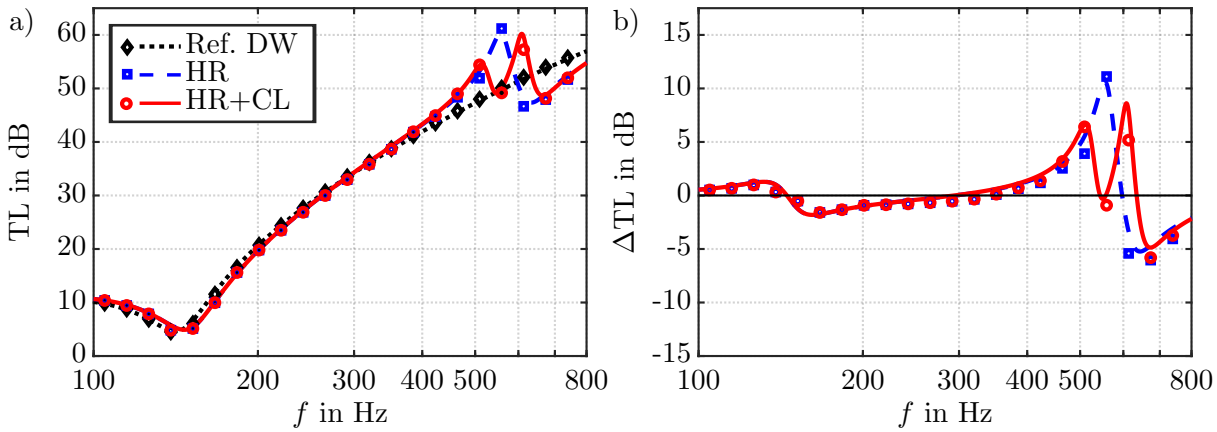

Figure 4.19: Comparison of the analytically calculated (lines) and numerically calculated (symbols) transmission loss TL and insertion loss ΔTL of a reference double wall (Ref. DW), a double wall with Helmholtz resonators (HR) and a double wall with Helmholtz resonators with integrated cantilevers (HR+CL). a) Transmission loss. b) Insertion loss.

resonator and of the Helmholtz resonator with integrated cantilevers compared to the reference double wall. Fig. 4.19 b) shows that the insertion loss of a double wall is positive between about 300 and 600 Hz by inserting the resonator panel with Helmholtz resonators. By integrating the cantilever into the resonator panel, the insertion loss is positive in two frequency ranges: approximately between 300 and 540 Hz and between 570 and 640 Hz. For the intermediate frequency range, the insertion loss is negative.

A distinct minimum in the insertion loss occurs at about 630 Hz for the double wall configuration with the embedded Helmholtz resonator panel (HR) and at about 680 Hz in case of the embedded resonator panel with integrated cantilevers (HR+CL). This minimum depends on the tonraum resonance frequency as described in Section 2.3.3. Using Eq. (2.63) with the volumetric filling ratio of approximately $\phi_{\mathrm{HR}} = 0.2$ and the higher resonance frequency $f_2 = 609$ Hz yields to a tonraum resonance frequency of $f_{\mathrm{TR,HRCL}} \approx 681$ Hz; compared to the tonraum resonance frequency of the double wall with the Helmholtz resonator panel only $f_{\mathrm{TR,HR}} \approx 631$ Hz (calculated with $\phi_{\mathrm{HR}} = 0.2$ and $f_{\mathrm{HR}} = 564$ Hz).

It can also be observed that the transmission loss of the resonator panel is significantly reduced in the high-frequency range compared to the reference double wall. This is due to the fact that the resonators in the double wall are decoupled from the surrounding air space. The resulting smaller air gap leads to a reduced transmission loss [81]. The Helmholtz resonator panel with integrating cantilevers can be designed, so that

- the tonraum resonance frequency is shifted to higher frequencies, where sound insulation, such as porous material can absorb acoustic sound more efficiently,
- the two resonance frequencies of the coupled resonator correspond to two frequencies to be attenuated, such as pronounced excitation frequencies,
- the frequency band of improved transmission loss is broadened.

4.4.2. Experimental validation

This subsection describes the experiments performed to validate the transfer matrix model of the resonator panel. The validation is conducted for a large Helmholtz resonator panel with integrated cantilevers in a test setup in a laboratory. The test panel has a width of $W_{\mathrm{p}} = 1$ m and a length of $L_{\mathrm{p}} = 1.2$ m and consists of 252 unit cells. The geometric dimensions of the resonators and of the resonator panel are listed in Table 4.7. The resonator panel was fabricated from the same closed-cell PMI-based rigid foam, which was also used for the unit cell resonator of the impedance tube measurements and has a surface mass density of $m''_{\mathrm{res}} = 0.37\,\mathrm{kg/m^2}$. Similar to the unit cell, the resonator panel was fabricated by milling. The panel was bonded with epoxy resin to the back plate, which

Table 4.7: Geometric and material data of the resonator panel used in the experimental validations.

Description	Symbol	Value	Unit
Panel width	W_p	1000	mm
Panel length	L_p	1200	mm
Unit cell width	W	65	mm
Unit cell length	L	70	mm
Foam panel height	H_p	35	mm
Cantilever width	w	5	mm
Cantilever length	l	36	mm
Cantilever height and res. wall thickness	t_s	4.5	mm
Slit width	w_s	1.8	mm
Density	ρ_CL	32.2	kg/m^3
Young's modulus	E_CL	34.33	MPa
Structural loss factor	η_CL	0.05	-

represents the cabin lining and consists of a 2 mm thick glass fiber reinforced plastic plate, with the material data given in Table 4.4 and resulting surface mass density of $m''_\mathrm{lin} = 4$ kg/m^2. Figs. 4.20 a) and b) show the milled structure of the resonators from the closed-cell foam, before it was glued to the glass fiber reinforced plastic plate. The transmission loss of the Helmholtz resonator panel was validated under diffuse field sound excitation, according to ISO 15186-1 [39] as explained in Section 2.5.3. The test specimens were mounted in an approximately rigid wooden frame in a test window between a reverberation room and a hemi-anechoic chamber. The test panel inside the wooden frame is shown in Fig. 4.21 a). In the reverberation room, a diffuse sound field was excited by a dodecahedron loudspeaker with a total sound pressure level of 120 dB, which was measured by a 1/2 inch diffuse field microphone on a rotating beam. Fig. 4.21 b) shows the specimen inside the transmission window and the setup of the microphone on the rotating beam in the reverberation room. In the receiving room, the sound intensity spectrum was measured

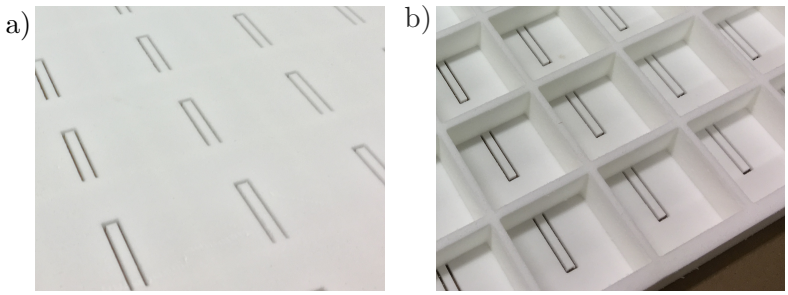

Figure 4.20: Photos of the resonator panel with integrated cantilevers. a) External view. b) Internal view of the resonator cavities and cantilevers.

a) b)

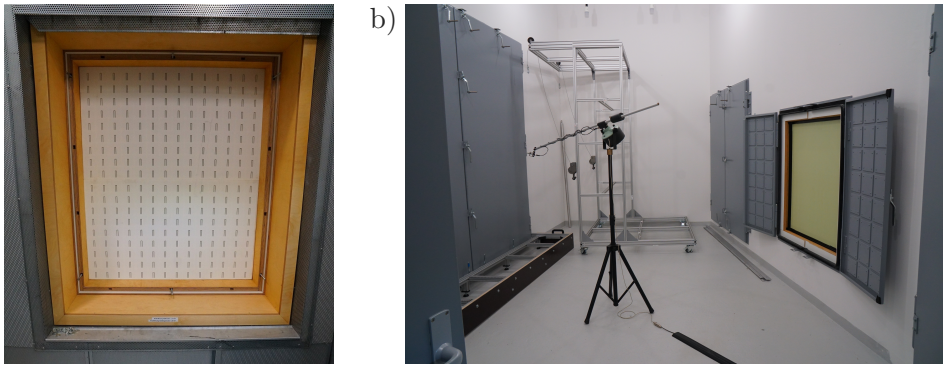

Figure 4.21: Photos of the measurement setup. a) Test panel mounted in a rigid wooden frame, view from the receiving room. b) Test panel inside the transmission window, view from the reverberation room.

in 1/12th-octave bands with a hand-held intensity probe from Brüel&Kjaer, type 3599, with a 12 mm spacer between the microphones.

The analytical results of the transmission loss are obtained using the transfer matrix method, as described in Section 2.4. The resonance frequencies required in the derived transfer matrix Eq. (3.67) are calculated using the analytical models of Sections 3.2 to 3.5, taking into account the mechanical and viscous losses. The calculated eigenfrequencies result in approximately $f_{\mathrm{HR}} = 584$ Hz, $f_{\mathrm{CL1}} = 538$ Hz, and $f_{\mathrm{CL,V}} = 554$ Hz, with damping ratios of about 5 % for the Helmholtz resonator and 2.5 % for the cantilever. The corresponding resonance frequencies of the coupled system are approximately $f_1 = 495$ Hz and $f_2 = 635$ Hz. In Eq. (3.67), $m''_{\mathrm{s}} = 4.54\,\mathrm{kg/m^2}$ is the surface mass density of the entire resonator panel, which includes the surface mass density contributions from the back panel $m''_{\mathrm{lin}} = 4\,\mathrm{kg/m^2}$, the foam panel $m''_{\mathrm{res}} = 0.37\,\mathrm{kg/m^2}$, and the epoxy resin $m''_{\mathrm{res}} = 0.17\,\mathrm{kg/m^2}$.

To measure the transmission loss of the resonator panel with uncoupled Helmholtz resonators, all cantilevers were fixed with pins to prevent them from oscillating, as shown in Fig. 4.22 a). The mass-equivalent wall without resonators was obtained experimentally by closing the resonators with tape, as shown in Fig. 4.22 b).

To compare the analytical transfer matrix results with the experimental results under

a) b)

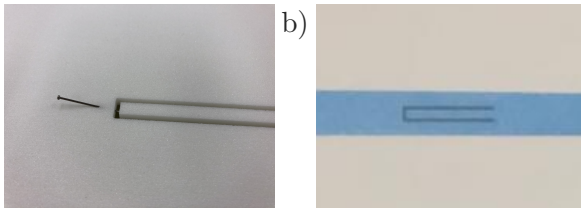

Figure 4.22: Photos of the specimen. a) Cantilever fixed by a pin. b) Helmholtz resonator neck closed with tape.

the diffuse field incidence, the transmission coefficient, determined from the transfer matrix, is corrected to account for the finite-size of the panel with Eq. (2.73), as described in Section 2.4.5. The diffuse field transmission coefficient of the finite plate $\tau_{\mathrm{f,diff}}$ is obtained by integration over the incidence angles θ, where the integration is performed over the limiting angle $\theta_{\mathrm{lim}} = 73°$, as estimated in a previous experiment for the given laboratory [81]. In the following, the analytical transmission loss is validated first for the single resonator wall and then for a double wall setup.

4.4.2.1. Single wall

The measurement results are compared with the analytical results of the single wall in Fig. 4.23 a), showing the transmission loss of the panel with closed resonators, with Helmholtz resonators acting alone (HR), and with Helmholtz resonator with integrated cantilevers (HR+CL). The insertion loss with respect to the panel with closed resonators is shown in Fig. 4.23 b).

The comparison shows good agreement and thus validates the transfer matrix model under diffuse field excitation. Similar to the results of the impedance tube measurements of the transmission loss of the unit cell, the measured transmission loss at the resonance frequencies is lower compared to the calculated transmission loss. As mentioned earlier, this behavior can be attributed to the rough surface inside the resonator necks. It is observed that the maximum insertion loss is obtained at the resonance frequencies of the Helmholtz resonators around 590 Hz and of the coupled resonators around 500 and 635 Hz, which is in good agreement with the calculated resonance frequencies.

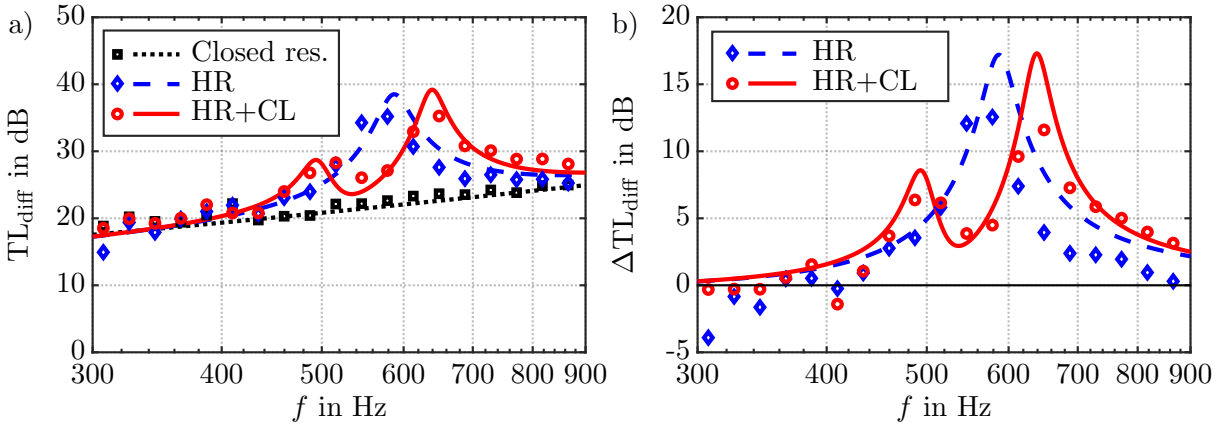

Figure 4.23: Comparison of the analytically calculated (lines) and experimentally measured (symbols) transmission loss $\mathrm{TL_{diff}}$ and insertion loss $\Delta\mathrm{TL_{diff}}$ under diffuse field excitation of a finite-size panel with closed resonators, a Helmholtz resonator panel (HR) and a Helmholtz resonator panel with integrated cantilever (HR+CL). a) Transmission loss $\mathrm{TL_{diff}}$. b) Insertion loss $\Delta\mathrm{TL_{diff}}$.

4.4.2.2. Double wall

The considered double wall setup of the Helmholtz resonator panel is shown in Fig. 4.24 a). In this configuration, a second wall is mounted with a spacing $H_{\mathrm{DW}} = 125$ mm from the resonator back plate, with the Helmholtz resonators placed inside the cavity. A homogeneous 0.5 mm thick glass fiber reinforced plastic plate, with a surface mass density of $m''_{\mathrm{fus}} = 1\ \mathrm{kg/m^2}$ and the material data given in Table 4.4 was installed as the second wall. A 25 mm thick layer of melamine foam insulation (trade name Basotect) with the material data given in Table 4.8 was installed in between the resonator plate and the second wall. Fig. 4.24 b) illustrates the corresponding reference configuration of an empty double wall, where the resonator panel was replaced by a mass equivalent, 6.5 mm thick medium-density fiberboard, with the material data given in Table 4.5 and the surface mass density $m''_{\mathrm{s}} = 4.55\ \mathrm{kg/m^2}$.

The transmission loss of the multi-layered setup is again obtained by multiplying the four transfer matrices of each layer

$$\mathbf{T}_{\mathrm{DW,HRCL}} = \mathbf{T}_{\mathrm{HRCL}} \cdot \mathbf{T}_{\mathrm{F}} \cdot \mathbf{T}_{\mathrm{Foam}} \cdot \mathbf{T}_{\mathrm{fus}}, \tag{4.13}$$

where $\mathbf{T}_{\mathrm{F}}$ is the transfer matrix of the 65 mm thick fluid layer air, $\mathbf{T}_{\mathrm{Foam}}$ is the transfer matrix of the 25 mm thick melamine foam layer, calculated as a limp porous material. The transfer matrix of the mass-equivalent double wall is calculated by

$$\mathbf{T}_{\mathrm{DW}} = \mathbf{T}_{\mathrm{res}} \cdot \mathbf{T}_{\mathrm{F}} \cdot \mathbf{T}_{\mathrm{Foam}} \cdot \mathbf{T}_{\mathrm{fus}}, \tag{4.14}$$

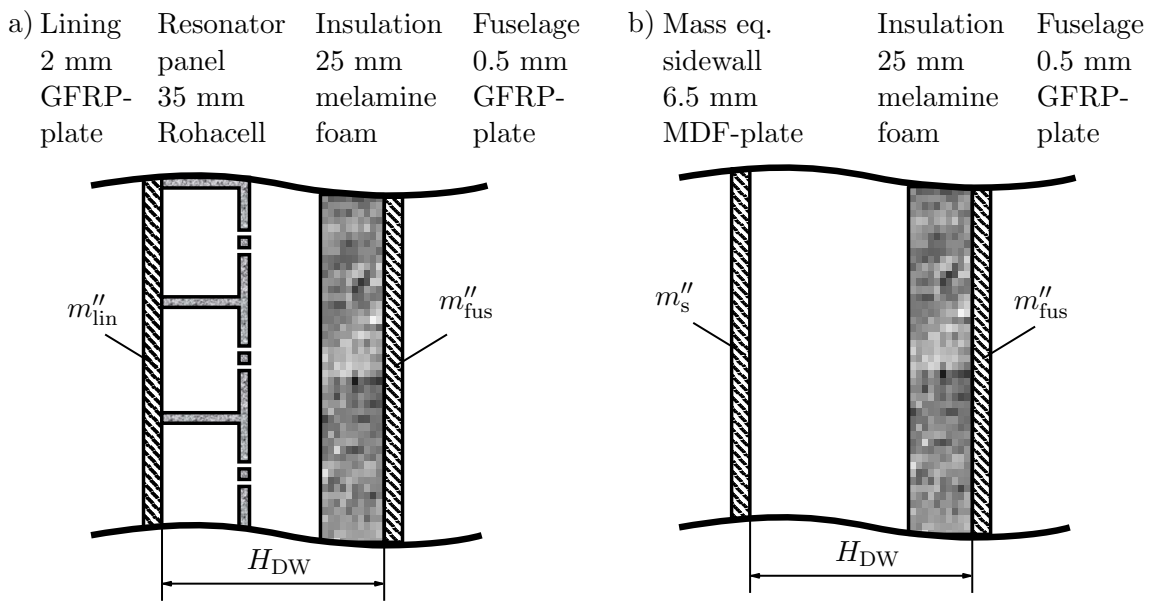

Figure 4.24: Schematic drawing of the double wall setup. a) Double wall with active Helmholtz resonators with integrated cantilevers. b) Mass equivalent reference double wall.

Table 4.8: Porous material parameters of a melamine foam [66].

Description	Symbol	Value	Unit
Density	ρ_{Foam}	10.3	kg/m^3
Porosity	φ	0.993	-
Flow resistivity	σ	13100	Ns/m^4
Tortuosity	α_∞	1.01	-
Viscous char. length	Λ	199	μm
Thermal char. length	Λ'	445	μm

where $\mathbf{T}_{\text{res}}$ is the transfer matrix of a limp acoustic wall with the surface mass density m_{s}'' and the fluid layer has a thickness of 100 mm.

Fig. 4.25 a) shows the comparison of the analytically determined (lines) and experimentally determined (symbols) transmission loss of the Helmholtz resonator panel with integrated cantilevers installed in a double wall setup. Fig. 4.25 b) shows the insertion loss with respect to the mass-equivalent double wall with closed resonators.

The figures show good overall agreement between the measured and analytical results. Deviations are observed at the second resonance frequency, where the measured insertion loss is lower than the calculated values. This discrepancy can be attributed to the rough surface inside the resonator neck. At the second resonance frequency, which is closer to the resonance frequency of the Helmholtz resonator, the effects of increased viscous losses caused by the rough surfaces become more pronounced.

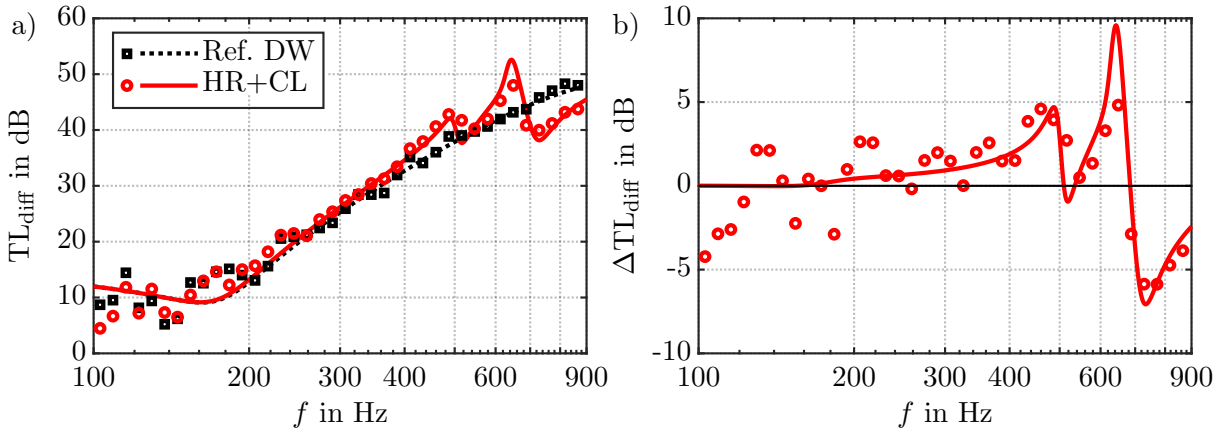

Figure 4.25: Comparison of the analytically calculated (lines) and experimentally measured (symbols) transmission loss TL_{diff} and insertion loss $\Delta\text{TL}_{\text{diff}}$ under diffuse field excitation of a of a reference double wall (Ref. DW), and a double wall with Helmholtz resonators with integrated cantilevers (HR+CL). a) Transmission loss TL_{diff}. b) Insertion loss $\Delta\text{TL}_{\text{diff}}$.

5. Parameter studies

In this chapter, parameter studies are performed for different geometric and material properties of the resonator to investigate their influence on the resonance frequencies, on the absorption coefficient, and on the transmission loss behavior of the Helmholtz resonator with integrated cantilever. Parts of this chapter have also been published in Ref. [57].

5.1. Eigenfrequency analysis

Parameter variations are performed for different resonator geometries to highlight the tuning possibilities for the eigenfrequencies as well as the coupling behavior between the acoustic oscillator (HR) and the mechanical oscillator (CL). Since the focus of this study is on tuning the resonance frequencies, structural and viscous losses are neglected in the eigenfrequency analysis. In Appendix A.3, a parameter study on varying slit width is conducted as an example, taking damping into consideration. In the parameter variation, the resonator was modeled according to Table 4.1 while one or two parameters were varied simultaneously. Unless otherwise stated, all other parameters remained unchanged.

Similar to the verification, the bold lines in the figures show the analytical resonance frequencies calculated with the derived system of equations in Eq. (3.39), where the number of modes inside the cavity was fixed to 20 modes in y and z direction ($N_y = N_z = 20$). The results of the simplified model with constant pressure distribution inside the cavity, calculated with Eq. (3.48), are shown as thin lines for comparison.

5.1.1. Cantilever length

Figs. 5.1 a)-c) show the influence of the cantilever length l on the resonance frequencies of the coupled system f_1, f_2 and of the uncoupled Helmholtz resonator f_{HR} and cantilever f_{CL1}. The influence is shown for three different cavity volumes obtained by varying the resonator height H ($H = 20$ mm, 40 mm and 60 mm) while keeping the other geometric parameters constant. In Figs. 5.1 d)-f) the resonance frequencies of the cantilever coupled to the cavity volume $f_{\mathrm{CL,V}}$ are compared with the resonance frequencies of the cantilever

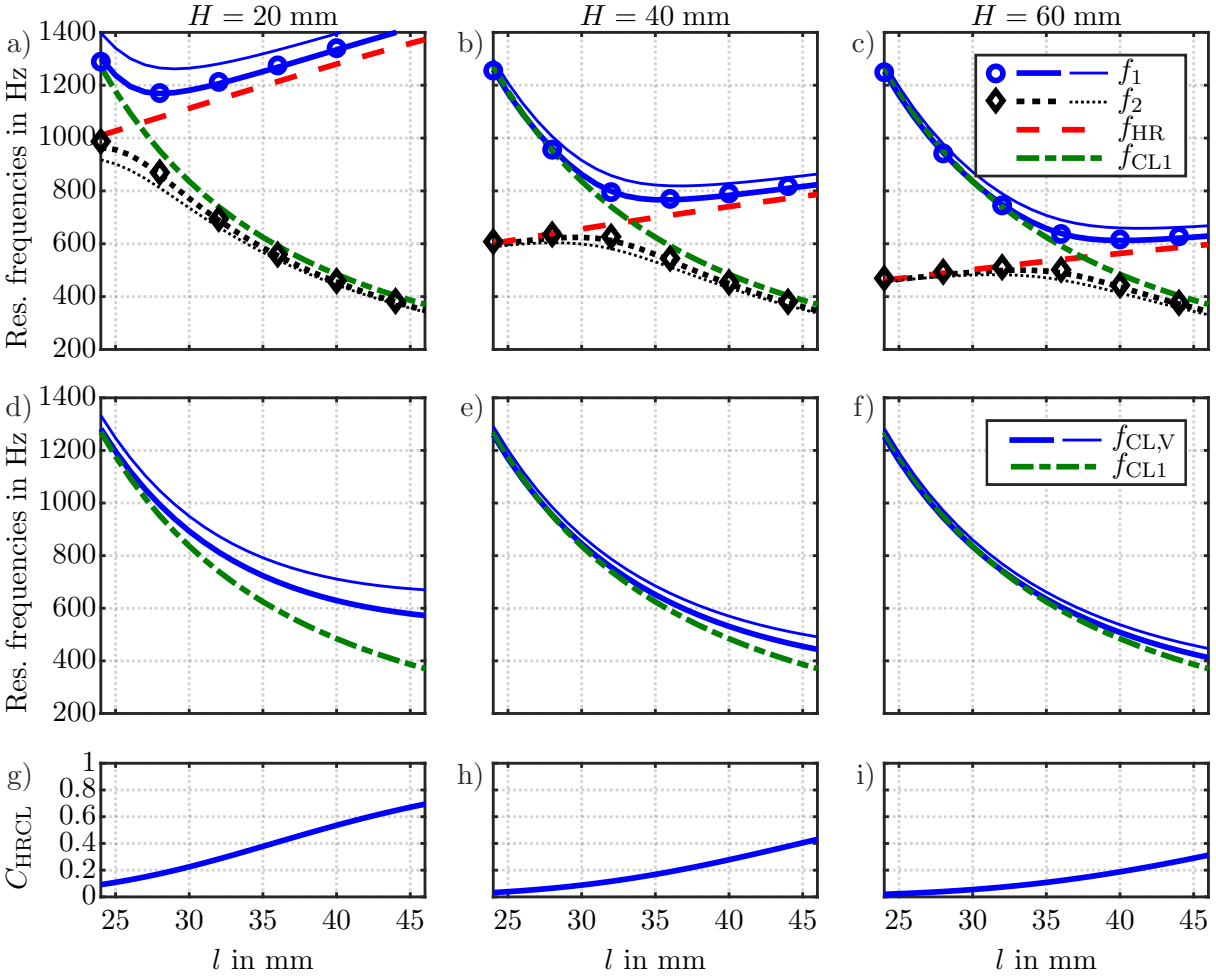

Figure 5.1: a)-f) Calculated resonance frequencies of the resonator system depending on cantilever length and cavity volume. Bold lines: analytical model, calculation considering higher-order acoustic modes inside the cavity. Thin lines: simplified analytical model assuming constant pressure distribution. Symbols: simplified analytical model with using $f_{\mathrm{CL,V}}$ from Eq. (3.47). a)-c) Comparison of f_1, f_2, f_{HR} and f_{CL1}. d)-f) Comparison of f_{CL1} and $f_{\mathrm{CL,V}}$. g)-i) Coupling parameter.

in vacuo f_{CL1}. Figs. 5.1 g)-i) show the coupling parameter C_{HRCL}, as defined in Eq. (3.44).

In general, the resonance frequency of the Helmholtz resonator increases with increasing cantilever length, since the area of the neck S_{HR} increases. In contrast, the in vacuo resonance frequency of the cantilever decreases with increasing cantilever length. At the cantilever length where f_{HR} and f_{CL1} are equal, the resonance frequencies of the coupled system f_1 and f_2 approach each other to a minimum frequency difference, but they do not become equal. For small and large cantilever lengths, f_{HR} and f_{CL1} are far apart and the resonance frequencies of the coupled system approach those of the uncoupled system. While the resonance frequencies of the coupled and uncoupled systems are nearly equal for small cantilever lengths, an offset can be observed for large cantilever lengths. This offset

is largest for the resonator designs in a) with the smallest cavity volume V_{cav}. This can be explained by the coupling parameter C_{HRCL}, which increases with decreasing volume V_{cav}, since the cavity volume is in the denominator in Eq. (3.44). Thus, the coupling parameter is inversely proportional to V_{cav}. Furthermore, the coupling becomes weaker for smaller cantilever lengths l, as shown in Figs. 5.1 g)-i). The influence of the cavity volume V_{cav} can be seen in Figs. 5.1 a)-c). The volume is increased from $V_{\mathrm{cav}} = l_x \cdot l_y \cdot l_z = 33\ \mathrm{cm}^3$ in Fig. 5.1 a) over $V_{\mathrm{cav}} = 99\ \mathrm{cm}^3$ in Fig. 5.1 b) to $V_{\mathrm{cav}} = 165\ \mathrm{cm}^3$ in Fig. 5.1 c). With increasing resonator volume, the coupling parameter (see Figs. 5.1 g)-i)) and thus the coupling behavior is reduced, which is visible in the decreasing offset for larger cantilever lengths and in the decreasing minimum frequency difference at cantilever lengths where f_{HR} and f_{CL1} are nearly equal. The larger the volume, the more the resonance frequencies of the coupled system approach each other. From about 185 Hz minimum frequency difference between f_1 and f_2 for a resonator volume of $V_{\mathrm{cav}} = 33\ \mathrm{cm}^3$, the difference becomes 110 Hz for the resonator with $V_{\mathrm{cav}} = 99\ \mathrm{cm}^3$ and about 55 Hz for the largest resonator. This can be physically explained by the displacement of the moving air mass in the resonator neck and the displacement of the moving cantilever, both of which lead to a volume change in the cavity.

$$\Delta V = \Delta V_{\mathrm{HR}} + \Delta V_{\mathrm{CL}} = -S_{\mathrm{HR}} u_{\mathrm{HR}} - S_{\mathrm{CL}} \bar{u}_{\mathrm{CL}}. \tag{5.1}$$

The relative volume change $\Delta V / V_{\mathrm{cav}}$ is significantly lower for higher cavity volumes V_{cav} and thus leads to a weaker coupling behavior via the acoustic stiffness of the cavity. The mean displacements of the air mass in the neck and cantilever are frequency-dependent. They have their largest amplitudes at their respective resonance frequencies. Therefore, the volume change in the cavity reaches a maximum when both the Helmholtz resonator and the cantilever have the same uncoupled resonance frequency. This effect is visible in a strong coupling behavior at the cantilever length where f_{HR} and f_{CL1} are equal.

For comparison, the calculated results of the resonance frequencies with the simplified equations assuming a constant pressure distribution are plotted as thin lines. The qualitative trend of the resonance frequencies calculated with this assumption is the same as for the resonance frequencies determined with non-uniform pressure in the cavity, but an offset is visible. This offset is more pronounced for resonators with smaller cavity volumes V_{cav} or larger cantilever lengths l. This means that the offset is higher for strongly coupled resonators, where the coupling or the stiffness of the air volume is overestimated in the simplified analytical model. It can be observed that the offset is larger for the higher resonance frequency f_2 than for the lower resonance frequency f_1. This phenomenon shows that the first part of Eq. (3.48), namely $\frac{1}{2}\left(f_{\mathrm{HR}}^2 + f_{\mathrm{CL,V}}^2\right)$, does not accurately represent the mean of f_1^2 and f_2^2. Figs. 5.1 d)-f) show the resonance frequencies of the cantilever f_{CL1} and the cantilever stiffened by the air volume in the cavity $f_{\mathrm{CL,V}}$. The stiffening effect of

the air volume results in higher resonance frequencies $f_{\mathrm{CL,V}}$ and is more pronounced for larger cantilever lengths and smaller resonator cavities. The resonance frequencies plotted as thin lines determined with Eq. (3.41), assuming a constant pressure distribution, are higher than the resonance frequencies calculated with the derived model considering higher-order acoustic modes inside the cavity. The offset is more pronounced the larger the cantilever length l and the smaller the resonator volume V_{cav}. Thus, the calculation of $f_{\mathrm{CL,V}}$ with the simplified model overestimates the stiffening effect of the cavity and leads to too high mean values of f_1^2 and f_2^2.

The simplified model, which assumes that the pressure inside the cavity is constant, provides reasonably accurate results for systems that are weakly coupled. This can be achieved, as shown for the present case, with large cavity volumes or small cantilever lengths. If the resonance frequencies of the coupled system are to be determined with an accuracy of less than 5 %, the coupling parameter C_{HRCL} should be less than 0.07.

However, the accuracy of the results using the simplified model for f_1 and f_2 in Eq. (3.48) can be improved, if the resonance frequencies $f_{\mathrm{CL,V}}$ are calculated analytically with the derived model (Eq. (3.47)) which considers higher-order modes in the cavity for computing $f_{\mathrm{CL,V}}$. This approach is illustrated with symbols in Figs. 5.1 a)-c).

5.1.2. Cantilever width and cavity volume

The influence of the cantilever width and the cavity volume, realized by changing the size of the resonator base area, on the resonance frequencies of the coupled system f_1, f_2 and of the uncoupled Helmholtz resonator f_{HR} and cantilever f_{CL1} is visualized in Figs. 5.2 a)-c). The influence is shown for three cantilever widths $w = 5$ mm, 15 mm and 25 mm and thus different cantilever areas S_{CL}. The resonator base is chosen to have a square shape with equal length L and width W, which is varied in this parameter variation. In Figs. 5.2 d)-f) the resonance frequencies of the cantilever stiffened by the cavity volume $f_{\mathrm{CL,V}}$ are compared with the resonance frequencies of the cantilever in vacuo f_{CL1}. Figs. 5.2 g)-i) show the coupling parameter C_{HRCL}.

A general trend is that f_{HR} decreases with increasing L and W, due to the increasing cavity volume V_{cav}. f_{HR} increases with increasing cantilever width w due to the increasing resonator neck area S_{HR}. Since f_{CL1} is the resonance frequency of the cantilever in vacuo, neither changing the cavity volume nor the cantilever width has any effect, and thus f_{CL1} remains constant. For values of L where f_{CL1} and f_{HR} are equal, the resonance frequencies of the coupled system f_1 and f_2 approach each other to a minimum frequency difference, but do not become equal. The minimum frequency difference depends on the cantilever width and becomes smaller the narrower the cantilever and the smaller the additional

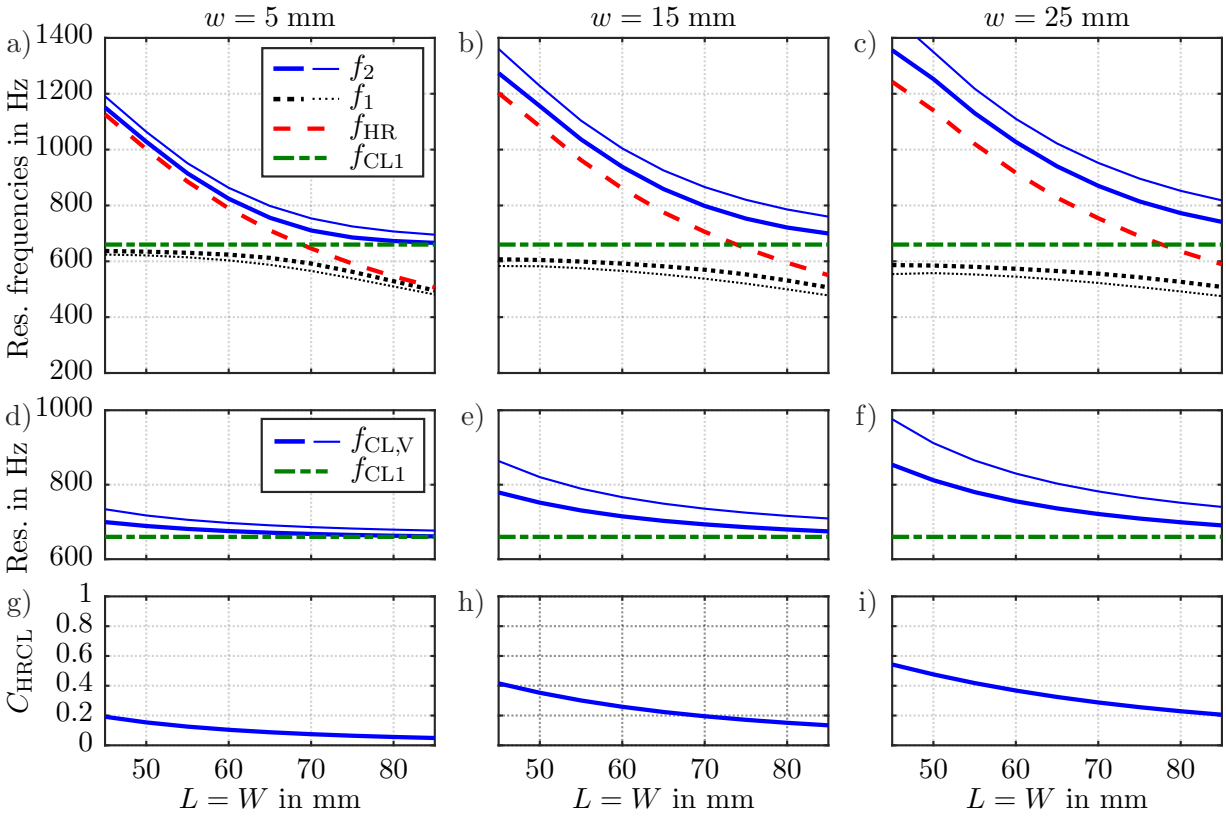

Figure 5.2: a)-f) Calculated resonance frequencies of the resonator system depending on the cavity volume and cantilever width. Bold lines: analytical model, calculation considering higher-order acoustic modes inside the cavity. Thin lines: simplified analytical model using constant pressure distribution. a)-c) Comparison of f_1, f_2, f_{HR} and f_{CL1}. d)-f) Comparison of f_{CL1} and $f_{\mathrm{CL,V}}$. g)-i) Coupling parameter C_{HRCL} depending on the length L and width $W = L$ of the resonator for varying cantilever widths w.

effect of the stiffness of the air volume in the cavity; see Fig. 5.2 a) for the smallest cantilever and Fig. 5.2 c) for the widest cantilever. The effect of the additional stiffness due to the cavity on the resonance frequency of the cantilever is shown in Fig. 5.2 d)-f). The smaller the cavity and the larger the cantilever width, the higher the resonance frequency $f_{\mathrm{CL,V}}$, since the additional stiffness increases.

For smaller and larger resonator edge lengths, f_{HR} and f_{CL1} are far apart and f_1 and f_2 approach the resonance frequencies of the uncoupled system. There is an offset between the resonance frequencies of the coupled and uncoupled systems for larger cantilever areas, which becomes more pronounced as the cantilever becomes wider, as in Figs. 5.2 b)-c). The reason for this is that larger cantilever widths result in a higher coupling strength, since the coupling parameter C_{HRCL} is proportional to the cantilever width w, cf. Eq. (3.44). This effect is also visible in Figs. 5.2 g)-i), where the cantilever width increases from 5 mm in g) over 15 mm in h) to 25 mm in i).

The comparison with the simplified model for constant pressure (thin lines) again shows

that the overall trend can be represented, while the resonance frequencies have an offset to the resonance frequencies calculated with the model considering higher-order acoustic modes inside the cavity. This offset is more pronounced for the higher resonance frequency f_2 and for resonators with wider cantilevers and thus larger cantilever areas. Larger cantilever areas lead to higher coupling strengths, which again shows that the coupling behavior, i.e. the stiffening effect of the cavity, is overestimated in the simplified model. The simplified model gives reasonably accurate results for narrow cantilevers, as can be seen in Fig. 5.2 a).

5.1.3. Cantilever thickness

The influence of the thickness of the top plate t_s, i.e. the length of the resonator neck and the thickness of the cantilever, on the resonance frequencies of the coupled system f_1, f_2 and of the uncoupled Helmholtz resonator f_{HR} and cantilever f_{CL1} is visualized in Fig. 5.3 a). Fig. 5.3 b) shows the influence of the cantilever thickness on the resonance frequency of the cantilever stiffened by the cavity $f_{CL,V}$ compared to f_{CL1}. The coupling parameter C_{HRCL} is shown in Fig. 5.3 c).

The thickness of the top plate varies from 1 mm to 8 mm, while the thickness of all other sidewalls is kept constant at 5 mm, as specified in Table 4.1. The height of the resonator was adjusted to ensure that the cavity volume remained constant throughout this parameter study. The resonance frequency of the cantilever f_{CL1} increases as the thickness of the top plate t_s increases, while the resonance frequency of the Helmholtz resonator

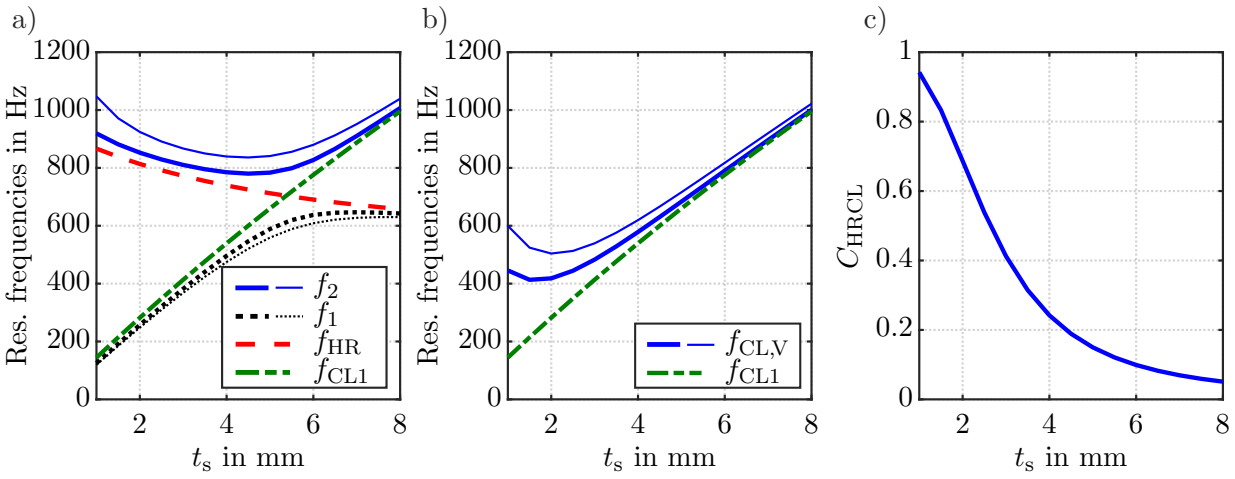

Figure 5.3: a)-b) Calculated resonance frequencies of the resonator system depending on the thickness of the resonator top plate t_s, i.e. the length of the resonator neck. Bold lines: analytical model, calculation considering higher-order acoustic modes inside the cavity. Thin lines: simplified analytical model with constant pressure distribution. a) Comparison of f_1, f_2, f_{HR} and f_{CL1}. b) Comparison of f_{CL1} and $f_{CL,V}$. c) Coupling parameter C_{HRCL} depending on the thickness of the resonator top plate t_s.

f_{HR} decreases. Analogous to the other parameter variations, for the specific thickness of the top plate where f_{CL1} and f_{HR} are equal, f_1 and f_2 approach to a minimum frequency difference but do not become equal due to the high coupling strength. For small and large values of t_{s}, f_{HR} and f_{CL1} are far apart and the resonance frequencies of the coupled system f_1 and f_2 approach those of the uncoupled system. There is no offset between the resonance frequencies of the coupled and uncoupled systems for large values of t_{s}. This behavior can be explained by the coupling parameter, depicted in Fig. 5.3 c): The coupling parameter decreases, as t_{s} increases, which is also evident from Eq. (3.44), because t_{s} is in the denominator of the coupling parameter. Conversely, for thinner cantilevers (smaller values of t_{s}), the coupling parameter increases, resulting in a visible offset for small t_{s} between the resonance frequencies of the coupled and uncoupled system. This inverse relationship arises because the bending stiffness ($E_{\mathrm{CL}}I$), which scales with the cube of the cantilever thickness, increases significantly with t_{s}. A higher bending stiffness reduces the influence of pressure variations within the cavity on the vibration of the cantilever, thus lowering the coupling parameter.

The comparison with the simplified model, plotted as thin lines, again shows an offset, especially for the higher resonance frequency f_2. This offset increases for small values of t_{s}. When the cantilever becomes very thin, its surface mass density $m''_{\mathrm{CL}} = \rho_{\mathrm{CL}} t_{\mathrm{s}}$ is very small and this leads to higher resonance frequencies of the modified cantilever stiffened by the air cavity $f_{\mathrm{CL,V}}$ calculated with the simplified model in Eq. (3.41); as shown in Fig. 5.3 b). This means that the stiffening effect of the cavity on the cantilever is overestimated in the simplified model, leading to an overestimated coupling behavior for thin cantilevers. As explained in Section 5.1.1, the higher value of $f_{\mathrm{CL,V}}$ in the simplified model leads to a shifted mean value of f_1 and f_2 and therefore especially the higher resonance frequency f_2 is overestimated in this case.

5.1.4. Slit width

The influence of the slit width w_{s}, i.e. the width of the resonator neck, on the resonance frequencies f_1, f_2, f_{HR} and f_{CL1} is visualized in Fig. 5.4 a). The influence on the modified cantilever resonance frequency $f_{\mathrm{CL,V}}$ is depicted in Fig. 5.4 b) and the influence on the coupling parameter C_{HRCL} is shown in Fig. 5.4 c). As in the other parameter studies, the resonance frequencies were calculated without considering damping, as the primary focus was on the tuning behavior of the resonance frequencies. However, in Appendix A.3, the same parameter study is conducted with damping included, given that the viscous losses in very narrow slits significantly influence on the resonance frequencies of the uncoupled Helmholtz resonator.

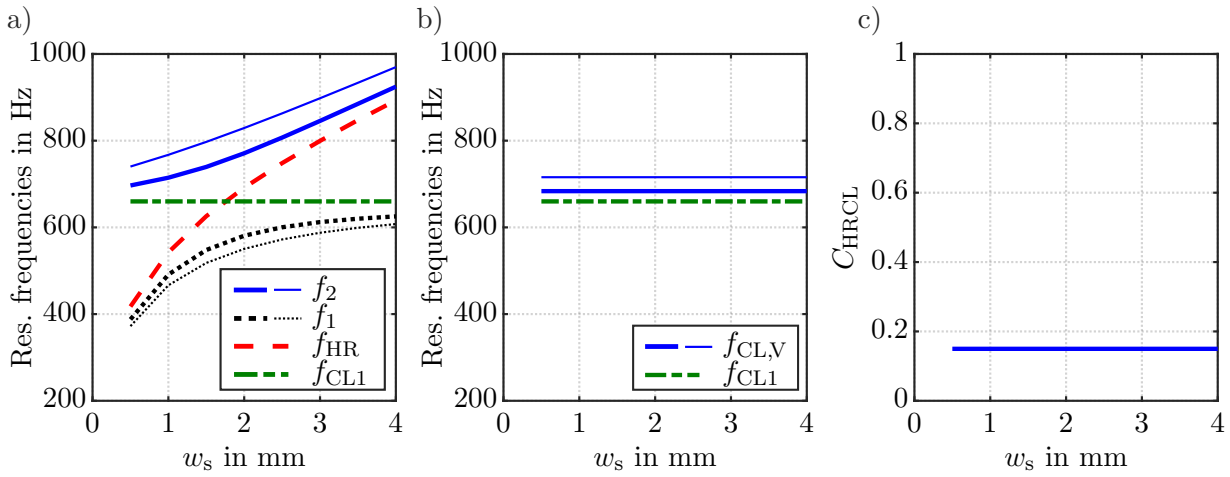

Figure 5.4: a)-b) Calculated resonance frequencies of the resonator system depending on the slit width w_s of the resonator neck. Bold lines: analytical model, calculation considering higher-order acoustic modes inside the cavity. Thin lines: simplified analytical model with constant pressure distribution. a) Comparison of f_1, f_2, f_{HR} and f_{CL1}. b) Comparison of f_{CL1} and $f_{CL,V}$. c) Coupling parameter C_{HRCL} depending on the slit width w_s of the resonator neck.

As the slit width increases, the neck area S_{HR} increases and therefore the resonance frequency of the Helmholtz resonator f_{HR} increases. The resonance frequency of the cantilever in vacuo f_{CL1} is not affected and remains constant. For a slit width where f_{HR} and f_{CL1} are equal, f_1 and f_2 approach to a minimum frequency difference, but do not become equal. This is consistent with earlier explanations that the system is strongly coupled at this resonator geometry. For small and large values of the slit width, the resonance frequencies of the coupled system approach those of the uncoupled system f_{HR} and f_{CL1}, where no offset is visible. This means that the slit width does not affect the coupling behavior between the oscillators. This can also be seen in Figs. 5.4 b) and c), which show that $f_{CL,V}$ and C_{HRCL} are constant and therefore independent of the slit width w_s.

Due to the assumption of the constant pressure distribution in the simplified model (thin lines), the stiffness of the air volume is overestimated, resulting in lower (f_1) and higher (f_2) resonance frequencies of the coupled system and in higher values of $f_{CL,V}$.

5.1.5. Young's modulus

As an example, a material parameter variation is performed for the Young's modulus E_{CL} of the resonator material. The influence of the Young's modulus on the resonance frequencies f_1, f_2, f_{HR} and f_{CL1} is visualized in Fig. 5.5 a). Fig. 5.5 b) shows the influence on $f_{CL,V}$, and Fig. 5.5 c) shows the coupling parameter C_{HRCL}. The resonance frequency of the Helmholtz resonator is not affected by the cantilever material, while the resonance frequency of the cantilever increases with increasing values of E_{CL}, since its bending

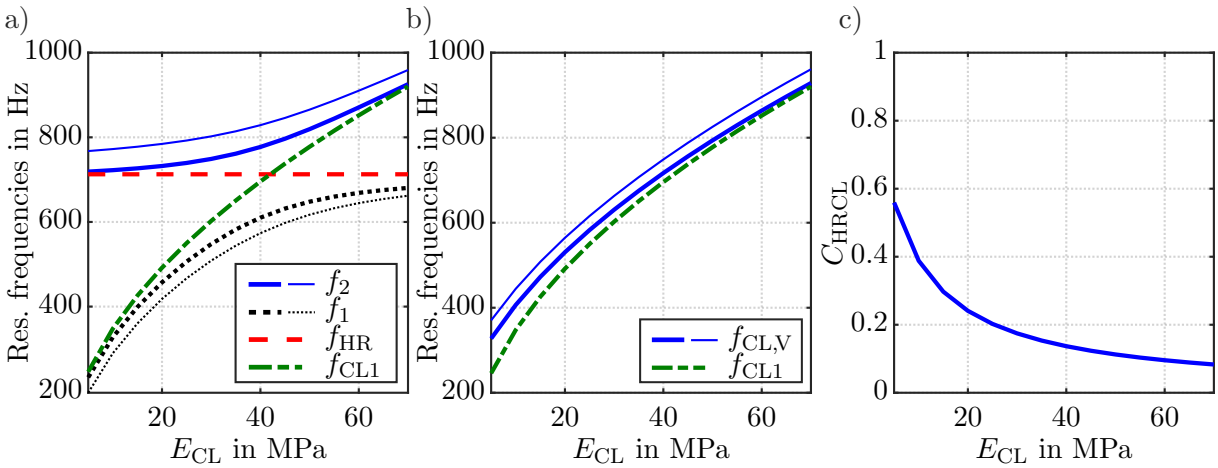

Figure 5.5: a)-b) Calculated resonance frequencies of the resonator system depending on Young's modulus E of the resonator material. Bold lines: analytical model, calculation considering higher-order acoustic modes inside the cavity. Thin lines: simplified analytical model using constant pressure distribution. a) Comparison of f_1, f_2, f_{HR} and f_{CL1}. b) Comparison of f_{CL1} and $f_{CL,V}$. c) Coupling parameter C_{HRCL} depending on Young's modulus E_{CL} of the resonator material.

stiffness increases. For small and large values of E_{CL}, the resonance frequencies of the coupled system f_1 and f_2 approach those of the uncoupled system f_{HR} and f_{CL1}, where no offset is visible. The resonance frequencies of the coupled system f_1 and f_2 approach each other up to a minimum frequency difference for the Young's modulus at which the resonance frequencies of the uncoupled system are equal.

Fig. 5.5 c) illustrates that the coupling parameter decreases as E_{CL} increases. Similar to the effect of cantilever thickness t_s, the young's modulus influences the bending stiffness of the cantilever ($E_{CL}I$). A higher bending stiffness reduces the impact of pressure variations within the cavity on the vibration of the cantilever, thereby decreasing the coupling parameter. This relationship is further illustrated in Fig. 5.5 b), where the stiffening effect of the air cavity diminishes with increasing E_{CL}, i.e. with increasing bending stiffness of the cantilever. Consequently, the difference between $f_{CL,V}$ and f_{CL1} decreases, reflecting the reduced influence of the cavity on the cantilever's dynamic response.

The values of the resonance frequencies of the coupled system calculated with the simplified model are lower for f_1 and higher for f_2, and thus the coupling effect is overestimated; especially, the higher resonance frequency shows large deviations.

5.1.6. Summary

In summary, the main results of the parameter variations are:

- The Helmholtz resonator with integrated cantilever exhibits two resonant modes that are coupled by the cavity acting as a spring.

- The coupling is weak, if the resonance frequencies of the uncoupled Helmholtz resonator and cantilever are substantially different.
- The coupling is strong, if the resonance frequencies of the uncoupled Helmholtz resonator and cantilever are equal or nearly equal.
- The strength of the coupling also depends on the area and mass of the cantilever and the volume of the cavity. The coupling is strong for a large area and/or for small values of the cantilever mass and the cavity volume.
- If the uncoupled systems have the same resonance frequencies, the coupled system exhibits two distinct resonance frequencies that are close to each other.
- The minimum frequency difference between the two resonance frequencies of the coupled system can be reduced by small cantilever areas and large cavity volumes.
- The assumption of a constant pressure distribution in the resonator cavity of the simplified model leads to overestimated coupling conditions, resulting in lower and higher calculated resonance frequencies for f_1 and f_2, respectively.
- The simplified model gives reasonably accurate results for the resonance frequencies when the system is weakly coupled. Weak coupling can be achieved either when the uncoupled frequencies f_{HR} and f_{CL1} are far apart, when the area S_{CL} is very small, e.g. for very narrow cantilevers, when the cavity volume of the resonator is large, or when the thickness or the Young's modulus of the cantilever are large.
- The coupling parameter C_{HRCL} quantifies the coupling strength. The parameter variation shows that the simplified model gives results, with an accuracy of less than 5 % error, when the C_{HRCL} is less than 0.07.
- Calculation of f_1 and f_2 with the simplified model in Eq. (3.48), leads to accurate results if $f_{\mathrm{CL,V}}$ is calculated with the model considering non-uniform pressure inside the cavity. This approach has been shown exemplarily for the variation of the cantilever length l in Figs. 5.1 a)-c) and applies equally to the other parameter variations.
- The resonance frequency of the cantilever f_{CL1} can be tuned without changing the resonance frequency of the Helmholtz resonator f_{HR} by modifying the material parameter, such as the Young's modulus or density. However, the modified resonance frequency of the cantilever f_{CL1} also affects the coupling parameter and thus the coupling behavior of the resonator.

- The slit width w_s can be used to tune the resonance frequency of the Helmholtz resonator f_HR, while neither the resonance frequency of the cantilever f_CL1 nor the coupling behavior is affected. This can be a practical method to tune the coupled resonator system.

The advantage of the analytical model compared to numerical simulations (e.g. using the finite element model used in the verification) is a better physical understanding of the coupling behavior between the Helmholtz resonator and the cantilever. In addition, the CPU time for calculating the resonance frequencies of the coupled system can be greatly reduced with the derived analytical model. For example, to perform the parameter variation of the changing cantilever length, the CPU time of the analytical model was about 500 times less than the CPU time of the finite element simulations for the same parametric study. This higher computational efficiency also makes the analytical model more useful for implementations within optimization loops.

5.2. Absorption coefficient

In this section, parameter variation is performed to study the influence of slit width w_s, cantilever thickness t_s, and cantilever length l on the absorption coefficient of the Helmholtz resonator with integrated cantilever. These geometric parameters were chosen since the slit width and cantilever thickness mainly control the viscous losses inside the neck (see Eq. (3.5)), and the cantilever length has a large influence on the resonance frequencies of both the uncoupled Helmholtz resonator and the cantilever in vacuo.

The absorption coefficient is calculated using the verified and validated model of Section 3.6. The geometric and material data of the resonator were modeled according to Table 4.1, with the dimensions according to Fig. 3.1.

5.2.1. Slit width

The analysis of the influence of the slit width w_s on the absorption coefficient of the Helmholtz resonator with integrated cantilever is performed for three different slit widths ($w_\mathrm{s} = 1$ mm, $w_\mathrm{s} = 2$ mm and $w_\mathrm{s} = 3$ mm) and plotted in Figs. 5.6 a)-c). As an example for this parameter study, the absorption coefficient is evaluated in combination with the input impedance of the resonator Z_res (see Eq. (3.49)) and in combination with the frequency response functions of the fluid volumes displaced by the motion of the fluid volume in the Helmholtz resonator neck $S_\mathrm{HR}u_\mathrm{HR}$ and by the cantilever motion $S_\mathrm{CL}u_\mathrm{CL}$. The real and imaginary parts of the normalized input impedance $Z_\mathrm{res}/(\rho_0 c_0)$ are plotted in Figs. 5.6 d)-f) and Figs. 5.6 g)-i), respectively. The frequency response functions are plotted for the

amplitudes and phase angles of the displaced volumes in Figs. 5.6 j)-l) and Figs. 5.6 m)-o), respectively.

In Figs. 5.6 a)-c) it can be seen that the maximum absorption of the Helmholtz resonator (dashed blue curves) decreases with increasing slit width and that the resonance frequency is shifted to higher values, as the area of the neck increases. 100 % sound absorption is achieved when the impedance is perfectly matched to the characteristic impedance of the surrounding fluid. In this case, the real part of the normalized impedance is unity and the imaginary part is zero. This is the case for the Helmholtz resonator with a slit width of $w_\mathrm{s} = 1$ mm, as evident from Fig. 5.6 d) for the real part and from Fig. 5.6 g) for the imaginary part of the normalized impedance. At about 520 Hz, the imaginary part is zero, while the real part is 1 ($\mathrm{Re}(Z_\mathrm{res})/(\rho_0 c_0) = 1$) and the Helmholtz resonator has an absorption coefficient of 1. At the resonance frequency, the amplitude of the fluid volume displaced by the fluid in the Helmholtz resonator neck ($S_\mathrm{HR} u_\mathrm{HR}$) exhibits a maximum, while a phase change occurs ($\Phi = \pi/2$), as visible from the dashed blue lines in Figs. 5.6 j) and m), respectively. For the resonators with wider slits ($w_\mathrm{s} = 2$ mm and $w_\mathrm{s} = 3$ mm) the real part of the impedance is less than 1 over the whole frequency range of interest, combined with reduced absorption maxima. This shows that, in addition to tuning the resonance frequency of the Helmholtz resonator, the slit width can also be used to tune the real part of the resonator input impedance in order to match it with the characteristic impedance of the fluid.

The red curves describe the behavior of the Helmholtz resonator with integrated cantilever, while in Figs. 5.6 j)-o) the frequency response functions are visualized separately for each degree of freedom: The fluid volume displaced by the cantilever is plotted as dotted red curves and the fluid volume displaced by the Helmholtz resonator is plotted as solid red curves.

In general, the Helmholtz resonator with integrated cantilever exhibits two resonances with high absorption, while the absorption coefficient decreases between the resonance frequencies. For the Helmholtz resonator with integrated cantilever, the imaginary part of the input impedance (see the red solid lines in Figs. 5.6 g)-i)) crosses the x-axis, i.e. $\mathrm{Im}(Z_\mathrm{res}) = 0$, three times. The first and third frequencies at which $\mathrm{Im}(Z_\mathrm{res}) = 0$ correspond to the resonance frequencies f_1 and f_2 of the coupled resonator and to the absorption maxima with the magnitude of the absorption coefficient depending on the real part of the impedance. At these resonance frequencies, both degrees of freedom exhibit a phase change ($\Phi = \pi/2$), while the displacement amplitudes experience a local maximum, as visible in Figs. 5.6 m)-o) and Figs. 5.6 j)-l), respectively.

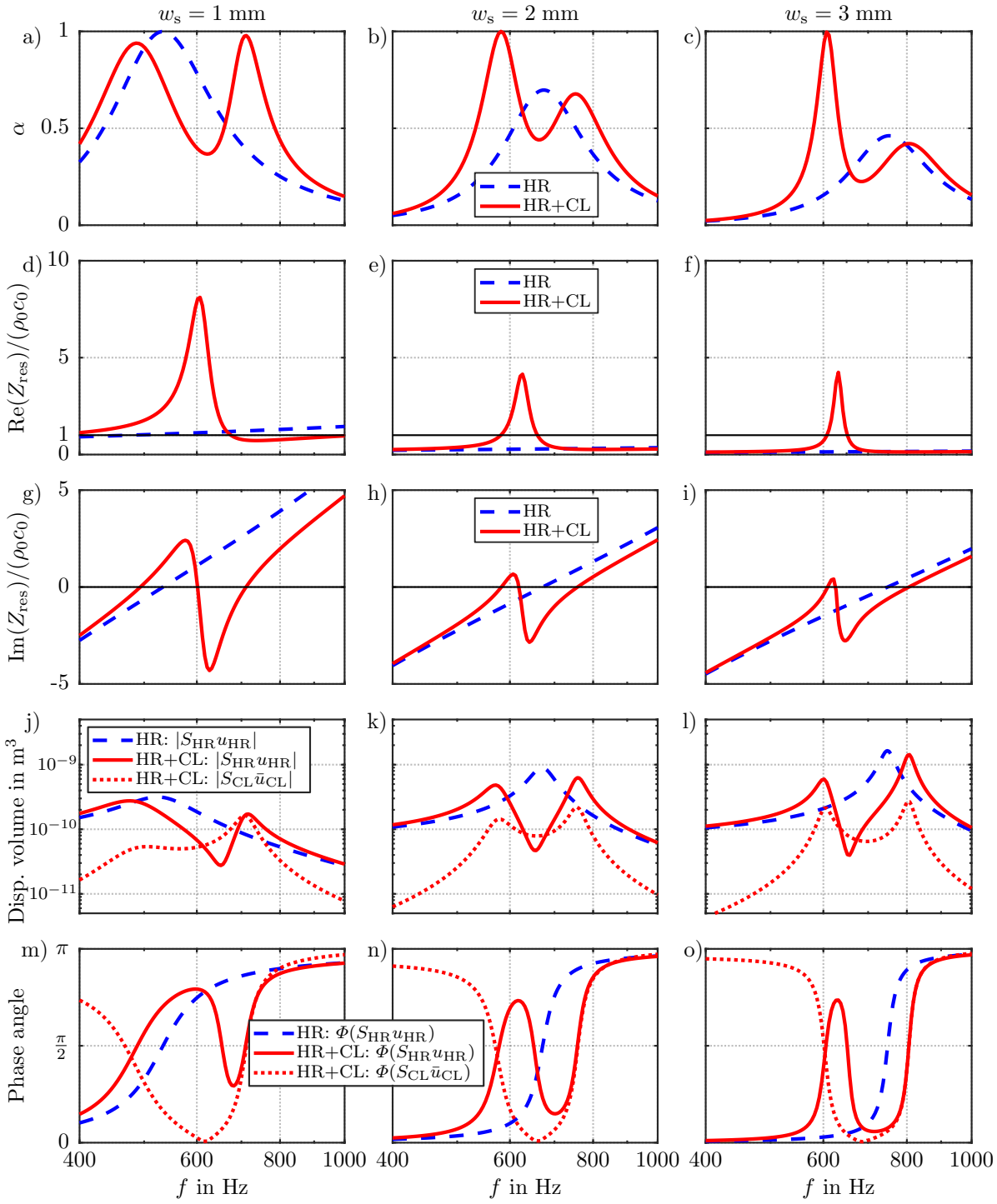

Figure 5.6: Absorption coefficient, input impedance and frequency response function evaluated for the resonator design for three different slit widths ($w_s = 1$ mm, $w_s = 2$ mm and $w_s = 3$ mm). a)-c) Absorption coefficient. d)-f) Real part of the dimensionless input impedance. g)-i) Imaginary part of the dimensionless input impedance. j)-l) Amplitude of the displaced volume. m)-o) Phase angle of the displaced volume.

At the second frequency, where $\mathrm{Im}(Z_{\mathrm{res}}) = 0$, the real part of the input impedance is greatly increased, as shown in Figs. 5.6 d)-f). If the real part of the input impedance is greater than one, the resonator is highly damped, resulting in poorer impedance matching to the incident sound wave and in a reduction in the absorption coefficient, as visible in Figs. 5.6 a)-c). The high damping behavior of the resonator, can be explained by the frequency response functions in Figs. 5.6 j)-o). At this frequency, the magnitude of the fluid volumes displaced by the motion of the cantilever and of the fluid motion in the Helmholtz resonator neck are equal $|S_{\mathrm{CL}}\bar{u}_{\mathrm{CL}}| = |S_{\mathrm{HR}}u_{\mathrm{HR}}|$, while the cantilever and Helmholtz resonator move in opposite directions, as evident from the phase angles.

With increasing frequencies, the real part of the impedance decreases again and is ideally matched ($\mathrm{Re}(Z_{\mathrm{res}})/(\rho_0 c_0) = 1$) at about 655 Hz for all three resonator designs, while the imaginary part is negative and therefore not matched. As discussed in Section 4.2.1, at this frequency, the cantilever acts as a tuned mass damper in the coupled system. The tuned mass damper (cantilever) leads to a reduced amplitude and a phase change of the other degree of freedom, i.e. in the present case the motion of the fluid volume in the Helmholtz resonator neck (solid red lines in Figs. 5.6 j)-o). This results in a reduced absorption coefficient. The exact frequency at which $\mathrm{Re}(Z_{\mathrm{res}})/(\rho_0 c_0) = 1$ depends on the damping behavior of the system and would be $\omega_{\mathrm{CL,V}}$ if the system had no damping.

The integration of the cantilever results in an increased damping behavior of the resonator, which can improve the impedance matching at certain frequencies. This can be observed in Fig. 5.6 b) for a resonator with a slit width of $w_{\mathrm{s}} = 2$ mm, where two resonance frequencies with high absorption are visible. In addition, the frequency range of high absorption can be broadened. The magnitude of the absorption coefficient at the local minimum depends on the damping of the coupled system, as well as on the frequency difference of the resonance frequencies of the coupled system f_1 and f_2. For the resonator configurations shown, the frequency difference is smallest for the resonator with the slit width of 2 mm in Fig. 5.6 b) and correspondingly the reduction of the absorption coefficient between the two peaks is smallest.

Fig. 5.7 shows the effect of varying the slit width from 0.5 mm to 5 mm, where high absorption is indicated by yellow areas and low absorption is indicated by blue areas. The black lines indicate the resonance frequencies of the coupled resonator system f_1 and f_2. For small slit widths (from 0.5 to about 2 mm), where high attenuation occurs due to viscous losses in the resonator neck, two frequency regions of high absorption can be obtained. The local minimum of the absorption coefficient becomes less pronounced as the frequency difference between the two resonance frequencies becomes smaller. In the eigenfrequency study, this was found to be at the slit width where f_{HR} and f_{CL} are equal. For slits wider than 2 mm, the absorption coefficient decreases at the higher resonance

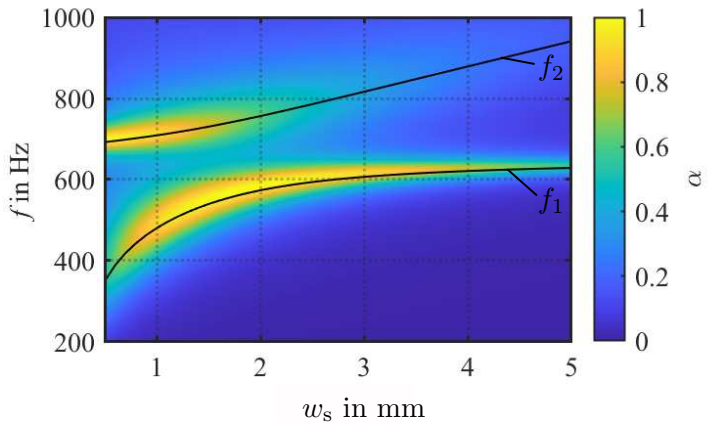

Figure 5.7: Parameter study for the absorption coefficient α with a variation of the slit width w_s from $w_s = 0.5$ mm to 5 mm (other dimensions according to Table 4.1). The black lines indicate the resonance frequencies of the coupled resonator system f_1 and f_2.

frequency f_2, which is close to the resonance frequency of the Helmholtz resonator. On the other hand, at the lower resonance frequency f_1, which is close to the cantilever resonance frequency, the absorption coefficient becomes very narrow-banded with peak values still above 0.5.

5.2.2. Cantilever thickness

In Fig. 5.8 a), the influence of the cantilever thickness, i.e. the slit length t_s, on the absorption coefficient is shown for three different values ($t_s = 5$ mm, $t_s = 6$ mm and $t_s = 7$ mm). It can be observed that the absorption behavior of the resonators with a cantilever thickness of 6 and 7 mm, represented by the dashed blue and solid red lines, respectively, is approximately the same in the low-frequency range up to 700 Hz. As evident from the eigenfrequency analysis in Fig. 5.3, for the resonator designs with $t_s = 6$ mm and $t_s = 7$ mm, the lower resonance frequency is dominated by the resonance frequency of the Helmholtz resonator and coupling effects. This is reflected in Fig. 5.3, where the lower resonance frequency f_1 (dotted black line) approaches the resonance frequency of the uncoupled Helmholtz resonator f_{HR} (dashed red line). In the higher frequency range, however, the absorption behavior is significantly different, because the second resonance frequency is dominated by the resonance frequency of the cantilever. The resonator with a thicker cantilever ($t_s = 7$ mm) exhibits the second resonance at higher frequencies, leading to a more pronounced drop in the absorption coefficient between the two resonances.

In Fig. 5.8 b), a parameter variation of the cantilever thickness is performed for cantilever thicknesses between 1 and 8 mm. The two black lines represent the resonance frequencies of the coupled system f_1 and f_2. While the sound absorption at the second

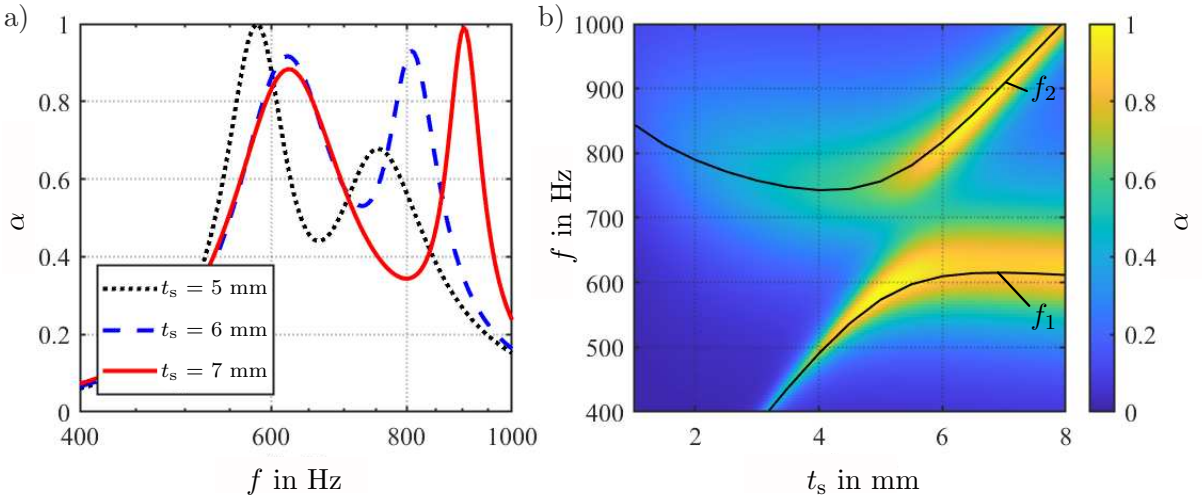

Figure 5.8: Parameter study for the absorption coefficient α with a variation of the cantilever thickness t_s (other dimensions constant according to Table 4.1). a) Absorption coefficient spectrum for three different cantilever thicknesses ($t_\mathrm{s} = 5$ mm, $t_\mathrm{s} = 6$ mm and $t_\mathrm{s} = 7$ mm). b) Absorption coefficient for a cantilever thickness variation from $t_\mathrm{s} = 1$ mm to 8 mm. The black lines indicate the resonance frequencies of the coupled resonator system f_1 and f_2.

resonance frequency is very low for thin cantilevers ($t_\mathrm{s} \leq 4$ mm), two frequency ranges of high absorption can be obtained for cantilevers thicker than 5 mm. The cantilever thickness, i.e. the slit length, determines the viscous losses in the neck, and longer slits lead to a more damped behavior of the resonator. To maximize the absorption coefficient at the local minimum, the resonance frequencies of the coupled system f_1 and f_2 should be close to each other. This is realized by cantilever thicknesses of about 5.5 mm to 6 mm, with $\alpha \geq 0.5$ in a broadband frequency range. For longer slits, the resonance frequencies drift further apart, resulting in a reduced value of α between the two resonance frequencies. For cantilevers thicker than 5 mm, the absorption coefficient is greater than 0.5 in a frequency band of about 150 Hz at the first resonance frequency f_1, which is close to the resonance frequency of the Helmholtz resonator, while the absorption is narrow-band at the second resonance frequency f_2, which is close to the resonance frequency of the cantilever.

5.2.3. Cantilever length

The influence of the cantilever length on the absorption coefficient is shown for three different cantilever lengths ($l = 30$ mm, $l = 32$ mm and $l = 34$ mm) in Fig. 5.9 a). The figure shows that for the resonator with a cantilever length of $l = 32$ mm (dashed blue line) the absorption coefficient at the local minimum between the peaks is reduced the least. On the one hand, this is due to a good impedance matching, which is not shown for this parameter variation. On the other hand, the frequency difference between the resonance frequencies f_1 and f_2 is the smallest for this resonator design, resulting in higher values

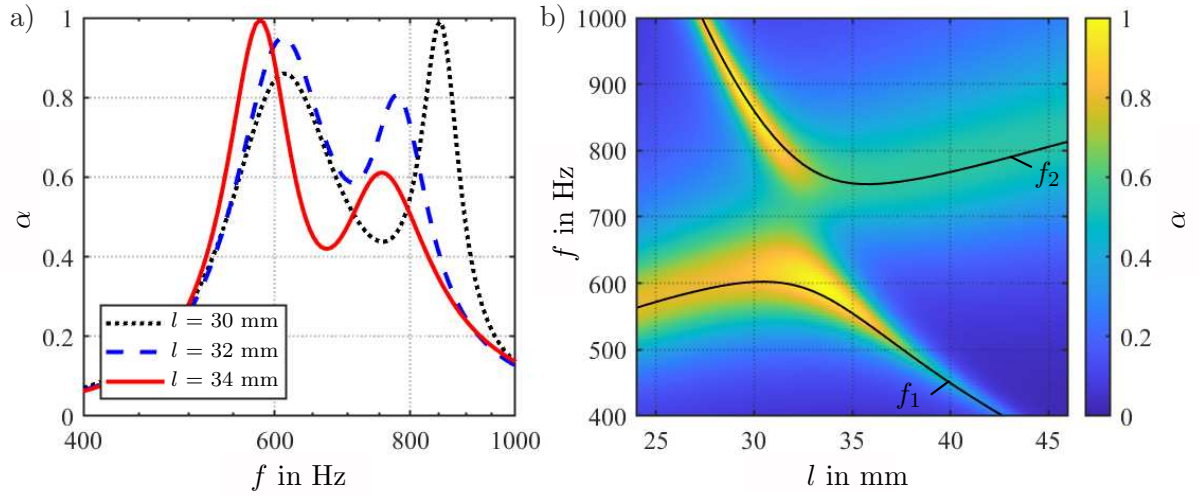

Figure 5.9: Parameter study for the absorption coefficient α with a variation of the cantilever length l (other dimensions constant according to Table 4.1). a) Absorption coefficient spectrum for three different cantilever lengths ($l = 30$ mm, $l = 33$ mm and $l = 36$ mm). b) Absorption coefficient for a cantilever length variation from $l = 24$ mm to 46 mm. The black lines indicate the resonance frequencies of the coupled resonator system f_1 and f_2.

of the absorption coefficient at the local minimum.

Fig. 5.9 b) shows the parameter variation for cantilever lengths from 24 mm to 46 mm. The black lines indicate the resonance frequencies of the coupled resonator system f_1 and f_2. For cantilever lengths less than 33 mm, two absorption peaks higher than 0.7 can be achieved. A broadband absorption behavior with $\alpha \geq 0.4$ is observed for cantilever lengths between 30 and 35 mm. For larger cantilevers, the absorption coefficient at the higher resonance frequency, which is attributed to the Helmholtz resonator resonance frequency, is greater than 0.5 in a frequency band of about 120 Hz. The absorption coefficient at the lower resonance frequency, which is attributed to the cantilever, becomes very narrow-banded for cantilevers longer than 37 mm.

5.2.4. Summary

The main findings of the parameter variations on the absorption behavior of the Helmholtz resonator with integrated cantilever are:

- The absorption behavior is determined by the viscous losses in the neck, which depend on the ratio of the slit length to slit width. The damping behavior decreases for short slits and for wide slits resulting in low values of the absorption coefficient. In return, the damping behavior increases for long and narrow slits.

- The absorption behavior can be broadened, if the input impedance is well matched to the impedance of the surrounding fluid and if the resonance frequencies of the

coupled system are close to each other, which is the case, if the resonance frequencies of the Helmholtz resonator f_{HR} and of the cantilever f_{CL1} are equal or nearly equal. The slit width w_{s} is an effective geometric parameter to obtain both. With the slit width, the resonance frequency of the Helmholtz resonator can be tuned independently from the resonance frequency of the cantilever, without changing the coupling behavior. In addition, the slit width has a large influence on the viscous losses in the neck and can thus be used to achieve impedance matching at the resonance frequencies.

- If the resonance frequencies of the coupled system are further apart and approach those of the uncoupled system, the absorption behavior at the resonance frequency corresponding to the cantilever is narrow-band, while the absorption behavior at the resonance frequency corresponding to the Helmholtz resonator is broadband. Two high absorption maxima can still be observed, if the resonance frequency of the cantilever is higher than the resonance frequency of the Helmholtz resonator for the specific configuration.

5.3. Transmission loss

In this section, the parameter variation is performed to study the influence of geometric parameters on the transmission loss of the resonator. The study is carried out again exemplarily for the cantilever length l, the cantilever thickness t_{s}, the slit width w_{s} and the cantilever width w. The transmission loss is calculated for normal incidence sound using the verified and validated model from Section 3.7, where the resonator is positioned inside the tube, such that the resonator opening is parallel to the sound direction. The geometric and material data of the resonator were modeled according to Table 4.1, with the dimensions according to Fig. 3.1.

5.3.1. Cantilever length

The influence of the cantilever length l on the transmission loss of the Helmholtz resonator with integrated cantilever is shown for three different cantilever lengths ($l = 28$ mm, $l = 32$ mm and $l = 36$ mm) and plotted in Fig. 5.10 a). At a cantilever length of 32 mm (dashed blue line), the magnitudes of the two transmission loss maxima are nearly equal. This configuration optimally uses the potential of Helmholtz resonators with integrated cantilevers, i.e. having two regions with high sound transmission loss. The other two resonator designs, on the other hand, have unbalanced transmission loss maxima. One of the

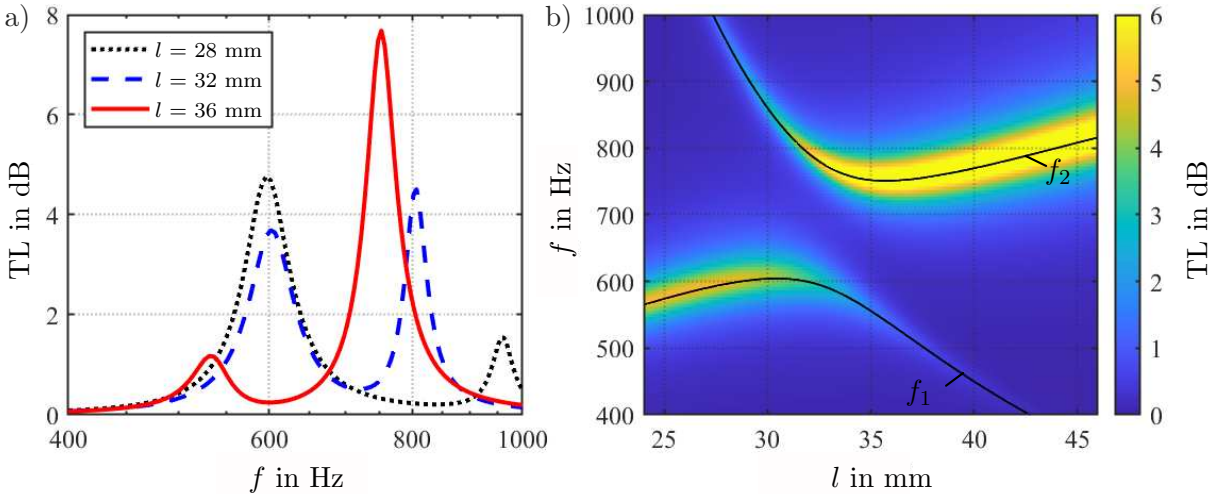

Figure 5.10: Parameter study for the transmission loss TL with a variation of the cantilever length l (other dimensions constant according to Table 4.1). a) Transmission loss spectrum for three different cantilever lengths (l = 28 mm, l = 32 mm and l = 36 mm). b) Transmission loss for a cantilever length variation from l = 24 mm to 46 mm. The black lines indicate the resonance frequencies of the coupled resonator system f_1 and f_2.

two peaks is smaller than the other and can almost be neglected in comparison. The balanced case of transmission loss occurs when the resonance frequencies f_1 and f_2 are highly coupled, as shown in Fig. 5.10 b). The figure shows the parameter variation for a changing cantilever length from 24 mm to 46 mm and examines the influence on the transmission loss. The black lines represent the resonance frequencies of the coupled system f_1 and f_2. High transmission loss is marked in yellow, while all transmission loss values greater than 6 dB are plotted in yellow. The color bar is not extended to higher transmission loss values to improve the contrast for transmission loss values between 3 and 6 dB. Blue areas indicate a low transmission loss of zero or close to zero. The figure shows, that two regions of high transmission loss can be obtained when the cantilever has a length between approximately 30 to 34 mm. For these cantilever lengths, the resonator system exhibits strong coupling, resulting in resonance frequencies that do not match those of either the cantilever or the Helmholtz resonator. For cantilevers shorter than 30 mm, a broadband and high transmission loss is observed at the lower resonance frequency f_1, which is close to the resonance frequency of the Helmholtz resonator. Whereas the transmission loss at the higher resonance frequency f_2 is narrow-band with a maximum value of about 3 dB. For cantilevers longer than 35 mm, the second resonance frequency f_2 is close to the resonance frequency of the Helmholtz resonator and high transmission loss behavior can be achieved, while the transmission loss at the lower resonance frequency, approaching f_{CL1}, decreases.

5.3.2. Cantilever thickness

The influence of the cantilever thickness, i.e. the slit length t_s, on the transmission loss is shown for three different values ($t_s = 4.5$ mm, $t_s = 6$ mm and $t_s = 7.5$ mm) in Fig. 5.11 a). Like the variation of the cantilever length, Fig. 5.11 a) shows one specific resonator design ($t_s = 6$ mm; dashed blue line) with two transmission loss maxima having nearly the same magnitude. While the transmission loss of the other two resonator designs shown is unbalanced with one large and one small peak. To obtain two balanced transmission loss peaks, the resonator should be designed so that the resonance frequencies of the uncoupled Helmholtz resonator f_{HR} and the cantilever in vacuo f_{CL1} are nearly equal, resulting in two coupled resonance frequencies close to each other. The comparison of the transmission loss values between the resonator with a 6 mm thick cantilever (dashed blue line) and with a 7.5 mm thick cantilever (solid red line) shows that the transmission loss at the lower resonance frequency does not differ much in these cases. However, the thicker cantilever ($t_s = 7.5$ mm) leads to a higher second resonance frequency of the coupled system with a much lower transmission loss value than the 6 mm thick cantilever.

Fig. 5.11 b) shows the parameter variation of the cantilever thickness for thicknesses between 1 mm and 8 mm. The figure shows that the transmission loss of Helmholtz resonators with integrated cantilevers increases with decreasing cantilever thickness. The thinner the cantilever and hence the shorter the slit length, the lower the viscous losses in the neck R_{HR}, which are proportional to the ratio of slit length to slit width (t_s/w_s), as indicated in Eq. (3.5). The higher the impedance mismatch to the surrounding fluid, the

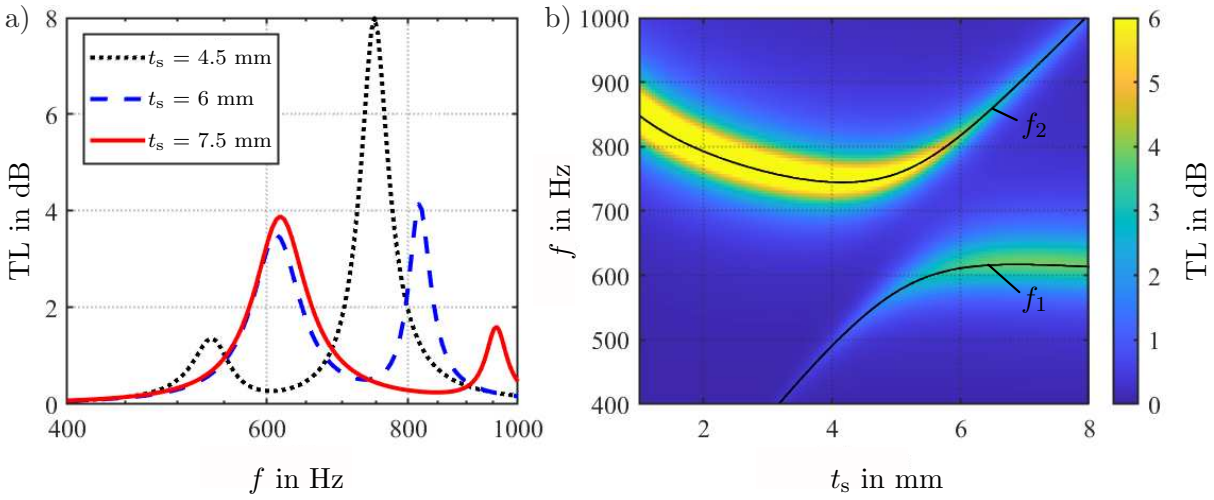

Figure 5.11: Parameter study for the transmission loss TL with a variation of the cantilever thickness t_s (other dimensions constant according to Table 4.1). a) Transmission loss spectrum for three different cantilever thicknesses ($t_s = 4.5$ mm, $t_s = 6$ mm and $t_s = 7.5$ mm). b) Transmission loss for a cantilever thickness variation from $t_s = 1$ mm to 8 mm. The black lines indicate the resonance frequencies of the coupled resonator system f_1 and f_2.

higher the transmission loss of a resonator. An impedance mismatch leads to reflection of the incoming sound wave and thus to low sound transmission, combined with correspondingly high transmission loss values. As the viscous losses in the neck increase, as is the case with resonators of increasing neck length, the impedance mismatch is reduced, resulting in lower transmission loss values.

For cantilever thicknesses less than 4 mm, the transmission loss behavior is most pronounced at the second resonance frequency f_2, corresponding approximately to f_{HR}, and nearly vanishes at the first resonance frequency f_1. For cantilevers thicker than 6 mm, the first resonance frequency f_1 corresponds approximately to the resonance frequency of the Helmholtz resonator and shows a higher and more broadband transmission loss behavior as the second resonance frequency f_2, where the transmission loss behavior is narrow-band and has a maximum value of about 2 dB. For cantilevers with a thickness of about 6 mm, two frequencies with high transmission loss can be obtained. In this case, the resonance frequency of the uncoupled Helmholtz resonator f_{HR} and the cantilever in vacuo f_{CL1} are nearly the same, resulting in two resonance frequencies of the coupled system that are close to each other and do not correspond to either f_{HR} or f_{CL1}.

5.3.3. Slit width

The analysis of the influence of the slit width w_{s} on the transmission loss of the Helmholtz resonator with integrated cantilever is performed for three different slit widths ($w_{\mathrm{s}} = 1\,\mathrm{mm}$, $w_{\mathrm{s}} = 2\,\mathrm{mm}$ and $w_{\mathrm{s}} = 3\,\mathrm{mm}$) and plotted in Fig. 5.12 a). The figure shows that the value of the transmission loss of the resonator depends on the damping behavior. Overall, the transmission loss of the resonator with a 1 mm wide slit is lower than the transmission loss of the resonators with wider slits ($w_{\mathrm{s}} = 2\,\mathrm{mm}$ and $w_{\mathrm{s}} = 3\,\mathrm{mm}$). As explained above, viscous losses depend on the ratio of slit length to slit width ($t_{\mathrm{s}}/w_{\mathrm{s}}$) and increase with decreasing slit width. An increased damping behavior leads to a reduced impedance mismatch between the resonator and the surrounding fluid and thus to lower values of the transmission loss. For the resonator designs shown here, the resonator with a slit width of 2 mm exhibits two resonance frequencies with transmission losses above 2 dB, while the transmission loss at the first resonance frequency is lower than at the second.

Fig. 5.12 b) shows a parameter variation of the slit width between 0.5 mm and 5 mm. This figure also reveals that the transmission loss at the second resonance frequency is higher for all slit widths shown. For the lower resonance frequency, the highest values are obtained with slit widths between 1 and 3 mm. This is the region where the system is highly coupled and the resonance frequencies of the coupled system do not approach those

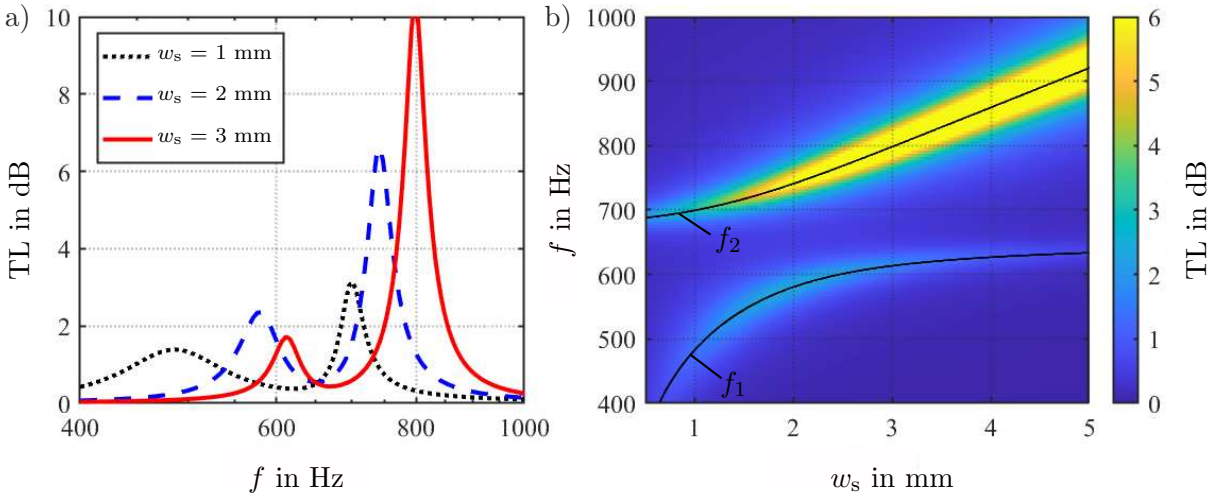

Figure 5.12: Parameter study for the transmission loss TL with a variation of the slit width w_s (other dimensions constant according to Table 4.1). a) Transmission loss spectrum for three different slit widths ($w_s = 1$ mm, $w_s = 2$ mm and $w_s = 3$ mm). b) Transmission loss for a slit width variation from $w_s = 0.5$ mm to 5 mm. The black lines indicate the resonance frequencies of the coupled resonator system f_1 and f_2.

of the uncoupled Helmholtz resonator or the cantilever in vacuo. The figure illustrates that a Helmholtz resonator with integrated cantilever should be designed differently than the design chosen for this parameter variation, where f_{HR} and f_{CL1} are nearly equal when the slit width is approximately $w_s \approx 1.8$ mm. To obtain high transmission loss at both resonance frequencies, the slit width, for which f_{HR} and f_{CL1} are nearly equal, should be larger to reduce the damping behavior of the resonator and thus increase the transmission loss potential. The effect of less damped resonators is also clearly visible in this figure, as the transmission loss around the second resonance frequency becomes more broadband and higher in magnitude with decreasing damping effect due to increasing slit width.

5.3.4. Cantilever width

The influence of the cantilever width w on the transmission loss of the Helmholtz resonator with integrated cantilever is depicted in Fig. 5.13 a) for three different widths ($w = 2$ mm, $w = 5$ mm and $w = 10$ mm). It can be seen that the resonance frequencies of the coupled system f_1 and f_2 drift further apart with increasing cantilever width. Furthermore, the decrease in transmission loss between f_1 and f_2 is more pronounced the wider the cantilever and the larger the frequency difference between f_1 and f_2. For this parameter variation, the influence of the coupling behavior is clearly visible: The coupling parameter (see Eq. (3.44)) is proportional to the cantilever width. And as explained earlier, a lower coupling parameter results in a smaller distance between f_1 and f_2 and a smaller reduction in transmission loss between the resonance frequencies. The influence is also visible

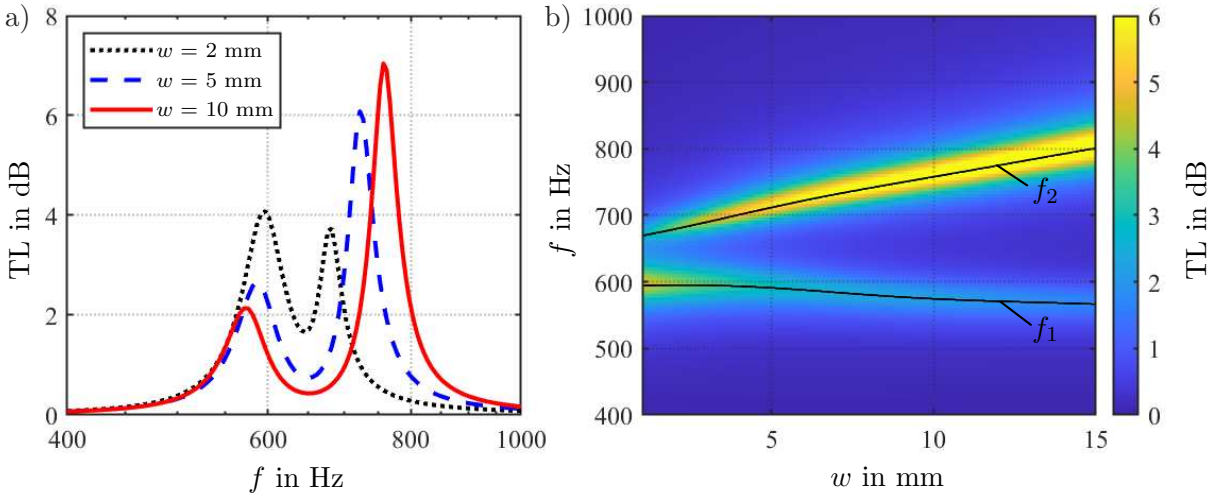

Figure 5.13: Parameter study for the transmission loss TL for a variation of the cantilever width w (other dimensions constant according to Table 4.1). a) Transmission loss spectrum for three different cantilever widths ($w = 2$ mm, $w = 5$ mm and $w = 10$ mm). b) Transmission loss for a cantilever width variation from $w = 1$ mm to 15 mm. The black lines indicate the resonance frequencies of the coupled resonator system f_1 and f_2.

in Fig. 5.13 b), where the parameter variation has been performed for cantilever widths between 1 mm and 15 mm. With increasing cantilever width, the resonance frequencies f_1 and f_2 (black solid lines) drift further apart, leading to a more pronounced decrease in transmission loss between the resonance frequencies, marked by the dark blue areas. The parameter variation indicates that the cantilever width should be smaller than the 10 mm (used in the other parameter variations) to reduce the coupling parameter and obtain a high transmission loss between the two resonance frequencies.

5.3.5. Summary

The main results of the parameter variation studying the transmission loss of Helmholtz resonators with integrated cantilevers are as follows:

- High viscous losses in the Helmholtz resonator neck, which occur with thick cantilevers or narrow slits, adversely affect the transmission loss behavior.
- If the resonator system is weakly coupled and the resonance frequency of the cantilever in vacuo f_{CL1} is lower than the resonance frequency of the Helmholtz resonator f_{HR}, the transmission loss becomes very low at the lower resonance frequency.
- Low values of the coupling parameter, as they occur for narrow cantilevers, lead to higher values of the local minimum between the two resonance frequencies. This behavior of the resonator is favorable for increasing the sound transmission loss in a broadband frequency range.

6. Resonator design for an aircraft-like functional model

One possible application of Helmholtz resonators with integrated cantilevers is the implementation of the resonators inside an aircraft sidewall. This chapter begins with a description of a conventional aircraft sidewall and the requirements for noise control means to be installed inside an aircraft sidewall. Secondly, the cost function for an optimal design of the resonators adapted to the aircraft application is derived and an optimization algorithm is performed numerically. The functional model is described in the third section, followed by transmission loss measurements with the functional model in a laboratory test setup with aircraft-representative wall masses and spacings. The chapter concludes with the experimental tuning of the resonance frequencies of the resonator panel. Parts of this chapter have been published in Ref. [58].

6.1. Aircraft sidewall specification

The specification of the aircraft sidewall depends on the aircraft type. In this study, the requirements are taken from a short-haul aircraft. The conventional aircraft sidewall can be considered acoustically as a double wall. It consists of the inner cabin lining and the outer fuselage skin, stiffened by frames and stringers. Typically, two insulation blankets are embedded between the two walls. The insulation blankets are named after their locations: The primary insulation is attached to the stiffened fuselage skin, which is the primary structure of the aircraft. Similarly, the secondary insulation is attached to the back of the cabin lining, also referred to as the secondary structure. For a typical short-haul aircraft, the fuselage structure has an average surface mass density m''_{fus} between 4.35 kg/m^2 and 6.25 kg/m^2 [113]. In the literature, the surface mass density of the cabin lining m''_{lin} varies between 1.61 kg/m^2 [116] and 1.76 kg/m^2 [113]. Normally, the two insulation blankets consisting of glass wool have a thickness of 2 inch [94], if the glass wool is in its original state. After integration, the thickness of the insulation layer H_{GW} is compressed to about 35 to 40 mm due to wrapping with a cover sheet and installation conditions inside the aircraft[139]. The surface mass density of the insulation layer m''_{GW} including the cover

sheet lies approximately between 0.35 kg/m^2 and 0.47 kg/m^2 [41]. The distance between the primary and secondary structure, hereafter called the wall spacing H_{DW}, typically is about 100 mm [113]. The objective of this study is to implement new means of noise control within the actual aircraft sidewall. The total surface mass density of the aircraft sidewall should not be significantly increased. In a research project with an aircraft manufacturer [52], it was found that the noise control means can be implemented inside the secondary insulation blanket or replace the secondary insulation blanket, resulting in a maximum height of $H_{\mathrm{GW}} = 35$ mm and a maximum surface mass density of 0.46 kg/m^2 for the noise control means including the secondary insulation. The thermal requirements of the insulation blankets inside the aircraft sidewall and the question whether the thermal comfort of the passengers can be ensured with a reduced number of insulation blankets are beyond the scope of this work. It was partly answered in combination with further requirements for new noise control means in Ref. [52]. To maximize the effect of the embedded resonators on the transmission loss improvement of the double wall, the resonator cavities should take as much space of the double wall spacing as possible [81], meaning that the filling ratio is maximized. For this reason, the resonators are installed so that they cover the entire back wall of the lining panel, and replace the secondary insulation layer, as also illustrated in Fig. 4.14 a) for the single wall and Fig. 4.17 for the double wall.

In this study, the following values and components were defined for a representative aircraft sidewall, hereafter referred to as the reference double wall (ref. DW):

- Surface mass density of the primary structure/outer fuselage skin: $m''_{\mathrm{fus}} = 5.5$ kg/m^2, represented in the experiments by a 8 mm thick medium-density fiberboard (MDF) with the material data given in Table 4.5.
- Surface mass density of the secondary structure/cabin lining, $m''_{\mathrm{lin}} = 1.6$ kg/m^2, embodied in the experiments by a 0.8 mm thick glass fiber reinforced plastic (GFRP) plate with the material data given in Table 4.4.
- Primary insulation layer: thickness $H_{\mathrm{GW}} = 35$ mm, surface mass density $m''_{\mathrm{GW}} = 0.35$ kg/m^2, embodied in the experiments by two layers of aircraft-certified glass wool (MICROLITE ®AA Premium by Johns Manville [62]) wrapped in 15 µm Tirul 18 foil [64], with the material data given in Table 4.6.
- The secondary insulation layer is replaced by the resonator panel and not considered in the mass-equivalent reference double wall.
- Wall spacing $H_{\mathrm{DW}} = 100$ mm.

The reference double wall, used in this study, is schematically shown in Fig. 6.1.

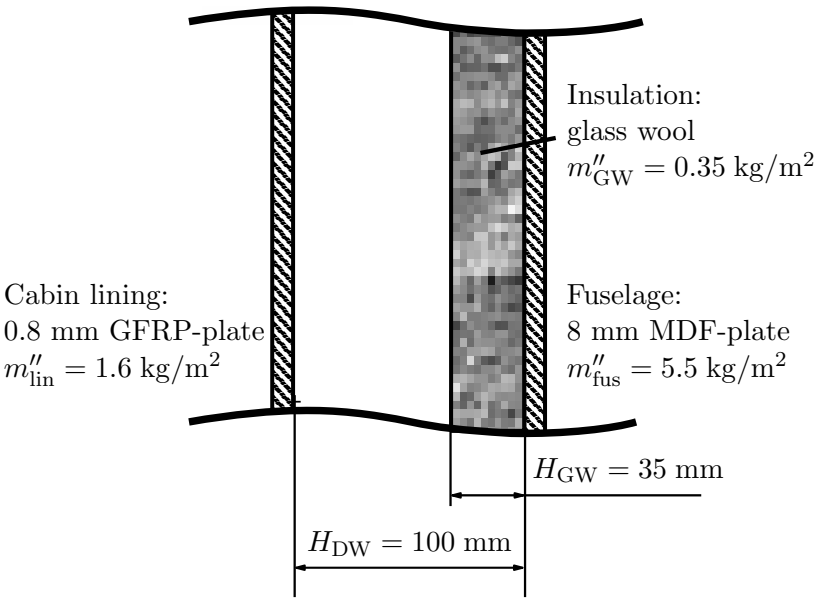

Figure 6.1: Schematic drawing of the reference double wall used in this study.

6.2. Cost function and optimization

As described in Section 4.4, the Helmholtz resonator panel with integrating cantilevers can be designed for different target applications. The resonator can be designed so that

- the two resonance frequencies of the Helmholtz resonator with cantilever correspond to two frequencies to be damped, such as two tones radiated by the aircraft engines,
- the frequency band of improved transmission loss of the double wall with resonators with cantilevers broadens compared to the frequency band of the double wall with embedded Helmholtz resonators alone,
- the tonraum resonance frequency is shifted to higher frequencies. At the tonraum resonance frequency, the transmission loss of the double wall with embedded resonators is significantly reduced compared to a double wall without resonators. If this frequency can be shifted to higher frequencies, the sound insulation, such as porous material, can absorb sound more efficiently.

At the current stage of engine development for a future aircraft, the dominant engine tones are not yet identified. This means that neither the resonance frequencies of the coupled resonator nor of the tonraum can be defined. Therefore, the focus of this study is to increase the bandwidth of the improved transmission loss.

Since the effect of Helmholtz resonators embedded in double walls is to improve the transmission loss in a broadband frequency range, roughly between the double wall resonance frequency and the resonance frequency of the Helmholtz resonator, the cost function

now focuses on further extending the frequency range over which the transmission loss of the double wall exceeds that of a mass-equivalent double wall without resonators. For an exemplary resonator panel, Fig. 6.2 a) shows the transmission loss of the aircraft-related reference double wall (ref. DW), a double wall with embedded Helmholtz resonators (HR), and a double wall with embedded Helmholtz resonators with integrated cantilevers (HR+CL) for two cantilever designs. The transmission loss values were calculated using the transfer matrix method, from Section 3.8. The insertion loss values with respect to the reference double wall are shown in Fig. 6.2 b). The insertion loss of the double wall with embedded Helmholtz resonators (dashed blue line) is positive in a frequency interval between the lower frequency of about $f_\mathrm{l} = 125$ Hz and the upper frequency $f_\mathrm{u} = 200$ Hz. Introducing the relative bandwidth B of the improved transmission loss

$$B = \frac{f_\mathrm{u} - f_\mathrm{l}}{\sqrt{f_\mathrm{u} f_\mathrm{l}}}, \tag{6.1}$$

results in $B_\mathrm{HR} \approx 47$ % for the double wall with embedded Helmholtz resonators. If the cantilever has the same resonance frequency as the Helmholtz resonator (solid red line, $f_\mathrm{CL} = f_\mathrm{HR}$), the interval of positive insertion loss is extended to about 215 Hz. Using the Helmholtz resonator with integrated cantilever increases the relative bandwidth to $B_\mathrm{HRCL} \approx 55$ %. The dash-dotted green lines represent the transmission and insertion loss

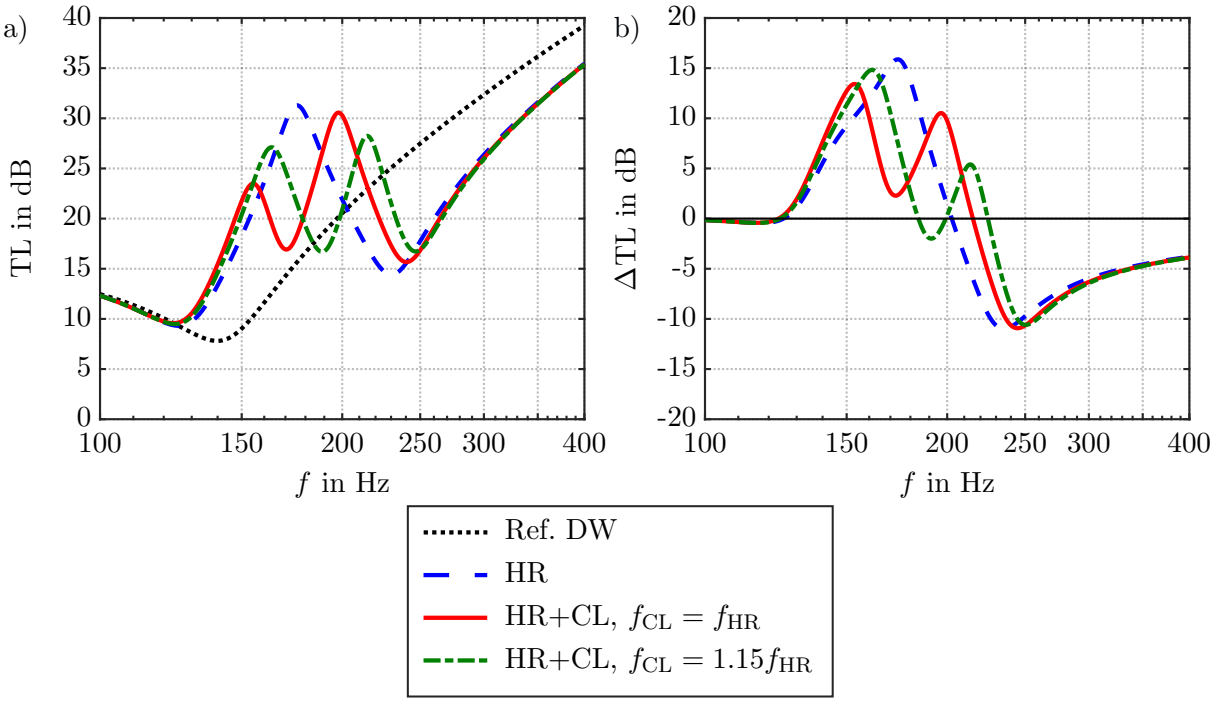

Figure 6.2: a) Transmission loss and b) Insertion loss of an exemplary resonator panel inserted into a double wall setup to explain the relative bandwidth.

of a double wall with Helmholtz resonators with integrated cantilever, where the resonance frequency of the uncoupled cantilever is 1.15 times higher than the resonance frequency of the uncoupled Helmholtz resonator ($f_{\mathrm{CL}} = 1.15 f_{\mathrm{HR}}$). This frequency tuning results in a more pronounced drop in transmission loss in between the two resonance frequencies, with the result, that the insertion loss is negative between 185 and 200 Hz. In this case, the continuous relative bandwidth $B_{\mathrm{HRCL,cont}}$, corresponding to the largest interval with continuously positive insertion loss and the summed relative bandwidth $B_{\mathrm{HRCL,sum}}$ of the two intervals with positive insertion loss can be calculated. The continuous relative bandwidth in the interval from about 125 to 185 Hz is $B_{\mathrm{HRCL,cont}} \approx 40$ %, while the summed relative bandwidth (125 - 185 Hz and 200 - 225 Hz) is about $B_{\mathrm{HRCL,sum}} \approx 51$ %.

To compare the relative bandwidth of positive insertion loss from the Helmholtz resonator with integrated cantilever B_{HRCL} with that of the Helmholtz resonator alone B_{HR}, the percentage difference in the relative bandwidth

$$\varepsilon = \left(\frac{B_{\mathrm{HRCL}}}{B_{\mathrm{HR}}} - 1 \right) \cdot 100\% \tag{6.2}$$

is defined. The value 1 is subtracted from the ratio of the relative bandwidths, so that no change in the bandwidth results in a value of 0 %, while an increase in the relative bandwidth of the Helmholtz resonator with integrated cantilevers results in positive values and a decrease results in negative values. In this study, the cost function is to maximize the **continuous relative bandwidth** of positive insertion loss under the constraints described. That means, the goal is to have one large gapless interval where the transmission loss is improved, i.e. where the insertion loss is positive. This results in the optimization problem of defining the geometry parameter of the unit cell to maximize the percentage difference in the continuous relative bandwidth

$$\varepsilon_{\mathrm{cont}} = \left(\frac{B_{\mathrm{HRCL,cont}}}{B_{\mathrm{HR,cont}}} - 1 \right) \cdot 100\%. \tag{6.3}$$

The design variables are limited by the aircraft sidewall space and weight requirements to be met (as detailed in Section 6.1) and by the following production contraints:

- The minimum slit width was limited to 2 mm because it is the thinnest conventional milling head available with a length of 35 mm.
- Since the very lightweight closed-cell foam is relatively brittle, the width of the cantilever as well as the thickness of the resonator walls have a minimum value of 5 mm.
- The target size of the panel is defined by the size of the transmission window of the

laboratory facilities with the width $W_\mathrm{p} = 1.2$ m and length $L_\mathrm{p} = 1$ m. The milling table at the university facilities has a size of about 1.3 m by 0.7 m, so that the panel must be produced in two parts, where each part has a size of $L_\mathrm{p} = 1$ m by $W_\mathrm{p}/2 = 0.6$ m.

The design variables are further constrained by:

- The length L and width W of the unit cell are assumed to realize an integer number (n_L and n_W) of unit cells on the length L_p and width $W_\mathrm{p}/2$ of the resonator plates, so that the plate has a high number of active resonators.

- The cantilever length, width, and thickness are limited by the unit cell size.

- The maximum surface mass density of 0.46 kg/m^2 for the noise control means includes the surface mass density contributions from the foam material of the resonator panel m''_res and the bonding material m''_g. The surface mass density of the bonding material was estimated from the resonator panel of Section 4.4.2 to be less than $m''_\mathrm{g} = 0.2$ kg/m^2. Therefore, the resulting maximum surface mass density of the resonator panel is $m''_\mathrm{res,max} = 0.26$ kg/m^2. The panel will be built from the closed-cell foam (density ρ_CL), which was also used for the models of the experimental validation in Chapter 4.

The optimization problem for the objective value $\varepsilon_\mathrm{cont}$ can be formulated as follows:

$$
\begin{array}{lll}
\underset{H_\mathrm{p}, n_\mathrm{L}, n_\mathrm{W}, t_\mathrm{s}, w_\mathrm{s}, l, w}{\text{maximize}} & \varepsilon_\mathrm{cont}(p_i) & \\
\text{with respect to } p_i & H_\mathrm{p} \in [5\ \mathrm{mm}, 35\ \mathrm{mm}], & \text{(Foam panel height)} \\
& n_\mathrm{L} \in \mathbb{N}, & \text{(Number of columns of unit cells)} \\
& n_\mathrm{W} \in \mathbb{N}, & \text{(Number of rows of unit cells)} \\
& t_\mathrm{s} \in [5\ \mathrm{mm}, H_\mathrm{p}], & \text{(Cantilever height)} \\
& w_\mathrm{s} \in [2\ \mathrm{mm}, (W - t_\mathrm{s})/2], & \text{(Slit width)} \\
& l \in [0\ \mathrm{mm}, L - t_s - w_s], & \text{(Cantilever length)} \\
& w \in [5\ \mathrm{mm}, W - t_s - 2w_s], & \text{(Cantilever width)} \\
\text{subject to} & L = L_\mathrm{p}/n_\mathrm{L}, & \text{(Foam panel length)} \\
& W = (W_\mathrm{p}/2)/n_\mathrm{W}, & \text{(Foam panel width)} \\
& m''_\mathrm{res} \leq m''_\mathrm{res,max}. & \text{(Foam panel surface mass density)}
\end{array}
$$

The actual value of the foam surface mass density m''_res is calculated with the design

variables p_i via:

$$m''_{\mathrm{res}} = \rho_{\mathrm{CL}} \cdot \left(L_{\mathrm{p}} W_{\mathrm{p}} H_{\mathrm{p}} - n_{\mathrm{W}} n_{\mathrm{L}} (L - t_{\mathrm{s}})(W - t_{\mathrm{s}})(H_{\mathrm{p}} - t_{\mathrm{s}}) - t_{\mathrm{s}}((l + w_{\mathrm{s}})(w + 2w_{\mathrm{s}}) - lw)\right). \tag{6.4}$$

In order to find the optimal values of the geometric parameters of the resonator panel, the analytical models are used for optimization calculations. The optimization was performed numerically using a Matlab-implemented code [134] of the Global Optimization Toolbox. The Genetic Algorithm (GA) was used for the present optimization problem.

The genetic algorithm, first formalized by John Holland in the 1970s [50], is an adaptive method inspired by the principles of natural selection. This algorithm iteratively improves a population of potential solutions by mimicking biological evolution. Because of its ability to handle large, nonlinear, and multidimensional problems, the genetic algorithm is particularly well-suited for engineering applications. The algorithm is effectively used for tasks ranging from optimizing design parameters to improving control systems [34]. In this context, a genetic algorithm has also been used, for example, to optimize the design of acoustic resonators [91].

The vector p, containing the design parameters, was programmed with the constraints as described above. All dimensions were constrained to be integer values in millimeters to align with manufacturing tolerances, which are of a similar scale. The optimization algorithm converged to the set of design parameters, listed in Table 6.1. The convergence of the objective value and the corresponding design parameters are shown in Fig. 6.3 a) and b), respectively. The optimization results show that the maximum percentage difference in the continuous relative bandwidth is approximately $\varepsilon_{\mathrm{cont}} = 11$ %. Fig. 6.3,c) compares the insertion loss of the double wall setups (HR and HR+CL) for the resonator panels with the optimal design variables, demonstrating an expanded frequency range with continuous positive insertion loss when the cantilever is integrated.

Table 6.1: Optimization results for the objective value and the design variables of the resonator

#	Description	Symbol	Value	Unit
1	Foam panel height	H_{p}	35	mm
2	Number of columns of unit cells	n_{L}	6	-
3	Number of rows of unit cells	n_{W}	4	-
4	Cantilever height	t_{s}	5	mm
5	Slit width	w_{s}	2	mm
6	Cantilever length	l	56	mm
7	Cantilever width	w	5	mm
-	Objective value	$\varepsilon_{\mathrm{cont}}$	11	%

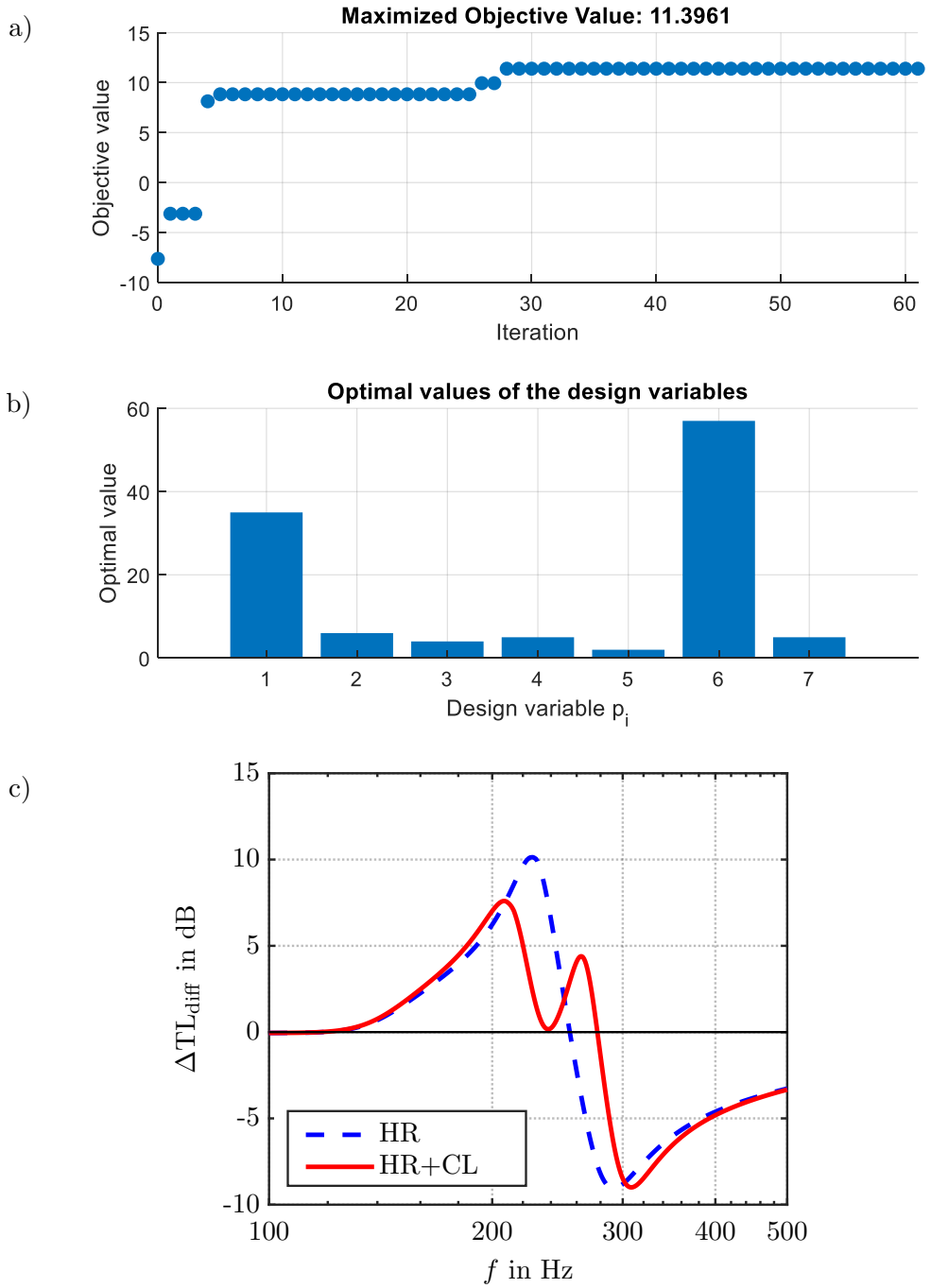

Figure 6.3: Optimization results. a) Iteration results of the objective value. b) Optimal values of the design variables. c) Calculated insertion loss of the double wall setup with resonators with respect to the reference double wall.

6.3. Description of functional model

Solving the optimization problem has revealed that the integrated cantilevers inside the Helmholtz resonators lead to the highest improvement of the continuous relative

bandwidth for a geometry combination of the cantilever with length $l = 56$ mm, width $w = 5$ mm and thickness $t_s = 5$ mm. The optimal slit width was determined to be $w_s = 2$ mm, while the optimal height, length and width of the unit cell are $H_p = 35$ mm, $L = 147$ mm, and $W = 165$ mm, respectively. Note that all parameters, except the cantilever length and the unit cell size, are at the lower limits imposed by the manufacturing constraints. The panel is manufactured by milling. The size of the milling head and the force on the remaining thin-walled structures are the main factors for the lower values of the constraints. The resonator panel could also be fabricated by pack foaming in a counterpart, where wall thicknesses of 2 mm could be realized according to the manufacturer of the foam. This manufacturing method was not used in this work because it is more suitable for serial production than for prototypes.

Based on the identified parameters, a resonator test panel was designed and manufactured. The geometric and material data are listed in Table 6.2 and the technical drawing of the resonator panel is shown in Fig. 6.4.

The resonator test panel consists of 48 unit cells and has a total length L_p of 1 m and a width W_p of 1.2 m. The test panel milled from the foam has an approximate surface mass density of $m''_{res} = 0.26$ kg/m^2, corresponding to the maximum surface mass density $m''_{res,max}$. The foam panel was bonded to the glass fiber reinforced plastic plate ($m''_{lin} = 1.6$ kg/m^2) with epoxy resin. The total surface mass density of the back plate, the foam plate, and the epoxy resin is approximately $m''_s = 2$ kg/m^2. Thus, the amount of resin with $m''_g = 0.14$ kg/m^2 provides a means to further optimize the weight of the resonator plate. With these geometric dimensions, the resonance frequencies calculated with the models of

Table 6.2: Geometric and material data of the resonator panel used to improve the insertion loss of the aircraft double wall in a broadband frequency range.

Description	Symbol	Value	Unit
Panel width	W_p	1000	mm
Panel length	L_p	1200	mm
Unit cell width	W	147	mm
Unit cell length	L	165	mm
Foam panel height	H_p	35	mm
Cantilever width	w	5	mm
Cantilever length	l	56	mm
Cantilever height	t_s	5	mm
Slit width	w_s	2	mm
Density	ρ_{CL}	32.2	kg/m^3
Young's modulus	E_{CL}	34.33	MPa
Structural loss factor	η_{CL}	0.05	-

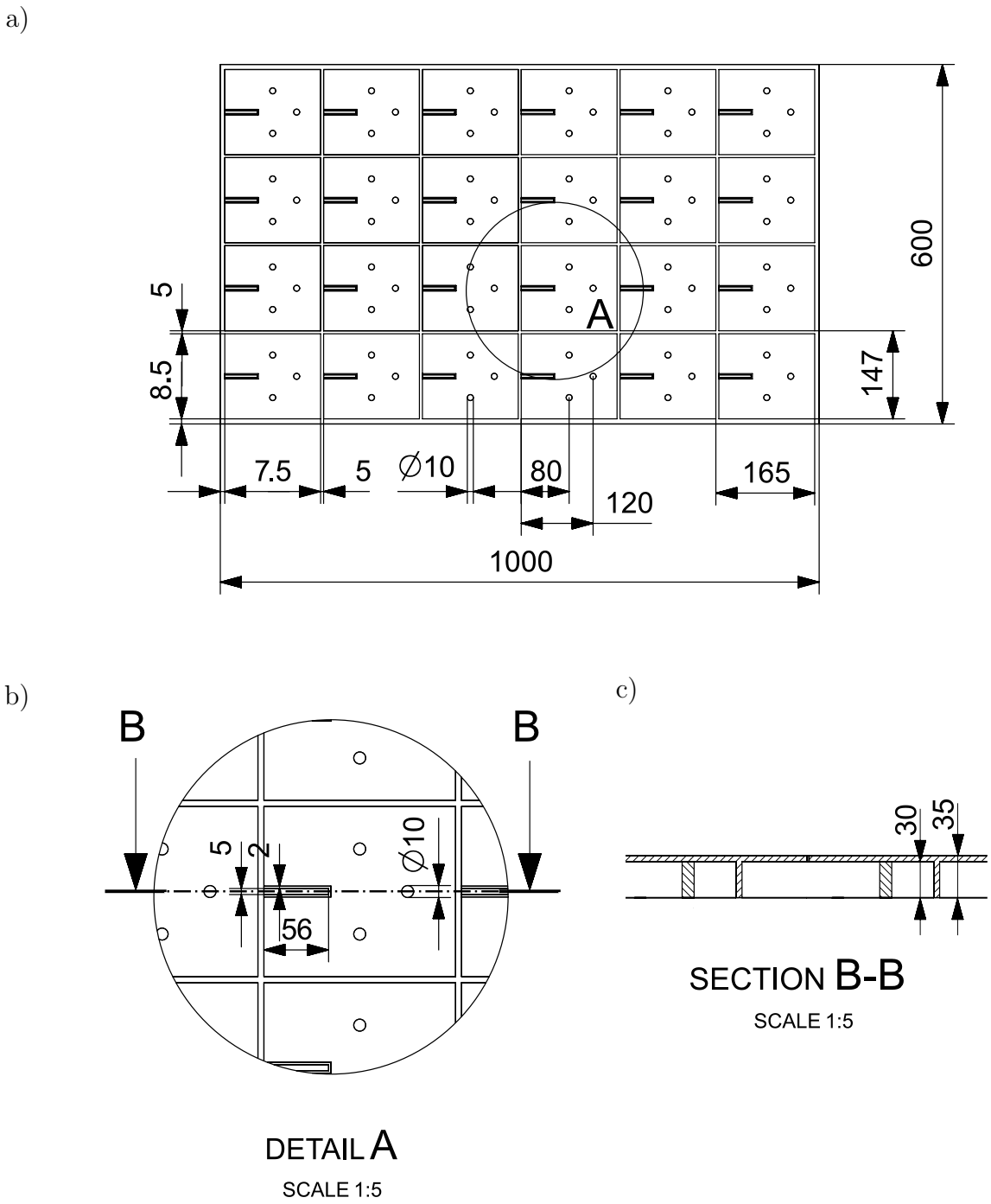

Figure 6.4: Technical drawing of the designed resonator panel. The complete panel consists of two half-panels. a) Top view of the panel. b) Detailed view of a resonator cavity. c) Sectional view of a resonator cavity and cantilever.

Chapter 3, taking into account the damping behavior, are approximately $f_{\mathrm{HR}} = 228$ Hz, $f_{\mathrm{CL1}} = 247$ Hz, and $f_{\mathrm{CL,V}} = 253$ Hz, with damping ratios of about 6 % for the Helmholtz resonator and 5 % for the cantilever. The damping ratios were estimated from Eq. (3.46), using the calculated complex-valued resonance frequencies.

Dimensional measurements of the final panel have shown that manufacturing variations result in differences in the height H of the resonator panel. Instead of the intended height of 35 mm, the manufactured panel has a height of 38 mm. This results in a larger cavity volume V_{cav} and lower values of resonance frequency of the Helmholtz resonator. Therefore, the analysis results for the intended resonator layout design (nominal design) and the dimensions of the manufactured panel (actual design) will be compared in the following section.

6.4. Measurement of transmission loss and comparison with analytical data

The transmission loss measurements were performed using the same setup and procedure as described in Sections 2.5.3 and 4.4.2. Two different configurations were investigated: Firstly, the resonator panel is installed as a single wall inside the transmission window. And secondly, the resonator panel is installed in an aircraft-like double wall setup.

6.4.1. Single wall

In a first step, transmission loss measurements were performed with the single wall. For this purpose, the Helmholtz resonator panel with integrated cantilevers was installed in the transmission window without the second wall and the insulation, as shown in Fig. 6.5 a) and b) for the view from the reverberation room and the view from the receiving room, respectively.

Three different configurations were measured: Firstly, all resonators were closed with

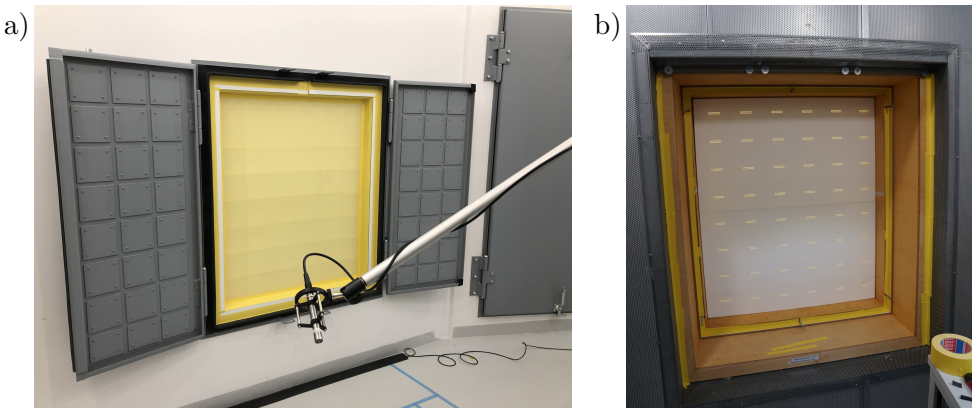

Figure 6.5: Photos of the measurement setup. a) Test panel inside the transmission window, view from the reverberation room. b) Test panel mounted in a rigid wooden frame, view from the receiving room.

tape (closed res.) so that the resonators and cantilevers were inactive, as visible exemplarily in Fig. 4.22 a). Secondly, the movement of the cantilevers was fixed by pins so that only the Helmholtz resonators were active (HR), as shown in Fig. 4.22 b). Thirdly, the coupled resonator system of Helmholtz resonator and cantilever was active (HR+CL). The measurement results (symbols) are compared with the analytical results (curves) in Fig. 6.6a) for the transmission loss and in Fig. 6.6b) for the insertion loss. The insertion loss was determined with respect to the panel with closed resonators.

In Fig. 6.6b), the analytical insertion loss results for the nominal resonator design are shown as thin curves, and the bold curves represent the results for the manufactured design. As expected from the manufacturing inaccuracies mentioned above, the measured resonance frequency of the Helmholtz resonator is lower (218 Hz) than the target resonance frequency (228 Hz). The transmission loss and the insertion loss of the double wall with resonators experience one distinct peak for the Helmholtz resonator panel at the resonance frequency and two distinct peaks for the Helmholtz resonator panel with integrated cantilevers at the resonance frequencies of the coupled system at about $f_1 = 205$ Hz and $f_2 = 260$ Hz. Overall, it is observed that the experimentally determined transmission and insertion loss values agree well with the analytical results calculated for the manufactured resonator (bold lines) in the frequency range around the resonance frequencies.

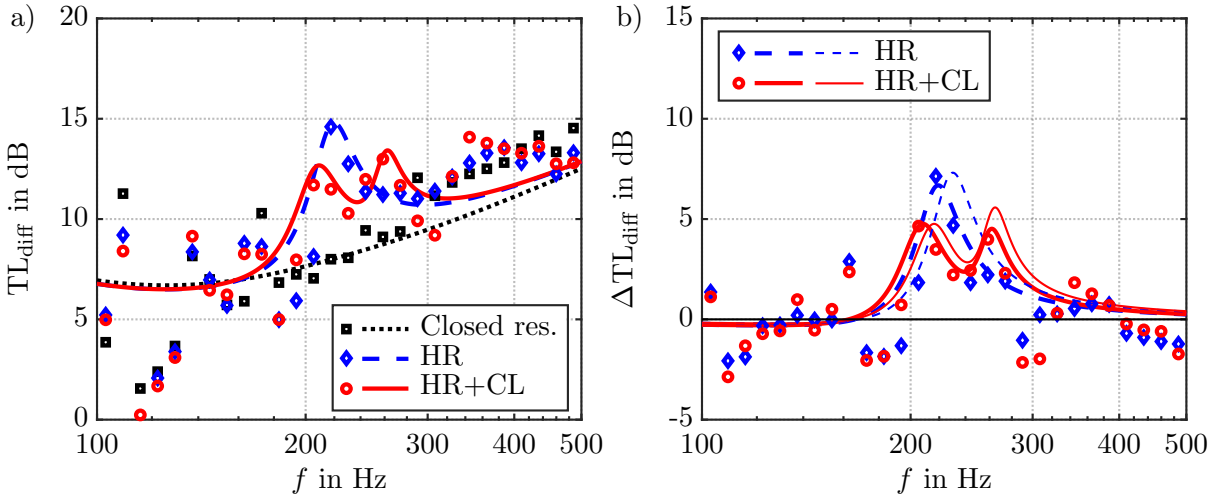

Figure 6.6: Comparison of experimental (symbols) and analytical (curves) results for the diffuse field sound transmission loss $\mathrm{TL_{diff}}$ and insertion loss $\Delta\mathrm{TL_{diff}}$ (with respect to the closed resonators) of the Helmholtz resonator panel with integrated cantilevers (single wall). Thin lines: nominal design; bold lines: actual design. a) Transmission loss $\mathrm{TL_{diff}}$. b) Insertion loss $\Delta\mathrm{TL_{diff}}$.

6.4.2. Double wall setup

This subsection presents the results of transmission and insertion loss measurements for the double wall setup with the embedded resonator plate. The double wall setup with the resonator panel is shown in Fig. 6.7 a). The reference for the insertion loss is a mass-equivalent double wall where all resonators have been made inactive with tape. In order to maintain the same wall spacing for this mass-equivalent reference double wall, the second wall was moved away from the first wall to regain the preselected wall spacing $H_{\mathrm{DW}} = 100$ mm, now measured between the second wall and the closed resonator panel surface, as shown in Fig. 6.7 b). This ensures that the reference double wall has the same surface mass densities and the same wall spacing. An insulation layer of aircraft-certified glass wool is applied to the wall representing the primary structure.

The measured results are compared with the analytical results and are shown in Fig. 6.8a) for the transmission loss and in Fig. 6.8b) for the insertion loss. The analytically determined insertion loss results (see Fig. 6.8b)) are plotted in bold lines for the manufactured resonator design and in thin lines for the nominal design. The transmission and insertion loss results show clear peaks at the resonance frequencies of the Helmholtz resonator (dashed blue curve) at about 218 Hz and of the coupled resonator panel (solid red curve) at about 205 and 260 Hz. At the tonraum resonance frequency of about 280 Hz for the Helmholtz resonator and 300 Hz for the resonator with integrated cantilever, the transmission and insertion loss values of the double wall setup are greatly reduced.

In the frequency region around the resonance frequencies, the measurement results are

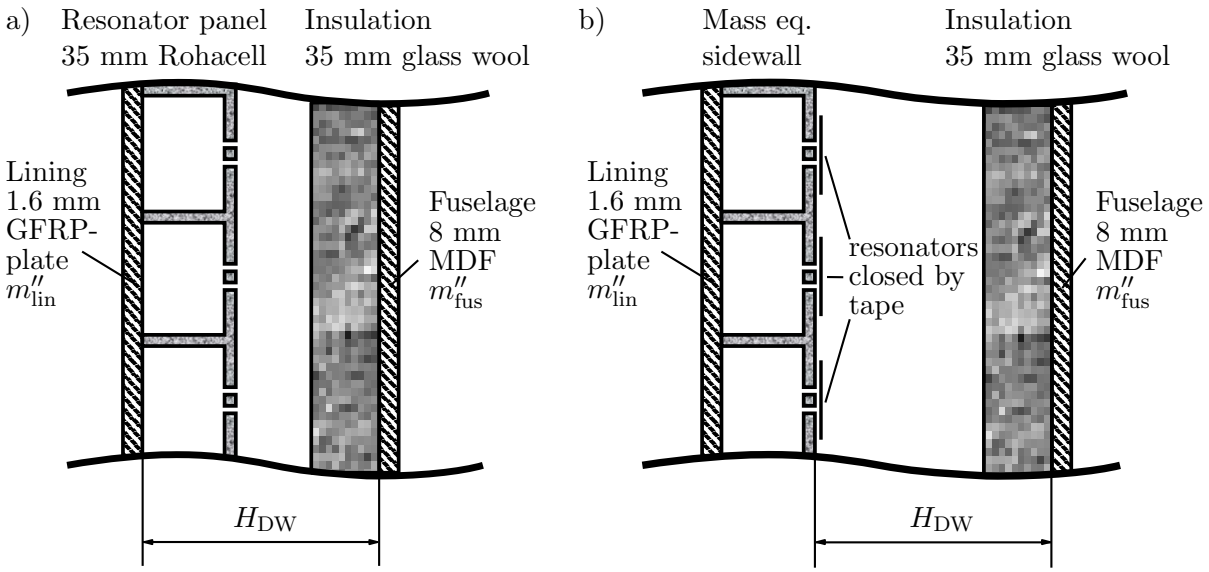

Figure 6.7: Schematic drawing of the double wall setup. a) Double wall with active Helmholtz resonators with integrated cantilevers. b) Double wall with inactive Helmholtz resonators (mass equivalent reference double wall)

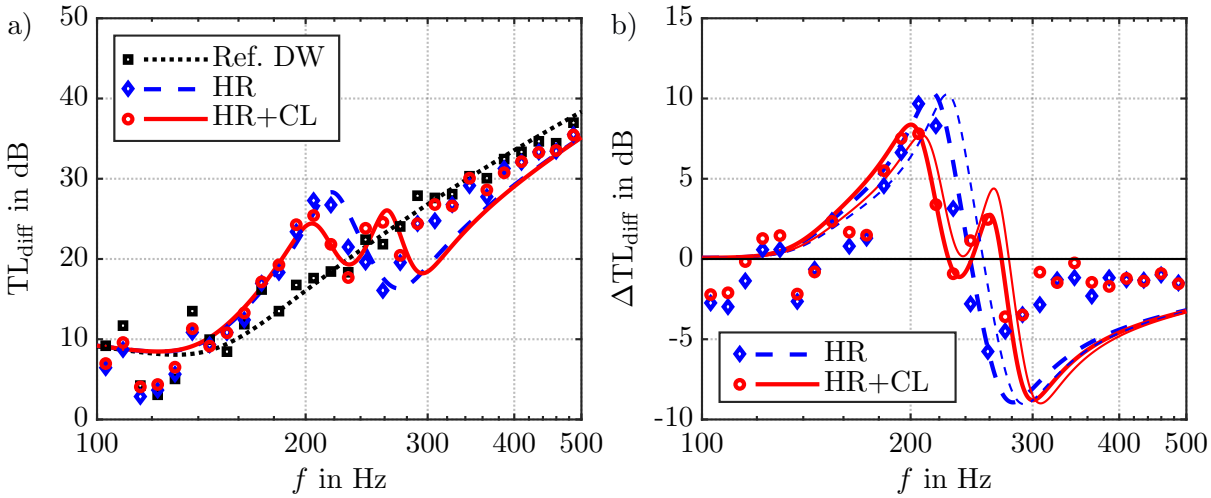

Figure 6.8: Comparison of experimental (symbols) and analytical (curves) results for diffuse field sound transmission loss $\mathrm{TL_{diff}}$ and insertion loss $\Delta\mathrm{TL_{diff}}$ (with respect to the mass-equivalent double wall) of an aircraft-related double wall with embedded resonator panel. Thin curves: nominal design; bold curves: manufactured design. a) Transmission loss $\mathrm{TL_{diff}}$. b) Insertion loss $\Delta\mathrm{TL_{diff}}$.

in good agreement with the analytical results for the dimensions of the manufactured panel (bold lines). The decrease in transmission loss and insertion loss at the tonraum resonance frequency seems to be attenuated in the experiments. This can be attributed to damping effects such as for example mechanical losses of the individual walls or of the frame in which the plates are mounted. Both of these potential loss mechanisms are not considered in the analytical model. However, the modal behavior around the resonance frequencies of the Helmholtz resonator with integrated cantilever can be accurately calculated with the analytical model, which is the focus of the derived model.

Due to the lower (than originally designed) resonance frequency of the Helmholtz resonator, the coupled system is not optimally tuned. The resonance frequencies of the coupled system f_1 and f_2 are further apart than designed, resulting in a more pronounced decrease in transmission loss between the resonance frequencies and to a negative insertion loss between f_1 and f_2. In the parameter variations in Section 5.3, it was also observed that increasing the frequency spacing between f_1 and f_2 leads to a larger decrease in transmission loss between the resonance frequencies. For the manufactured resonator panel installed in the double wall, see bold line in Fig. 6.8 b), the insertion loss is negative between 232 and 242 Hz. Therefore, the continuous relative bandwidth is reduced compared to the uncoupled Helmholtz resonator panel inside the double wall, while the summed relative bandwidth is almost the same. In contrast, the insertion loss of the nominal design (thin line) is not negative between the two resonance frequencies and is continuously positive between about 100 and 276 Hz. In comparison, the insertion loss of the Helmholtz

resonator panel inside the double wall is positive between about 100 and 250 Hz. The difference corresponds to a relative percentage change in the contiuous relative bandwidth of $\varepsilon_{\mathrm{cont}} = 11$ %. This result also corresponds to the objective value of the optimization algorithm.

As concluded in the parametric study in Section 5.3, the resonance frequencies of the uncoupled Helmholtz resonator and the cantilever in vacuo should be equal or close to equal for the resonator to be strongly coupled and for the drop in transmission loss to be reduced. The larger resonator height of the manufactured resonator panel results in a larger cavity volume and thus in a lower resonance frequency of the Helmholtz resonator, while the resonance frequency of the cantilever remains unchanged. Therefore, to account for the Helmholtz resonator resonance frequency shift, the resonance frequency of the cantilever should also be lowered in an iterative design modification. To lower the resonance frequency, the cantilever must be either longer or thinner, or made of a different material (with a lower Young's modulus E_{CL} or a higher density ρ_{CL}), which cannot be realized retroactively in the manufactured model. However, the resonance frequency can be lowered by adding masses to the tip of the cantilever, which will be investigated experimentally in the next section.

6.5. Tuning the cantilever resonance frequency with tip masses

To evaluate the influence of masses applied to the cantilever tip on the transmission loss of a Helmholtz resonator with integrated cantilever, an experimental parameter variation with impedance tube measurements is performed in a first step. In a second step, masses are applied to the cantilevers of the aircraft-like functional model described in this chapter.

6.5.1. Experimental feasibility study with impedance tube measurements

In general, adding a mass to the tip of the cantilever decreases its resonance frequency without affecting the resonance frequency of the uncoupled Helmholtz resonator, as the geometry of the resonator remains unchanged. Since the surface mass density of the cantilever m''_{CL} appears in the denominator of the coupling parameter, see Eq. (3.44), applying masses to the cantilever reduces the coupling parameter compared to a cantilever without masses, assuming all other parameters remain constant.

This feasibility study of tuning the cantilever resonance frequency with a tip mass was performed experimentally because cantilevers with mass are not yet implemented in

the analytical model. A model of a Helmholtz resonator with integrated cantilever was manufactured for the experimental parameter variation. The same material was used as for the experimental validations, while the geometric parameters are listed in Table 6.3. Aluminum tape with a size of 2 mm by 3 mm was applied as an additional mass at the tip of the resonator, as visible on Fig. 6.9 a). The mass was increased from 0 mg to 2 mg in about 0.5 mg steps. The influence of the mass on the transmission loss of the coupled resonator system compared to the resonator acting as a Helmholtz resonator alone is depicted in Fig. 6.9 b).

For clarity, the figure shows only the transmission loss of two mass increments: An added mass of 1 mg and an added mass of 2 mg. The configuration with an added mass of 1 mg shows the configuration with the lowest drop in transmission loss between the two resonance frequencies in this experimental parameter study, and the configuration with an added mass of 2 mg was the largest investigated added mass.

The resonance frequency of the uncoupled Helmholtz resonator (dashed blue line) is about 537 Hz. By allowing the cantilever to move without any applied mass (solid red line), the resonance frequencies of the coupled system are 532 and 621 Hz. The first resonance frequency is very close to the resonance frequency of the Helmholtz resonator and the second resonance frequency is much higher. The frequency difference is $\Delta f = 89$ Hz.

By applying a mass of 1 mg to the tip of the cantilever, as represented by the dash-dotted green line, both resonance frequencies of the coupled system are lowered and the frequency difference between them is reduced to $\Delta f = 58$ Hz, with the result that the drop in transmission loss between the two resonance frequencies could be reduced. As shown quantitatively in Table 6.4, the transmission loss in between the two resonance

Table 6.3: Geometric and material data of the resonator used in the parametric study, where masses are applied to the tip of the cantilever.

Description	Symbol	Value	Unit
Resonator width	W	65	mm
Resonator length	L	70	mm
Resonator height	H	40	mm
Cantilever width	w	3	mm
Cantilever length	l	34	mm
Cantilever height and res. wall thickness	t_s	5	mm
Slit width	w_s	2	mm
Density	ρ_CL	32.2	kg/m^3
Young's modulus	E_CL	34.33	MPa
Structural loss factor	η_CL	0.05	-

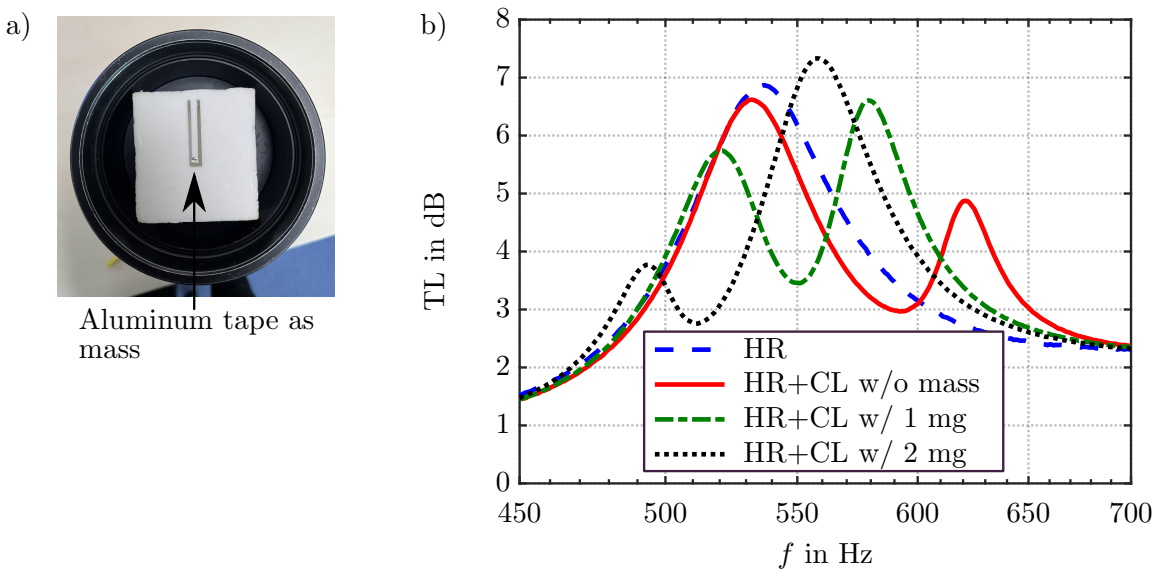

Figure 6.9: Experimental parameter study of the transmission loss TL of a Helmholtz resonator with an integrated cantilever and a mass at the tip of the cantilever; variation of the additional mass applied. a) Photo of the resonator in the impedance tube with a mass at the tip of the cantilever. b) Transmission loss results.

frequencies could be increased from $\mathrm{TL}_{\mathrm{min}} = 2.95$ dB to 3.45 dB by adding the tip mass of 1 mg. As the mass at the tip of the cantilever is further increased, the benefit of the added mass decreases. The frequency difference between the two resonances increases again and the value of the transmission loss at the local minimum $\mathrm{TL}_{\mathrm{min}}$ is reduced, as visible in Fig. 6.9 b).

The experimental parameter study reveals the potential of tip masses to retroactively tune the resonance frequency of the cantilever. Properly chosen, the tip mass can lead to both a reduced drop in transmission loss and a reduced frequency difference between the two resonance frequencies of the coupled system. In the following subsection, tip masses are also applied to the cantilevers of the aircraft-like functional model to overcome the manufacturing inaccuracies in an iterative design modification. In this case, the manufacturing deviation corresponds to a few millimeters in the resonator height.

Table 6.4: Frequency difference Δf and minimum transmission loss $\mathrm{TL}_{\mathrm{min}}$ in between the two resonance frequencies of the coupled system depending on tip masses applied to the cantilever.

Description	$\mathrm{TL}_{\mathrm{min}}$ dB	Δf Hz
HR + CL with no mass	2.95	89
HR + CL with 1 mg	3.45	58
HR + CL with 2 mg	2.75	64

6.5.2. Aircraft-like functional model with tip masses

In the previous subsection, it was shown that masses on the cantilever tip can reduce the coupling parameter, since the surface mass density of the cantilever m''_{CL} is in the denominator of the coupling parameter. As shown in the parameter study in Chapter 5, reducing the coupling parameter results in two resonance frequencies of the coupled system being closer to each other, and therefore results in a less pronounced drop in transmission loss between the two resonance frequencies. Furthermore, the resonance frequency of the cantilever can be tuned independently of the resonance frequency of the Helmholtz resonator, since the resonator geometry is not changed.

In this study, the resonance frequency of the cantilever is tuned by applying masses at the cantilever tip to overcome the manufacturing deviation in the resonator cavity size. The aim is to raise the insertion loss between the two resonance frequencies so as to maximize the continuous positive insertion loss range.

Analogous to the experimental parameter study in the impedance tube, aluminum tape was applied to the tip of the cantilever to form the mass, as shown in Fig. 6.10. The size of the tape was increased in an iterative experimental process until the insertion loss between the resonance frequencies was zero or higher. An insertion loss greater than zero was measured with aluminum tape with the size of approximately 5 mm by 5 mm and the weight of approximately 2.25 mg. In total, the mass of 2.25 mg, applied to 48 unit cells, results in a cumulative weight increase of 108 mg, which is about 0.03 % of the foam mass of the resonator panel without the back plate and adhesive.

The measurement results for the resonator panel installed inside the representative aircraft double wall are presented in Fig. 6.11 a) for the transmission loss and Fig. 6.11 b) for the insertion loss with respect to the reference double wall. In Figs. 6.11 a) and b), the dash-dotted green lines represent the measurement results for the configuration, where the masses are applied at the tip. As intended, the resonance frequencies of the coupled system are lower and closer to each other compared to the configuration without applied mass (solid red line). The frequency difference is reduced from about 55 Hz to 50 Hz,

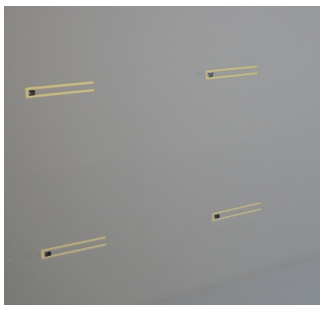

Figure 6.10: Photo of the aluminum tape on the tip of the cantilevers.

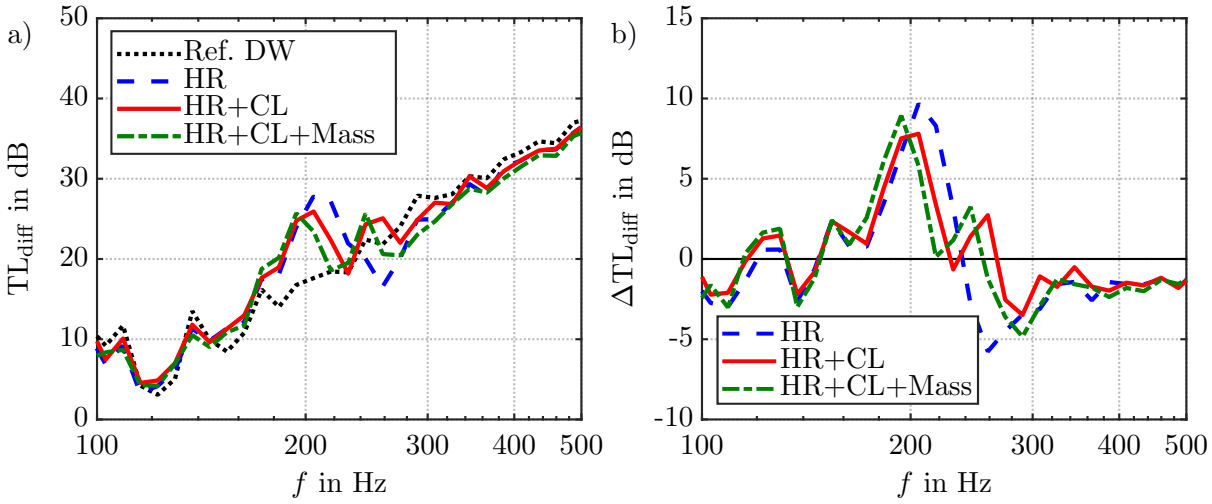

Figure 6.11: Experimental diffuse field sound transmission loss $\mathrm{TL_{diff}}$ and insertion loss $\Delta\mathrm{TL_{diff}}$ (with respect to the mass-equivalent double wall) of the Helmholtz resonator panel with integrated cantilevers and applied tip masses (of 2.25 mg) installed inside an aircraft-related double wall. a) Transmission loss $\mathrm{TL_{diff}}$. b) Insertion loss $\Delta\mathrm{TL_{diff}}$.

resulting in a smaller drop in transmission loss and a continuous positive insertion loss between 148 Hz and 257 Hz ($B_{\mathrm{cont,HRCL}} \approx 55.9\,\%$). In comparison, for the configuration with uncoupled Helmholtz resonator (dashed blue line), the insertion loss is positive approximately between 148 Hz and 237 Hz ($B_{\mathrm{cont,HR}} \approx 47.5\,\%$). The resulting percentage difference in the continuous relative bandwidth is $\varepsilon_{\mathrm{cont}} \approx 17.6\,\%$. $\varepsilon_{\mathrm{cont}}$ is the object function of the optimization, defined for a frequency interval with continuously positive insertion loss. Although $\varepsilon_{\mathrm{cont}}$ indicates a theoretical improvement in the double wall setup with Helmholtz resonators with integrated cantilevers, in practical applications a noticeable effect of noise control means is typically achieved when the improvement in transmission loss is higher than 3 dB.

Therefore, in the following, the masses on the cantilevers were further iteratively increased to achieve a continuous frequency band, where the insertion loss is 3 dB or higher. The mass on each cantilever was increased in approximately 2.25 mg steps (corresponding to aluminum tape with the size of 5 mm by 5 mm) to 6.75 mg. Even if the highest mass of 6.75 mg is applied to all 48 cantilevers, the total weight is only about 0.1 % of the foam mass of the resonator panel without the back plate and adhesive, and thus still negligible. For the sake of clarity, only the measurement results for the resonator plate with additional tip masses of 6.75 mg are shown in the following figure, since they show the optimal value for an increased bandwidth with an insertion loss of 3 dB. The measurement results for the resonator panel installed inside the representative aircraft double wall are presented in Fig. 6.12a) for the transmission loss and Fig. 6.12b) for the insertion loss with respect to the reference double wall. As expected, the measurement results

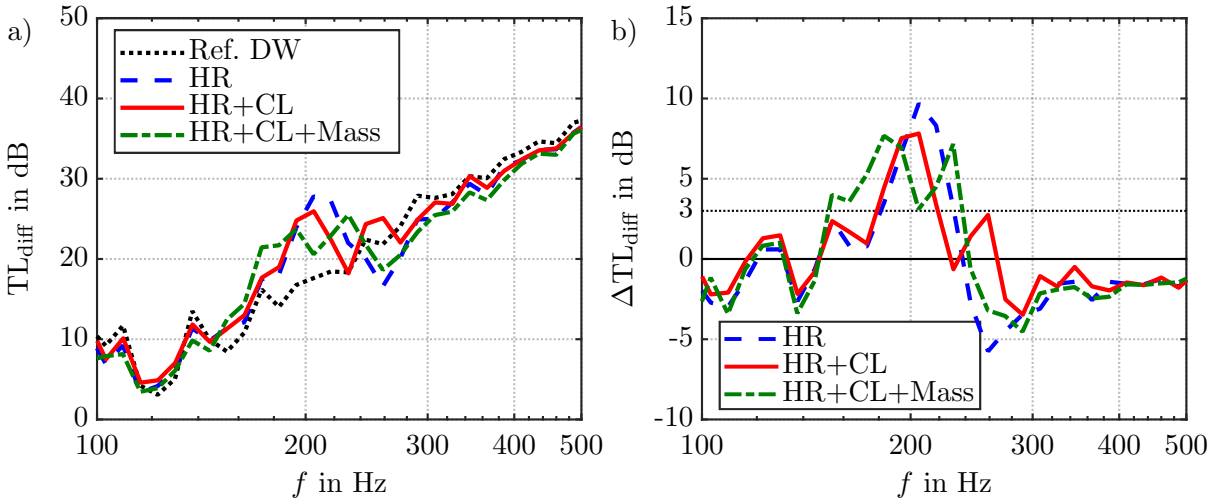

Figure 6.12: Experimental diffuse field sound transmission loss $\mathrm{TL_{diff}}$ and insertion loss $\Delta\mathrm{TL_{diff}}$ (with respect to the mass-equivalent double wall) of the Helmholtz resonator panel with integrated cantilevers and applied tip masses (of 6.75 mg) installed inside an aircraft-related double wall. a) Transmission loss $\mathrm{TL_{diff}}$. b) Insertion loss $\Delta\mathrm{TL_{diff}}$.

show that the frequency difference between the resonance frequencies could be further reduced to approximately 47 Hz by applying the higher masses. The subsequent effect is, that the drop in transmission and insertion loss between the two resonance frequencies of the coupled system can be reduced. While the insertion loss of the double wall with the resonator plate without tip masses on the cantilever (solid red curve) is negative between f_1 and f_2 at about 230 Hz, the insertion loss of the double wall with the resonator plate with masses on the cantilever tips (dash-dotted green curve) is about 3 dB between f_1 and f_2 at about 205 Hz.

The insertion loss is enhanced by more than 3 dB in the frequency range from approximately 150 to 238 Hz when the resonator panel with Helmholtz resonators and integrated cantilevers with tip masses is installed inside the double wall. This corresponds to a relative bandwidth of about 47 %. In comparison, the insertion loss of the resonator panel with only the Helmholtz resonators active shows a 3 dB improvement within the narrower frequency range of 180 to 235 Hz, corresponding to a relative bandwidth of about 27 %. Consequently, the integrated cantilevers result in a relative percentage difference of the continuous 3 dB bandwidth of approximately 74 %, effectively enhancing the low-frequency performance of the double wall setup.

In conclusion, masses applied to the cantilever tip could be useful as a tuning mechanism to

- overcome manufacturing limitations (such as minimum cantilever thicknesses) or manufacturing variations,

- modify the resonance frequency of the cantilever without changing the resonator geometry and the resonance frequency of the Helmholtz resonator,
- reduce the coupling parameter between the two resonance mechanisms, resulting in two resonance frequencies of the coupled system with a smaller frequency difference and a less pronounced drop in transmission loss between the two resonance frequencies.

Especially in the low end of the frequency range of interest, the trade-off between a low resonance frequency of the Helmholtz resonator, realized by small neck areas or long neck lengths, and a low resonance frequency of the cantilever, realized by thin cantilevers (directly leading to short neck lengths) or long cantilevers (directly leading to larger neck areas, if the slit width remains constant), can be overcome by applying tip masses. Masses at the cantilever tip are not yet included in the analytical model, but their application shows a high potential for further optimization of the coupled system of a Helmholtz resonator with integrated cantilever.

7. Conclusion and outlook

The aim of the present work was to provide a noise control means that has the potential to be implemented in the aircraft sidewall in order to improve the transmission loss of the aircraft double wall over a broad frequency band in the low-frequency range. While stand-alone Helmholtz resonators are only effective in a limited frequency range centered around their resonance frequency, the integration of appropriately tuned Helmholtz resonators within the double wall spacing can result in a broad improvement in transmission loss. The margin of transmission loss improvement is highly dependent on the ratio of the Helmholtz resonator resonance frequency to the double wall resonance frequency, as well as on the volumetric filling ratio of the Helmholtz resonator cavity to the double wall spacing. To further extend the effective bandwidth of integrated Helmholtz resonators modified devices exhibiting multiple resonance frequencies are generally recommendable.

In addition to high acoustic effectiveness, these treatments must also meet other aircraft-specific requirements, particularly stringent weight and space constraints. The challenge was to develop a lightweight yet effective Helmholtz resonator design exhibiting multiple resonance frequencies.

The new resonator design presented in this thesis consists of a Helmholtz resonator with a U-shaped slit, such that a cantilever was formed, which leads to a second resonance frequency, broadening the frequency range with high noise reduction. The resonator is made of a lightweight closed-cell foam, an unusual material for acoustic resonators. Compared to other Helmholtz resonators with two resonance frequencies, the weight and volume of the resonator are not affected by the modification, which is a major advantage.

For the design of the new resonator, an analytical model for the Helmholtz resonator with integrated cantilever has been derived in this thesis. Due to the lightweight material of the resonator, the fluid-structure interaction between the acoustic and mechanical modes cannot be neglected and is included in the analytical model. The analytical model was used to determine the resonance frequencies of the coupled resonator system, which includes the Helmholtz resonator and the cantilever. This model was also used to analyze the absorption and transmission behavior of the system. It was further extended to handle multi-layered structures using the transfer matrix method. Verification and validation of these models were performed using finite element simulations and experimental results, re-

spectively. Parameter studies were carried out using these analytical models to investigate the tuning mechanisms of the coupled resonator system and the influence of geometric parameters on noise reduction. Subsequently, optimization calculations were performed to identify the optimal geometric parameters. The objective was to design an aircraft-like functional model capable of extending the frequency range of high transmission loss of the double wall, particularly in the low-frequency range.

The following summarizes how the research questions of Section 1.4 were answered throughout the thesis:

- *How can Helmholtz resonators with integrated cantilevers be modeled?*

  The integration of the cantilever into the Helmholtz resonator neck results in a coupled system of an acoustic oscillator, i.e. the Helmholtz resonator, and a mechanical oscillator, i.e. the cantilever. Both oscillators are coupled by the resonator cavity, which acts as a spring. The deformation of the cantilever and the air movement in the neck of the Helmholtz resonator induce a pressure variation inside the cavity and vice versa. The pressure field inside the cavity is assumed to be non-uniform and approximated by the modal expansion method for the boundary conditions of a rigid-walled waveguide. This modeling approach of a non-uniform pressure field is especially important for Helmholtz resonators with integrated cantilevers made of lightweight materials. The model is derived for rigid cavities and must be adopted if the acoustic behavior of Helmholtz resonators with elastic walls is to be considered. The analytical model allows optimization problems or parameter studies to be solved about 500 times faster than comparative finite element simulations.

- *How can the model of the Helmholtz resonator with integrated cantilever be simplified?*

  The derived model can be simplified by assuming a constant pressure distribution inside the cavity. This is a reasonable assumption when the dimensions of the cavity are much smaller than the acoustic wavelength. The comparison of the two models indicates that the assumption of a constant pressure distribution in the cavity of the simplified model leads to overestimated coupling conditions, resulting in higher and lower calculated resonance frequencies. The simplified model gives reasonably accurate results when the system is weakly coupled. Weak coupling can be achieved either when the uncoupled frequencies f_{HR} and f_{CL1} are far apart, when the area of the cantilever is very small, or when the cavity volume of the resonator is large. In addition, the coupling becomes negligible for resonators made of materials with high density and high Young's modulus. It has been shown that the simplified model can also be used for strongly coupled resonator systems if the resonance frequency of the

cantilever stiffened by the air volume in the cavity $f_{\mathrm{CL,V}}$ is calculated analytically beforehand with the derived model taking into account the pressure modes in the cavity.

- *How can the resonance frequencies be tuned?*

  The resonance frequencies of the coupled resonator system can be tuned by tuning the resonance frequencies of the isolated Helmholtz resonator and cantilever, which are coupled via the air volume in the resonator cavity. If the resonance frequencies of the uncoupled Helmholtz resonator and cantilever are substantially different, the coupling is weak and the two resonance frequencies of the coupled resonator system nearly correspond to those of the uncoupled Helmholtz resonator and cantilever. In return, if the uncoupled systems have (nearly) the same resonance frequencies, the coupling is strong and the coupled system exhibits two distinct resonance frequencies that are close to each other, but do not become equal. To describe the strength of the coupling between the two modes, a coupling parameter has been introduced that depends on the area and mass of the cantilever and the volume of the cavity. Reducing the coupling parameter also reduces the frequency spacing between the two resonance frequencies of the coupled system. The slit width is an effective way to tune the resonance frequencies of the system: Adjusting the slit width changes the resonance frequency of the Helmholtz resonator without affecting the resonance frequency of the cantilever or the coupling parameter.

- *How do the geometric dimensions of the resonator influence the noise reduction behavior of the Helmholtz resonator with integrated cantilever?*

  The noise reduction of the Helmholtz resonator with integrated cantilever can be improved compared to that of a conventional Helmholtz resonator by considering the following design guidelines: The dimensions of the cantilever and the Helmholtz resonator cavity should be designed such that the resonance frequencies of the uncoupled Helmholtz resonator and of the cantilever in a vacuo are equal or nearly equal. This results in a strongly coupled resonator system with broadband noise reduction behavior. As seen in the parameter studies, it is advantageous to have the cantilever resonance frequency slightly higher, resulting in two frequency ranges with significant improvement in noise reduction. In addition, this configuration allows for subsequent tuning of the cantilever resonance frequency (by applying additional masses to the cantilever tip) in order to reduce the frequency difference between the two resonance frequencies or to compensate for manufacturing inaccuracies.

  The absorption behavior is mainly determined by the viscous losses in the neck

region, which depend on the ratio of slit length to slit width. The attenuation increases for narrower or longer slits, i.e. small areas of the Helmholtz resonator neck and thick cantilevers, resulting in higher absorption coefficient values. Conversely, the transmission loss is adversely reduced when high viscous losses occur in the neck of the Helmholtz resonator. Thus, for high transmission loss, it is advantageous to have wide and short slits.

- *Is it possible to further improve the transmission loss of aircraft double walls by inserting Helmholtz resonators with integrated cantilevers compared to conventional Helmholtz resonators?*

  It was found that Helmholtz resonators with cantilevers can increase the bandwidth of the transmission loss improvement but not for every combination of the geometric parameters. Optimization calculations were performed to determine a resonator design that result in a transmission loss improvement, exceeding that of the double wall with the uncoupled Helmholtz resonator.

  Finally, it was experimentally demonstrated that a resonator panel with integrated cantilevers, installed in an aircraft-like double wall setup, can increase the frequency range of improved transmission loss compared to a resonator panel, where the Helmholtz resonators act alone. To achieve the improvement, it is important, that the resonance frequencies of Helmholtz resonator and the cantilever are optimally tuned. This has been achieved experimentally by adding masses to the cantilever tips. The relative bandwidth of the frequency range, where the transmission loss was improved by 3 dB, could be increased from about 27 % for the Helmholtz resonator panel to about 47 % for the panel with integrated cantilevers, which corresponds to a relative improvement of about 74 %. These results were achieved at a resonator filling ratio of 27 % inside the double wall. A comprehensive study investigating the range in which Helmholtz resonators with integrated cantilevers enhance the transmission loss bandwidth of double walls for varying filling ratios has not yet been conducted.

The answers to the research questions highlight the potential of Helmholtz resonators with integrated cantilevers and their use as a means of low-frequency noise reduction within the aircraft sidewall. However, further optimization potential has been identified throughout this thesis and should be addressed in futureresearch:

- To lower the resonance frequency of the cantilever without changing the resonance frequency of the Helmholtz resonator, research could focus on reducing the spring stiffness of the cantilever. This can be achieved, for example, by selectively reducing

the thickness of the cantilever at its root. Compared to the approach of adding masses to the cantilever tip, this method decreases the overall mass of the system by the amount of material removed from the cantilever.

- The experiments have shown that small manufacturing inaccuracies result in shifted resonance frequencies, such that the coupled resonator system is not optimally tuned. Therefore, the necessary balance between manufacturing cost and accuracy must be found. It should be noted that the resonance frequency of the cantilever can be tuned subsequently by adding tip masses to correct for manufacturing tolerances.

- The production of the foam resonator panel by milling is very laborious. For series production, the panel should be built by direct foaming in a negative mold. In addition to faster and more accurate manufacturing, another advantage is that the wall thickness can be reduced. Thinner resonator walls reduce weight and increase resonator volume while lowering the resonance frequency. Furthermore, the manufacturing process for bonding the resonator panel to the back wall should be optimized to weight by reducing the amount of adhesive used.

- The analytical model provides a good means to design the coupled resonator system. However, to increase the potential of the resonator, it can be extended to include
  - waveguides with elastic walls,
  - cantilevers with masses at the tip,
  - and additional resonance mechanisms. For example, membranes inside the resonator body, additional cantilevers or perforated cantilevers can be used to introduce additional resonance mechanisms. In the case of perforated cantilevers, the vibration of the air mass within the perforations provides an additional degree of freedom.

The presented Helmholtz resonator with integrated cantilever is not limited to be only embedded in aircraft sidewalls. The concept can also be used in other applications, such as in cars, trains or aircraft engine liners. It can moreover be implemented in applications where Helmholtz resonators are already commonly used, such as in room acoustics, to extend noise reduction to a second resonance frequency.

As a final conclusion, the derived model of the Helmholtz resonator with integrated cantilever helps to understand the physical behavior of the resonator and to design an effective resonator with two resonance frequencies. Particularly advantageous is, that the improved noise control behavior of the resonator - compared to a conventional Helmholtz resonator with only one resonance frequency - is achieved without increasing the weight or

the volume of the resonator, which makes it interesting for applications with high weight and space requirements.

Bibliography

[1] A. Abbad, N. Atalla, M. Ouisse, and O. Doutres. Numerical and experimental investigations on the acoustic performances of membraned Helmholtz resonators embedded in a porous matrix. *Journal of Sound and Vibration*, 459:114873, 2019.

[2] J. F. Allard and N. Atalla. *Propagation of Sound in Porous Media: Modelling Sound Absorbing Materials*. John Wiley & Sohns, Chichester, 2nd edition, 2009.

[3] J. F. Allard and Y. Champoux. New empirical equations for sound propagation in rigid frame fibrous materials. *The Journal of the Acoustical Society of America*, 91 (6):3346–3353, 1992.

[4] J. F. Allard, B. Castagnède, M. Henry, and W. Lauriks. Evaluation of tortuosity in acoustic porous materials saturated by air. *Review of Scientific Instruments*, 65: 754–755, 1994.

[5] American Society for Testing and Materials ASTM E2611 – 09. Standard Test Method for Measurement of Normal Incidence Sound Transmission of Acoustical Materials Based on the Transfer Matrix Method. Technical report, American National Standards Institute (ANSI), 2009.

[6] Y. Atalla and R. Panneton. Inverse acoustical characterization of open cell porous media using impedance tube measurements. *Canadian Acoustics - Acoustique Canadienne*, 33(1):11–24, 2005.

[7] M. S. Atwal and M. J. Crocker. The effect on the transmission loss of a double wall panel of using helium gas in the gap. In *NOISE-CON 85 - Computers for noise control; Proceedings of the National Conference on Noise Control Engineering*, 1985.

[8] U. Berardi. The increase of the sound absorption through rectangular slot perforations. In *Proceedings of Meetings on Acoustics*, 2013.

[9] R. Berger. *Über die Schalldurchlässigkeit*. Königlich Technische Hochschule zu München, 1911.

[10] D. A. Bies and C. H. Hansen. *Engineering Noise Control: Theory and Practice*. Spon Press, 4th edition, 2014.

[11] M. A. Biot. Theory of Propagation of Elastic Waves in a Fluid-Saturated Porous

Solid. I. Low-Frequency Range. *The Journal of the Acoustical Society of America*, 28(2):168–178, 1956.

[12] D. T. Blackstock. *Fundamentals of physical acoustics*. Wiley, New York, 2000.

[13] J. Blauert and N. Xiang. *Acoustics for Engineers: Troy Lectures*. SpringerLink Bücher. Springer-Verlag Berlin Heidelberg, 3rd edition, 2009.

[14] P. Bonfiglio, F. Pompoli, and R. Lionti. A reduced-order integral formulation to account for the finite size effect of isotropic square panels using the transfer matrix method. *The Journal of the Acoustical Society of America*, 139(4):1773–1783, 2016.

[15] T. Bravo, C. Maury, and C. Pinhède. Enhancing sound absorption and transmission through flexible multi-layer micro-perforated structures. *The Journal of the Acoustical Society of America*, 134(5):3663–3673, 2013.

[16] L. M. Brechovskich. *Waves in layered media*. Applied mathematics and mechanics. Acad. Press, New York, 2nd edition, 1980.

[17] E. Brommundt and D. Sachau. *Schwingungslehre Mit Maschinendynamik*. Springer Vieweg, 3rd edition, 2018.

[18] B. Brouard, D. Lafarge, and J. F. Allard. A general method of modelling sound propagation in layered media. *Journal of Sound and Vibration*, 183(1):129–142, 1995.

[19] J. E. Cambridge, J. L. Davy, and J. Pearse. The influence of finite and infinite wall cavities on the sound insulation of double-leaf walls. *The Journal of the Acoustical Society of America*, 141(1):207–218, 2017.

[20] G. Campa and S. M. Camporeale. Application of Transfer Matrix Method in Acoustics. In *European COMSOL Conference 2010*, pages 1–6, 2010.

[21] CarbonScout. Technische Materialdaten Tafel GC 202 EN 60893-3-2, 2018.

[22] Y. Champoux and J. F. Allard. Dynamic tortuosity and bulk modulus in air-saturated porous media. *Journal of Applied Physics*, 70(4):1975–1979, 1991.

[23] J. D. Chazot, O. Robin, J. L. Guyader, and N. Atalla. Diffuse acoustic field produced in reverberant rooms: A boundary diffuse field index. *Acta Acustica united with Acustica*, 102(3):503–516, 2016.

[24] C. Claeys, N. G. Rocha de Melo Filho, L. Van Belle, E. Deckers, and W. Desmet. Design and validation of metamaterials for multiple structural stop bands in waveguides. *Extreme Mechanics Letters*, 12:7–22, 2017.

[25] COMSOL Multiphysics. *Structural Mechanics Module*. Comsol Multiphysics User's Guide, 2008.

[26] COMSOL Multiphysics. *Acoustics Module*. Comsol Multiphysics User's Guide, 2010.

[27] COMSOL Multiphysics. *Comsol multiphysics reference manual*. Comsol Multiphysics User's Guide, 2013.

[28] L. Cremer. Theorie der Schalldämmung dünner Wände bei schrägem Einfall. *Akustische Zeitschrift 7*, 3(1):81–104, 1942.

[29] M. J. Crocker. *Handbook of Noise and Vibration Control*. John Wiley & Sohns, Hoboken, New Jersey, 2007.

[30] M. J. Crocker, P. K. Raju, and B. Forssen. Measurement of Transmission Loss of Panels By the Direct Determination of Transmitted Acoustic Intensity. *Noise control engineering*, 17(1):6–11, 1981.

[31] S. A. Cummer, J. Christensen, and A. Alù. Controlling sound with acoustic metamaterials. *Nature Reviews Materials*, 1:16001, 2016.

[32] O. Dazel, F. Sgard, F.-X. Becot, and N. Atalla. Expressions of dissipated powers and stored energies in poroelastic media modeled by u,U and u,P formulations. *The Journal of the Acoustical Society of America*, 123(4):2054–2063, 2008.

[33] N. de Melo Filho, L. Van Belle, C. Claeys, E. Deckers, and W. Desmet. Dynamic mass based sound transmission loss prediction of vibro-acoustic metamaterial double panels applied to the mass-air-mass resonance. *Journal of Sound and Vibration*, 442: 28–44, 2019.

[34] K. Deb. *Multi-Objective Optimization using Evolutionary Algorithms*. John Wiley & Sons, Chichester, England, 2001.

[35] M. E. Delany and E. N. Bazley. Acoustical properties of fibrous absorbent materials. *Applied Acoustics*, 3(2):105–116, 1970.

[36] A. Dell, A. Krynkin, and K. V. Horoshenkov. The use of the transfer matrix method to predict the effective fluid properties of acoustical systems. *Applied Acoustics*, 182: 108259, 2021.

[37] DIN EN ISO 10534-1:2001-10. Acoustics – Determination of sound absorption coefficient and impedance in impedance tubes – Part 1: Method using standing wave ratio (ISO 10534-1:1996); German version EN ISO 10534-1:2001. Standard, DIN Deutsches Institut für Normung e.V., Oct. 2001.

[38] DIN EN ISO 10534-2:2001-10. Acoustics – Determination of sound absorption coefficient and impedance in impedance tubes – Part 2: Transfer-function method (ISO 10534-2:1998); German version EN ISO 10534-2:2001. Standard, DIN Deutsches Institut für Normung e.V., Oct. 2001.

[39] DIN EN ISO 15186-1:2003-12. Measurement of sound insulation in buildings and of building elements using sound intensity, Part 1: Laboratory measurements (ISO 15186-1:2000); German version EN ISO 15186-1:2003. Standard, DIN Deutsches Institut für Normung e.V., Dec. 2003.

[40] C. Droz, O. Robin, M. Ichchou, and N. Atalla. Improving sound transmission loss at ring frequency of a curved panel using tunable 3D-printed small-scale resonators. *The Journal of the Acoustical Society of America*, 145(1):EL72–EL78, 2019.

[41] S. Ebnesajjad. *Polyvinyl Fluoride: Technology and Applications of PVF (Plastics Design Library)*. William Andrew, 2012.

[42] Evonik Operations GmbH. Product Information ROHACELL® HF, Smart Materials, 2022. `https://products.evonik.com/assets/32/98/ROHACELL_HF_2022_April_EN_243298.pdf` (Accessed 15 Februray 2023).

[43] F. J. Fahy. *Foundations of Engineering Acoustics*. Elsevier Academic Press, San Diego, 2001.

[44] F. J. Fahy and P. Gardonio. *Sound and Structural Vibration: Radiation, Transmission and Response*. Elsevier Academic Press, Oxford, UK, 2007.

[45] H. V. Fuchs. *Applied acoustics: Concepts, absorbers, and silencers for acoustical comfort and noise control*. Springer, Berlin, Germany, 2013.

[46] S. B. Gebrekidan, H. J. Kim, and S. J. Song. Investigation of Helmholtz resonator-based composite acoustic metamaterial. *Applied Physics A: Materials Science and Processing*, 125(1):1–7, 2019.

[47] B. Ghanbarian, A. G. Hunt, R. P. Ewing, and M. Sahimi. Tortuosity in porous media: A critical review. *Soil Science Society of America Journal*, 77(5):1461–1477, 2013.

[48] S. Ghinet, P. Bouche, T. Padois, L. Pires, O. Doutres, T. C. Kone, K. Triki, F. Abdelkader, R. Panneton, and N. Atalla. Experimental validation of acoustic metamaterials noise attenuation performance for aircraft cabin applications. In *Proceedings of 2020 International Congress on Noise Control Engineering (Inter-Noise 2020)*, pages 222–232, 2020.

[49] S. Güttel and F. Tisseur. The nonlinear eigenvalue problem. *Acta Numerica*, 26: 1–94, 2017.

[50] J. H. Holland. *Adaptation in natural and artificial systems*. Complex Adaptive Systems. Bradford Books, Cambridge, 1992.

[51] V. Hongisto. *Airborne Sound Insulation of Wall Structures - Measurement and Prediction Methods*. PhD thesis, Helsinki University of Technology, 2000.

[52] H. Hoppen and W. Gleine. KonzIso - Konzeptstudien für neue leichtgewichtige Flugzeugkabinen-Isolierungen mit guten Schallisolationseigenschaften im tieferen Frequenzbereich: Abschlussbericht für das LuFo V-2 Vorhaben Flight-LAB - Flugtest im Labor. Technical report, Hochschule für Angewandte Wissenschaften Hamburg, Hamburg, 2020.

[53] H. Hoppen, F. Langfeldt, and W. Gleine. Schallabsorber mit einem Helmholtz-Resonator, 2019. Deutsches Patent-und Markenamt: DE102019106685B420210121.

[54] H. Hoppen, F. Langfeldt, W. Gleine, and O. von Estorff. Gekoppelter Helmholtz-Resonator mit schwingfähigem mechanischem Resonator. In *Proceedings of DAGA 2019*, pages 433–436, 2019.

[55] H. Hoppen, F. Langfeldt, W. Gleine, and O. von Estorff. Aircraft side wall with improved low-frequency sound insulation using a lining panel with Helmholtz resonators. In *Proceedings of the 26th International Congress on Sound and Vibration, ICSV 2019*, pages 1–8, 2019.

[56] H. Hoppen, H. Suresh, F. Langfeldt, W. Gleine, and O. von Estorff. Impact of surface roughness on acoustic resonators made of closed-cell lightweight foams. In *Proceedings of the 27th International Congress on Sound and Vibration, ICSV 2021*, pages 1–8, 2021.

[57] H. Hoppen, F. Langfeldt, W. Gleine, and O. von Estorff. Helmholtz resonator with two resonance frequencies by coupling with a mechanical resonator. *Journal of Sound and Vibration*, 559(May), 2023.

[58] H. Hoppen, F. Langfeldt, W. Gleine, and O. von Estorff. Anwendung von Helmholtz-Resonatoren mit integrierten Biegebalken in der Flugzeugkabine. In *Proceedings of DAGA 2023*, pages 592–595, 2023.

[59] K. Idrisi. *Heterogeneous (HG) Blankets for Improved Aircraft Interior Noise Reduction*. PhD thesis, Virginia Polytechnic Institute and State University, 2008.

[60] K. Idrisi, M. E. Johnson, A. Toso, and J. P. Carneal. Increase in transmission loss of a double panel system by addition of mass inclusions to a poro-elastic layer: A comparison between theory and experiment. *Journal of Sound and Vibration*, 323 (1-2):51–66, 2009.

[61] U. Ingard. On the Theory and Design of Acoustic Resonators. *The Journal of the Acoustical Society of America*, 25(6):1037–1061, 1953.

[62] Johns Manville. OEM Insulation Microlite® AA Premium NR Blankets Data Sheet Microlite, 2020. `https://www.jm.com/content/dam/jm/global/en/oem/aerospace/microlite-aa/JM_Microlite_AA_Premium_NR_Data_Sheet.pdf` (Ac-

cessed 16 February 2023).

[63] D. L. Johnson, J. Koplik, and R. Dashen. Theory of dynamic permeability and tortuosity in fluid saturated porous media. *Journal of Fluid Mechanics*, 176(1987): 379–402, 1987.

[64] A. T. Joos. *Untersuchungen des mit Phasenwechsel verbundenen instationären Transports von Wasser in Isolierungen.* PhD thesis, Technische Universität Hamburg-Harburg, 2011.

[65] M. R. F. Kidner, C. R. Fuller, and B. Gardner. Increase in transmission loss of single panels by addition of mass inclusions to a poro-elastic layer: Experimental investigation. *Journal of Sound and Vibration*, 294(3):466–472, 2006.

[66] N. Kino and T. Ueno. Comparisons between characteristic lengths and fibre equivalent diameters in glass fibre and melamine foam materials of similar flow resistivity. *Applied Acoustics*, 69(4):325–331, 2008.

[67] L. Kinsler. *Fundamentals of Acoustics.* ohn Wiley & Sons, Nashville, TN, 4th edition, 2000.

[68] A. I. Komkin and A. I. Bykov. Inertial attached neck length of Helmholtz resonators. *Acoustical Physics*, 62(3):269–279, 2016.

[69] U. R. Kristiansen and T. E. Vigran. On the design of resonant absorbers using a slotted plate. *Applied Acoustics*, 43(1):39–48, 1994.

[70] H. L. Kuntz, R. A. Prydz, F. J. Balena, and R. J. Gatineau. Development and testing of cabin sidewall acoustic resonators for the reduction of cabin tone levels in propfan-powered aircraft. Technical Report NASA CR-4388, 1991.

[71] M. H. Kurdi, G. Scott Duncan, and S. S. Nudehi. Optimal Design of a Helmholtz Resonator With a Flexible End Plate. *Journal of Vibration and Acoustics*, 136(3): 031004, 2014.

[72] D. Lafarge, P. Lemarinier, J. F. Allard, and V. Tarnow. Dynamic compressibility of air in porous structures at audible frequencies. *The Journal of the Acoustical Society of America*, 102(4):1995–2006, 1997.

[73] Z. Laly, C. Mechefske, S. Ghinet, and C. T. Kone. Numerical design of acoustic metamaterial based on parallel Helmholtz resonators for multi-tonal noise control. In *Inter-Noise 2022 - 51st International Congress and Exposition on Noise Control Engineering*, 2022.

[74] Z. Laly, C. Mechefske, S. Ghinet, C. T. Kone, and N. Atalla. Design and analysis of periodic acoustic metamaterial sound insulator using finite element method. *Noise Control Engineering Journal*, 71(5):344–364, 2023.

[75] S. A. Lane. Coupled Helmholtz Resonators for Acoustic Attenuation. *Journal of Vibration and Acoustics*, 123(January 2001):11–17, 2001.

[76] S. Langer. *Schalltransmission durch Isolierverglasung*. PhD thesis, Technische Universität Braunschweig, 2001.

[77] F. Langfeldt and W. Gleine. Design of acoustic partitions with thin plate-like acoustic metamaterials. In *Proceedings of the International Congress on Acoustics*, pages 4870–4877, 2019.

[78] F. Langfeldt and W. Gleine. Optimizing the bandwidth of plate-type acoustic metamaterials. *The Journal of the Acoustical Society of America*, 148(3):1304–1314, 2020.

[79] F. Langfeldt, W. Gleine, and O. von Estorff. Enhancing the low-frequency noise reduction of a double wall with membrane-type acoustic metamaterials. In *Proceedings of the Inter-Noise 2016 - 45th International Congress and Exposition on Noise Control Engineering: Towards a Quieter Future*, pages 7551–7562, 2016.

[80] F. Langfeldt, H. Hoppen, and W. Gleine. Resonance frequencies and sound absorption of Helmholtz resonators with multiple necks. *Applied Acoustics*, 145:314–319, 2019.

[81] F. Langfeldt, H. Hoppen, and W. Gleine. Broadband low-frequency sound transmission loss improvement of double walls with Helmholtz resonators. *Journal of Sound and Vibration*, 476:115309, 2020.

[82] F. Langfeldt, A. Khatokar, and W. Gleine. Plate-type acoustic metamaterials with integrated Helmholtz resonators. *Applied Acoustics*, 199:109019, 2022.

[83] A. Leblanc and A. Lavie. Three-dimensional-printed membrane-type acoustic metamaterial for low frequency sound attenuation. *The Journal of the Acoustical Society of America*, 141(6):EL538–EL542, 2017.

[84] H. P. Lee, S. Kumar, S. Garg, and K. M. Lim. Assessment of in-cabin noise of wide-body aircrafts. *Applied Acoustics*, 194:108809, 2022.

[85] R. Lerch, G. Sessler, and D. Wolf. *Technische Akustik : Grundlagen und Anwendungen*. Springer, Berlin, Heidelberg, 2009.

[86] R. S. Li, X. W. Sun, G. G. Xu, X. L. Gao, Y. Cao, and J. H. Tian. Improving low-frequency sound transmission loss of double panels with a plate-type acoustic metamaterial. *Materials Today Communications*, 39:109139, 2024.

[87] G. Liao, C. Luan, Z. Wang, J. Liu, X. Yao, and J. Fu. Acoustic Metamaterials: A Review of Theories, Structures, Fabrication Approaches, and Applications. *Advanced Materials Technologies*, 6(5):1–29, 2021.

[88] P. S. Liu and G. F. Chen. General introduction to porous materials. In *Porous Materials*, pages 1–20. Elsevier, 2014.

[89] Q. Lu, X. Li, X. Zhang, M. Lu, and Y. Chen. Perspective: Acoustic Metamaterials in Future Engineering. *Engineering*, 17:22–30, 2022.

[90] K. Lühe. *Rechnerische und messtechnische Untersuchung zur Modellierung absorbierender Wandverkleidungen bei der akustischen Auslegung von Flugzeugkabinen.* B.Sc. thesis, Hamburg University of Applied Sciences, 2014.

[91] C. Lv, X. Wang, and Y. Mei. Optimization method of acoustic filter structures composed of helmholtz resonators based on genetic algorithm. *Journal of Physics: Conference Series*, 2468(1):012019, 2023.

[92] D. Maa. Theory of microslit absorbers. *Shengxue Xuebao/Acta Acustica*, 25(6): 481–485, 2000.

[93] J. C. MacBain and J. Genin. Natural frequencies of a beam considering support characteristics. *Journal of Sound and Vibration*, 27(2):197–206, 1973.

[94] P. Martignac. *Management of the risks linked to the trial installation of new insulation blankets for single-aisle aircraft.* PhD thesis, KTH, 2012.

[95] J. M. Mason and F. J. Fahy. The use of acoustically tuned resonators to improve the sound transmission loss of double-panel partitions. *Journal of Sound and Vibration*, 124(2):367–379, 1988.

[96] Matelys Research Lab. Acoustical Porous Material Recipes, Propagation models assuming a motionless skeleton, 2023. `https://apmr.matelys.com/PropagationModels/index.html` (Accessed: 6 Oktober 2023).

[97] D. N. May, K. J. Plotkin, R. G. Selden, and B. H. Sharp. Lightweight Sidewalls for Aircraft Interior Noise Control. Technical Report NASA CR-172490, 1985.

[98] A. McKay, I. Davis, J. Killeen, and G. J. Bennett. SeMSA: a compact super absorber optimised for broadband, low-frequency noise attenuation. *Scientific Reports*, 10(1): 1–15, 2020.

[99] U. Michel. Abschlussbericht zum Projekt "Leiser Flugverkehr", Minderung des Triebwerkslärms. Technical report, Berlin, 2004.

[100] J. Michielsen. *Low-frequency acoustic optimization of a double-wall panel by means of vibration absorbers.* PhD thesis, Eindhoven University of Technology, 2015.

[101] R. N. Miles. *Physical Approach to Engineering Acoustics.* Mechanical Engineering Series. Springer, Cham, Switzerland, 1st edition, 2020.

[102] J. S. Mixson and J. F. Wilby. Interior Noise. In H. H. Hubbard, editor, *Aeroacoustics*

of flight vehicles: theory and practice. Volume 2: Noise Control. NASA, Washington, DC, 1991.

[103] M. Möser, S. Zimmermann, and R. Ellis. *Engineering Acoustics: An Introduction to Noise Control*. Springer Berlin Heidelberg, 2013.

[104] K. A. Mulholland, H. D. Parbrook, and A. Cummings. The transmission loss of double panels. *Journal of Sound and Vibration*, 6(3):324–334, 1967.

[105] M. L. Munjal. *Acoustics of ducts and mufflers with application to exhaust and ventilation system design*. John Wiley & Sons, Nashville, TN, 1987.

[106] C. J. Naify, C. M. Chang, G. McKnight, and S. R. Nutt. Experimental and FEA evaluation of membrane-type locally resonant acoustic metamaterial arrays for aircraft interior sound insulation. In *17th AIAA/CEAS Aeroacoustics Conference 2011 (32nd AIAA Aeroacoustics Conference)*, pages 1–4, 2011.

[107] C. J. Naify, C. Huang, M. Sneddon, and S. Nutt. Transmission loss of honeycomb sandwich structures with attached gas layers. *Applied Acoustics*, 72(2-3):71–77, 2011.

[108] A. Nilsson and B. Liu. *Vibro-Acoustics, Volume 1*. Springer, Berlin, Germany, 1st edition, 2015.

[109] M. P. Norton and D. G. Karczub. *Fundamentals of Noise and Vibration Analysis for Engineers*. Cambridge University Press, 2nd edition, 2003.

[110] S. S. Nudehi, G. S. Duncan, and U. Farooq. Modeling and Experimental Investigation of a Helmholtz Resonator With a Flexible Plate. *Journal of Vibration and Acoustics*, 135(4):041102, 2013.

[111] O. Olivieri, J. S. Bolton, and T. Yoo. Measurement of transmission loss of materials using a standing wave tube. In *Institute of Noise Control Engineering of the USA - 35th International Congress and Exposition on Noise Control Engineering (Inter-Noise 2006)*, pages 5285–5292, 2006.

[112] R. Panneton. Comments on the limp frame equivalent fluid model for porous media. *The Journal of the Acoustical Society of America*, 122(6):EL217–EL222, 2007.

[113] L. D. Pope, E. G. Wilby, C. M. Willis, and W. H. Mayes. Aircraft interior noise models: Sidewall trim, stiffened structures, and cabin acoustics with floor partition. *Journal of Sound and Vibration*, 89(3):371–417, 1983.

[114] A. Putra, A. Y. Ismail, R. Ramlan, M. R. Ayob, and M. S. Py. Normal incidence of sound transmission loss of a double-leaf partition inserted with a microperforated panel. *Advances in Acoustics and Vibration*, 2013(1):216493, 2013.

[115] R. T. Randeberg. *Perforated Panel Absorbers with Viscous Energy Dissipation Enhanced by Orifice Design*. PhD thesis, Norwegian University of Science and Technology, 2000.

[116] J. D. Revell, F. J. Balena, and L. R. Koval. Interior Noise Control by Fuselage Design for High-speed Propeller-Driven Aircraft. *Journal of Aircraft*, 19(1):39–45, 1982.

[117] D. Rhazi and N. Atalla. A simple method to account for size effects in the transfer matrix method. *The Journal of the Acoustical Society of America*, 127(2):EL30–EL36, 2010.

[118] K. Rosenkranz. *Bestimmung der Materialparameter von polymeren, geschlossenzelligen Hartschäumen*. Project Report, Hamburg University of Applied Sciences, 2020.

[119] K. Sakagami, M. Morimoto, and M. Yairi. A note on the effect of vibration of a microperforated panel on its sound absorption characteristics. *Acoustical Science and Technology*, 26(2):204–207, 2005.

[120] A. Sanada and N. Tanaka. Extension of the frequency range of resonant sound absorbers using two-degree-of-freedom Helmholtz-based resonators with a flexible panel. *Applied Acoustics*, 74(4):509–516, 2013.

[121] H. Scheel and C. Thomas. Integration einstellbarer, akustischer Materialien im Flugzeugbau. In *Proceedings of DAGA 2018*, pages 54–55, 2018.

[122] A. Selamet and Z. L. Ji. Circular asymmetric Helmholtz resonators. *The Journal of the Acoustical Society of America*, 107(5):2360–2369, 2000.

[123] F. C. Sgard, N. Atalla, and C. K. Amedin. Vibro-acoustic behavior of a cavity backed by a plate coated with a meso-heterogeneous porous material. *Acta Acustica united with Acustica*, 93(1):106–114, 2007.

[124] B. H. Sharp. A Study of Techniques to Increase the Sound Insulation of Building Elements. Technical Report WR 73-5, Wyle Labratory, El Segundo, Carlifornia, 1973.

[125] T. Simsek. *Messung von Schwingungen mit einem Laser-Vibrometer durch ein transparentes Impedanzrohrstück*. B.Sc. thesis, Hamburg University of Applied Sciences, 2021.

[126] G. R. Sinambari and S. Sentpali. *Ingenieurakustik*. Springer Vieweg, 5th edition, 2014.

[127] J. Smits and C. Kosten. Sound absorption by slit resonators. *Acta Acustica united with Acustica*, 1(3):114–122, 1951.

[128] B. H. Song and J. S. Bolton. A transfer-matrix approach for estimating the characteristic impedance and wave numbers of limp and rigid porous materials. *The Journal of the Acoustical Society of America*, 107(3):1131–1152, 2000.

[129] S. Y. Song, X. H. Yang, F. X. Xin, S. W. Ren, and T. J. Lu. Modeling of roughness effects on acoustic properties of micro-slits. *Journal of Physics D: Applied Physics*, 50(23), 2017.

[130] M. R. Stinson. The propagation of plane sound waves in narrow and wide circular tubes, and generalization to uniform tubes of arbitrary cross-sectional shape. *The Journal of the Acoustical Society of America*, 89(2):550–558, 1991.

[131] W. C. Strack, G. Knip, A. L. Weisbrich, J. Godston, and E. Bradley. Technology and Benefits of Aircraft Counter Rotation Propellers. Technical Report NASA-TM-82983, 1982.

[132] S. Sugie, J. Yoshimura, and T. Iwase. Effect of inserting a helmholtz resonator on sound insulation in a double-leaf partition cavity. *Acoustical Science and Technology*, 30(5):317–326, 2009.

[133] S. Tang, C. Ng, and E. Lam. Experimental investigation of the sound absorption performance of compartmented helmholtz resonators. *Applied Acoustics*, 73(9):969–976, 2012.

[134] The MathWorks Incc. Genetic Algorithm, 2024. `https://de.mathworks.com/help/gads/genetic-algorithm.html` (Accessed 16 May 2024).

[135] C. Thomas. *Beeinflussung des akustischen Verhaltens von Doppelwandsystemen durch den Einsatz mikroperforierter Absorber*. BoD – Books on Demand, 2006.

[136] I. Tiseo. Global distribution of CO2 emissions 2022, by sector, 2024. `https://www.statista.com/statistics/1129656/global-share-of-co2-emissions-from-fossil-fuel-and-cement/` (Accessed 10 May 2024).

[137] I. Vér and L. Beranek. *Noise and Vibration Control Engineering: Principles and Applications*. John Wiley & Sons, 2005.

[138] M. Villot, C. Guigou, L. Gagliardini, and L. Gagliardini. Predicting the acoustical radiation of finite size multi-layered structures by applying spatial windowing on infinite structures. *Journal of Sound and Vibration*, 245(3):433–455, 2001.

[139] M. Wörner. *Wärme- und Stofftransport in einer Flugzeugkabine unter besonderer Berücksichtigung des Feuchtetransportes*. PhD thesis, TU Hamburg, 2006.

[140] M. Xu, A. Selamet, and H. Kim. Dual helmholtz resonator. *Applied Acoustics*, 71 (9):822–829, 2010.

[141] Z. Xu, X. Peng, X. Liu, F. Xin, and T. J. Lu. Modified theory of a microperforated panel with roughened perforations. *Europhysics Letters*, 125(3):34004, 2019.

[142] F. Yang, E. Wang, X. Shen, X. Zhang, Q. Yin, X. Wang, X. Yang, C. Shen, and W. Peng. Optimal Design of Acoustic Metamaterial of Multiple Parallel Hexagonal Helmholtz Resonators by Combination of Finite Element Simulation and Cuckoo Search Algorithm. *Materials*, 15(18), 2022.

[143] X. Yang, X. Shen, D. Hu, X. Wang, H. Song, R. Zhao, C. Zhang, C. Shen, and M. Yang. An investigation of modular composable acoustic metamaterials with multiple nonunique chambers. *Materials*, 16(24), 2023.

[144] Z. Yang, H. M. Dai, N. H. Chan, G. C. Ma, and P. Sheng. Acoustic metamaterial panels for sound attenuation in the 50-1000 Hz regime. *Applied Physics Letters*, 96 (4):16–19, 2010.

[145] L. Zhang, W. Zhang, and F. Xin. Broadband low-frequency sound absorption of honeycomb sandwich panels with rough embedded necks. *Mechanical Systems and Signal Processing*, 196:110311, 2023.

[146] M. Zollner and E. Zwicker. *Elektroakustik*. Springer Berlin, Heidelberg, 3rd edition, 2003.

A. Appendix

A.1. Derivation of the equation of motion of the air volume in the neck

In this section, the equation of motion for the displacement u_{HR} of the fluid volume of the air inside the Helmholtz resonator neck is derived. Fig. A.1 a) shows the three-dimensional view of the Helmholtz resonator with integrated cantilever. The blue colored area represents the section plane for the cross section depicted in Fig. A.1 b). A Cartesian coordinate system is defined with the origin at the cantilever root. The z-coordinate points along the cantilever axis and the x-coordinate inside the Helmholtz resonator cavity. In Fig. A.1 b), the blue colored area represent the fluid volume that is enclosed by the Helmholtz resonator neck.

Fig. A.1 c) shows the d'Alembert free-body diagram of the fluid volume in the Helmholtz resonator neck. The forces acting on the fluid volume are

- the exciting force arising from the pressure outside of the resonator p acting on the resonator neck area: $F_{\mathrm{pressure,out}} = S_{\mathrm{HR}} p$,
- the force arising from the pressure inside the resonator cavity p_{cav} acting on the resonator neck: $F_{\mathrm{pressure,cav}} = S_{\mathrm{HR}} p_{\mathrm{cav}}$
  (in this study, a non-uniform pressure distribution in the cavity is taken into account as modeled in Eq. (3.17)),
- the friction force F_{friction}, arising from the resistance due to viscous losses in the boundary layer in the neck, and
- the inertial forces of the fluid volume: $F_{\mathrm{inertia}} = m_{\mathrm{HR}} a_{\mathrm{HR}}$, where m_{HR} and $a_{\mathrm{HR}} = -\omega^2 u_{\mathrm{HR}}$ are the mass and acceleration of the fluid volume, respectively.

F_{friction} describes the friction force due to viscous losses in the boundary layer in the neck and is split into

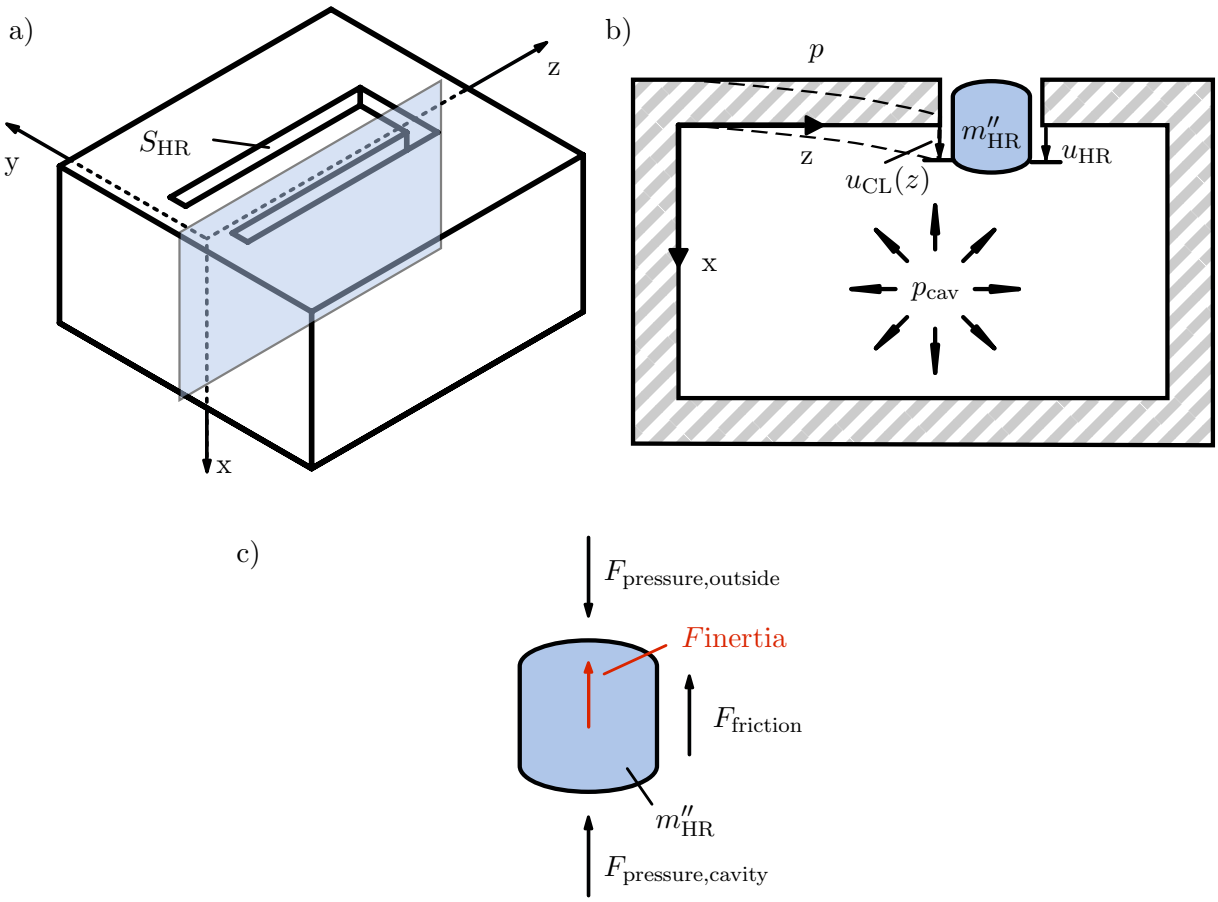

Figure A.1: a) Three-dimensional view of the resoantor. b) Cross section of the resonator. c) Dynamic free-body diagram (d'Alembert formulation) of the fluid volume. (b) and c) The blue colored areas represent the fluid volume that is enclosed by the Helmholtz resonator neck.)

- the part arising at the boundary between the fluid volume and the resonator body (which depends on the particle velocity of the air mass in the neck $v_{\mathrm{HR}} = \mathrm{i}\omega u_{\mathrm{HR}}$, since the resonator body is assumed to be rigid) and
- the part arising at the boundary between the fluid volume and the cantilever (which depends on the relative velocity between the air mass and the cantilever $v_{\mathrm{HR}} - \bar{v}_{\mathrm{CL}}(z) = \mathrm{i}\omega\,(u_{\mathrm{HR}} - \bar{u}_{\mathrm{CL}})$, where $\bar{u}_{\mathrm{CL}} = 1/l \int_0^l u_{\mathrm{CL}}(z)\,\mathrm{d}z$ is the mean displacement of the cantilever over the cantilever length l.

The friction force is directly proportional to the damping coefficient b_{HR} and the relative velocity of the air mass in the neck [108] and is thus calculated via

$$F_{\mathrm{friction}} = \frac{1}{2} b_{\mathrm{HR}} v_{\mathrm{HR}} + \frac{1}{2} b_{\mathrm{HR}} \left(v_{\mathrm{HR}} - \bar{v}_{\mathrm{CL}}\right). \tag{A.1}$$

The factor 1/2 means that approximately one half of the slit boundary is attributed to the cantilever and the other half to the top plate of the resonator.

The equilibrium of all forces is zero and leads to

$$F_{\text{pressure,outside}} - F_{\text{pressure,cavity}} - F_{\text{friction}} - F_{\text{inertia}} = 0. \tag{A.2}$$

After inserting the expression for the forces, dividing by the neck area S_{HR} and rearranging Eq. (A.2), the equation of motion of the fluid volume of the air inside the Helmholtz resonator neck results to

$$-\omega^2 u_{\text{HR}} m''_{\text{HR}} + \mathrm{i}\omega \frac{b_{\text{HR}}}{S_{\text{HR}}} \left(\frac{1}{2} u_{\text{HR}} + \frac{1}{2} \left(u_{\text{HR}} - \bar{u}_{\text{CL}} \right) \right) = p - p_{\text{cav}}, \tag{A.3}$$

where the ratio $b_{\text{HR}}/S_{\text{HR}}$ forms the resistance R_{HR}, calculated according to Eq. (3.5). The resistance accounts for the ratio of slit length to width, which has a significant influence on the viscous losses within the resonator.

A.2. Supplemental equations of the analytical model

Hereinafter the formulas are listed to calculate the elements of the system matrix in Eq. (3.39). The elements of the coupling vectors **b** in Eq. (3.26) and **c** in Eq. (3.31) can be determined by

$$b_{m_y m_z} = \frac{2l_y}{\pi m} \cos\left(\frac{\pi m_y}{2}\right) \sin\left(\frac{w\pi m_y}{2l_y}\right) \cdot \left[A_1 \cdot b_{m_{z1}} + B_1 \cdot b_{m_{z2}} + C_1 \cdot b_{m_{z3}} + D_1 \cdot b_{m_{z4}}\right], \tag{A.4}$$

where

$$b_{m_{z1}} = \frac{l_z \left(k_1 l_z \sin(k_1 l) \cos(\frac{\pi l m_z}{l_z}) - \pi m_z \cos(k_1 l) \sin(\frac{\pi l m_z}{l_z})\right)}{k_1^2 l_z^2 - \pi^2 m_z^2}, \tag{A.5}$$

$$b_{m_{z2}} = \frac{l_z \left(k_1 l_z \cos(k_1 l) \cos(\frac{\pi l m_z}{l_z}) + \pi m_z \sin(k_1 l) \sin(\frac{\pi l m_z}{l_z}) - k_1 l_z\right)}{\pi^2 m_z^2 - k_1^2 l_z^2}, \tag{A.6}$$

$$b_{m_{z3}} = \frac{l_z \left(k_1 l_z \sinh(k_1 l) \cos(\frac{\pi l m_z}{l_z}) + \pi m_z \cosh(k_1 l) \sin(\frac{\pi l m_z}{l_z})\right)}{k_1^2 l_z^2 + \pi^2 m_z^2}, \tag{A.7}$$

$$b_{m_{z4}} = \frac{l_z \left(k_1 l_z \cosh(k_1 l) \cos(\frac{\pi l m_z}{l_z}) + \pi m_z \sinh(k_1 l) \sin(\frac{\pi l m_z}{l_z}) - k_1 l_z\right)}{k_1^2 l_z^2 + \pi^2 m_z^2}. \tag{A.8}$$

The elements of the coupling vectors **e** in Eq. (3.27) and **g** in Eq. (3.36) are calculated

$$e_{m_y m_z} = e_{m_{y1}} \cdot e_{m_{z1}} + e_{m_{y2}} \cdot e_{m_{z2}} + e_{m_{y3}} \cdot e_{m_{z3}}, \tag{A.9}$$

where

$$e_{m_{y1}} = \frac{l_y}{m_y \pi} \left(\sin\left(\frac{m_y \pi (l_y - w)}{2l_y}\right) - \sin\left(\frac{m_y \pi (-2w_\mathrm{s} + l_y - w)}{2l_y}\right)\right), \tag{A.10}$$

$$e_{m_{y2}} = \frac{l_y}{m_y \pi} \left(\sin\left(\frac{m_y \pi (2w_\mathrm{s} + l_y + w)}{2l_y}\right) - \sin\left(\frac{m_y \pi (l_y + w)}{2l_y}\right)\right), \tag{A.11}$$

$$e_{m_{y3}} = \frac{l_y}{m_y \pi} \left(\sin\left(\frac{m_y \pi (2w_\mathrm{s} + l_y + w)}{2l_y}\right) - \sin\left(\frac{m_y \pi (-2w_\mathrm{s} + l_y - w)}{2l_y}\right)\right), \tag{A.12}$$

$$e_{m_{z1}} = e_{m_{z2}} = \frac{l_z}{m_z \pi} \sin\left(\frac{m_z \pi\, l}{l_z}\right), \tag{A.13}$$

$$e_{m_{z3}} = \frac{l_z}{m_z \pi} \left(\sin\left(\frac{m_z \pi (l + w_\mathrm{s})}{l_z}\right) - \sin\left(\frac{m_z \pi\, l}{l_z}\right)\right). \tag{A.14}$$

The value D in Eq. (3.32) can be obtained by

$$\begin{aligned} d =& w(A_1^2 d_1 + 2A_1 B_1 d_2 + 2A_1 C_1 d_3 + 2A_1 D_1 d_4 + B_1^2 d_5 + 2B_1 C_1 d_6 + 2B_1 D_1 d_7 \\ &+ C_1^2 d_8 + 2C_1 D_1 d_9 + D_1^2 d_{10}), \end{aligned} \tag{A.15}$$

where

$$d_1 = \frac{2k_1 l + \sin(2k_1 l)}{4k_1}, \tag{A.16}$$

$$d_2 = \frac{\sin^2(k_1 l)}{2k_1}, \tag{A.17}$$

$$d_3 = \frac{\cos(k_1 l)\sinh(k_1 l) + \sin(k_1 l)\cosh(k_1 l)}{2k_1}, \tag{A.18}$$

$$d_4 = \frac{\sin(k_1 l)\sinh(k_1 l) + \cos(k_1 l)\cosh(k_1 l) - 1}{2k_1}, \tag{A.19}$$

$$d_5 = \frac{l}{2} - \frac{\sin(2k_1 l)}{4k_1}, \tag{A.20}$$

$$d_6 = \frac{\sin(k_1 l)\sinh(k_1 l) - \cos(k_1 l)\cosh(k_1 l) + 1}{2k_1}, \tag{A.21}$$

$$d_7 = \frac{\sin(k_1 l)\cosh(k_1 l) - \cos(k_1 l)\sinh(k_1 l)}{2k_1}, \tag{A.22}$$

$$d_8 = \frac{2k_1 l + \sinh(2k_1 l)}{4k_1}, \tag{A.23}$$

$$d_9 = \frac{\sinh^2(k_1 l)}{2k_1}, \tag{A.24}$$

$$d_{10} = \frac{\sinh(2k_1 l) - 2k_1 l}{4k_1}. \tag{A.25}$$

The value h is calculated

$$h = w\left(A_1 \frac{\sin(k_1 l)}{k_1} + B_1 \frac{1 - \cos(k_1 l)}{k_1} + C_1 \frac{\sinh(k_1 l)}{k_1} + D_1 \frac{\cosh(k_1 l) - 1}{k_1}\right). \tag{A.26}$$

A.3. Supplemental parameter study with considered damping behavior

In this section, the influence of the slit width w_s on the resonance frequencies is studied exemplarily with taking into account the damping behavior. The resonator was modeled according to Table 4.1. Fig. A.2 a) shows the influence of the slit width w_s on the real part of f_1, f_2, f_{HR} and f_{CL1}. The influence on the real part of the modified cantilever resonance frequency $f_{CL,V}$ is depicted in Fig. A.2 b) and the influence on the coupling parameter C_{HRCL} is shown in Fig. A.2 c). In Fig. A.2, the bold lines show the real part of the complex-valued calculated resonance frequencies, where the damping behavior is considered in the calculations. For comparison, the calculated results of the resonance frequencies neglecting the damping are plotted as thin lines.

Fig. A.2 shows the same quantitative behavior of the resonance frequencies as the parameter study neglecting the damping behavior, plotted in Fig. 5.4. The explanations are repeated here, to avoid flipping back and forth: As the slit width increases, the neck area S_{HR} increases and therefore the real part of the resonance frequency of the Helmholtz resonator f_{HR} increases. The real part of the resonance frequency of the cantilever in vacuo f_{CL1} is not affected and remains constant. For a slit width where f_{HR} and f_{CL1} are equal, f_1 and f_2 approach a minimum frequency difference, but do not become equal, signifying that the system is strongly coupled at this resonator geometry.

For small and large values of the slit width, the real part of the resonance frequencies of the coupled system approach those of the uncoupled system f_{HR} and f_{CL1}, where no offset

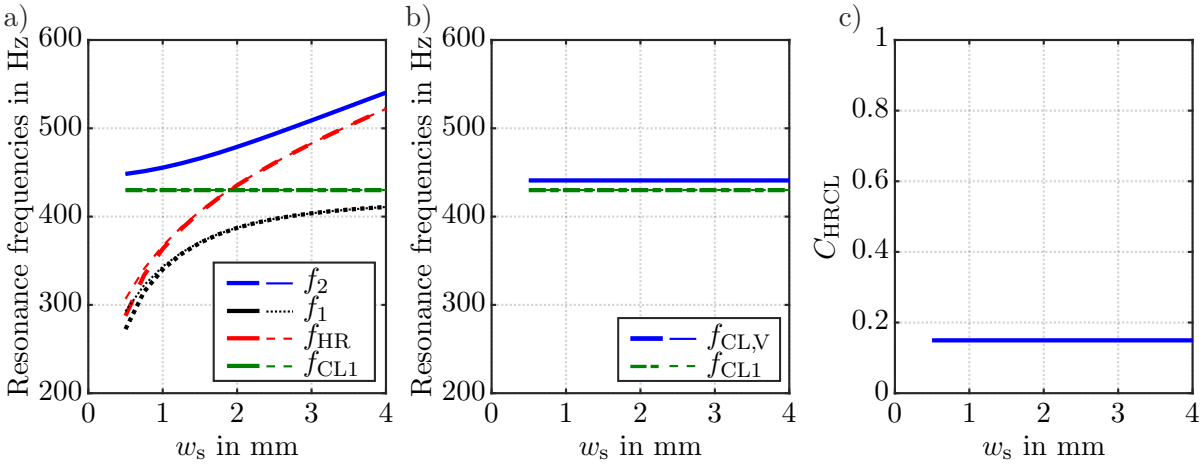

Figure A.2: a)-b) Real part of the calculated resonance frequencies of the resonator system depending on the slit width w_s of the resonator neck. Bold lines: analytical model, calculation considering damping behavior. Thin lines: without damping behavior. a) Comparison of f_1, f_2, f_{HR} and f_{CL1}. b) Comparison of f_{CL1} and $f_{CL,V}$. c) Coupling parameter C_{HRCL} depending on the slit width w_s of the resonator neck.

is visible. This means that, even with considering damping, the slit width does not affect the coupling behavior between the oscillators. This is in line with former explanations, that the coupling behavior depends on the stiffening effect of the cavity and on the physical parameters of the cantilever, such as density and Young's modulus, which remain constant.

However, in Fig. A.2 a) it can be seen that for small values of w_s ($w_\mathrm{s} < 1$ mm) the real parts of the resonance frequency of the Helmholtz resonator f_HR and of the first resonance frequency of the coupled system f_1 calculated with considering the damping (bold lines) deviate from the resonance frequencies, when the damping is neglected (thin lines). The narrower the slit of the resonator, the higher the viscous losses, leading to lower resonance frequencies of the Helmholtz resonator, as seen in Ref. [56]. For small values of w_s, the lower resonance frequency of the coupled system f_1 is dominated by the resonance frequency of the Helmholtz resonator f_HR, and thus when damping is considered in the calculations, f_1 is also lower than when damping is neglected. The higher resonance frequency of the coupled system f_2 approaches f_CL1 for small values of w_s and is not affected by the damping behavior.

In Chapter 3, it was stated after Ref. [25] that the damped angular resonance frequency ω_d can be estimated with a relative error lower than 2 % by $\omega_\mathrm{d} \approx \omega_0(1 + \mathrm{i}\zeta)$ as long as $\zeta < 0.2$. To verify this behavior, the calculated damping ratios of the complex-valued resonance frequencies ($\zeta = \mathrm{Im}(\omega_\mathrm{d})/\mathrm{Re}(\omega_\mathrm{d})$) and the relative error between the resonance frequency without damping and the real part of the resonance frequency with damping are plotted over the slit width w_s in Fig. A.3 a) and b), respectively.

Fig. A.3 shows that for slit width $w_\mathrm{s} < 0.75$ mm the damping ratios of f_1 and f_HR rise above $\zeta > 0.2$, while the corresponding relative errors are higher than 2 %, which confirms the estimation from Ref. [25]. For larger slit width, the relative error is lower than 2 %

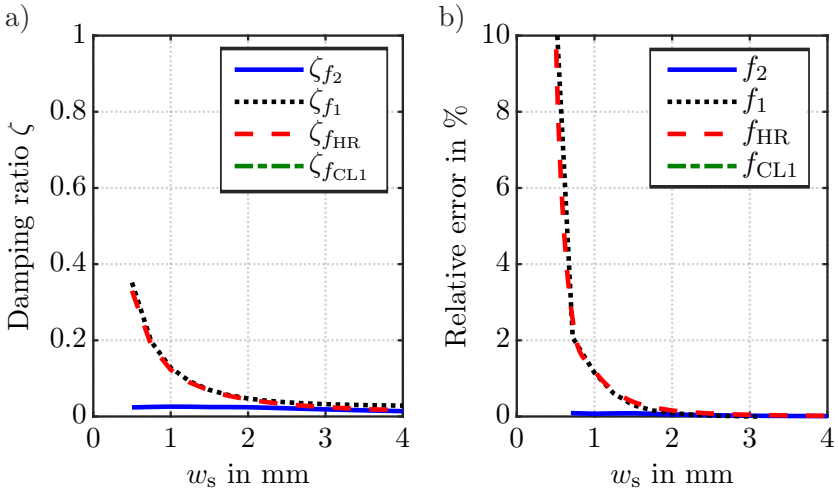

Figure A.3: Calculated damping ratios and relative errors of the resonance frequencies of the resonator system depending on the slit width w_s a) Damping ratio ζ. b) Relative errors.

for all calculated resonance frequencies. That means for this resonator configuration the damped angular resonance frequency can be estimated accurately by Eq. (3.46) for slit width larger than 0.75 mm. This the case for all other parameter studies and for all physical models used in the experiments.